Progress Towards a High Precision Measurement of the Neutron Spin–Electron Angular Correlation in Polarized Neutron β Decay with Ultra-Cold Neutrons

Thesis by

Junhua Yuan

In Partial Fulfillment of the Requirements
for the Degree of
Doctor of Philosophy

California Institute of Technology
Pasadena, California

2006
(Defended October 3, 2005)

Acknowledgements

I would like to express my sincere acknowledgment of the many individuals who helped me throughout this long journey. The very first person I would like to fully acknowledge is my research advisor and mentor, Professor Bradley Filippone, for his guidance, constant support, and strong influence throughout all my research development. It has been a great privilege for me to work with Professor Filippone and learn from his experience.

I would also like to acknowledge Professors Frank Porter, Robert Mckeown, and Mark Wise for kindly participating in my thesis committee, for their time and helpful suggestions.

I would also like to acknowledge a number of people who have been very supportive all those years. I would like to specifically thank Dr. Takeyasu Ito, Dr. Jeff Martin, Dr. Bryan Tipton, and Dr. Brad Plaster, for all the fruitful discussions, valuable suggestions, and unconditional help. I would also like to thank Robert Carr for his help, Pat Huber for his computer support, Jim Pendlay and Ray Cortez for their technical help, and Kim Stapp and Leona Kershaw for their administrative help. I would also like to acknowledge members of the UCNA collaboration who made this experiment going.

Finally, I would like to thank my whole family for the encouragement, especially my wife, Rongjing, for her love, support, and understanding.

Abstract

A measurement of the angular correlation between the neutron spin and the direction of emission of the electron in polarized neutron decay (the "A" asymmetry), when combined with results from the neutron lifetime, provides a determination of the Cabibbo-Kobayashi-Maskawi (CKM) matrix element V_{ud}. The value of V_{ud} determined from neutron beta decay can also be compared with the value determined from measurements of the superallowed $0^+ \rightarrow 0^+$ nuclear beta decay, and the value determined by requiring that the CKM matrix be unitary. This provides a sensitive way to search for new physics beyond the standard model.

Four measurements of the "A" asymmetry using cold neutron beams at reactor were carried out since 1985, all of which quote a combined statistical and systematic uncertainty of about 1% in the determination of "A." Unfortunately, the agreement between these four measurements is poor and the results also disagree with both the $0^+ \rightarrow 0^+$ nuclear beta decay and the CKM unitarity results. In order to understand the origin of these discrepancies, a high precision (0.2%) measurement of "A" using ultra-cold neutrons (UCN) is in progress at the Los Alamos Neutron Science Center (the UCNA experiment), with very different systematic effects than those in the reactor experiments.

The essential elements of the UCNA experiments, including a dedicated spallation-driven solid deuterium UCN source developed by the collaboration, the UCN guides, and the superconducting spectrometer (SCS) including the beta detector system, are described, focusing on the UCN source and the spectrometer. The developed UCN source produced the highest stored density of UCN ever. The UCN were successfully transported out of the source along several meters of diamond-coated quartz guide tubes through the field of a 7-Telsla pre-polarizing magnet. The SCS magnet was successfully commissioned, demonstrating 10^{-4} uniformity over 3 meters. The beta detector package including a Multi-Wire Proportional Chamber (MWPC) backed with a plastic scintillator detector was constructed. Studies of the energy response, linearity, timing response, and position resolution of the detector package were carried out using a home-built 135keV electron gun and a Helmholtz spectrometer, and the results are presented. Studies of systematics for the UCNA experiment based on a full GEANT4 Monte Carlo simulation are presented. A large and uncharacterized part of the systematics, the electron backscattering of low energy electrons, was measured in detail using the 135keV electron gun. The results from the electron backscattering studies are presented.

Contents

List of Figures

List of Tables

Chapter 1

Introduction

1.1 Neutron beta decay in the standard model and the “A” asymmetry

In the standard model of elementary particles, the weak charged-current interaction of quarks is parameterized by the quark-mixing Cabibbo-Kobayashi-Maskawa (CKM) matrix, which rotates the quark mass eigenstates (d, s, b) to the weak eigenstates (d’, s’, b’)

$$\begin{pmatrix} d' \\ s' \\ b' \end{pmatrix} = \begin{pmatrix} V_{\mathrm{ud}} & V_{\mathrm{us}} & V_{\mathrm{ub}} \\ V_{\mathrm{cd}} & V_{\mathrm{cs}} & V_{\mathrm{cb}} \\ V_{\mathrm{td}} & V_{\mathrm{ts}} & V_{\mathrm{tb}} \end{pmatrix} \begin{pmatrix} d \\ s \\ b \end{pmatrix}$$

The Standard Model does not predict the content of the CKM matrix. The values of individual matrix elements are determined from weak decays of the relevant quarks. Since only three quark generations exist in the Standard Model, the CKM matrix must be unitary. For the top row of the CKM matrix, unitarity requires that

$$|V_{\mathrm{ud}}|^2 + |V_{\mathrm{us}}|^2 + |V_{\mathrm{ub}}|^2 = 1.$$

Neutron and nuclear beta decay can be used to determinate the largest matrix element V_{ud}, which, combining with V_{us} determined from Kaon decays and V_{ub} from B decays, leads to a direct test of CKM unitarity.

In neutron decay, a d-quark transforms into a u-quark with the emission of an electron and an electron antineutrino via W boson exchange. The transition matrix for d decay is

$$T_{fi} = \frac{g^2}{8} V_{\mathrm{ud}} \bar{\Psi}_u \gamma_\mu (1-\gamma_5) \Psi_d \frac{g^{\mu\nu} - q^\mu q^\nu / m_W^2}{q^2 - m_W^2} \bar{\Psi}_e \gamma_\nu (1-\gamma_5) \Psi_{\nu_e},$$

where g is the weak coupling constant, and q is the momentum transfer between quark and lepton.

Since $q^2 << m_W^2$ in neutron beta decay, T_{fi} is reduced to

$$\begin{aligned} T_{fi} &= \frac{G_F}{\sqrt{2}} V_{\rm ud} \bar{\Psi}_u \gamma_\mu (1-\gamma_5) \Psi_d \cdot \bar{\Psi}_e \gamma^\mu (1-\gamma_5) \Psi_{\nu_e} \\ &= \frac{G_F V_{\rm ud}}{\sqrt{2}} J^h_\mu J^{l\mu}. \end{aligned}$$

This is the well-known effective 4-fermion interaction with Fermi decay constant G_F:

$$\frac{G_F}{\sqrt{2}} = \frac{g^2}{8m_W^2}.$$

$J^{h\mu}$ and $J^{l\mu}$ are hadronic and leptonic weak currents:

$$\begin{aligned} J^{h\mu} &= \bar{\Psi}_u \gamma^\mu (1-\gamma_5) \Psi_d = J^{h,V}_\mu - J^{h,A}_\mu \\ J^{l\mu} &= \bar{\Psi}_e \gamma^\mu (1-\gamma_5) \Psi_{\nu_e}. \end{aligned}$$

Since the quarks are strongly interacting particles confined in nucleons, the hadronic matrix elements must be evaluated for nucleons rather than for quarks. These are constrained by the requirement of Lorentz invariance and the observation of parity violation:

$$\begin{aligned} J^{h,V}_\mu &= \bar{\Psi}_p [g_V(q^2)\gamma_\mu - i\frac{g_{WM}(q^2)}{2M_p}\sigma_{\mu\nu}q^\nu + g_S(q^2)q_\mu]\Psi_n \\ J^{h,A}_\mu &= \bar{\Psi}_p [g_A(q^2)\gamma_\mu\gamma_5 - i\frac{g_T(q^2)}{2M_p}\sigma_{\mu\nu}q^\nu\gamma_5 + g_P(q^2)q_\mu\gamma_5]\Psi_n, \end{aligned}$$

where $q_\mu = p_\mu - p'_\mu$ is the 4-moment transfer from the hadrons to the leptons. The form factors g_V, g_{WM}, g_S, g_A, g_T, and g_P are known as vector, weak magnetism, induced scalar, axial vector, induced tensor, and induced pseudoscalar coupling constants. The recoil parameter $R = \frac{E_0}{M_n} \sim 10^{-3}$ is small so that the momentum-transfer dependence of all form factors is often neglected (E_0 is the maximum total energy of electron). Conservation of the Vector Current(CVC) requires that:

$$\begin{aligned} g_V(0) &= 1 \\ g_{WM}(0) &= \kappa_p - \kappa_n = 3.70 \\ g_S(0) &= 0, \end{aligned}$$

where $\kappa_p = 1.79$ and $\kappa_p = -1.91$ are the anomalous magnetic moments of proton and neutron respectively.

As far as G-parity is concerned, these form factors can be divided into two classes. A G-parity transformation is composed of a charge conjugation C and an isospin rotation of π about the I_2 axis:

$G = Ce^{i\pi I_2}$. First class currents are defined by

$$\begin{aligned} GV_\mu^{\mathrm{I}}G^{-1} &= V_\mu^{\mathrm{I}} \\ GA_\mu^{\mathrm{I}}G^{-1} &= -A_\mu^{\mathrm{I}}, \end{aligned}$$

while the second class currents satisfy

$$\begin{aligned} GV_\mu^{\mathrm{II}}G^{-1} &= -V_\mu^{\mathrm{II}} \\ GA_\mu^{\mathrm{II}}G^{-1} &= A_\mu^{\mathrm{II}}. \end{aligned}$$

The g_V, g_{WM}, g_A, and g_P terms are first class and the g_S and g_T terms are second class according to the definition. Second class currents do not contribute to neutron beta decays in the standard model [1], and any observable second class currents would have important implications for physics beyond the Standard Model [2].

In solving for neutron decay rate, g_P enters in terms smaller than the recoil order, thus g_P is negligible in neutron decay. The Lagrangian for neutron beta decay within the Standard Model without second class currents and g_P can be written as:

$$\mathcal{L}_{int} = \frac{G_F}{\sqrt{2}} V_{\mathrm{ud}} \bar{\Psi}_p [\gamma_\mu (1 - \lambda\gamma_5) - i\frac{\kappa_p - \kappa_n}{2M_p}\sigma_{\mu\nu}q^\nu]\Psi_n \bar{\Psi}_e \gamma^\mu (1-\gamma_5)\Psi_{\nu_e},$$

where $\lambda = g_A/g_V$. Hence, in the Standard Model only two parameters, λ and V_{ud} are needed to describe free neutron beta decay.

Based on the interaction Lagrangian, the transition rate for a polarized neutron with no detected polarization of the electron can be written as [3]:

$$dW(\vec{\sigma}_n, \vec{p}_e, \vec{p}_{\bar{\nu}}) \propto p_e E_e (E_0 - E_e)^2 \,\mathrm{d}E_e \,\mathrm{d}\Omega_e \,\mathrm{d}\Omega_{\bar{\nu}} [1 + a\frac{\vec{p}_e \cdot \vec{p}_{\bar{\nu}}}{E_e E_{\bar{\nu}}} + <\vec{\sigma}_n> \cdot (A\frac{\vec{p}_e}{E_e} + B\frac{\vec{p}_{\bar{\nu}}}{E_{\bar{\nu}}} + D\frac{\vec{p}_e \times \vec{p}_{\bar{\nu}}}{E_e E_{\bar{\nu}}})],$$

where a, A, B and D are correlation coefficients. For example, A describes the angular correlation between the neutron spin and electron momentum. Within the Standard Model, a, A, B and D are given in lowest order (ignoring here proton recoil and radiative corrections) by

$$\begin{aligned} a &= \frac{1 - |\lambda|^2}{1 + 3|\lambda|^2} \\ A &= 2\frac{-|\lambda|^2 + Re(\lambda)}{1 + 3|\lambda|^2} \end{aligned}$$

$$\begin{aligned} B &= 2\frac{|\lambda|^2 + Re(\lambda)}{1+3|\lambda|^2} \\ D &= 2\frac{Im(\lambda)}{1+3|\lambda|^2}. \end{aligned} \tag{1.1}$$

The above formulae are only good to the order of 1%. When time reversal invariance is assumed, λ is real and D vanishes. If better precision is needed, each of these coefficients has to be corrected by inclusion of radiative corrections plus additional terms of recoil order as discussed in the next section.

The neutron lifetime τ_n is given by

$$\frac{1}{\tau_n} = \frac{G_F^2|V_{\mathrm{ud}}|^2}{2\pi^3} m_e^5(1+3\lambda^2)f^R, \tag{1.2}$$

where f^R is the radiatively corrected phase space factor.

A measurement of any of the coefficients a, A and B can determine the value of λ. Combining with a measurement of τ_n, the value of V_{ud} can be obtained.

It can be shown from equations 1.1 that

$$\frac{\delta|\lambda|}{|\lambda|} = 0.27\frac{\delta a}{a} = 0.24\frac{\delta A}{A} = 2.0\frac{\delta B}{B}.$$

Thus λ is much more sensitive to the precise value of a or A than B. Therefore, precise measurement of λ can be obtained from a measurement of either a or A.

Historically, measurement of "A" has provided the most precise value for λ. Up to now there were only three experiments to measure "a", and the best measurement was published in 1978 with an accuracy of 5%. The main reason for the poor accuracy is that all three measurements of "a" relied on precise spectrometry of protons with a traditional magnetic spectrometer. The 1978 result required the proton energy spectral shape to be measured to a precision of less than 0.5%, which is technically challenging considering that the proton energy is very low (maximum is 751 eV). Two experiments are proposed to measure "a" with an accuracy better than 1%. One is the "aSPECT" project [4], which uses a retardation spectrometer to perform precise proton spectrometry. The other is proposed to construct an asymmetry that directly yields "a", without requiring precise spectroscopy [5].

1.2 Radiative corrections and recoil corrections

The UCNA experiment was proposed to measure "A" to the order of 0.2%, while τ_n has already been measured to about 0.1% (However, Serebrov et al. [6] published in 2005 a new measurement of τ_n resulting (878.5±0.8)s, which differed from the previous world average value (885.7±0.8)s by 6.5

standard deviations). To obtain precise values of λ and V_{ud}, theoretical uncertainties in the formula relating A and λ(equation 1.1), τ_n, λ and V_{ud}(equation 1.2) should be calculated to better than 0.1%.

1.2.1 Recoil corrections

Based on the interaction Lagrangian:

$$\mathcal{L}_{int} = \frac{G_F}{\sqrt{2}} V_{\mathrm{ud}} \bar{\Psi}_p [g_V \gamma_\mu - g_A \gamma_\mu \gamma_5 - i \frac{g_{WM}}{2M_p} \sigma_{\mu\nu} q^\nu] \Psi_n \bar{\Psi}_e \gamma^\mu (1-\gamma_5) \Psi_{\nu_e},$$

the decay rate can be written as

$$\frac{dW}{dE_e d\Omega_e} \propto (a(x) + b(x)\beta P cos\theta_e),$$

where $\beta = p/E$, $x = E/E_0$, $\epsilon = (M_e/M_n)^2 \sim 0.3 \times 10^{-6}$, and P is the neutron polarization. The functions a(x) and b(x) are quadratic forms in the form factors g_V, g_A and g_{WM}, with coefficients that depend on x. Keeping the terms of $\mathcal{O}(R)$, where $R = \frac{E_0}{M_n} \sim 10^{-3}$ is the recoil parameter, and neglecting those of $\mathcal{O}(\epsilon, R^2)$, the coefficients in a(x) are shown in Table. 1.1, and the coefficients in b(x) are shown in Table. 1.2 [7].

Table 1.1: Terms in a(x)

Form factor	Coefficients		
	x^{-1}	1	x
g_V^2	0	1	$-4R$
g_A^2	$-2\epsilon/R$	$3-2R$	$-8R$
$g_V g_A$	$-2\epsilon/R$	$-2R$	$4R$
$g_V g_{WM}$	0	0	0
$g_A g_{WM}$	$-2\epsilon/R$	$-2R$	$4R$

Neglecting the momentum-transfer dependence of the form factors, the asymmetry A including recoil order corrections is obtained as [8, 9]

$$\begin{aligned} A &= \frac{b(x)}{a(x)} \\ &= \frac{-2\lambda^2 + 2\lambda}{1+3\lambda^2} + \frac{2(\lambda+\mu)}{(1+3\lambda^2)^2}[(\lambda^2 + \frac{2}{3}\lambda - \frac{1}{3})R + (-\lambda^3 - 3\lambda^2 - \frac{5}{3}\lambda + \frac{1}{3})Rx + 2\lambda^2(-\lambda+1)\frac{\epsilon}{Rx}] + \mathcal{O}(R^2, \epsilon) \\ &= A_0[1 + A_{\mu m}(A_1 E_0 + A_2 E + A_3/E)] + \mathcal{O}(R^2, \epsilon) \end{aligned}$$

Table 1.2: Terms in b(x)

Form factor	Coefficients	
	1	x
g_V^2	$-\frac{2}{3}R$	$\frac{2}{3}R$
g_A^2	$-2+\frac{4}{3}R$	$\frac{14}{3}R$
g_Vg_A	$2+\frac{2}{3}R$	$-\frac{32}{3}R$
g_Vg_{WM}	$-\frac{2}{3}R$	$\frac{2}{3}R$
g_Ag_{WM}	$\frac{4}{3}R$	$-\frac{10}{3}R$

where

$$\begin{aligned} A_{\mu m} &= \frac{\lambda+\mu}{\lambda(1-\lambda)(1+3\lambda^2)M_n} \\ A_1 &= \lambda^2+\frac{2}{3}\lambda-\frac{1}{3} \\ A_2 &= -\lambda^3-3\lambda^2-\frac{5}{3}\lambda+\frac{1}{3} \\ A_3 &= 2\lambda^2(1-\lambda). \end{aligned}$$

Here $\mu = \mu_p - \mu_n$ is the difference between the total magnetic moments of proton and neutron, E is the electron total energy with end point E_0, and A_0 is the lowest order formula in terms of λ (equation 1.1).

Including the momentum-transfer dependence of the form factors $g_i(q^2) = g_i(0)[1+t_i\frac{q^2}{M_n^2}+\mathcal{O}(q^4)]$ yields an additional term of $\mathcal{O}(R)$:

$$A = A_{q^2=0} + \frac{4\lambda-8\lambda^2-12\lambda^3}{(1+3\lambda^2)^2}(t_V-t_A)R(1-x),$$

where $t_V - t_A \sim -0.10 \pm 0.15$. Thus the additional term induces an uncertainty to “A” at the level of 0.1%.

1.2.2 Radiative corrections

Radiative corrections include both virtual and photon Bremsstrahlung contributions. Usually the bremsstrahlung photons are not detected in neutron beta decay experiments. Sirlin has introduced in his paper [10] a separation of the order-α radiative corrections into model independent (MI) and model dependent(MD) parts. The MI(outer) correction is defined as the sum of the photon bremsstrahlung correction and the small energy part of the virtual correction. The MD(inner) correction contains the medium and large energy(asymptotic) parts of the virtual contributions. The MD correction leads to a redefinition of g_V and g_A, which are used in the formula for any measurable quantity(τ_n, a, A, B) in neutron beta decay [10, 11, 12, 13, 14].

The MD correction to "A" is absorbed into the redefinition of g_V and g_A. The MI correction to "A" is on the order of 0.1% [12, 13, 14]. A numerical formula is obtained for the MI correction to "A" as [14]

$$A(E) = (1 - 0.00163 + 0.00210/E + 0.000491E)A_0,$$

where E is the total energy of electron in units of MeV. A_0 is the lowest order formula in terms of λ(equation 1.1).

A formula relating τ_n, λ and V_{ud} including one- and dominant two-loop radiative corrections and other small corrections from proton recoil, finite nucleon size etc. [8], has been obtained as [15]

$$|V_{\mathrm{ud}}|^2 = \frac{4908 \pm 4sec}{\tau_n(1+3\lambda^2)}.$$

1.3 World status of measurements of "A"

Up to today, all measurements of "A" have been made with neutron beams from reactors. Prior to 1990, essentially all of the measurements of angular correlations in neutron beta decay agreed reasonably well with one other albeit with large uncertainties:

$$A_0 = -0.1145 \pm 0.0015,$$

resulting in a common value of λ:

$$\lambda = -1.261 \pm 0.004$$

Since 1985, several measurements of the beta asymmetry("A") have been carried out. We now go on to discuss each of them.

PERKEO (1988)

A precise measurement [16, 17, 18] was made at the Institut Laue-Langevin (ILL) using the PERKEO spectrometer. In this experiment, a beam of cold neutrons are polarized by a super-mirror polarizer, strongly collimated to restrict the beam divergence, and then pass through the bore of a 2 m long superconducting magnet. A small fraction ($\sim 10^{-6}$) of the neutrons decay within the solenoid. The electrons spiral along the field lines and are deflected out of the beam at the ends of the solenoid by a set of transverse field coils. The electrons are then detected in plastic scintillators at the two ends of the solenoid. In this apparatus the signal-to-noise was improved by collecting all the electrons from a large decay volume. Another advantage to this scheme is that many electrons that backscatter from the scintillators either are reflected back into the scintillator by the magnetic mirror effect, or are detected a few tens of nanoseconds later in the scintillator at the other end. Timing information allows one to determine which scintillator was hit first, thus significantly reducing effects due to backscattering.

The PERKEO experiment determined the value of A_0 to be:

$$A_0 = -0.1146 \pm 0.0019,$$

resulting in a determination of λ of

$$\lambda = -1.262 \pm 0.005$$

The experiment was limited predominantly by systematic effects associated with the transverse magnetic fields at the ends of the solenoid, differences in the backgrounds in the two detectors, and the determination of the absolute neutron polarization.

IAE-PNPI (1991)

A measurement in which the recoil proton was measured in coincidence with the electron was carried out by the Institute for Atomic Energy (IAE) and the Petersburg Nuclear Physics Institute (PNPI) at the Gatchina reactor [19]. The experiment did not use a super-mirror polarizer and thus had relatively low polarization ($\sim 76\%$).

The IAE experiment determined the value of A_0 to be:

$$A_0 = -0.1116 \pm 0.0014,$$

resulting in a determination of λ of

$$\lambda = -1.2544 \pm 0.0036$$

The largest systematic effect in this experiment was the large correction required for the low polarization.

A claim was made later that the technique used to correct for the polarization in this experiment was in error. The magnitude of this effect is such as to reduce the value of A_0. The revised correction results in a new value of A_0 from this experiment [20]:

$$A_0 = -0.1135 \pm 0.0014,$$

resulting in a determination of λ of

$$\lambda = -1.2594 \pm 0.0038$$

ILL-TPC (1995)

This measurement was carried out at the Grenoble reactor at the Institute Laue-Langevin and involved having a cold neutron beam pass through a Time Projection Chamber (TPC). The direction of the track was reconstructed with crude angular information using the TPC. The result of the ILL-TPC measurement was [21]:

$$A_0 = -0.1160 \pm 0.0015,$$

resulting in a determination of λ of

$$\lambda = -1.266 \pm 0.0040$$

The primary systematic problem in this experiment was the background which resulted in 0.8% uncertainty in the background subtraction.

PERKEO II (2002)

An improved version of the PERKEO spectrometer, called PERKEO II, has provided new results. The primary difference is that instead of a superconducting solenoid, the experiment used a completely transverse magnetic field produced by a set of superconducting coils. This effectively reduces the systematic uncertainty due to magnetic mirror effects. The value of A_0 measured in Perkeo II was [22] :

$$A_0 = -0.1189 \pm 0.0012,$$

resulting in a determination of λ of

$$\lambda = -1.274 \pm 0.003$$

The remaining dominant limitations to the precision of a new measurement with PERKEO II are due to the precision with which the absolute value of the polarization can be measured and the backgrounds associated with the cold neutron beam from the reactor. The systematic uncertainty associated with the polarization measurement was primarily due to possible depolarization caused by the chopper wheel (which proved to be slightly magnetic) used to measure the wavelength dependence of the polarization. This problem has been addressed in a second set of measurements carried out at the ILL. The results from the improved PERKEO II run resulted in a value of [23]:

$$A_0 = -0.1189 \pm 0.0008,$$

resulting in a determination of λ of

$$\lambda = -1.2740 \pm 0.0021$$

Thus, the central value basically did not change but the uncertainty was reduced by 33%.

Combining both data sets resulted in a value of [24]:

$$A_0 = -0.1189 \pm 0.0007,$$

resulting in a determination of λ of

$$\lambda = -1.2739 \pm 0.0019$$

Summary

A summary of the previous measurements of “A” is shown in Table. 1.3. The results of the recent four measurements of beta asymmetry are shown in Fig. 1.1, along with V_{ud} determined from $0^+ \rightarrow 0^+$ nuclear beta decay [25], the unitarity of the CKM matrix(with values of V_{us} and V_{ub} from Particle Data Group (PDG) [26]). Fig. 1.1 is shown as V_{ud} versus λ. As mentioned before, λ determined from a beta asymmetry measurement combined with a measurement of the neutron lifetime τ_n can determine the value of V_{ud}. In Fig. 1.1, τ_n is a world average from PDG.

Table 1.3: Previous measurements of the beta asymmetry

Experiment	A_0	λ	Dominant systematic errors
Before 1990	-0.1145 ± 0.0015	-1.261 ± 0.004	(world average)
PERKEO	-0.1146 ± 0.0019	-1.262 ± 0.005	Detector backgrounds, absolute neutron polarization
IAE-PNPI	-0.1135 ± 0.0014	-1.2594 ± 0.0038	Low neutron polarization(76%)
ILL-TPC	-0.1160 ± 0.0015	-1.266 ± 0.0040	Detector backgrounds (induced 0.8% uncertainty)
PERKEO II	-0.1189 ± 0.0007	-1.274 ± 0.0019	Detector backgrounds, absolute neutron polarization

Fig. 1.1 clearly shows the disagreement between the four recent measurements of the beta asymmetry, and the disagreement with both the $0^+ \rightarrow 0^+$ beta decay and the CKM unitarity results. In

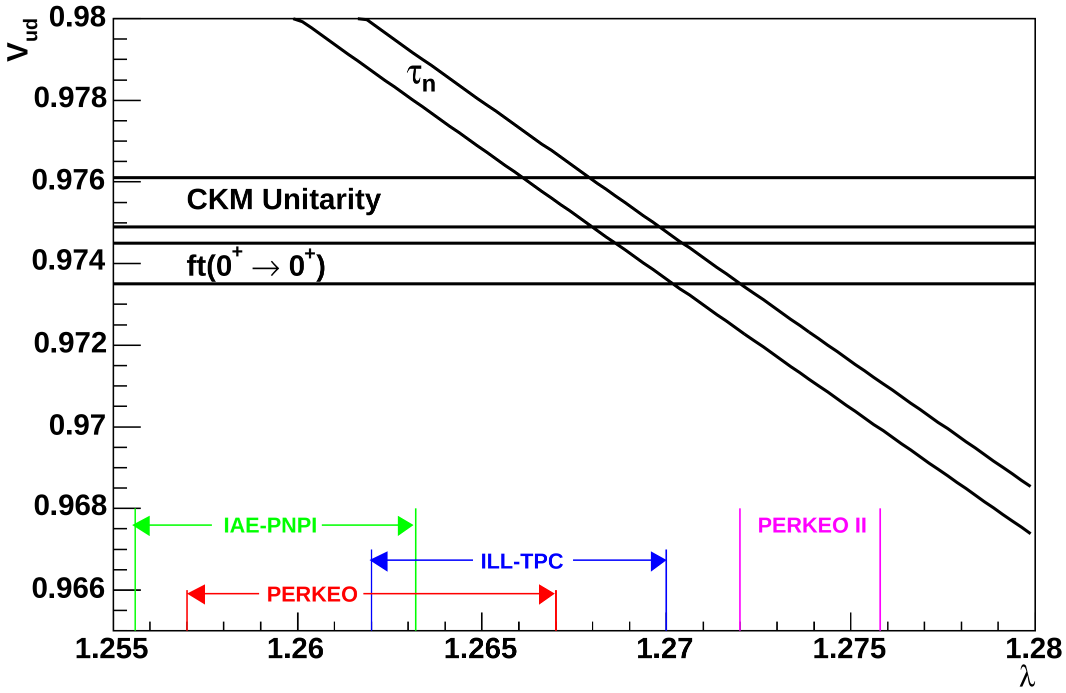

Figure 1.1: Comparison of $V_{\rm ud}$ determined from $0^+ \rightarrow 0^+$ nuclear beta decay, the unitarity of the CKM matrix, and the world recent measurements of beta asymmetry.

order to understand the origin of the discrepancies, it is essential to carry out new measurements with very different systematic effects than those in the reactor experiments. It is also equally important to improve the accuracy of these experiments in order to search for new physics with increased sensitivity.

The UCNA experiment is proposed to measure the beta asymmetry using Ultra-Cold Neutrons(UCN) from a spallation source, which provides significant advantages over reactor beam experiments, in terms of background and UCN polarization.

1.4 Design of the UCNA experiment

The key components of the UCNA experiment are the proton beamline, the UCN source, the Pre-Polarizer Magnet (PPM), the UCN guides, the UCN Polarizer/AFP, and the superconducting spectrometer (SCS), as shown schematically in Fig. 1.2.

The proton beamline is comprised of three small bending magnets(total deflection 3^o), four quadrupole magnets, and several steering magnets. The beamline is designed to transport 10 μC pulses(duration of each pulse ~ 600 μs) of 800 MeV protons to the UCN source. Proton pulses from the LANSCE proton accelerator can be deflected on demand from the linac using a Fast Kicker magnet. Normal operation of the beamline is to provide 4 proton pulses in a fraction of 1 s and to repeat this operation every 10 s.

The UCN source uses the short pulse of protons from the LANCSE proton accelerator incident on a tungsten spallation target to produce a flux of MeV neutrons. These neutrons are first cooled to < 100 K using conventional cold moderators, and then cooled to UCN (< 4 mK) using phonon interactions in the Solid Deuterium (SD2).

UCN guide tubes confine the UCN produced by the source and transport them to the superconducting spectrometer. The inner surfaces of these guides are coated with a diamond-like film that is laid down by pulsed laser deposition of graphite to ensure total external reflection of the UCN and to maintain a very high level of polarization of the UCN.

The UCN are polarized by passage through a 7 T solenoid magnet (Polarizer), which uses an analog of the Stern-Gerlach effect to polarize UCN. The spin of the UCNs can be flipped rapidly using an Adiabatic Fast Passage (AFP) resonator prior to injection into the 1 T superconducting spectrometer.

The spectrometer is a 4 m long superconducting solenoid with an entrance port transverse to the axis of the solenoid. Electrons from the neutron decay spiral around the spectrometer field and are directed into detectors at either end of the solenoid. The electron detectors(comprised of a multi-wire proportional chamber backed by a plastic scintillator) provide both energy and position information.

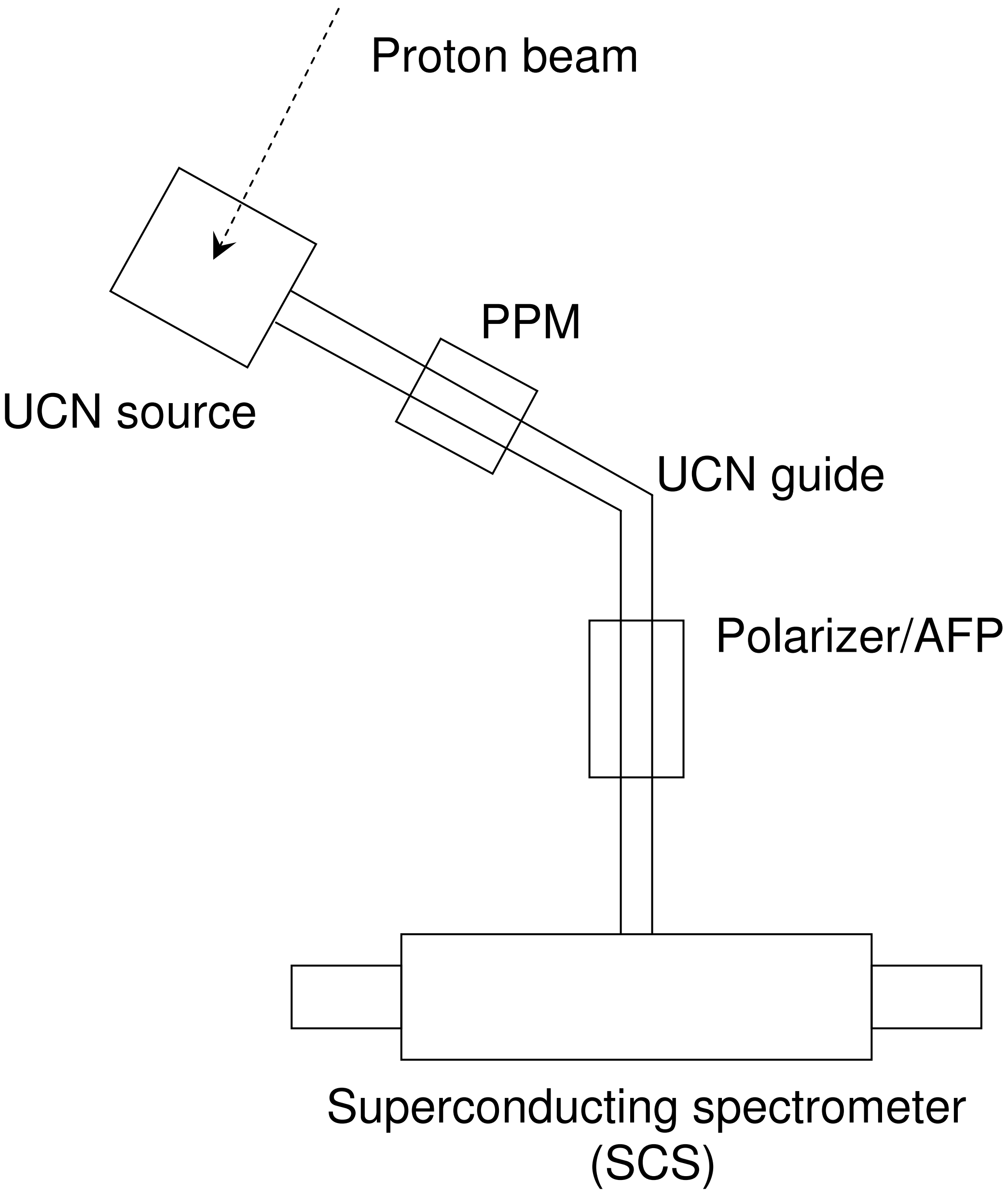

Figure 1.2: Schematic view of proton beam, UCN source, PPM, guides, Polarizer/AFP, and the Superconducting spectrometer.

More detailed descriptions of the UCN source, the UCN guide tubes, and the superconducting spectrometer are given below.

1.4.1 The UCN source

Ultra Cold Neutrons(UCN) are neutrons with kinetic energy less than 340 neV (velocity below about 8 m/s), which undergo total reflections at all angles on the surfaces of a variety of materials, thus can be confined in material bottles, or transported from the source to the experimental area via guide tubes [27, 28, 29]. UCN are very useful for the measurements of neutron lifetime and searches for neutron electric dipole moment. They are also useful in improved measurements of angular correlations in neutron beta decay, as is evident in the UCNA experiment. Available density of UCN is one of the major limiting factors in all measurements with UCN. Former UCN sources are based at nuclear reactors, extracting very low energy neutrons from the low energy tail of the Maxwell-Boltzmann thermal energy distribution in low temperature moderators. In some cases, receding turbine blades (Doppler shift effect), gravity, or both are used to further slow the neutrons. The highest bottled densities reported in the literature before 2004 was about 50 UCN/cm^3 [30, 31], which was obtained at the Insitut Laue-Langevin (ILL) reactor in Grenoble.

An superthermal UCN source was first proposed in 1975 by Golub and Pendlebury [32] with superfluid helium, in which roton creation is used to down-scatter cold neutrons to the UCN regime, and the rate of down scattering is larger than the combined nuclear absorption (essentially zero for helium-4) and up-scattering rate (suppressed by maintaining the superfluid at sufficiently low temperature), thus providing higher UCN densities than conventional UCN sources.

A few other materials, such as solid deuterium (SD2), also can be used for superthermal UCN production [33, 34]. Pokotilovski [35] suggested a pulsed UCN source by using a pulsed reactor to drive the SD2 and by opening and closing a shutter between the source and a storage bottle to reduce the contact time of the UCNs with the SD2. Serebrov et al. [36, 37] proposed the use of spallation as a pulsed source.

The limiting UCN density ρ_{UCN} one can obtain using a SD2 source is given by the product of the rate of UCN production R, and the lifetime of UCNs in the solid τ_{SD}: $\rho_{UCN} = R\tau_{SD}$.

A prototype spallation neutron driven SD2 UCN source has been built and tested at LANSCE, and the full scale SD2 UCN source was built later based on studies of the prototype source and tested. Results from studies of the prototype and full scale SD3 UCN source are presented in Chapter 6.

1.4.2 UCN guide tubes

The UCN are transported through 7-cm diameter quartz tubes coated with diamond-like films deposited by pulsed laser deposition (PLD) of graphite. In order to protect against accidental fracturing of the quartz, the guides are enclosed within stainless steel vacuum jackets. The PLD guides were tested using the ILL UCN source. The depolarization rate of UCN on the PLD guides was measured to be $< 2 \times 10^{-6}$/bounce (with magnetic gradient regions present almost identical to that expected near our polarizer magnet). The resultant mean depolarization should be below about 0.05% and therefore negligible for our measurements of the beta-asymmetry. The transmission of the PLD quartz guides was measured to be typically 95%/m.

1.4.3 The superconducting spectrometer (SCS)

A schematic view of the SCS is shown in fig. 1.3. The spectrometer is a 4-m long superconducting solenoid with a UCN entrance port transverse to the axis of the solenoid. The UCN decay tube lies at the center, along the axis of the SCS, and is defined by a 3-m long, 10-cm diameter UCN open-ended tube. The tube is mounted on a support structure that can be inserted and withdrawn from the warm bore of the SCS as a unit. A highly-uniform 1.0 T magnetic field is generated along the axis of the UCN decay tube by the superconducting solenoid. At the ends of the bottle, the magnetic field is reduced to 0.6 T in the region before the beta detectors. This field expansion region is 0.6 m in length. The strong magnetic field in the solenoid is used to determine the neutron spin direction and is used to guide the betas from neutron decay in the decay tube to the detectors. The beta detector system consists of a Multi-Wire Proportional Chamber(MWPC) backed by a plastic Scintillator detector. This detector system allows the determination of both position information (from the MWPC) and total energy information (from the scintillator). This geometry suppresses backscattering effects in three ways: Firstly, the pitch angle of the betas decreases as the beta moves from the high field to the low field region, which reduces the backscattering amplitude of electrons from the MWPC windows and the scintillator. Secondly, backscattering effects are suppressed because many of the backscattered betas are mirrored by the magnetic field “pinch” back into the detectors. Lastly, by using plastic scintillator the backscattering is reduced because of the low Z material, moreover, MWPC information can be used to tag some of the backscattering events from the scintillator. More detailed descriptions of the beta detector system are given in the following chapters.

To limit the effects of decay electrons scattering from magnetic inhomogeneities in the spectrometer field, the field along the axis in the decay volume must be uniform to better than 10^{-4}, and the field in the whole decay volume must be uniform to better than 5×10^{-4}, while taking account of the requirement of a 4-cm entrance port. Based on some initial analytical models we found that a single split-coil solenoid would not work, but that a multi-coil design looked promising. A minimization program was written to minimize field fluctuations with variation of coil currents. The solution we arrived at is 7 cm of windings followed by a 7cm gap, with this structure repeated 32 times, with a diameter of 50 cm (see Fig. 1.4). For the windings, we assumed for each coil a single

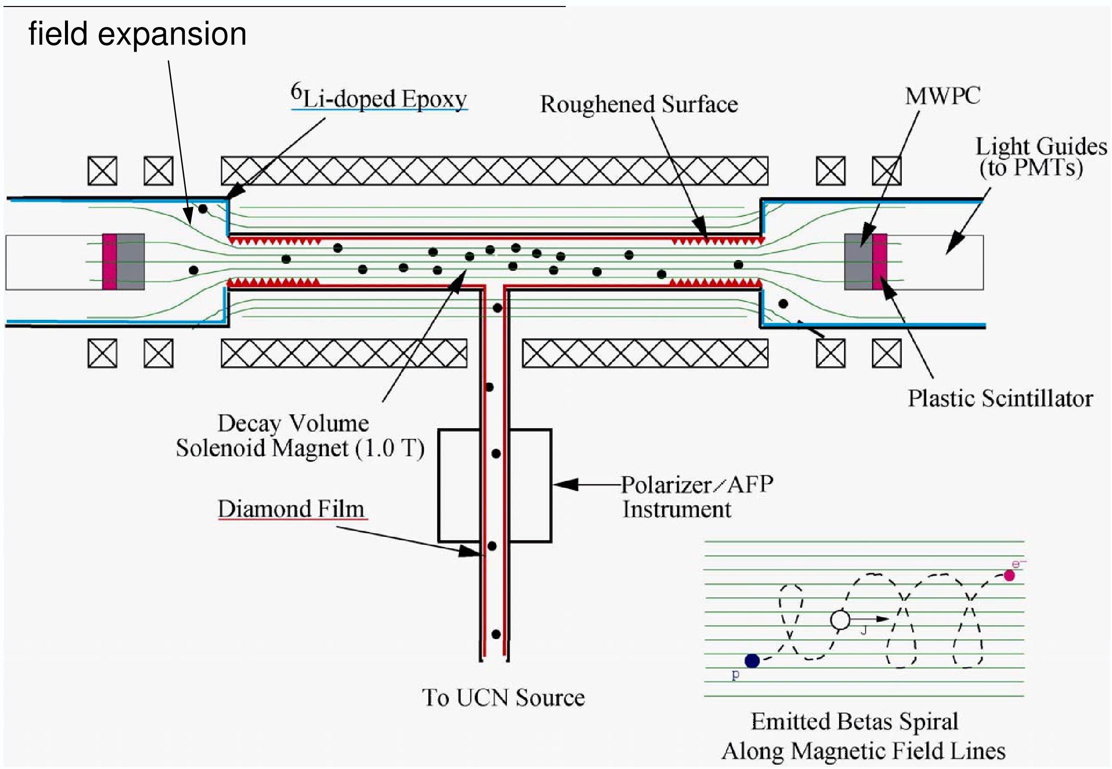

Figure 1.3: Schematic view of the SCS spectrometer.

layer of filaments spaced 1 mm apart for the full 7 cm. This gives 70 identical turns for each coil. To give us the correct field profile we put 6 different currents into the 32 coils (symmetric about the center). This gives us currents of 1600–1800 A. Of course we could reduce these currents with multiple layers of windings and we could reduce the number of different currents needed by varying the number of turns in the coils. The currents for each of the coils (symmetric about the center) are given in Table. 1.4, where coils are numbered from the center to the edge. In this design there are 6 different values for the coil currents (or windings). The SCS magnet was custom-built by

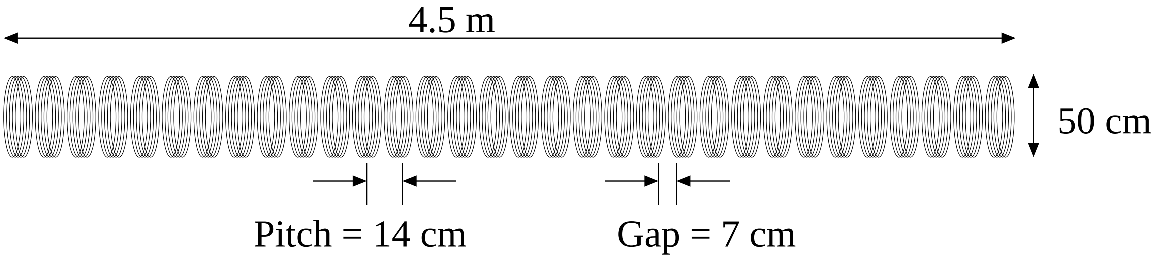

Figure 1.4: Schematic diagram of multi-coil design. Coils are 7 cm in width, spaced 14 cm apart. Diameter is 50 cm with 4.5 m total length. There are a total of 32 coils.

American Magnetics Incorporated (AMI). The field measured with a NMR probe along the axis of the SCS is shown in Fig. 1.5.

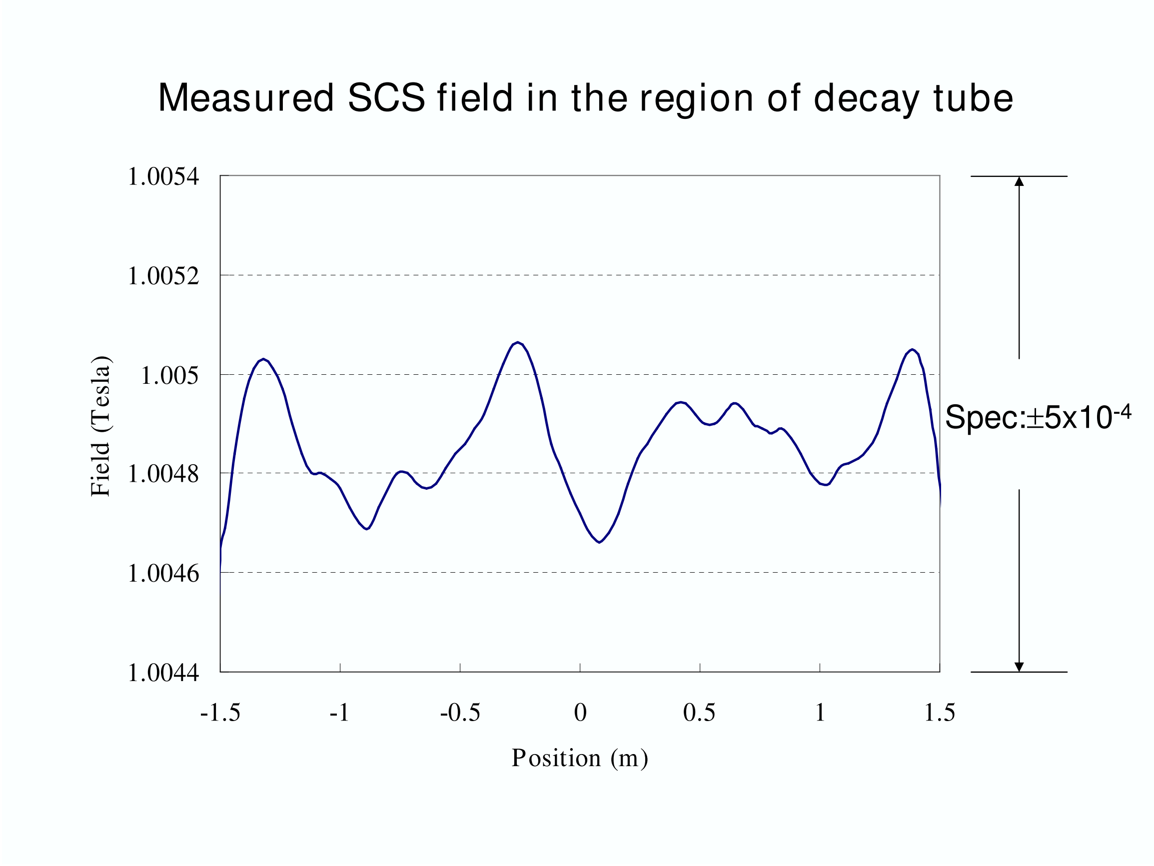

Figure 1.5: The SCS field profile measured with an NMR probe.

Table 1.4: Current for each coil in multi-coil design of SCS.

Coil Number	Amps
1–3	1600.2
4–6	1602.1
7–8	1606.0
9–10	1611.5
11–13	1628.2
14–16	1796.5

UCN detectors(^{6}LiF-coated Si surface barrier detectors) are mounted at both ends of the decay tube. These are used to monitor the UCN flux and to check for any changes in UCN density in the trap when the UCN spin is flipped. To eliminate detector backgrounds induced by UCN leaking from the decay tube, the inner walls of the SCS are covered by a layer of thin stainless steel sheet that is covered with ^{6}LiF, to effectively capture the UCN that are lost out of the ends of the decay tube. Furthermore, UCN absorbing structures covered with LiF coated foils are placed in the B-field expansion regions, in between the ends of the decay trap and the beta detectors.

Chapter 2

The β Detector System

The β detector system for the UCNA experiment consists of a Muti-Wire Proportional Chamber (MWPC) backed with a plastic scintillator detector, as is shown in Fig. 2.1 in a cutaway side view. Two identical beta detector systems are placed on each side of the SCS spectrometer. The end point electron kinetic energy in neutron beta decay is 782 keV. In this energy range, backscattering is a major concern in precise beta spectroscopy. Thus in the design and construction of the beta detector system, efforts are taken to reduce the backscattering effect, along with other experimental concerns specific for the UCNA experiment, such as energy and position resolution, detector background, and magnetic field shielding.

A MWPC back window is used to isolate the scintillator from the wirechamber gas (neopentane), In order to minimize the backscattering effect, a very thin mylar film is used as the back window. The wirechamber gas pressure is 100 Torr as will be discussed later, thus the scintillator detector is isolated in a volume with about 100 Torr pressure, the gas we choose for this volume is Nitrogen (We refer to this volume as N2 volume). To protect the wirechamber windows when pumping, filling, or venting the system, a gas handling system is developed.

2.1 The plastic scintillator detector

2.1.1 Design requirements

The purpose of the scintillator detector is to measure the energy of the electrons from the UCN beta decay. The central requirements of the full energy detector, the plastic scintillator detector, are as follows [38].

Firstly, a high energy resolution is required, which translates into high photoelectron (PE) collection for a scintillator. The minimal requirement is 100 PE per MeV electron energy, corresponding to 10% resolution at 1 MeV. However, this value should be as high as possible.

Secondly, a low energy threshold for detecting beta particles is required, which demands high

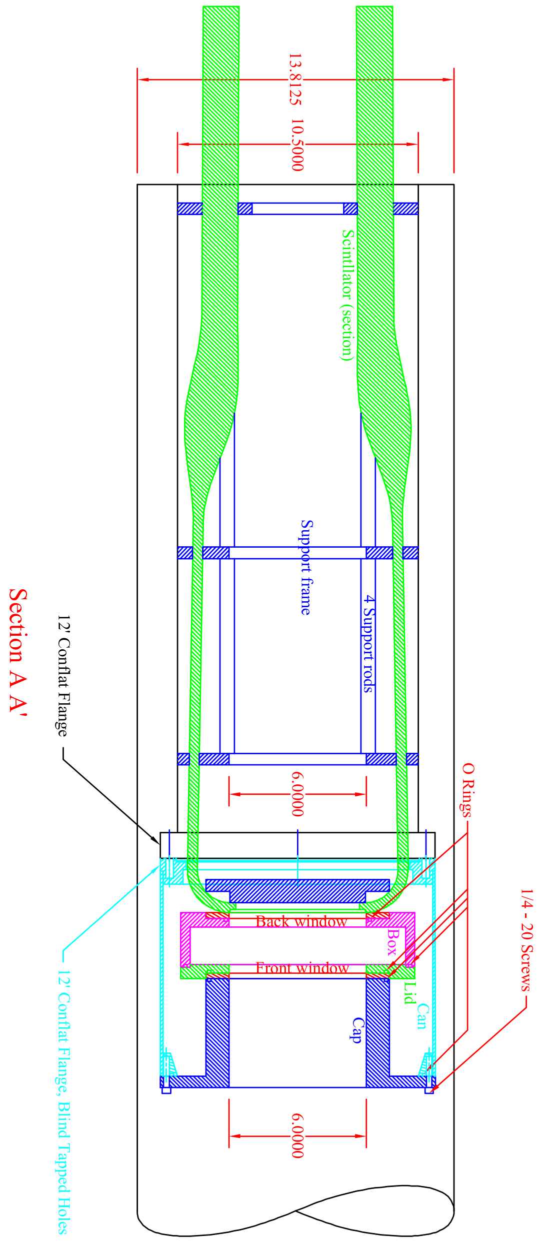

Figure 2.1: A side view of the UCNA beta detector system.

PE collection, as well as low dark noise and low background. With dark noise suppressed by the coincidence of 2 Photo-Multiplier Tubes (PMT), and efforts to reduce background, the low threshold requirement also translates into high PE collection.

Thirdly, the probability of electron backscattering should be suppressed, which leads to the utilization of a plastic scintillator as the detector medium because of its low average atomic number Z. Moreover, plastic scintillator and fast phototubes are preferred for the reason of fast timing response, which is of vital importance for distinguishing which detector system is hit first in the case when both detector systems record a hit as a result of backscattering.

Fourthly, the detector must be able to tolerate high magnetic field, which ranges from 0.6 T at the detector position to 300–400 G one meter further outside the spectrometer. This high magnetic field requires the use of long light guides and multi-layer magnetic shielding for the PMTs.

Fifthly, the transverse size of the detector is constrained by the inner diameter of the SCS bore and by the other uses of this space including cabling and the vacuum system.

Sixthly, the detector should achieve corrected linearity and position uniformity of 0.3%, and 0.1% response stability between neutron spin flips.

Lastly, the detector should easily interface with a front MWPC with minimal inactive material to minimized unidentified electron backscattering (called missed backscattering).

2.1.2 Plastic scintillator

The plastic scintillator is 15 cm in diameter and 3.5 mm thick. The transverse size of 15 cm is determined by the neutron decay fiducial volume, projected to the detector position after the magnetic field expansion region, which is a region where the magnetic field is changing from 1 T in the neutron decay tube to a 0.6 T nearly uniform field region where the scintillator is located. The thickness of 3.5 mm is determined by the range of maximum energy electrons from neutron decay, which is 3.1 mm in plastic scintillator for 782 keV electrons. Allowing a safety factor, this thickness of 3.5 mm gives near 100% full energy collection even for the electrons with the endpoint energy.

The thickness of 3.5 mm is also an optimization concerning backgrounds. The backgrounds are from ambient gamma ray and comic ray interactions. The probability of an individual gamma ray interaction with thin scintillator is relatively small, and consequently the total background rate from ambient gamma ray interactions will scale with the volume of the scintillator such that the thinnest possible scintillator is preferred to minimize this rate. On the other hand, cosmic rays have a 100% probability of depositing energy when crossing the scintillator. The minimum light produced in a 3.5 mm thick plastic scintillator occurs when they cross perpendicular to the scintillator face, which is about 700 keV equivalent electron energy deposition. These interactions are indistinguishable from neutron beta decays near the endpoint, but they could be rejected with a thicker scintillator, giving larger energy deposition above the endpoint. In the UCNA experiment, the cosmic background will be reduced to a negligible level by an extensive active veto system. Therefore the 3.5 mm thickness is chosen to limit gamma ray background.

The plastic scintillator is chosen to have high average light yield in the 400–430 nm wavelength region, which matches bi-alkali photocathode sensitivity (a bi-alkali photocathode is chosen for light-electron conversion for reasons discussed below) while still being long enough in wavelength to be effectively used with UVT light guide. Other scintillator characteristics include a attenuation length longer than one meter, a fast rise time, and high light yield. Eljen technologies provide inexpensive scintillators with such characteristics, and the EJ204 formulation has the best performance [39]. EJ204 is a fast plastic scintillator with polyvinyltoulene as the plastic base. A more expensive variant, EJ204V, is specially hardened to resist fluor degradation in ultra high vacuum condition. A summary of specifications for EJ204 is shown in Table. 2.1 and the emission light spectrum as a function of wavelength is shown in Fig. 2.2, Both of which are taken from the Eljen catalog.

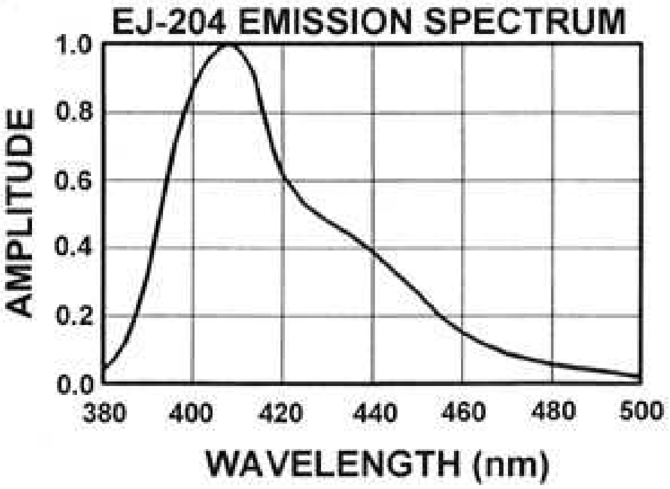

Figure 2.2: EJ204 emission spectrum.

Table 2.1: Physical and Scintillation Constants for EJ204

Features	EJ204 value
Scintillation Efficiency	10400 photons/1MeV e^-
Wavelength of Max. Emission	408 nm
Rise time	0.7 ns
Decay time	1.8 ns
Pulse width (FWHM)	2.2 ns
Density	1.032 g/cc
Refractive Index	1.58
Vapor Pressure	Vacuum compatible
C:H ratio	1:1.10

2.1.3 Light guide system

A light guide system is required to collect light from the scintillator. Two options are available for gathering the light: coupling guides to the back face of the scintillator, or coupling guides to the scintillator edge. In the limit of a very thin scintillator, 87% of the scintillation light can be read out from the back face by an index matched light guide, while 13% is wasted by transmitting out from the front face. For edge collection, 74% can be read out from the edge while 26% is wasted by transmitting out from both faces. While the light collection efficiency is not dramatically different, several practical reasons determine that edge collection is preferred. Firstly, the surface area of the back face is 176.7 cm^2 versus 16.5 cm^2 on the edge. This implies an order of magnitude more photocathode area is needed for back face readout than edge readout. Readout cost is likely to scale with the area, and so will the dark noise. Secondly, since the scintillator sits in a large 6000 Gauss magnetic field, any normal phototube has to be moved far from this field. The light guides (lucite) connecting the scintillator to the phototube will be a large source of background from cosmic muons producing Cerenkov light. By the same argument as above, edge collection can be accomplished with much thinner light guides, thus reducing this background. Lastly, it is preferable to use multiple phototubes as dark noise and some other backgrounds can be suppressed by requiring multiple phototube coincidence. However, it is difficult to adiabatically couple multiple tubes to a single round scintillator face without leaving gaps in coverage.

According to the field distribution from the SCS, the readout phototubes cannot be closer than one meter to the scintillator. At this position the magnetic field is about 300 Gauss, which is feasible to shield, as discussed below. Longer guides become mechanically difficult to handle as the lever arm at the connection to the scintillator is enormous, and light attenuation in guides begins to dominate.

It is more practical to use lucite thicker than the scintillator to couple to the scintillator edge for reasons of mechanical stability and ease of manufacture, thus one centimeter thick lucite is used to couple to the scintillator edge. The effective area mapping onto the phototubes is 47.1 cm^2, which maps onto twelve to thirteen 1 inch tubes (22 mm active diameter), three 2 inch tubes (45.7 mm active diameter), or one 3 inch tube. In order to have coincident readout while keeping excess photocathode area and readout electronics channels minimum, 2 to 4 tubes are ideal. Therefore, 2 inch tubes are chosen. Four 2 inch tubes are actually needed to match the guide area as one is fitting a rectangular area to a circular photocathode.

The light guide system is designed so that light is collected from the scintillator edge and propagates one meter to the phototubes, while adiabatically changing from rectangular geometry coupled to the scintillator to 45.7 mm diameter lucite clusters coupled to the phototubes. An additional constraint is that the transverse size of the detector should be able to fit into the 13.68” SCS warm bore and extra bore space is needed for vacuum pumping and cabling. A size of 10”, which is 10.5” of outside diameter minus 0.5” of vacuum nipple wall thickness, is taken as the transverse size. A side cutaway view of the scintillator with support structure as well as MWPC in front is shown in Fig. 2.1.

Most of the design work for the light guide system focused on making the coupling to the scintillator edge in this confined transverse space. In the final design, twelve strips of 39mm wide lucite attach to the edge of the scintillator concentrically around its diameter. After a 0.5 cm straight section, these strips are bent with a 3.5 cm bending radius, and are directed back towards the phototube. Near the end, the strips are adiabatically bent so that each group of 3 strips form a rectangular cluster of 39mm × 30mm (width of the lucite strip × 3 times of strip thickness) to coupling to the phototube. This design is labeled "Suzuno" after the Japanese company "Suzuno-giken" who manufactured it. A front schematic view of the design is shown in Fig. 2.3.

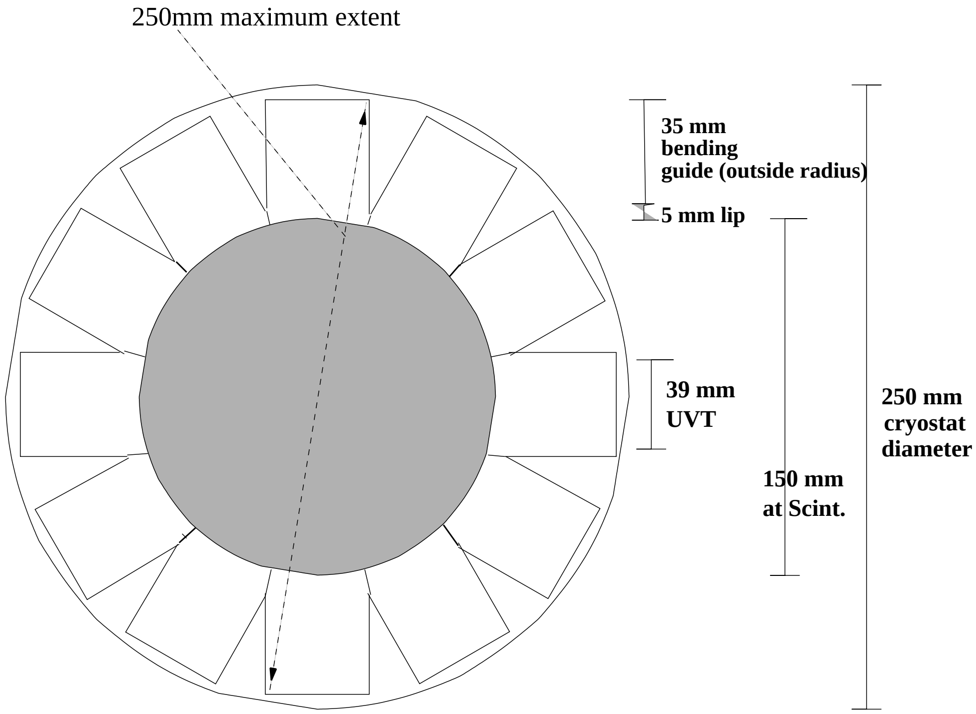

Figure 2.3: A front schematic view of the Suzuno scintillator design.

The 3.5 cm bending radius was chosen based on a simple photon tracking simulation, in which the light yield from a lucite arm attached to a square scintillator piece was measured. The bending radius of the arm was varied and the light yield obtained was compared to the "straight" case of no bend. The simulation shows that a bending radius of larger than 3 cm is enough for efficient light collection.

The light collection versus bending radius studied in a GEANT4 simulation shows that a Suzuno style detector with a 100 cm bending radius has light collection efficiency of 58%, which drops to 51% with the 3.5 cm bending radius for the real detector. In the case of 1.5-meter scintillator attenuation length, 80% efficient reflective wrap, and perfectly polished lucite surfaces, the light collection efficiency is 38%, which gives 3952 collected photons per MeV energy deposition. Using an average Burle 8850 PMT quantum efficiency of 22%, this gives an expected 869 photoelectrons per MeV for this detector, which is an optimistic estimate. Additional factors that are difficult to model are not included in the GEANT4 simulation, such as the losses in glue and grease joints, the adiabatic bending of the guide strips to couple to a phototube, and lucite surface imperfection. The observed light yield was 360–400 photoelectrons per MeV energy deposition.

In the UCNA experiment, the plastic scintillator is coupled to the light guide system with optical grease instead of glue, for the convenience of installing and debugging the Gain Monitoring System and the active cosmic muon veto detector at the back of the scintillator. The phototubes are glued to the light guide system.

2.1.4 Phototubes

Conversion of optical photons to electrical signals for the scintillator detector is made with four conventional phototubes per detector. Conventional phototubes as opposed to photodiodes were chosen, mainly for the reason of single photon resolution, cost, and availability of large active diameter, even though photodiodes offer magnetic field resistance.

The requirements for the 2” phototubes include low dark count, high gain, and a quantum efficiency peaking near 410 nm. This selects about one phototube candidate from each of the major companies, such as Burle8850, EMI9814, Photonis XP2262 and Hamamatsu R329-02. The Burle 8850 is favored as it is optimized for high performance single photon counting, along with other features. Table. 2.2 shows the comparison between Burle8850 [40] and EMI9814 [41]. The Burle tube is clearly a favorite according to this comparison. It has 2 times less dark count than the EMI9814. Its gain is higher even at a fraction of its maximum operating voltage. Tests at Kellogg show that the Burle8850 could run in single photon counting mode without a PM amplifier on its output. Single Photo-Electron (SPE) discrimination against noise is expected to be better with the Burle8850 tube due to its high yield first dynode.

Thus Burle8850 tubes were chosen to be used in the UCNA experiment for the beta scintillator detector. The quantum efficiency as a function of wavelength for the Burle8850 is shown in Fig. 2.4. The EJ204 scintillation spectrum averaged quantum efficiency of the Burle8850 is 22%.

Table 2.2: Comparison of phototubes for the UCNA scintillator

Features	Burle 8850	EMI 9814
Photocathode Material	Bialkali	Bialkali
Dynode Material	GaP/BeO	BeCu
"Nominal" Gain	1.6×10^7	7.1×10^6
	2000/3000V	1950/2300V
Dark cps Average	≈ 200	≈ 400
Rise time	2.1 ns	2 ns

2.1.5 Phototube shielding

The scintillator detector phototubes are expected to operate in a strong magnetic field of about 300 Gauss axial. The photocathode of the phototubes is positioned at -318cm from the center of SCS. 22" long steel shields will be used, which extend from about -290 to -345cm in the UCNA experiment. The magnetic field in this region is shown in Fig. 2.5.

The field has to be reduced below 0.1 G at the phototube position for its gain to be unaffected. A multi-layer magnetic shielding structure is needed to reduce the field. The design is shown in Fig. 2.6.

The design uses multiple layers of magnetic materials to step down the field. From outside to inside, the first layer is a 1/4"-thick 520 DOM steel tube with 4" ID, close-fitting the second layer of steel shield, which is made of cold-rolled mid-carbon steel (1026 grade) with 3.5" ID and 4" OD. Both layers are 22" in length. The 4" nominal ID of the outer shield was bored out using a boring bar on a lathe until it fit around the 4" OD of the inner tube. The third layer is a 3-layer close-packed copper wire (18 gauge) winding around a 3" OD 0.04"-thick cylinder of high μ metal (AD-MU-80 from Advance Magnetics). the length of the μ metal cylinder is 12", while the length of the coil winding is 15". A 15" long 0.004" thick AD-MU-80 μ metal foil is wrapped around the μ metal cylinder to provide the extra length support. There are about 324-325 turns of wire in each layer, and each layer is coated with a thin layer of 5-minute epoxy. The resistance of the resultant coil is 5.5 to 6 Ohms.

Tests were performed at Kellogg using several kilometers of copper wires with a DC current to mimic the magnetic field in Fig. 2.5. It was found that this field can be shielded to below 0.1 Gauss with a DC current in the coil winding ranging from about 950 to 1200 mA.

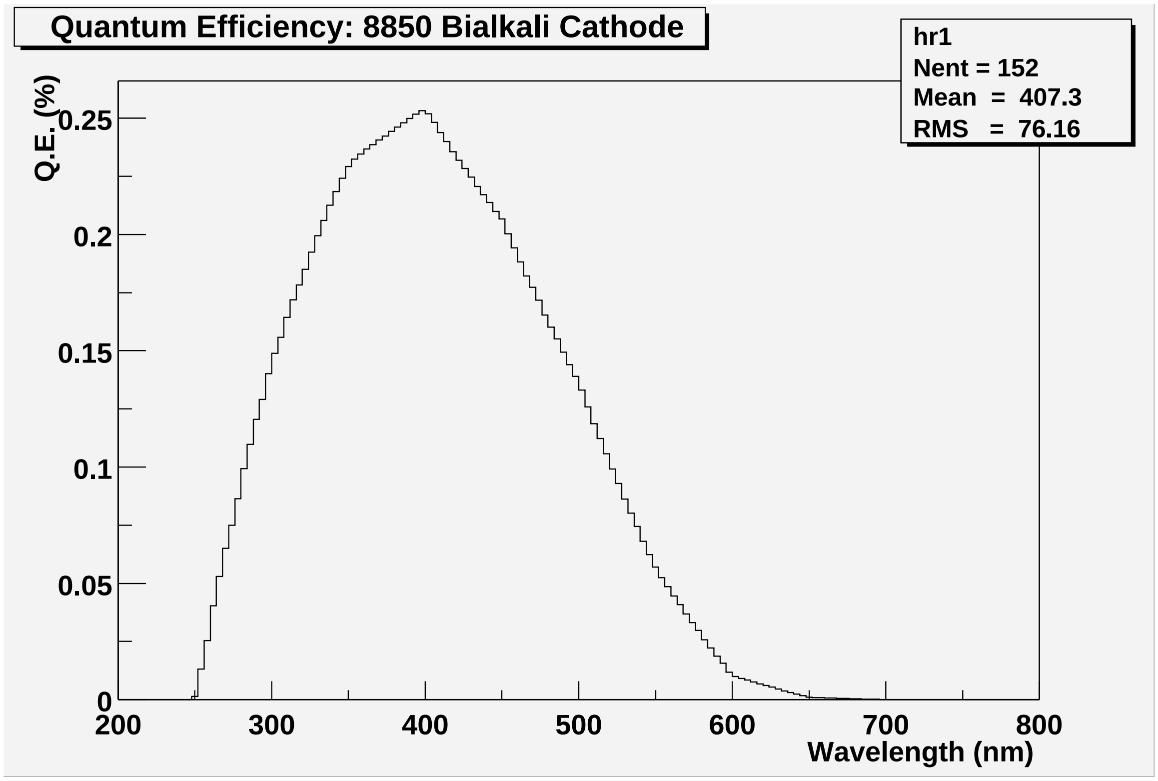

Figure 2.4: Quantum efficiency of the Burle 8850 tube.

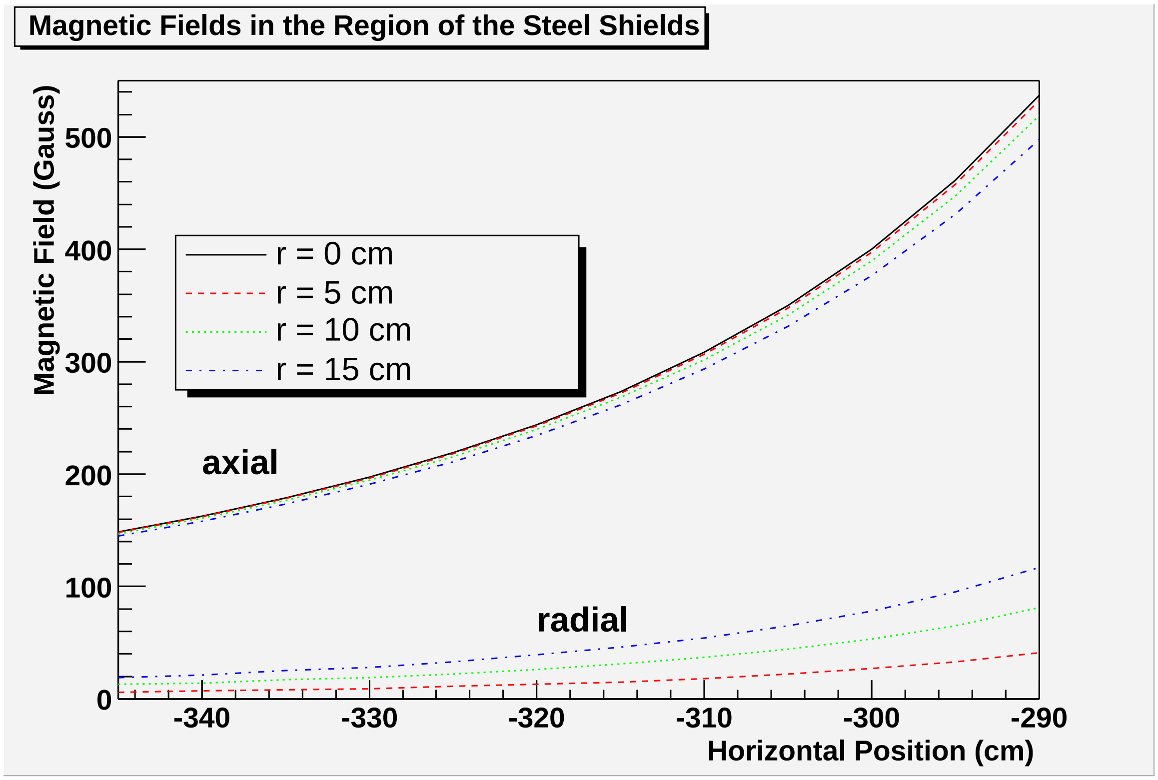

Figure 2.5: Magnetic field in the region of the phototubes.

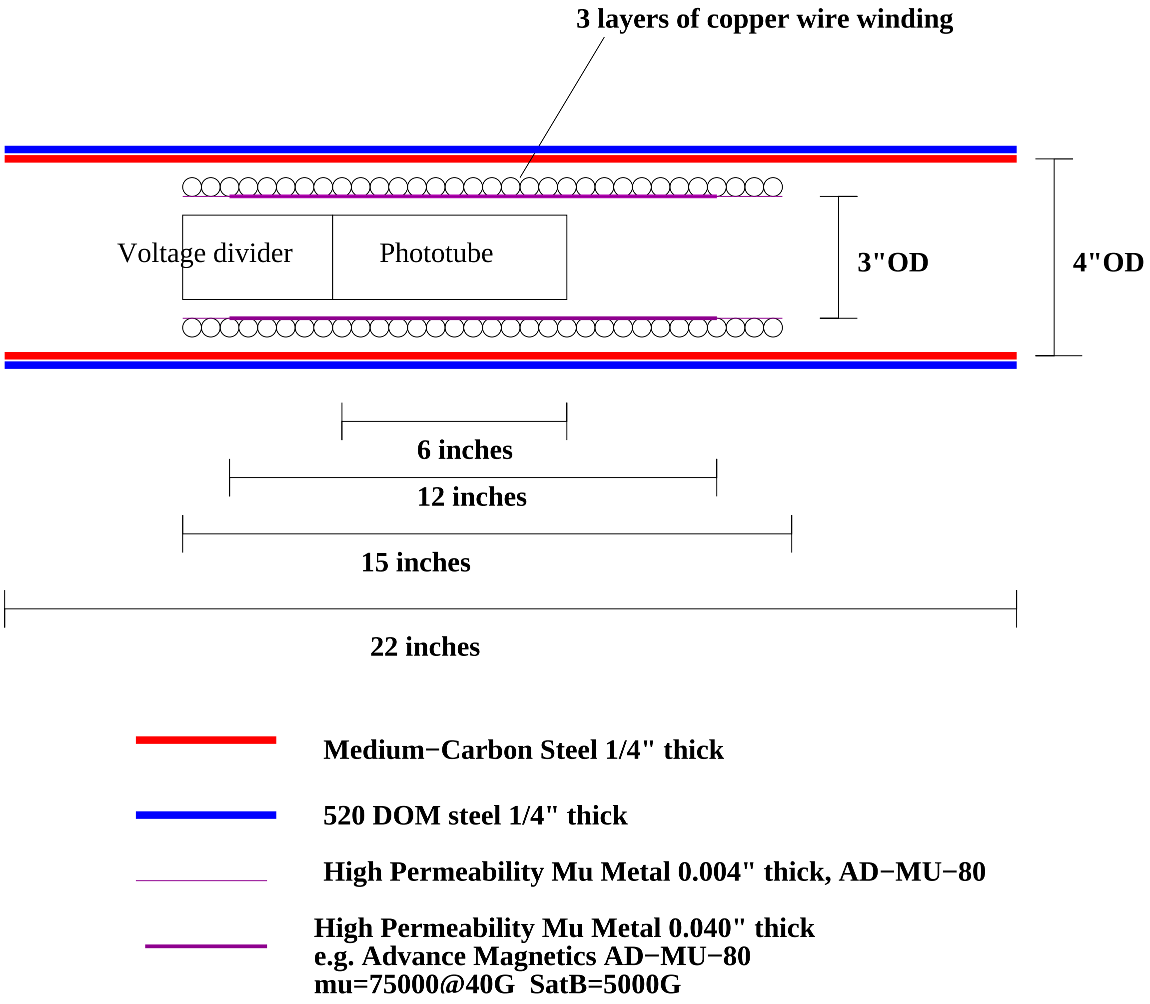

Figure 2.6: Side view of the magnetic shielding structure for the phototubes.

2.2 The multiwire proportional chamber

2.2.1 Design goals

With the plastic scintillator providing full energy information, the design goals for a MWPC in front of the scintillator are as follows [42].

Firstly, the MWPC should be able to help resolve the missed backscattering events. A major systematic effect in experiments measuring the beta asymmetry in neutron decay is backscattering. Regular backscattering events in which both scintillator detectors record a hit can be resolved by the timing information from the scintillator detectors, and thus will not introduce any measurable error. A missed backscattering event in which the backscattered electron leaves undetectably small energy deposition in the first detector (the plastic scintillator in the UCNA experiment has a threshold of about 20 keV) introduces an error in the asymmetry measurement. The MWPC in front of the plastic scintillator can help in resolving the missed backscattering events because of its sensitivity to small energy deposition and thereby provides a lower energy threshold than the plastic scintillator. Therefore, the MWPC should be able to provide a high counting efficiency for electrons in the energy range below 782 keV. This requires a reasonable energy deposition in the chamber gas and a low electronic noise level.

Secondly, backscattering from the MWPC should be as low as possible, to minimize the missed backscattering probability introduced by the MWPC.

Thirdly, the MWPC should be able to provide reasonable position resolution (2 mm), for the definition of the fiducial volume.

Fourthly, the MWPC should be able to minimize the background by requiring a coincidence of the plastic scintillator and the MWPC, because of its insensitivity to γ's.

2.2.2 Mechanical construction

The wire chamber as part of the β detector complex is shown in Fig. 2.1. A close-up view of the MWPC construction is shown in Fig. 2.7. An enclosure made by the *Lid* and the *Box* makes the gas chamber, in which three wire planes (1 cathode + 1 anode + 1 cathode plane) are located. The preamps for the anode and cathode signals are placed in the enclosure made by the *Lid* and the *Cap*, and this enclosure is connected to the scintillator volume through the four openings between the *Box* and the *Can*. These openings also provide space for the signal, power, and high voltage cables to reach from outside to this enclosure. Two 32-pin flat ribbon connector are epoxied into a cutout on the *Lid* to serve as the feed-through connectors for the cathode signals. On the side of the *Lid* facing the gas volume, there is a small PC board attached to each of the 32-pin flat ribbon connectors, which are inserted into a card edge connector mounted on each cathode frame when the *Lid* is pushed against the *Box*.

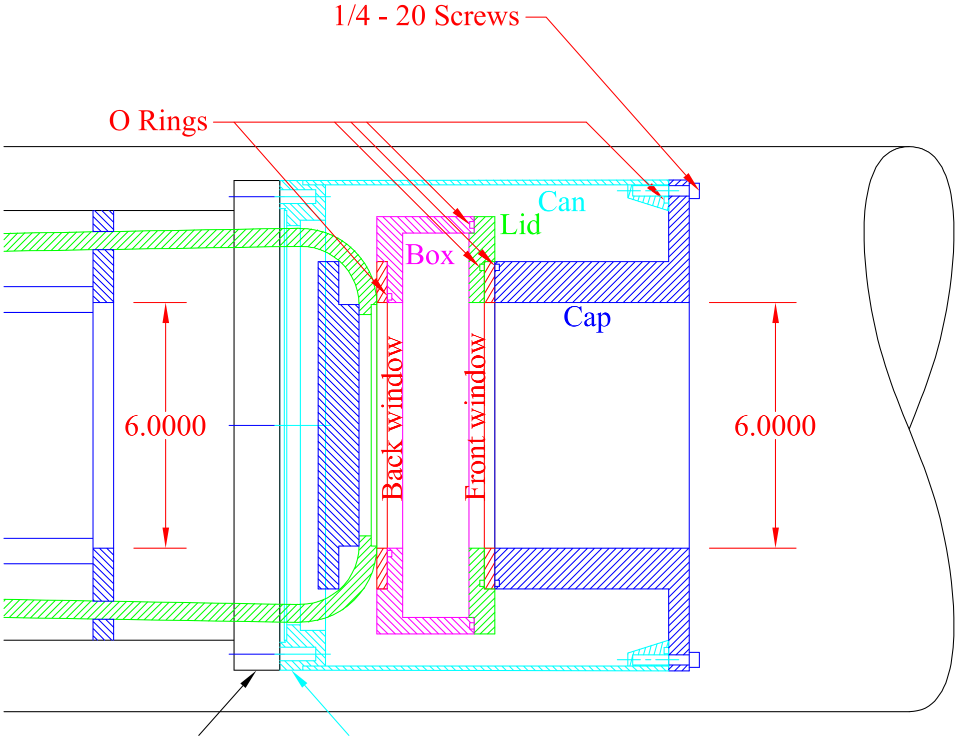

Figure 2.7: Close-up view of the MWPC construction.

2.2.3 Chamber gas

Backscattering occurring in the MWPC windows and the gas volume will not deposit any energy in the scintillator, thus leading to a potential missed backscattering event. Hence the MWPC windows should be as thin as possible. Since the MWPC front window provides the vacuum separation between the SCS vacuum and MWPC gas volume, the chamber gas pressure should be as low as possible. Since backscattering probability scales with the atomic number Z, the chamber gas should contain atoms with low Z. On the other hand, in order to resolve missed backscattering events, the counting efficiency of the MWPC should be as high as possible, which requires a high electron density. Therefore, the choice of chamber gas is likely to be a low pressure, heavy(large molecular mass), and low Z hydrocarbon gas.

Heavy hydrocarbon gases such as isobutane and pentane have been used as a wire chamber gas before. We favor pentane(C_5H_{12}) over isobutane (C_4H_{10}) as it has a larger molecular mass. Neopentane (C_5H_{12},also known as 2,2-Dimethylpropane), a variant of normal pentane, is much less reactive and has a higher vapor pressure (1125 mmHg) than n-pentane(normal pentane, C_5H_{12}). Thus neopentane was determined to be the ideal gas to be used in the UCNA experiment for MWPC chamber gas.

The pressure of the chamber gas is determined from measurements of counting efficiencies under different conditions of chamber gas pressure. The measurements were performed using a scaled-down prototype MWPC at Kellogg. The anode plane is made of 10 μm diameter gold plated tungsten wires in 2 mm spacing, and the cathode planes are made of 50 μm diameter gold plated tungsten wires in 1 mm spacing. The gap between the anode plane and each cathode plane is 8 mm. Signals from all the anode wires are ganged together to be read out, as are the signals from all the cathode wires. A ^{90}Sr source was used as the electron source. The prototype MWPC is backed by a plastic scintillator detector, which provides the trigger for data acquisition.

The counting efficiency, measured with the cathode signal, as a function of the applied anode bias was studied at Kellogg with 60, 80, 100, and 200 Torr neopentane. The studies show that even at pressure as low as 100 Torr, the efficiency curve presents a plateau with near 100% efficiency in a large enough range of anode bias (from about 2600 V to 3000 V). Therefore, neopentane at 100 Torr pressure is chosen as the wire chamber gas.

2.2.4 Front and back windows

The front window is what faces the UCN decay tube in the UCNA experiment, and is 15 cm in diameter. It has to support 100 Torr pressure difference between the MWPC gas and SCS vacuum. At the same time, the front window has to be as thin as possible to minimize the backscattering effect. Tests done at Kellogg show that 6 μm thick Mylar on a 15 cm diameter window can support up to 150 Torr pressure difference while bowing out a distance of about 3 cm (as measured at the center) with 100 Torr pressure difference. This bowing out distance would cause a large dead volume, considering that the effective gas thickness of the MWPC is 2 cm (the distance between the two cathode planes). Supporting the 6 μm Mylar window with 200 denier (1 denier = 0.05g/450m) Kevlar yarn strung in 0.5 cm spacing can reduce the bowing out distance to 0.6 cm, and increase the breaking pressure to about 260 Torr, while only increasing the average areal mass density of the front window by about 50%. 3.5 μm thick Aluminized Mylar film supported with 5 mm spacing 200 denier Kevlar yarns can also support more than 200 Torr pressure difference, and gives similar bowing distance. However, the gas leak rate through the 3.5 μm mylar is unacceptably high.

Therefore, 6 μm thick Aluminized Mylar film reinforced by 200 denier Kevlar yarns is used as the front window to support the 100 Torr pressure difference between the MWPC and the SCS vacuum. The Kevlar yarn is strung with 5 mm spacing, and epoxied onto an circular aluminum frame which is bolted into the opening of the window frame. The circular frame takes up 1 cm of the front window diameter. Therefore, the effective space for the front window is 14 cm in diameter. The front face of the Aluminized Mylar film was coated with 50 nm thick Nickel, to reflect UCN escaping from the decay tube.

The back window is 15 cm in diameter, and is the separation between the scintillator and MWPC. In order to minimize the backscattering effect, pressure in the scintillator volume is chosen to be close to 100 Torr, so that a very thin Mylar film can be used as the back window. In the experiment, the scintillator volume is filled with nitrogen of pressure about 5 Torr lower than the MWPC gas pressure, so that the back window bows to the side of the scintillator to avoid touching the back cathode plane. 6 μm thick Aluminized Mylar film was used as the back window.

The front window is positioned 5 mm from the front cathode plane, and the back window is positioned 5 mm from the back cathode plane.

2.2.5 Wire planes

The maximum diameter that the electron spiral can have in the UCNA experiment occurs for electrons with neutron decay end-point energy and emitted nearly perpendicularly to the holding field, and is about 4.0 mm at 1.0 T in the SCS. The fiducial area is to be defined so that events in which the neutron decay takes place less than this diameter from the wall of the decay tube are to be rejected (allowing a 10% safety factor). Therefore it is $100 - 1.1 * 4.0 * 2 = 91.2$ mm in diameter. The fiducial area projected to the MWPC face due to the field expansion region is thus $91.2/\sqrt{0.6} = 117.7$ mm in diameter. A position resolution of 2.54 mm will be sufficient for the purpose of defining the fiducial area. Therefore, 2.54 mm spacing is chosen for the anode plane. For proper operation of the MWPC, the gap between the anode plane and each cathode plane is normally three or four times larger than the wire spacing [43], hence 1 cm is chosen as the gap.

In order to achieve high enough gain with neopentane as the chamber gas, the diameter for the anode wires has to be small. 10 μm-diameter tungsten wires coated with gold are used for the anode wire plan, in which 64 anode wires are strung with 2.54 mm spacing, and both ends of the wires are soldered onto a 0.092 inch thick FR4 epoxy glass frame, with a tension of 9 g (about 80% of the break point) applied to each wire. A conductor track etched on the FR4 epoxy glass plate connects all the anode wires, and through a feed-through connector mounted on the LID connects to the HV box located outside the gas chamber.

While the anode wires together provide the energy deposition information of the hit, the 2 cathode planes give the X-Y position of the hit, with wires in the 2 cathode planes orthogonal to each other. The front and back windows cannot be used as cathodes, because the windows bow out by up to 0.6 cm (as measured at the center) due to the pressure difference across the windows. In order to minimize the backscattering effect, thin wires are also used for the cathode planes, instead of more conventional strips of conductors etched on a substrate such as a Mylar sheet. 50 μm diameter Aluminum wires coated with gold are used for the cathode wire planes. In each cathode plane, 64 wires are strung with 2.54 mm spacing with a 50 g tension, and both ends of the wire are soldered onto a 0.092 inch thick FR4 epoxy glass frame. Due to the cost limitation of readout channels in the DAQ peak sensing ADC, we are only able to read out 16 channels in each cathode plane, hence 64 wires have to be grouped into 16 strips. Simulations with GEANT4 on various grouping schemes have been performed, and have shown that grouping every 4 wires into a strip provides the best position resolution even though the fiducial area is a circle in the UCNA experiment, moreover, this scheme provides the most straightforward way to do analysis for the hit position. Therefore, every four wires are connected to one strip on the FR4 epoxy glass plate, which is connected to a card edge connector mounted on the plate. The card edge connector provides a connection to the amplifier located outside the gas volume via a feed-through connector mounted on the LID.

2.2.6 High voltage bias systems

Many of the high voltage components are in 100 Torr nitrogen, which presents a challenge for the high voltage cable. Tests done at Kellogg has shown that a specially made HV BNC cable from Dielectric Sciences can stand high voltage up to 3200 V in 100 Torr nitrogen. Studies of the MWPC gain as a function of the anode bias show that 2600 V or larger is required for the anode bias with respect to the cathode planes. Allowing a safety factor we operate at 2700 V.

In order to collect the charge deposited between the windows and the cathode planes (otherwise they are dead regions and contribute to the missed backscattering effect), the cathode planes are held at a positive potential with respected to the windows which are grounded. Studies of the collection efficiency as a function of the cathode bias showed that 400 V or larger is needed. Since 2700 V is chosen as the anode bias with respect to the cathode planes, and 3200 V or lower is the limit set for the anode bias with respect to ground, 400 V is chosen as the cathode bias with respect to ground.

2.2.7 Readout electronics

An overview of the MWPC readout electronics is shown in Fig. 2.8. The anode signal is fed to a Multi Channel System PA3300 amplifier module through a decoupling capacitor of 3.3 nF. The PA3000 module contains a charge sensitive preamplifier and a shaping amplifier. The gain and the shaping time are chosen to be 2 V/pC and 0.25 μs respectively.

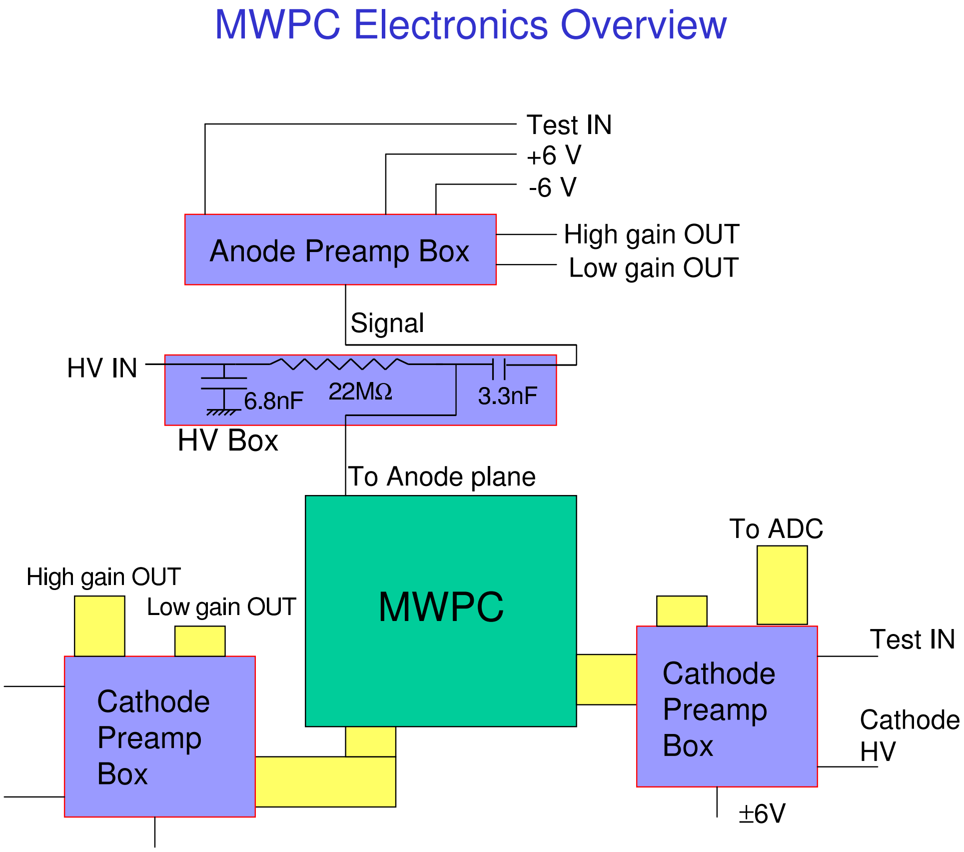

Figure 2.8: An overview of the MWPC readout electronics.

The signal from each of the 16 cathode strips is also fed to a PA3300 amplifier, and the 16 PA3300 amplifiers for each cathode plane are mounted on a Muti Channel Systems CPA16 carrier board, which provides a decoupling capacitor for each channel as well as power for the the amplifiers. The gain and shaping time for the cathode PA3300 are chosen to be 25 V/pC and 0.25 μs respectively.

The amplified anode and cathode signals are digitized by a CAEN peak sensing ADC 785. More detailed descriptions are given in Chapter 5.

2.3 Gas handling system

The gas model for the detector system is shown in Fig. 2.9. To avoid the wirechamber back window bending towards the wire plane, the pressure in the N2 volume is chosen to be around 95 Torr. To protect the wirechamber windows from breaking when pumping, filling, or venting the system, a gas handling system is developed, as is shown in Fig. 2.10 schematically.

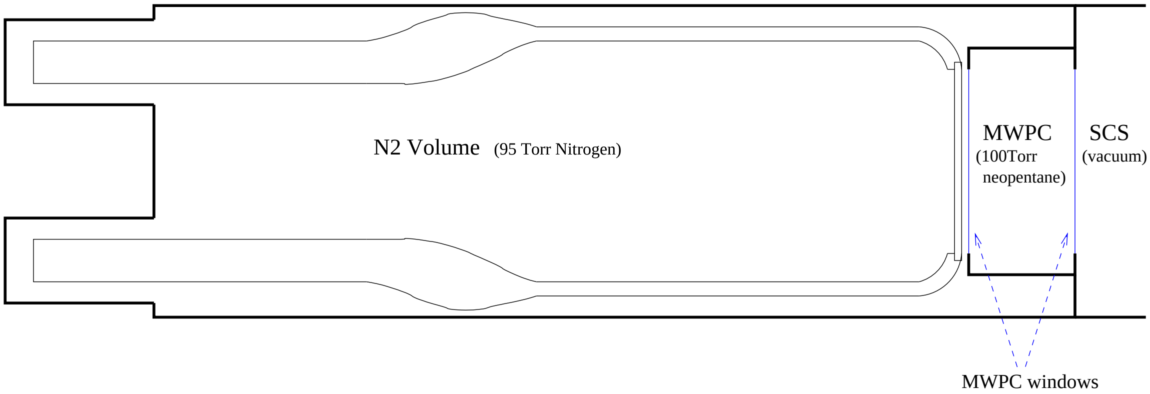

Figure 2.9: A overview of the gas model for the detector system.

The system uses a Mass Flow Controller(MFC) to read out the mass flow rate of the neopentane. The flow rate can be manually set by a needle valve put after the regulator (R2) of the neopentane bottle. In normal filling, the manual valve MV9 is closed. When the pressure of the wirechamber reaches 100 Torr, a feed back of the wirechamber pressure controls the proportional valve (PV), thus controlling the wirechamber pressure to be 100 Torr.

To protect from various disaster situations, four valves are used. Two solenoid valves (SV3 and SV4) controlled by two pressure switches (PS1 and PS2) with settings at 20 Torr are used, to protect from the situation where the pressure difference between the N2 volume and the wirechamber is more than 20 Torr. A check valve (CV2) with setting at 50 Torr is used, to avoid the situation where the pressure in the spectrometer is larger than the wirechamber by more than 50 Torr. A relief valve (RV3) set at 180 Torr is used, to protect from the situation where the pressure in the wirechamber is larger than the spectrometer by more than 180 torr.

During pumping out or venting, the three volumes are connected with MV5 and MV7 open. Pumping and venting speeds are controlled carefully to be always slower than 2 Torr/second, to suppress the pressure difference induced by gas dynamics.

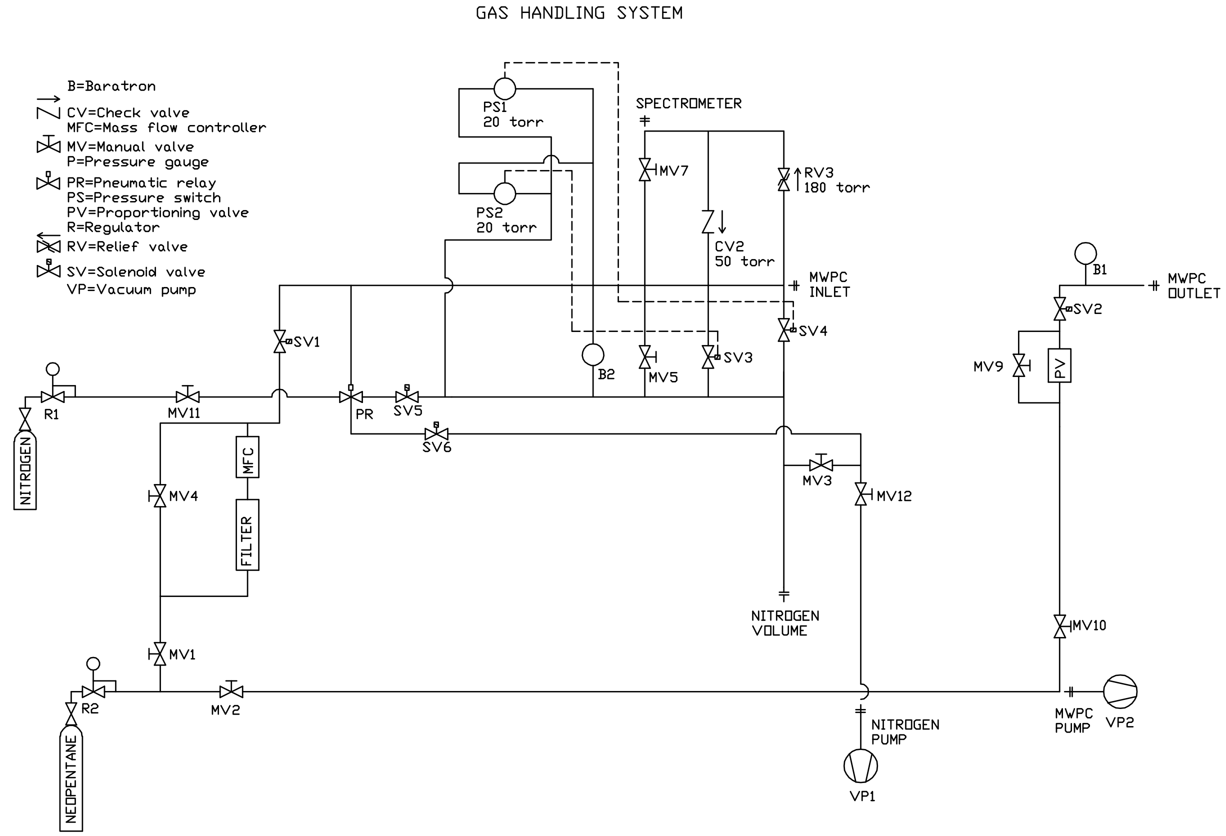

Figure 2.10: A schematic of the gas handling system.

2.4 Summary

The design philosophy for the beta detector system is presented in this chapter, along with detailed descriptions of the system. Offline calibration of the detector system is performed at Kellogg. The results from the calibration will be presented in the next chapter.

Chapter 3

Detector Calibration

3.1 Source of electrons

3.1.1 Kellogg 130 keV electron gun

The Kellogg Electron Gun was constructed to perform studies of electron backscattering and to calibrate detectors. The electron gun can produce mono-energetic beams up to 135 keV.

A schematic of the gun is shown in Fig. 3.1. Electrons were extracted from a hot filament by a potential of typically 6 kV in the source head. The filament is a standard loop filament, AEI model #1410. A picture of the filament is shown in Fig. 3.2.

The electrons were focused by an Einzel lens before passing through an additional acceleration potential of up to 130 kV minus the extractor voltage.

The electron beam current could be varied from a few electrons per second to several μA by adjusting the current passed through the filament. The resultant beam current remained stable after allowing the filament to warm up for typically half an hour.

After the acceleration column, two magnetic coils allowed steering of the beam in the horizontal and vertical directions.

A Faraday cup could be inserted into the beam to monitor the total current of the beam. A beam position monitor, consisting of a rotating wire which sweeps through the beam twice along two orthogonal axes, could be used to locate the beam within the beam pipe.

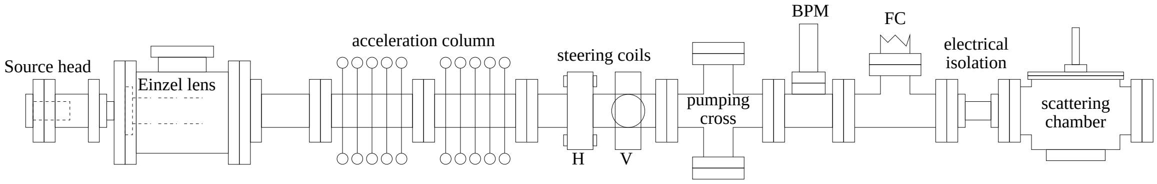

Figure 3.1: Schematic of the Kellogg Electron Gun. BPM indicates the location of the beam position monitor. FC indicates the location of the Faraday cup. H and V indicate the horizontal and vertical steering coils, respectively.

Figure 3.2: Filament AEI 1410 for the electron gun.

The energy of the electron gun was stable and reproducible. The energy was absolutely determined to the 1% level using a novel Helmholtz coil spectrometer (see next section). This spectrometer is iron-free and has a momentum resolution of 0.3% [44]. The energy of the electron gun was found to be monochromatic to better than the resolution of the spectrometer.

A scattering chamber is shown in Fig. 3.1 at the end of the electron gun. The chamber was used to study electron backscattering. It can be replaced by detectors or spectrometers to perform other studies.

The electron gun uses a fiber optic control system from Group3 Technology Ltd. [45]. A schematic of the control system is shown in Fig. 3.3. A loop controller card plugged into a control PC allows a LabView control program to supply control voltages to commercial power supplies, and read back the voltage setting from them. The interface of the LabView control program is shown Fig. 3.4. The LabView program allows saving of the settings of the power supplies and retrieving them later, thus an optimum tune for each energy can be saved on the computer.

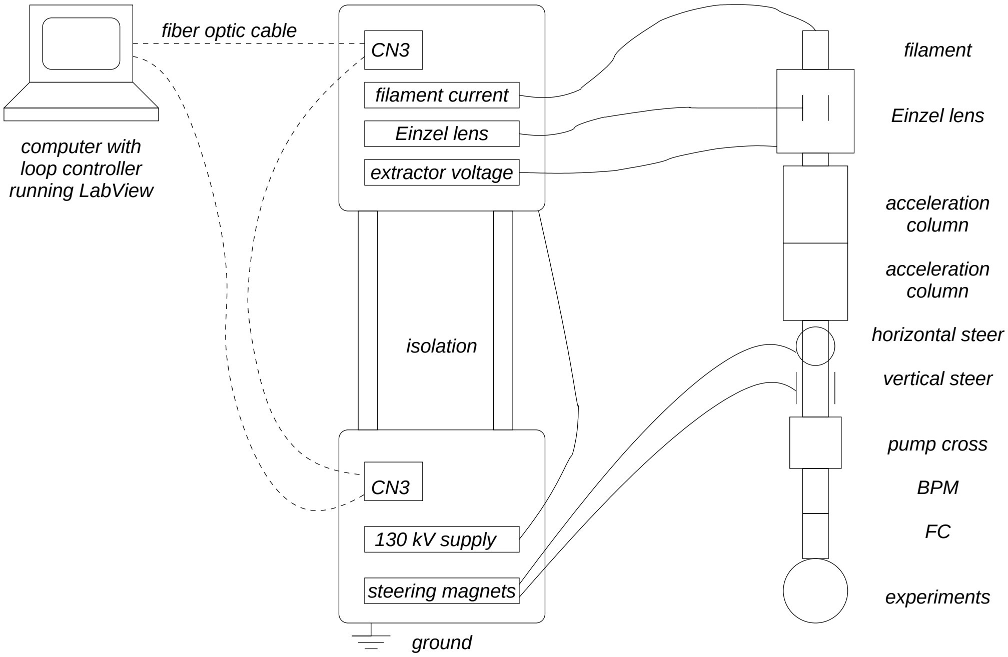

Figure 3.3: Schematic of the fiber optic control system of the Kellogg Electron Gun.

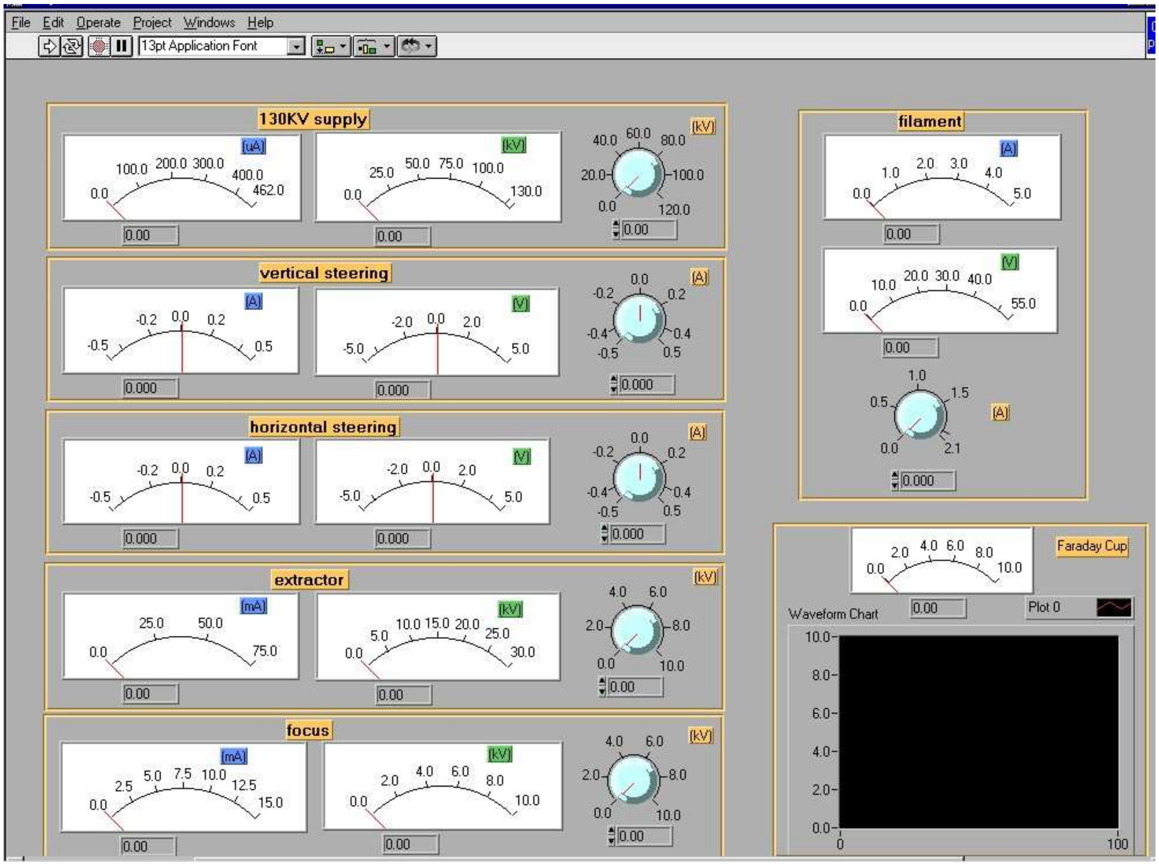

Figure 3.4: A screen shot of the interface of the LabView control program for the Electron Gun.

3.1.2 Double-focusing Helmholtz coil spectrometer

An iron-free, low-energy charged-particle magnetic spectrometer was designed using a Helmholtz coil geometry [44]. Through the fringe fields of the coils, the spectrometer provides focusing in both the dispersive and non-dispersive planes. By choosing the optimal deflecting angle and the positions of the source and the focal distance, a momentum resolution on the order of 0.3% is achieved. The spectromter is constructed to perform energy calibrations, and produce an energy-tunable monochromatic electron source for detector calibrations if a strong Sr-90 source is utilized.

In this section, we begin by presenting a simple first-order optical model for the Helmholtz spectrometer. Then we present simulations of the spectrometer properties via Monte-Carlo techniques using numerical 3-d ray tracing. Finally, we compare the simulations with measurements using a prototype spectrometer.

General discussions of β spectrometers, including magnetic and electrostatic spectrometers, can be found in many articles and reviews. An extensive treatment of magnetic spectrometers is in Siegbahn's paper [46]. Roy and Tremblay talked extensively about the design and operation issues of electrostatic β spectrometers [47]. Examples of iron-free double focusing spectrometers can be found in [48] and [49]. Siegbahn designed an iron-free double focusing spectrometer using two concentric coils with radii ρ_1 and ρ_2 and height h [48]. The space between ρ_1 and ρ_2 is used for electron optical arrangement. Our iron-free double-focusing design has some advantages: (a) it is very simple to build and operate, (b) it is easy to couple to accelerators, and (c) it does not need water-cooling. The resolution of our design is good(0.3%), and the solid angle of our design is 10^{-4} steradians.

3.1.2.1 First-order optical model

It is well known that a sector magnetic field with inclined field boundaries can have double-focusing properties, and that the momentum resolving power is twice as large as that for a sector field with perpendicular field boundaries [50].

As we show below, the Helmholtz-coil spectrometer can be modeled as a simple sector magnet with inclined field boundaries.

Helmholtz coils are two circular coaxial current rings of radius R, separated by a distance equal to R. Fig. 3.5 shows the magnetic field on the mid-plane between the two coils, as a function of r/R (r is the distance from the coil axis). This field is directed along the axis of the coils, and has a maximum value of B_0.

As shown in Fig. 3.5, the magnetic field changes sign at r_0. For a particle approaching the coils along the mid-plane, the oppositely directed magnetic field deflects the particle trajectory such that at the effective radius r_{eff}, the particle enters the field obliquely. This system thus effectively works

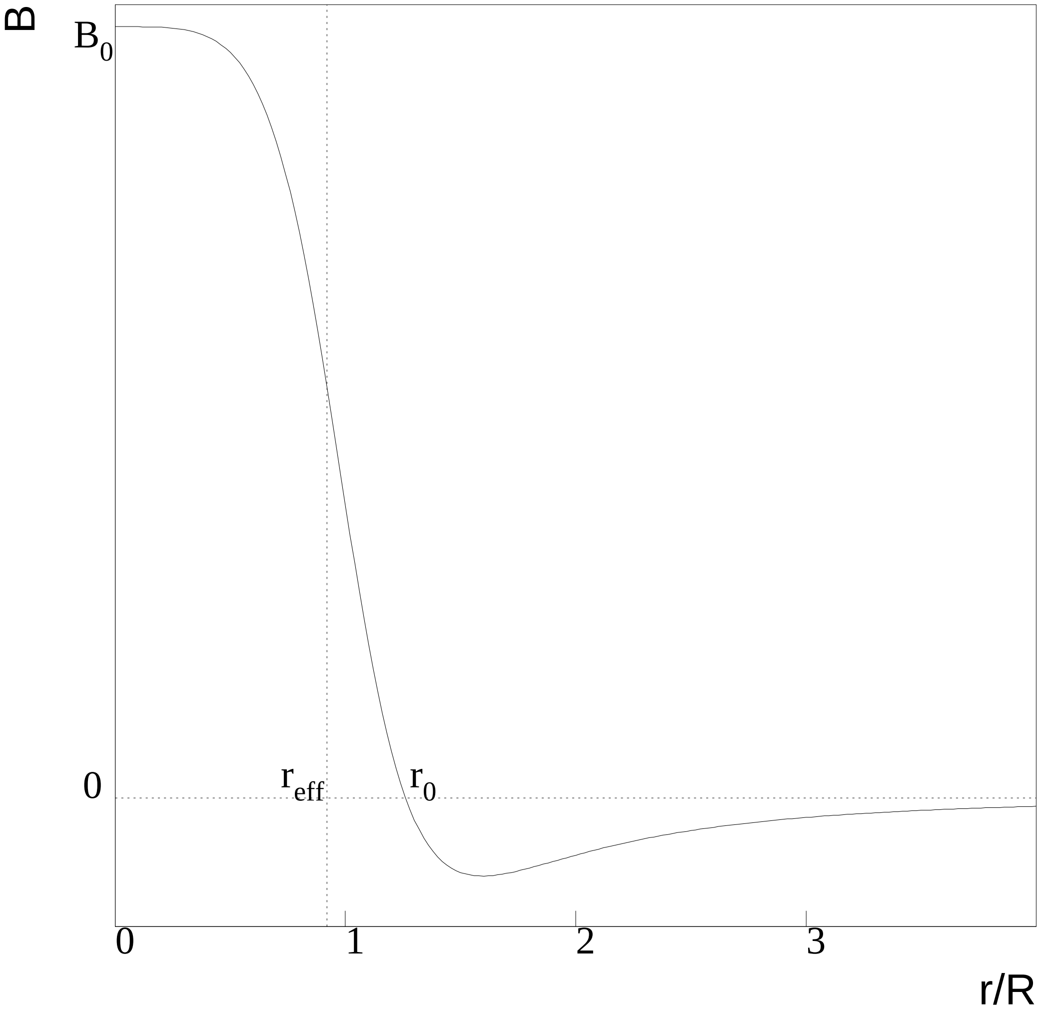

Figure 3.5: Mid-plane magnetic field for a Helmholtz coil.

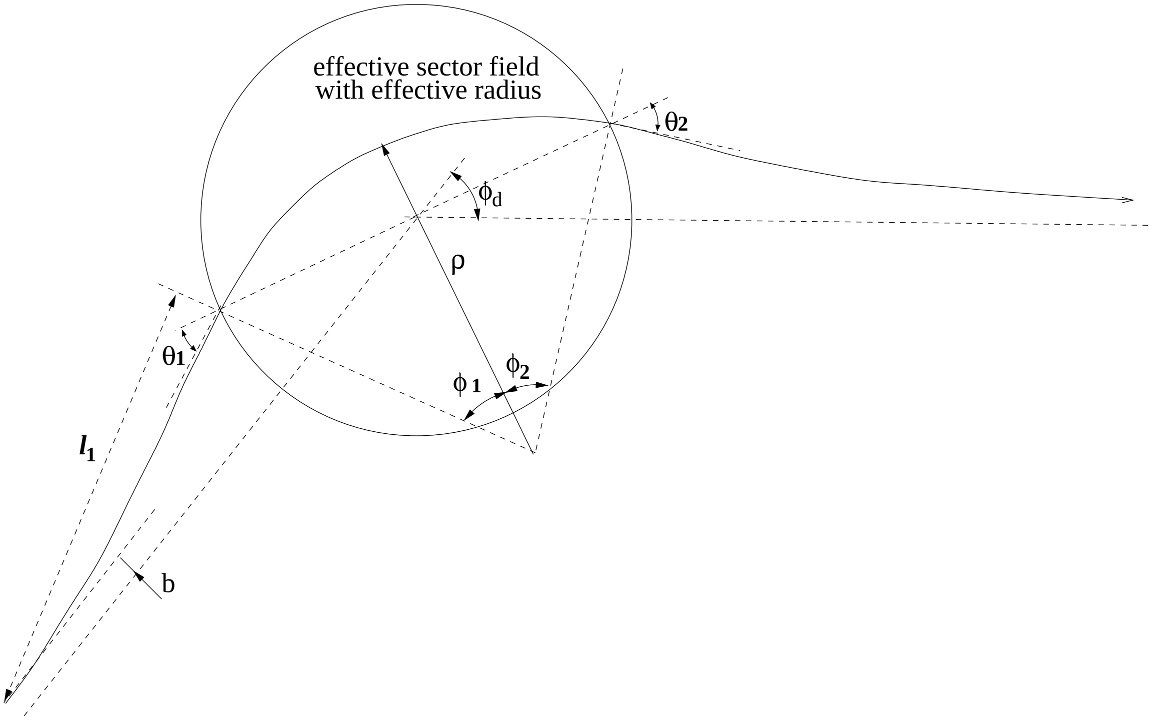

Figure 3.6: Schematic diagram of particle entering Helmholtz-coil field. In the first-order optical model, the field of the coils is effectively a uniform sector field with radius r_{eff}.

as a sector field with inclined field boundaries (see Fig. 3.6). The effective radius is chosen such that

$$\int_0^{r_{\text{eff}}} B_0 \,\mathrm{d}r = \int_0^{r_0} B(r)\,\mathrm{d}r. \tag{3.1}$$

Numerically we find $r_{\text{eff}} \simeq 0.917R$.

Fig. 3.6 shows the particle trajectory in the mid-plane between the two coils. In the first order model, the sector field is a uniform field with effective radius r_{eff}. Particles enter the magnetic field obliquely with angle θ_1, and leave the field obliquely with angle θ_2. As shown in Appendix A, $\theta_1 = \theta_2$.

The angle θ_1 is crucial for vertical focusing. By increasing the impact parameter b, we can increase θ_1, thus increasing the vertical focusing, and thereby obtaining a point-to-point double-focusing solution. In the following, we show that such solutions exist for $b > 0$ and derive them. For $b \simeq 0$, the vertical (non-dispersive) focusing is insufficient and there is no point-to-point double-focusing solution, but we may still get vertical point-to-parallel focusing.

When a source is placed at a distance l_1 from the effective field boundary, an image is formed at the other side a distance l_2 from the effective field boundary. The radius of curvature of the particle trajectory in the sector field is denoted as ρ. Using the formalism for a sector magnet with inclined field boundaries adjusted for double focusing [50], if l_1, l_2, θ_1, θ_2, ϕ_1,ϕ_2 satisfy the following equations:

$$\begin{aligned} l_1 &= \rho/\tan\theta_1 && (3.2) \\ l_2 &= \rho/\tan\theta_2 && (3.3) \\ \tan\phi_1 &= 2\tan\theta_1 && (3.4) \\ \tan\phi_2 &= 2\tan\theta_2, && (3.5) \end{aligned}$$

we can achieve point-to-point double focusing in both the dispersive and non-dispersive planes. For the case $\theta_1 = \theta_2$, we have $l_1 = l_2$ and $\phi_1 = \phi_2$, i.e., a symmetric solution.

For the central trajectory, the initial distance to the center of the coil axis r_i ($r_\mathrm{i} \simeq l_1 + r_\mathrm{eff}$), the impact parameter b, and the radius of the trajectory in the sector field ρ, can be chosen to satisfy the above relations.

Using the two independent equations (3.2) and (3.4), and the relationship between torque and angular momentum(noting that the magnitude of momentum is constant), we can express θ_1 in terms of r_i, b, and ρ. We combine the triangle relation and equation (3.4) to get another equation. Generally, we get two independent equations relating r_i, b, and ρ:

$$\begin{aligned} b + \left(\frac{5\sqrt{5}}{64a_1} - \frac{a_2}{a_1}\right)\frac{R^2}{\rho} - \frac{5\sqrt{5}R^3}{16a_1}\frac{1}{\rho r_\mathrm{i}} &= \rho - \sqrt{\rho^2 - r_\mathrm{eff}^2}, && (3.6) \\ \frac{r_\mathrm{eff}}{\sqrt{1 + (\frac{r_\mathrm{i} - r_\mathrm{eff}}{\rho})^2}} &= \rho - \sqrt{\rho^2 - r_\mathrm{eff}^2}, && (3.7) \end{aligned}$$

where r_eff, a_1 and a_2 are geometric factors: $r_\mathrm{eff} = 0.917R$, $a_1 = 0.911$, $a_2 = -0.183$. See Appendix A for detailed derivation of these two equations.

For a given R, solving the above two equations numerically for different b's, we obtain a sequence of solutions (b,r_i,ρ) for point-to-point double focusing.

As an example, Fig. 3.7 shows the point-to-point double focusing solutions for $R = 0.25$ m. Also shown in Fig. 3.7 is the deflecting angle ϕ_d for the double focusing solutions.

3.1.2.2 Numerical calculation of spectrometer properties

For a Monte-Carlo simulation of the spectrometer properties, there are two essential tasks. First, the calculation of the magnetic field in 3-d is done using numerical integration of the Biot-Savart Law. Second, the particle is traced through the magnetic field using finite difference techniques.

An example of such a calculation is shown in Fig. 3.8. In order to obtain reasonable values for ρ and r_i, we have chosen $b = 3$ cm to give a double focusing solution ($b = 3$ cm, $r_\mathrm{i} = 1.5$ m, $\rho = 0.41$ m). In the Monte-Carlo simulation, electrons from the source are emitted in random directions.

From Fig. 3.8, we find double focusing at 3 m $= (1.5 + 1.5)$ m along the central trajectory. This

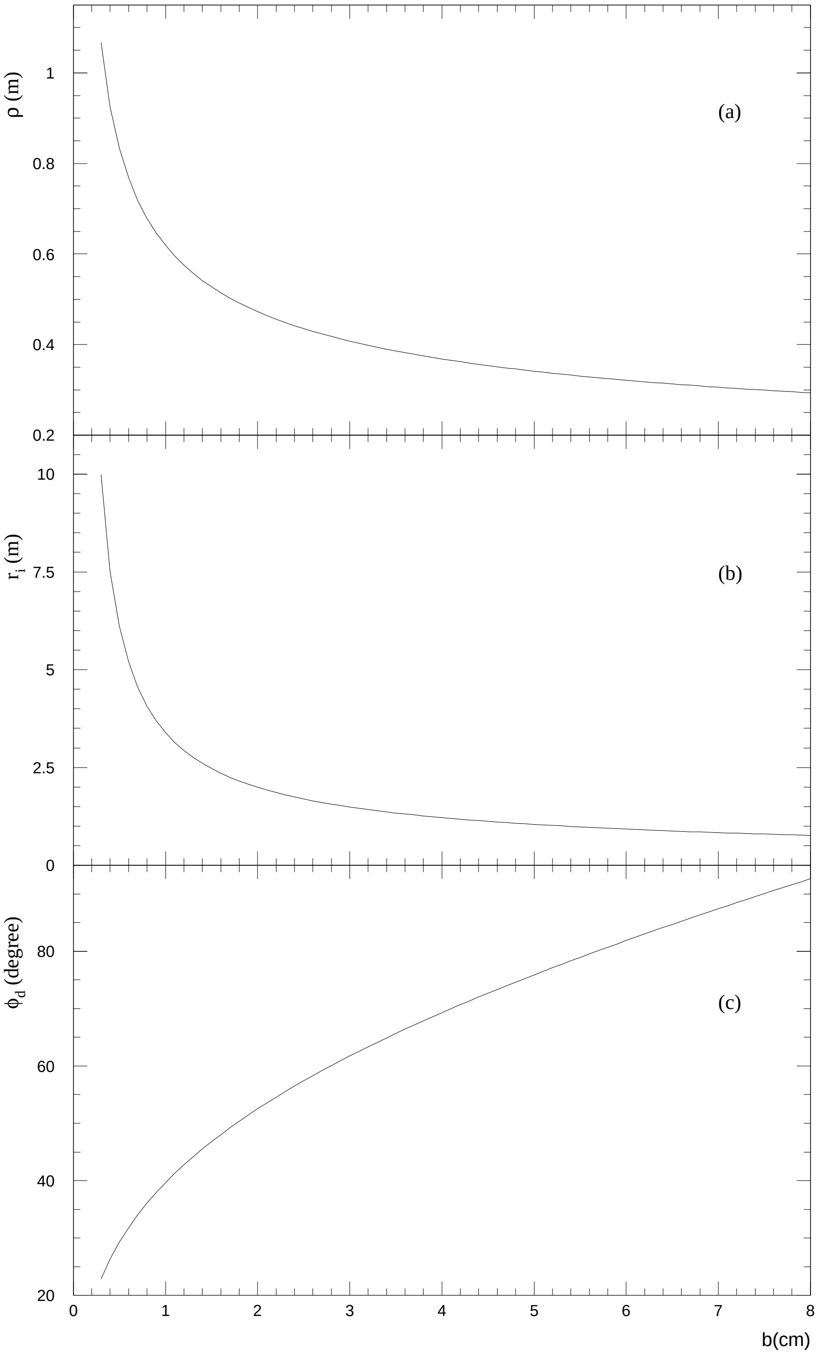

Figure 3.7: Solutions for point-to-point double focusing with $R = 0.25$ m. (*a*) ρ vs. b; (*b*) r_i vs. b; (*c*) ϕ_d vs. b.

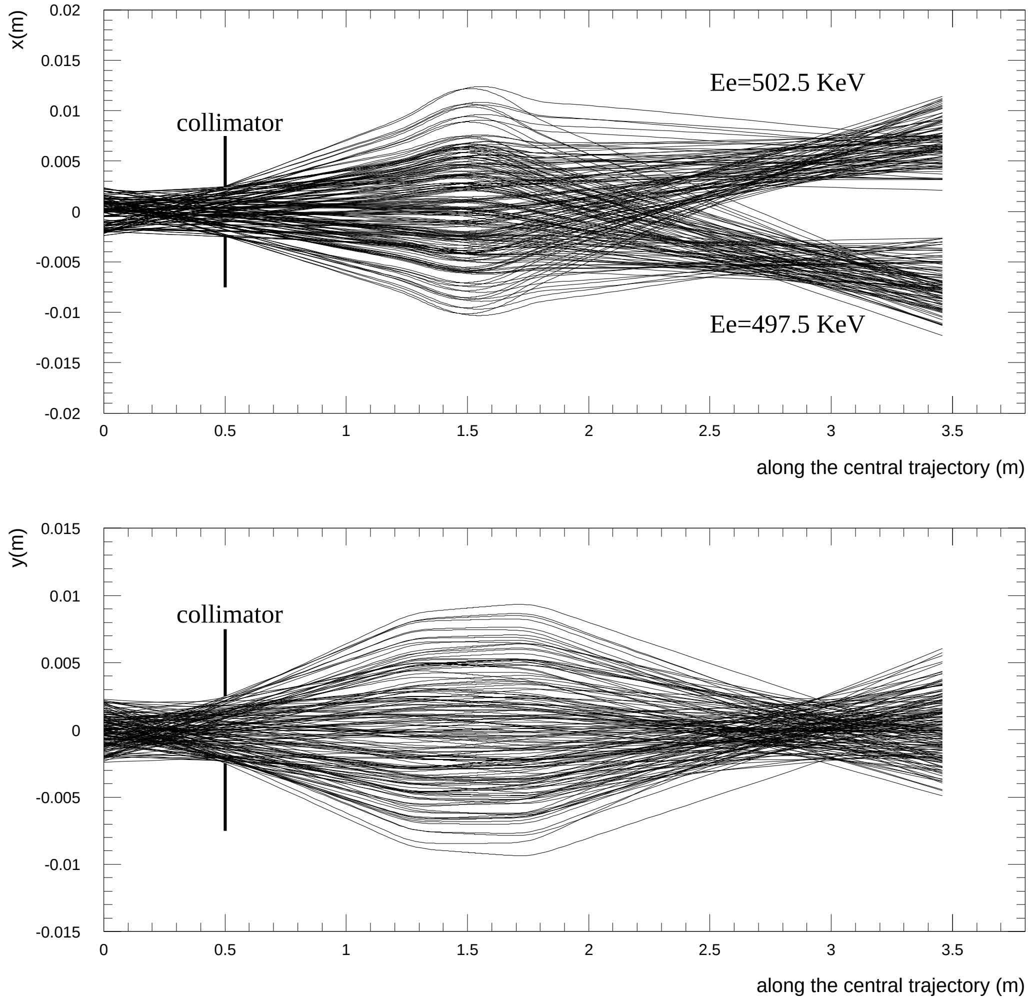

Figure 3.8: Double-focusing solutions. *Upper* figure is the dispersive plane; *lower* figure is the non-dispersive plane. The central trajectory ($x = y = 0$) is the trajectory of a 0.5 MeV electron moving from $r_i = 1.5$ m, with impact parameter $b = 3$ cm. A 5×5 mm collimator is put on the mid-plane at a distance of 50 cm from the source. In the usual notation, x is the displacement from the central trajectory in the dispersive plane, y is the displacement from the central trajectory in the non-dispersive plane.

is exactly what was expected for a symmetric solution. Hence the first-order model prediction and the Monte-Carlo Calculation are in agreement. The resolution of this system is $w_{\mathrm{s}}/4\rho = 0.3\%$ [50], where w_{s} is the source width taken to be 5 mm.

As we have discussed in Section 2, for $b = 0$, the vertical focusing is insufficient and there is no point-to-point double-focusing solution. However, we may still get vertical point-to-parallel focusing. We find ($b = 0$, $r_{\mathrm{i}} = 1.5$ m, $\rho = 0.44$ m) is a solution for vertical point-to-parallel focusing. The deflecting angle is calculated to be 55.6°. The Monte-Carlo simulation of this solution is shown in Fig. 3.9. We see there is point-to-parallel focusing in the non-dispersive plane, and point-to-point

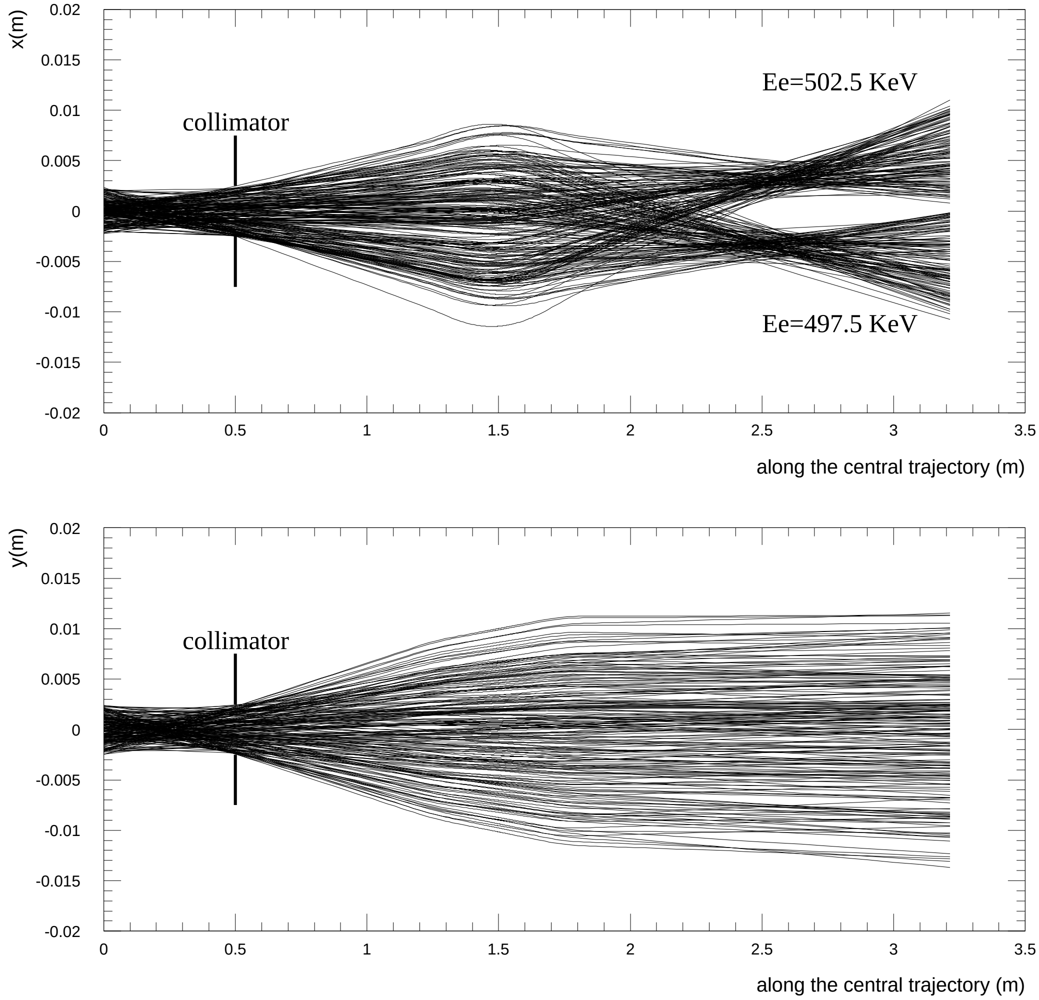

Figure 3.9: Focusing properties for vertical point-to-parallel solution. *Upper* figure is the dispersive plane; *lower* figure is the non-dispersive plane. The central trajectory ($x = y = 0$) is the trajectory of a 0.5 MeV electron moving from $r_i = 1.5$ m, with impact parameter $b = 0$. An 5×5 mm collimator is put on the mid-plane at a distance of 50 cm from the source.

focusing in the dispersive plane at 2.7 m= $(1.5 + 1.2)$ m along the central trajectory.

3.1.2.3 Measurements with a prototype spectrometer

In constructing the prototype spectrometer, we adopted the vertical point-to-parallel focusing solution ($b = 0$, $r_{\mathrm{i}} = 1.5$ m, $\rho = 0.44$ m). This solution was chosen because the $b = 0$ on-axis solution is easier to design mechanically than the off-axis double focusing solutions. Fig. 3.10 shows a schematic layout of the prototype spectrometer.

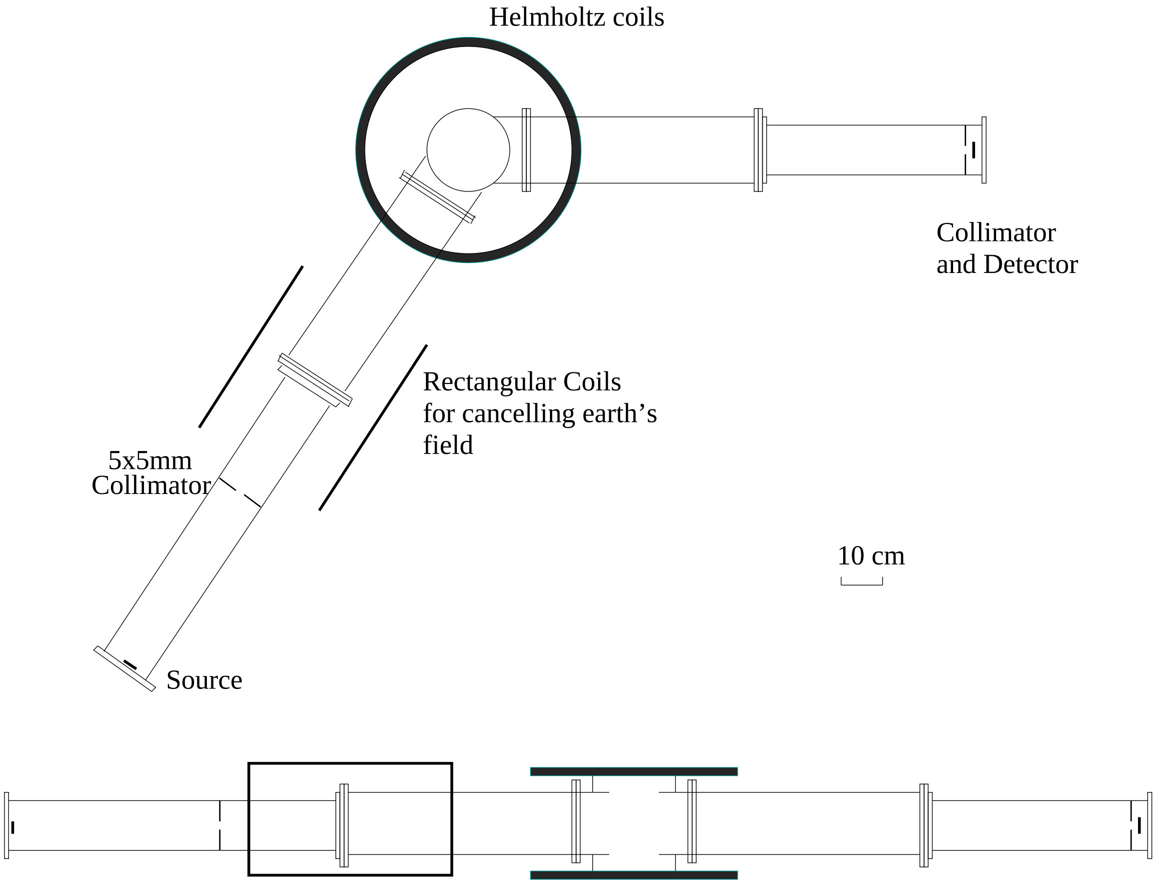

Figure 3.10: Schematic diagram of the prototype spectrometer. *Above*: top view; *Below*: side view.

The Helmholtz pair are two coaxial coils with radius 25 cm, separated by 25 cm. Each coil is made of 1510 turns of 1.024 mm diameter copper wire. The current in each coil is low enough that water cooling is not needed (see Fig. 3.12). We detect the electrons using a surface-barrier silicon detector with active area 200mm^2. A 5×5 mm collimator is put in the source arm. The collimator in the detector arm is 5×20 mm. A rectangular coil is placed around the source arm to cancel the horizontal component of the earth's field. The electron source, the silicon detector, and the electron paths are enclosed in a vacuum chamber. The vacuum pipe is made of non-magnetic stainless steel, so the magnetic field profile of the spectrometer can be easily calculated.

The source we use for testing the spectrometer is ^{113}Sn, with an absolute activity of 0.4μ C and a diameter of about 5 mm. The main conversion electron lines of the ^{113}Sn source are shown in Table 3.1.

Table 3.1: Dominant EC lines for ^{113}Sn

Energy (KeV)	intensity
363.748	28.7%
387.451	5.57%
390.862	1.13%

The source spectrum as measured directly with the silicon detector is shown in Fig. 3.11. The measured count rate as a function of spectrometer current is shown in Fig. 3.12

For a given deflecting angle, the current is proportional to the electron momentum, thus Fig. 3.12 represents a momentum spectrum of the source after passing the spectrometer. The two lower energy peaks are clearly separated. The momentum resolution is $\sigma_{\mathrm{P}}/P = 0.3\%$. For comparison, a Monte-Carlo simulation of the expected distribution for the lower energy peak is also shown in Fig. 3.12 as a dotted histogram.

The simulation agrees very well with the measurement, except for a small shift of the peak position corresponding to a deflecting angle difference of about 0.09°. Currently, the angle between the two arms of the spectrometer is not calibrated to that precision, so this discrepancy may result from the fact that the deflecting angle of the spectrometer is not 55.6°. We are investigating more precise methods to calibrate the angle.

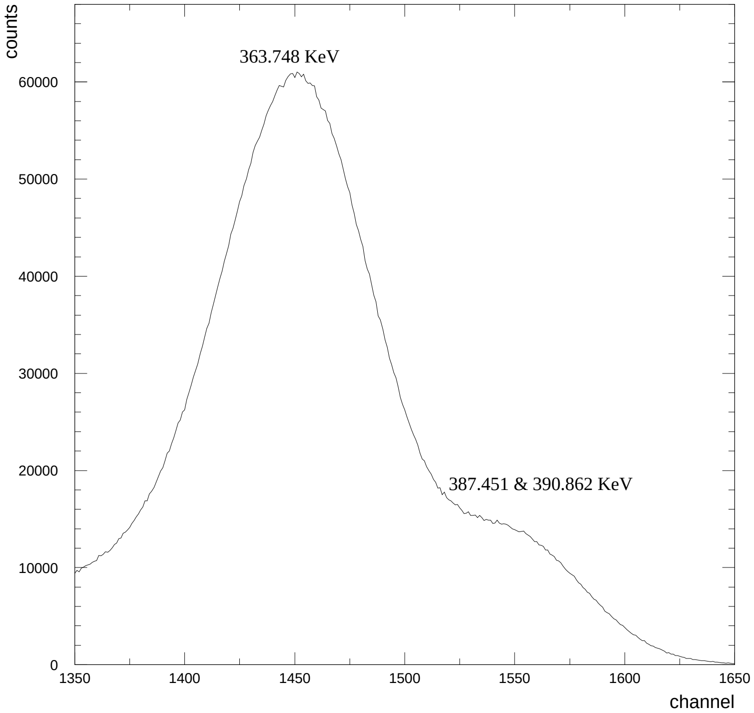

Figure 3.11: Source spectrum measured directly with the silicon detector.

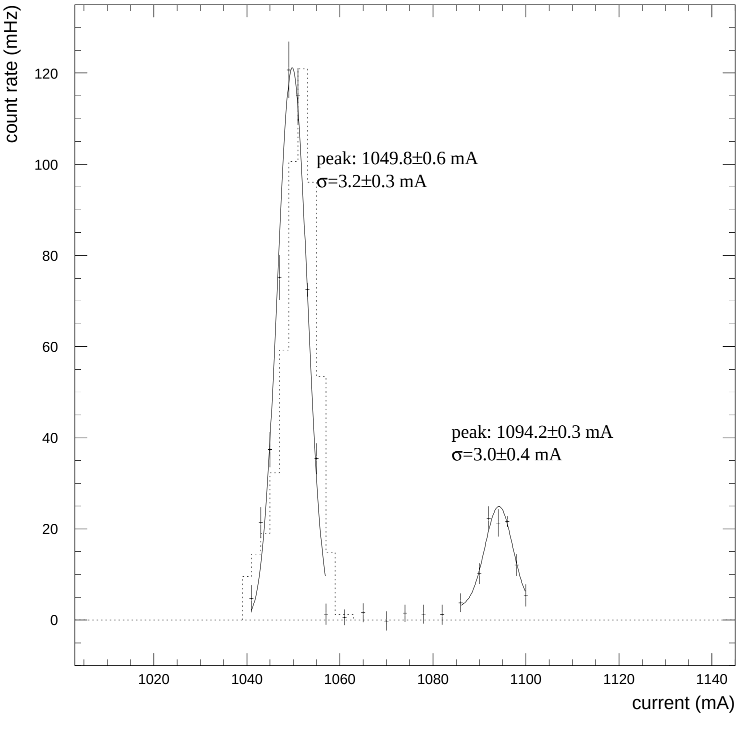

Figure 3.12: Source spectrum measured after passing through the spectrometer. Points are the measurements; solid lines are the fits of measurements to a Gaussian function; dotted histogram is the Monte-Carlo simulation of the lower energy peak.

3.2 The plastic scintillator detector

3.2.1 Studies of low-energy electron response

The plastic scintillator detector response to low-energy electrons (energy less than 130 keV) is studied using the Kellogg e- gun. The resolution of the Suzuno detector is presented, and non-linearity at low energies due to light quenching and dead layer effects of the plastic scintillator is studied. Two experimental setups are used. One is with the full Suzuno detector, the other is with a scintillator disk.

3.2.1.1 Studies with the full Suzuno detector

In this setup, the Suzuno detector is placed at the end of the e- gun tube. A 6 μm thick mylar film is used to seal the vacuum for the e- gun tube. There is a gap of about 1.2 cm of air between the mylar film and the detector. The electronics to measure the energy spectra are shown in Fig. 3.13.

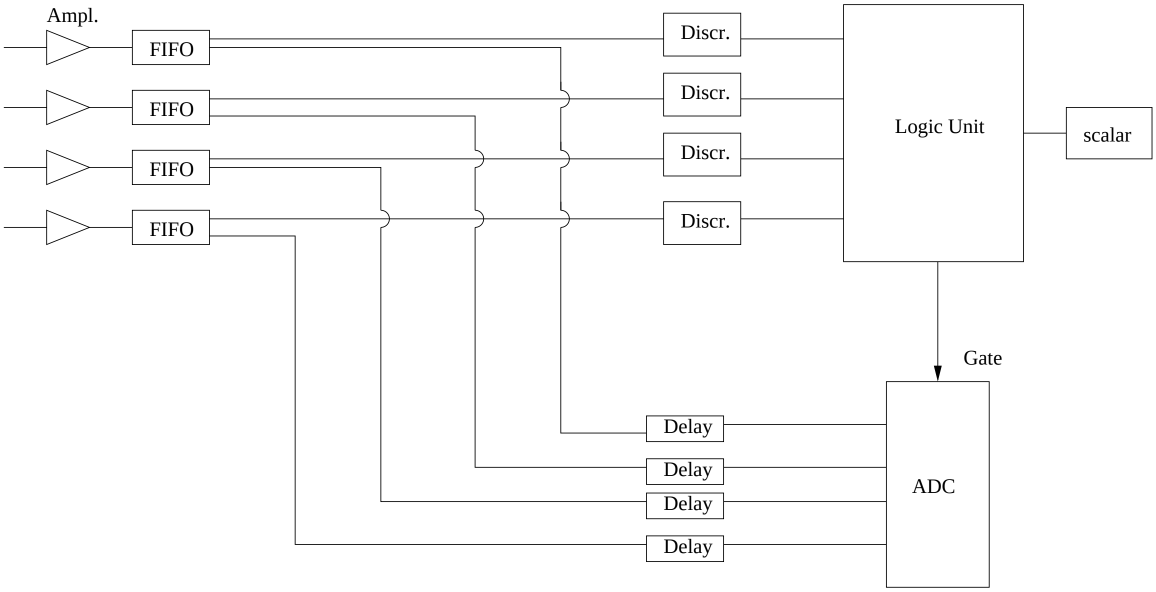

Figure 3.13: Electronics to measure the energy spectra

The discriminator threshold for each phototube is set to about half the amplitude of the Single Photo-Electron(SPE) pulse. When the beam is turned off, the background rates with different numbers of coincidence tubes are measured, as are shown in Table 3.2, where "n-fold" means a trigger is generated whenever there are "n" phototubes giving signal above discriminator threshold.

When the energy of the incident electrons is not too small(beam energy $\geq$ 40keV), the full energy peak is clearly seen in the ADC spectrum of the 4-tube sum, as is shown in Fig. 3.14 with a Gaussian fit for the peak, where the electron beam energy is 130keV.

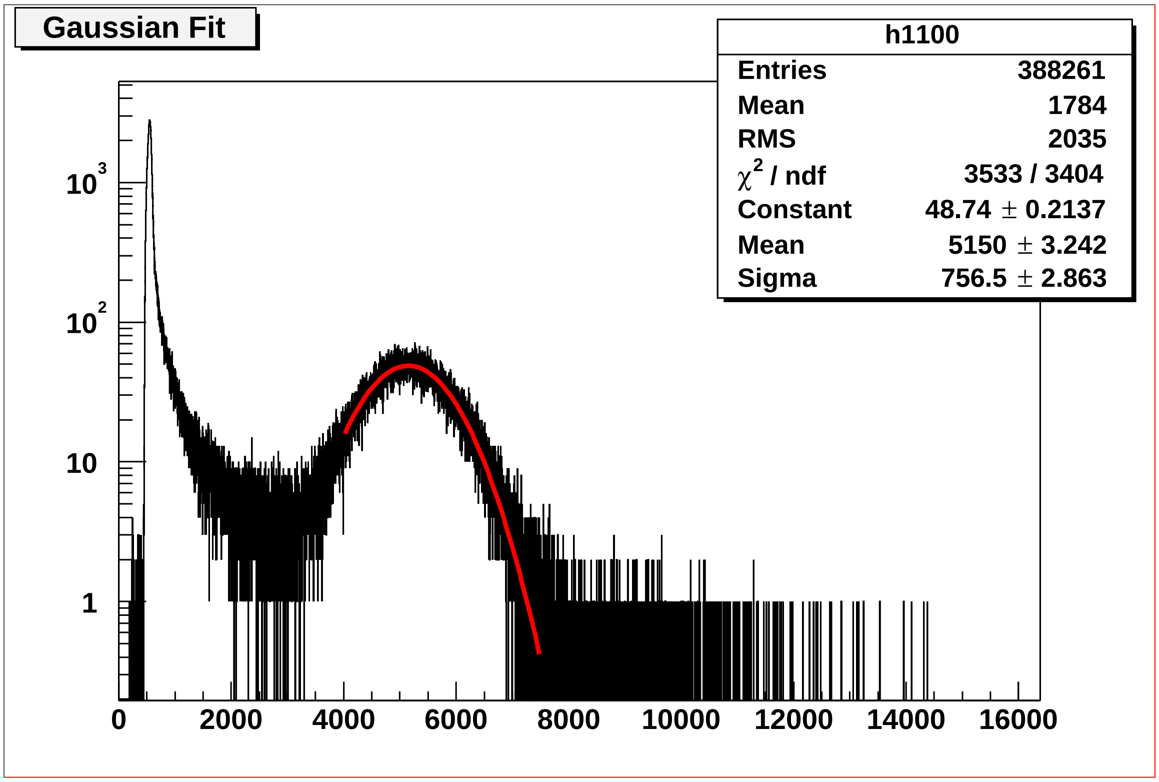

Figure 3.14: Gaussian fit, at 130keV of nominal beam energy, 6μm mylar + 12mm air gap.

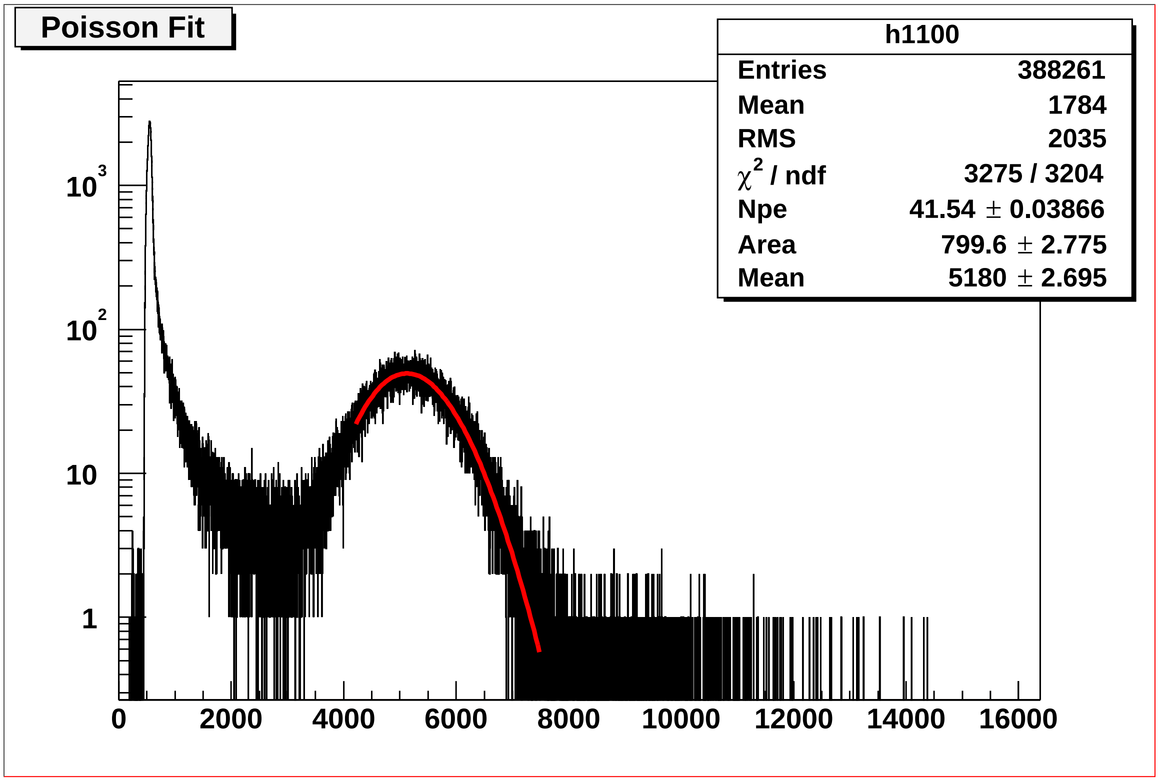

Figure 3.15: Same spectrum using Poisson fit, at 130keV of nominal beam energy.

Table 3.2: Background rates with different numbers of coincident PMTs

trigger	background rate(Hz)
1-fold	2240
2-fold	172
3-fold	81
4-fold	49

For plastic scintillator, the energy resolution should be dominated by the statistical fluctuation of the number of photo-electrons(NPE) generated by the photo cathode of the PMT. From the fitted peak and sigma, the NPE can be calculated by

$$NPE = (\frac{peak - pedestal}{\sigma})^2$$

and the energy resolution is related to NPE by $1/\sqrt{NPE}$. The NPE at 130 keV nominal beam energy is measured to be 46, i.e., 354 photo-electrons per MeV energy deposition.

Ideally a Poisson distribution should be applied to fit the full energy peaks. When the mean number of photo-electrons are large enough, the Gaussian distribution can be used as a convenient approximation to the Poisson distribution. As is shown in Fig. 3.14 and Fig. 3.15, the goodnesses of both fits are comparable. The error induced by the approximation gets larger with smaller NPE. For comparison, the full energy peaks at 35, 40, 43, 46, 50, 60, 70, 80, 90, 100, 110, 120 and 130 keV of nominal beam energies are fit with both Poisson and Gaussian functions. The extracted peak positions are compared in Fig. 3.16, where the x axis is the beam energy after subtracting the energy loss in 6 μm mylar and 12 mm air gap. This is simulated by Geant4.4.0, where the peak positions of the transmitted electron spectra are extracted. While it is easier using the NIST ESTAR database to calculate the energy loss in mylar and air gap, the energy loss from ESTAR is the mean energy loss. The above method uses the peak energy of the transmitted electron, instead of the mean energy. We found that Geant4.4.0 and NIST ESTAR agree very well on the mean energy losses, while Geant4.4.1 does not agree well with NIST ESTAR, thus Geant 4.4.0 was used to calculate the energy loss.

A linear fit of the calibration points is shown in Fig. 3.17. Fig. 3.18 is the residual of the linear fit. The calibration points are obtained with Poisson fitting. From Fig. 3.17 and Fig. 3.18, the nonlinearity of the Suzuno detector is clearly presented at this low energy, with a large error bar. A large part of the error bar is due to the error in determining the absolute energy of the electron. At the moment, we can only say that the non-linearity is less than 10% from 20 keV to 50 keV, and less than 2% from 50 keV to 130 keV. The linearity of plastic scintillators at higher energy is generally much better than at this low energy [51].

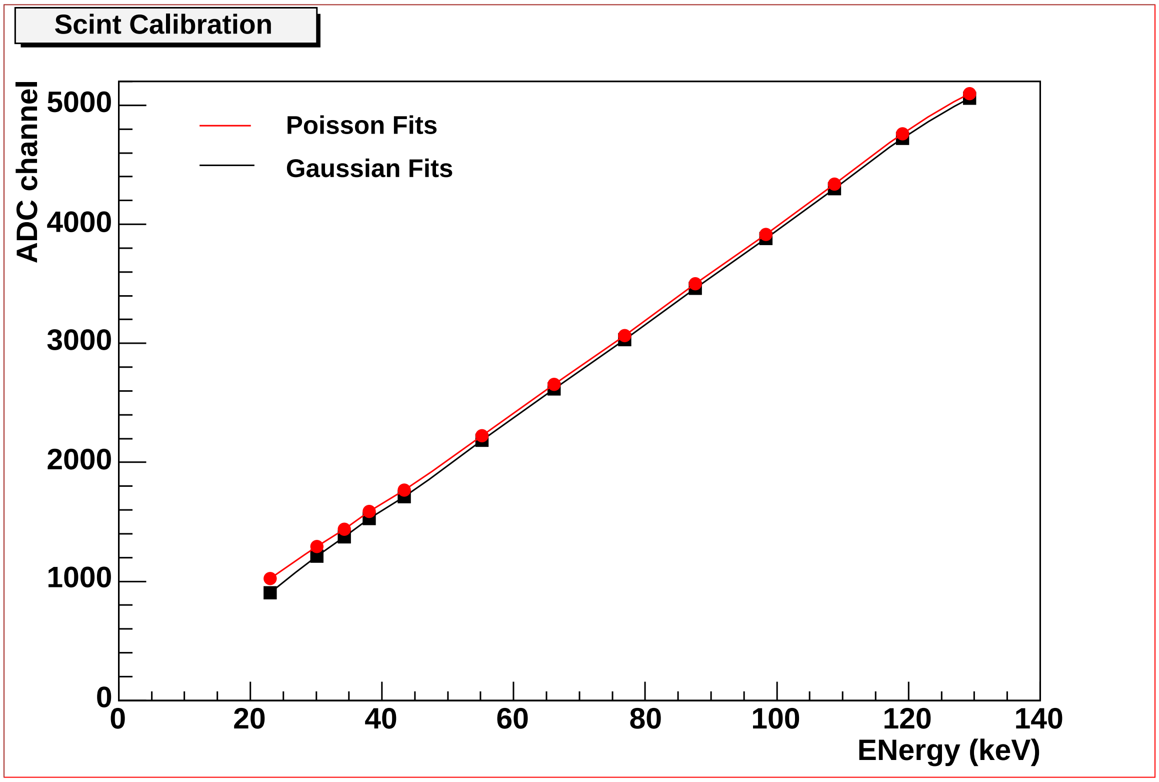

Figure 3.16: Calibration of Suzuno detector with both Poisson and Gaussian fits.

For plastic scintillators, non-linearity at low energies can be attributed to two factors. One is a dead layer on the surface of the scintillator, which induces electron energy loss, without generating photons. The other is quenching interactions between excited molecules created along the path of the incident electron [52, 53]. Since a higher ionizing power produces a higher density of excited molecules, more quenching interactions will take place. In this model put forward by Birks [52, 53], the light output per unit length, $\mathrm{d}L/\,\mathrm{d}x$, is related to the stopping power by

$$\frac{\mathrm{d}L}{\mathrm{d}x} = \frac{S\frac{\mathrm{d}E}{\mathrm{d}x}}{1 + k_{\mathrm{B}}\frac{\mathrm{d}E}{\mathrm{d}x}} \tag{3.8}$$

with S the absolute scintillation efficiency, and k_{B} the parameter relating the magnitude of quenching to the stopping power dE/dx. A simple transformation of Equation 3.8 gives

$$\frac{\mathrm{d}L}{\mathrm{d}E} = \frac{S}{1 + k_{\mathrm{B}}\frac{\mathrm{d}E}{\mathrm{d}x}},$$

where S and k_{B} are not the same as in Equation 3.8, but use the same name for simplicity. Integrating this equation gives the total light output L for a incident electron energy of E:

$$L(E) = \int_0^E \frac{S\,\mathrm{d}E}{1 + k_{\mathrm{B}}\frac{\mathrm{d}E}{\mathrm{d}x}}.$$

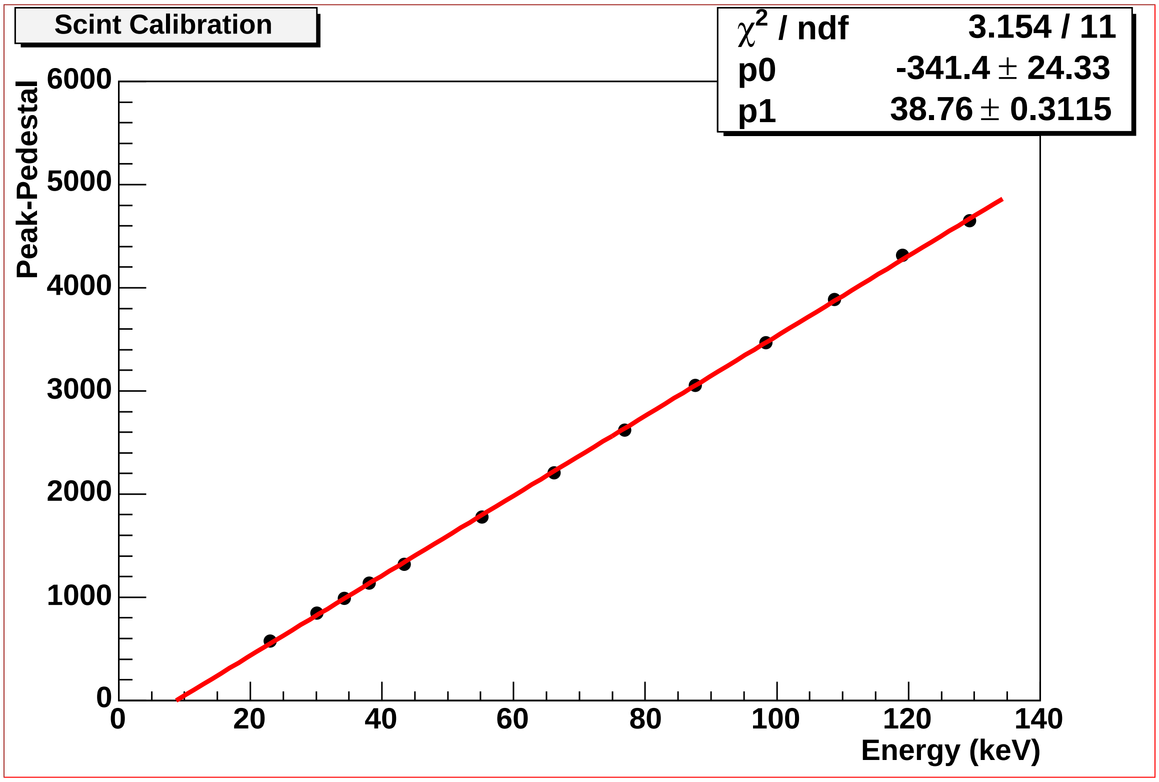

Figure 3.17: Linear fit of the calibration points.

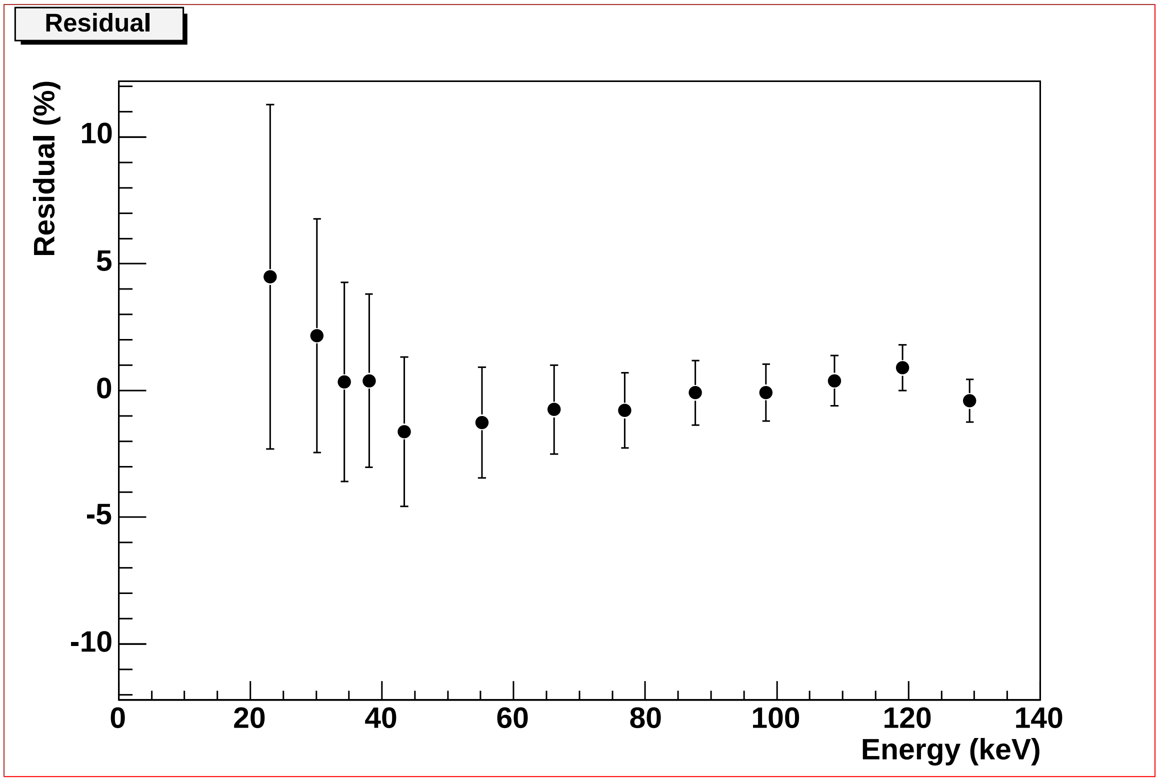

Figure 3.18: Residual of the linear fit.

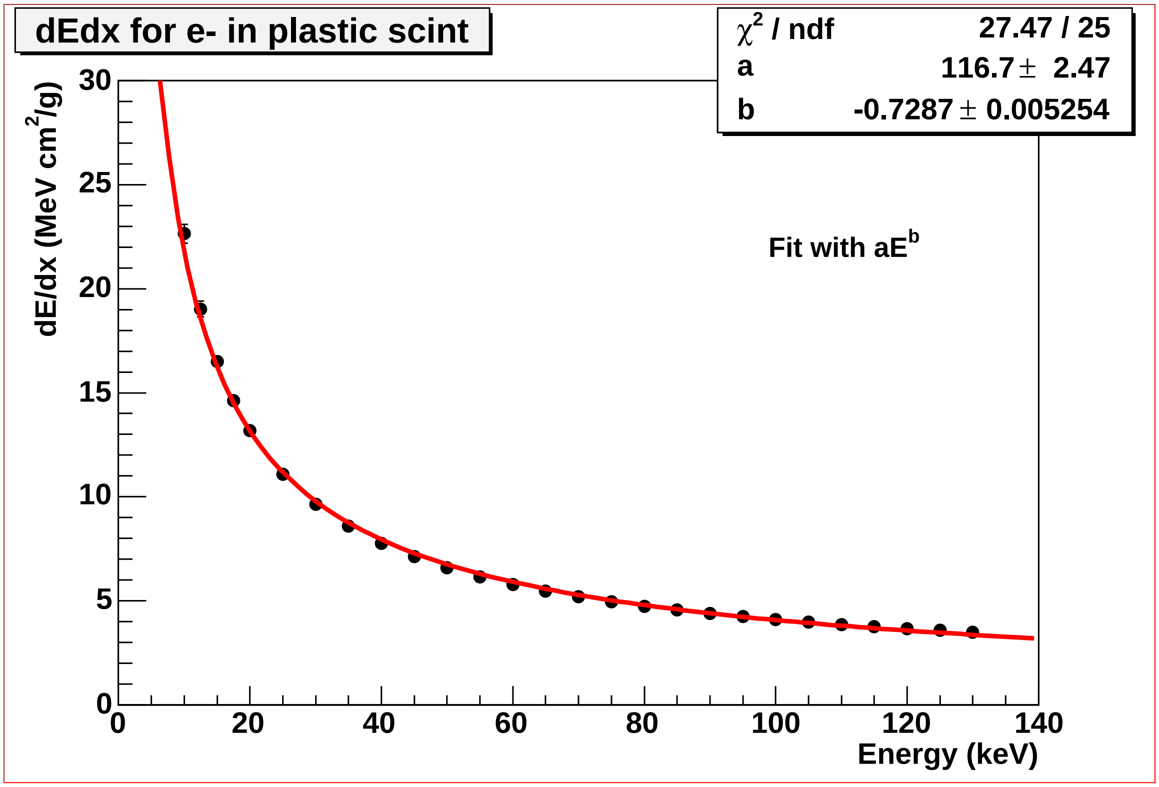

Figure 3.19: A fit of ESTAR dE/dx data with aE^{b}.

Including the dead layer effect will change the upper limit of integration:

$$L(E) = \int_0^{E-\Delta E} \frac{S\,\mathrm{d}E}{1 + k_{\mathrm{B}}\frac{\mathrm{d}E}{\mathrm{d}x}}, \tag{3.9}$$

where ΔE is the electron energy loss in the dead layer of thickness t.

$L(E)$ in Equation 3.9 is proportional to the Number of Photo-Electrons (NPE) obtained. In order to fit the experimental data points of NPE versus the incident electron energy with equation 3.9, we must know dE/dx. The NIST ESTAR database gives dE/dx for energies above 10 keV. We will fit the ESTAR dE/dx data for energies above 10 keV with a functional form of aE^{b} and extrapolate to lower energies, as is shown in Fig. 3.19, with a and b as the fitting parameters.

Integrating dE/dx gives the electron energy as a function of traveled path x:

$$E(x) = [E_0^{1-\mathrm{b}} - (1-b) * a * x]^{\frac{1}{1-b}}, \tag{3.10}$$

where E_0 is the initial electron energy. With a dead layer thickness of t, the integration upper limit of Equation 3.9 is

$$E_{\mathrm{up}} = [E^{1-\mathrm{b}} - (1-b) * a * t]^{\frac{1}{1-b}}.$$

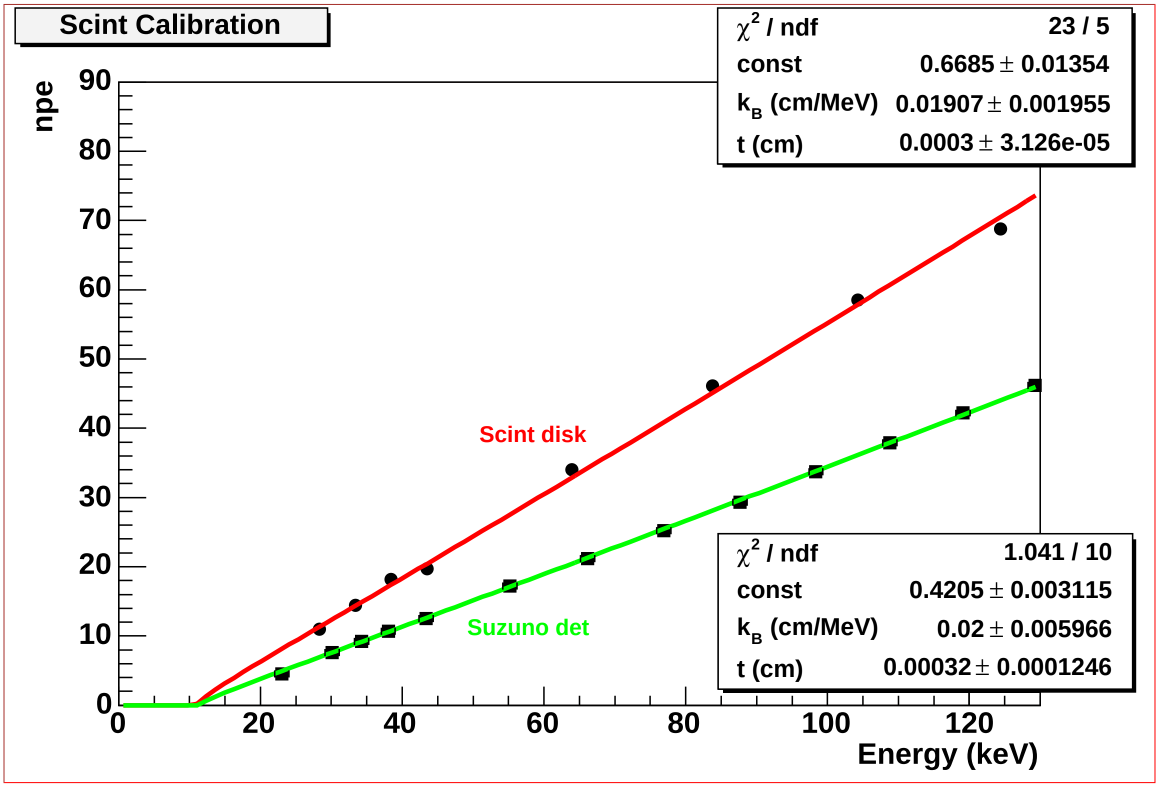

Figure 3.20: Fits of two sets of experimental data points with light quenching and dead layer effects. The green line is for the Suzuno detector setup, while the red line is for the scintillator disk setup.

Fitting the data points using Equation 3.9 with S, k_B and t as fitting parameters, we can extract the values of these parameters, as is shown in Fig. 3.20 as the green line marked *Suzuno det*.

3.2.1.2 Studies with the scintillator disk

To eliminate the uncertainty in the electron energy due to energy losses in the Mylar film and air gap, we placed a scintillator disk directly at the end of the e- gun tube. The vacuum is sealed with an O-ring between the e- gun tube and the scintillator disk. A phototube is placed at the center of the disk to collect light. The scintillator material is the same as what is used in the Suzuno detector. To block the light from the filament in the electron gun, we coat the scintillator disk with a 50 nm thickness of Aluminum. The energy loss in the Aluminum coating is negligible.

The energy spectra for beam energy at 25, 30, 35, 40, 60, 80, 100, 120keV is shown in Fig. 3.21 and Fig. 3.22. Even with a beam energy of 25 keV, the full energy peak is clearly seen. The peak at lowest channels is the pedestal.

A linear fit of the calibration points is shown in Fig. 3.23. Fig. 3.24 is the residual of the linear fit. The calibration points are obtained with Poisson fitting of the full energy peaks. From Fig. 3.23 and Fig. 3.24, the magnitude of non-linearity of the scintillator disk is consistent with the Suzuno

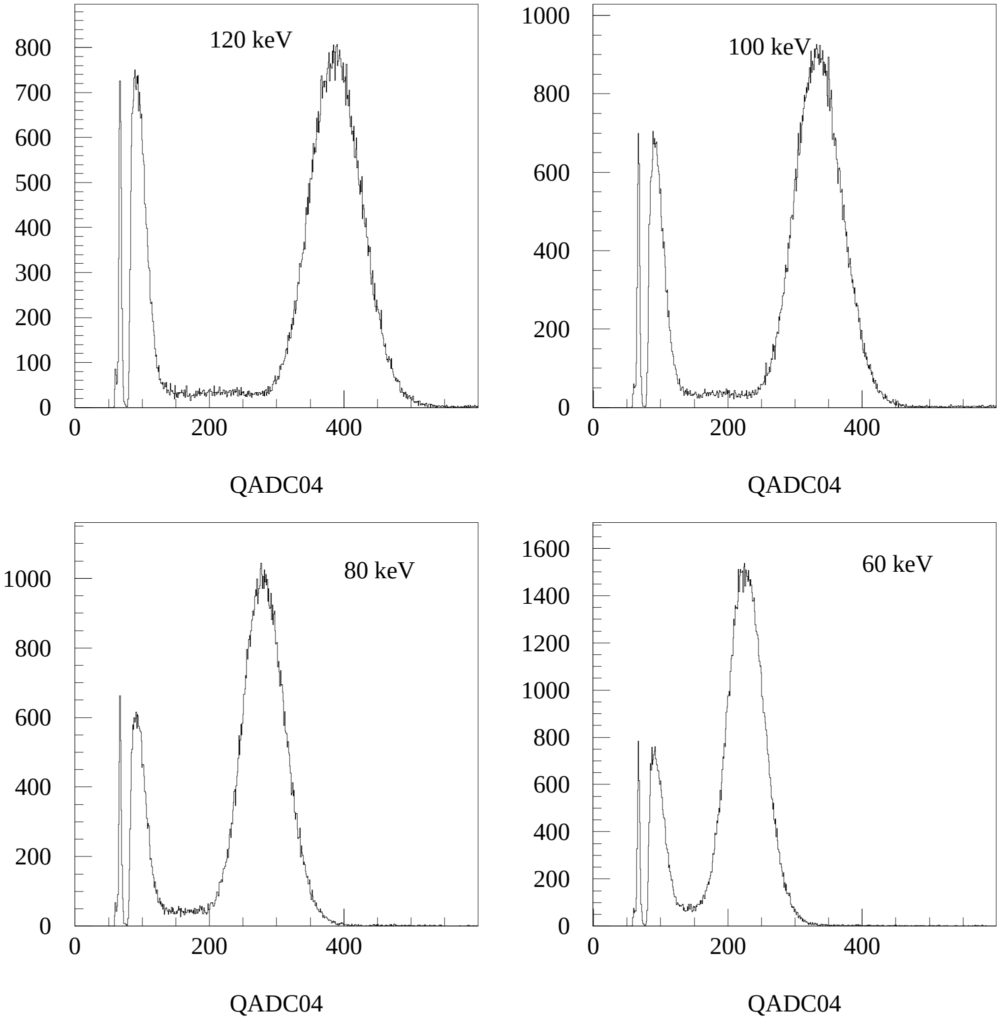

Figure 3.21: Energy spectra measured by a plastic scintillator disk directly coupled to a phototube for beam energy at 60, 80, 100 and 120 keV.

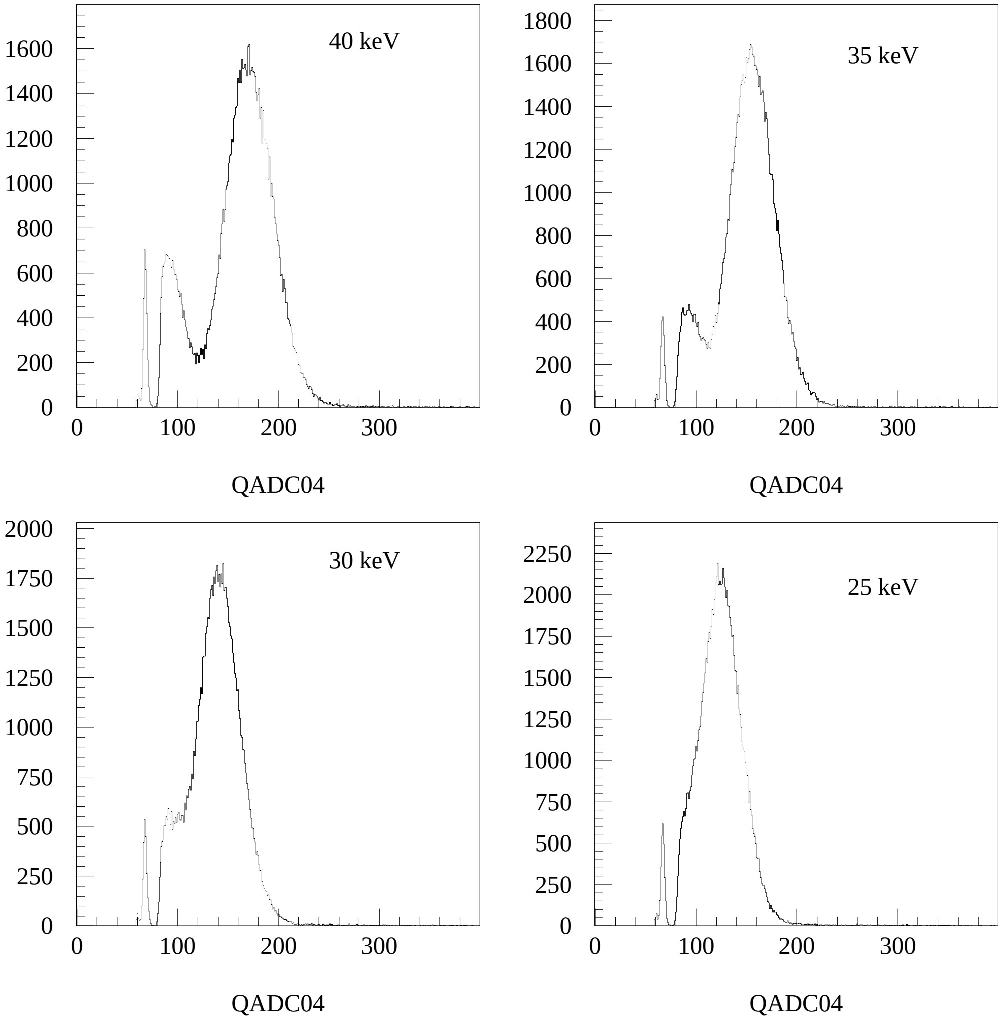

Figure 3.22: Energy spectra measured by a plastic scintillator disk directly coupled to a phototube for beam energy at 25, 30, 35 and 40 keV.

detector.

Fitting the non-linearity(the data points of NPE versus the incident electron energy) for the scintillator disk setup, using Equation 3.9 with S, k_{B} and t as fitting parameters, we can extract the values of these parameters, as is shown in Fig. 3.20 as the red line marked *Scint disk*.

3.2.1.3 Summary

Studies of NPE yields for the Suzuno detector show that approximately 360 NPE per MeV electron energy deposition can be obtained, passing the design goal of 100 NPE for the Suzuno detector. Evidence of non-linearity at low energies is obvious for both setups, and fitting the non-linearity with a model including both light quenching and dead layer effects reaches a common set of values for both setups, which is $k_{\mathrm{B}} = 0.019 \pm 0.002$ cm/MeV, $t = 3.0 \pm 0.3$ μm.

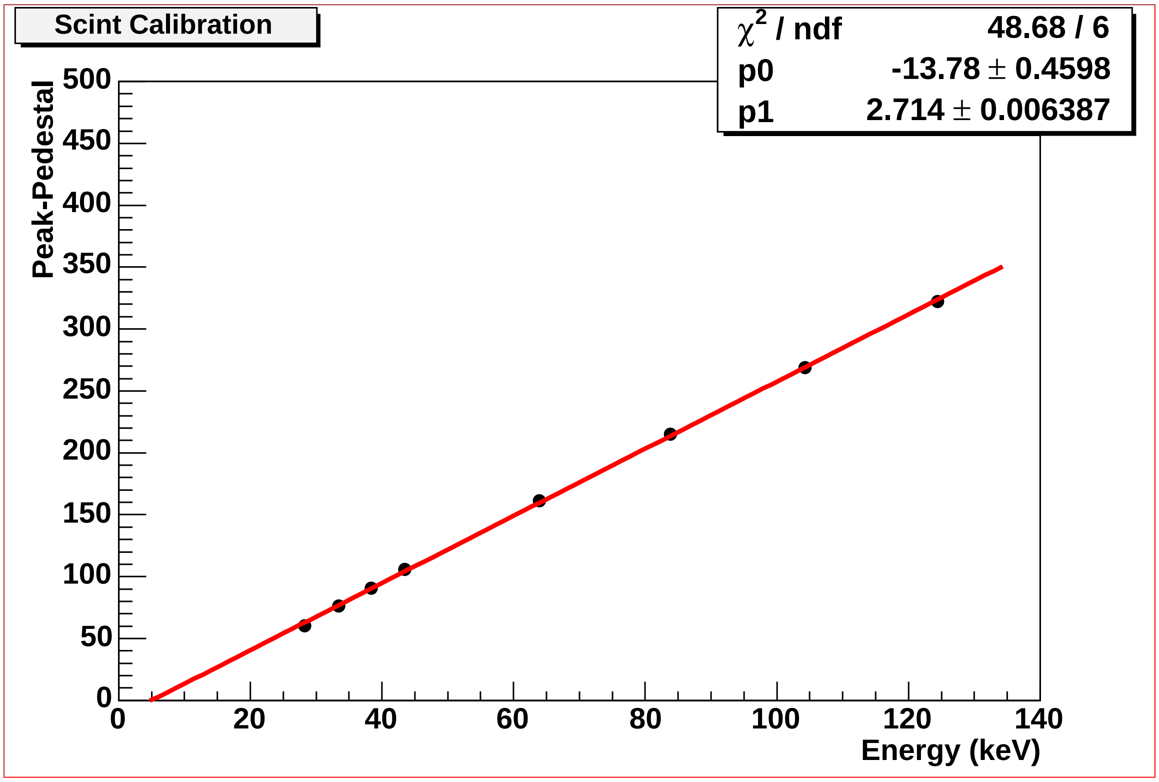

Figure 3.23: Linear fit of the calibration points for the scintillator disk.

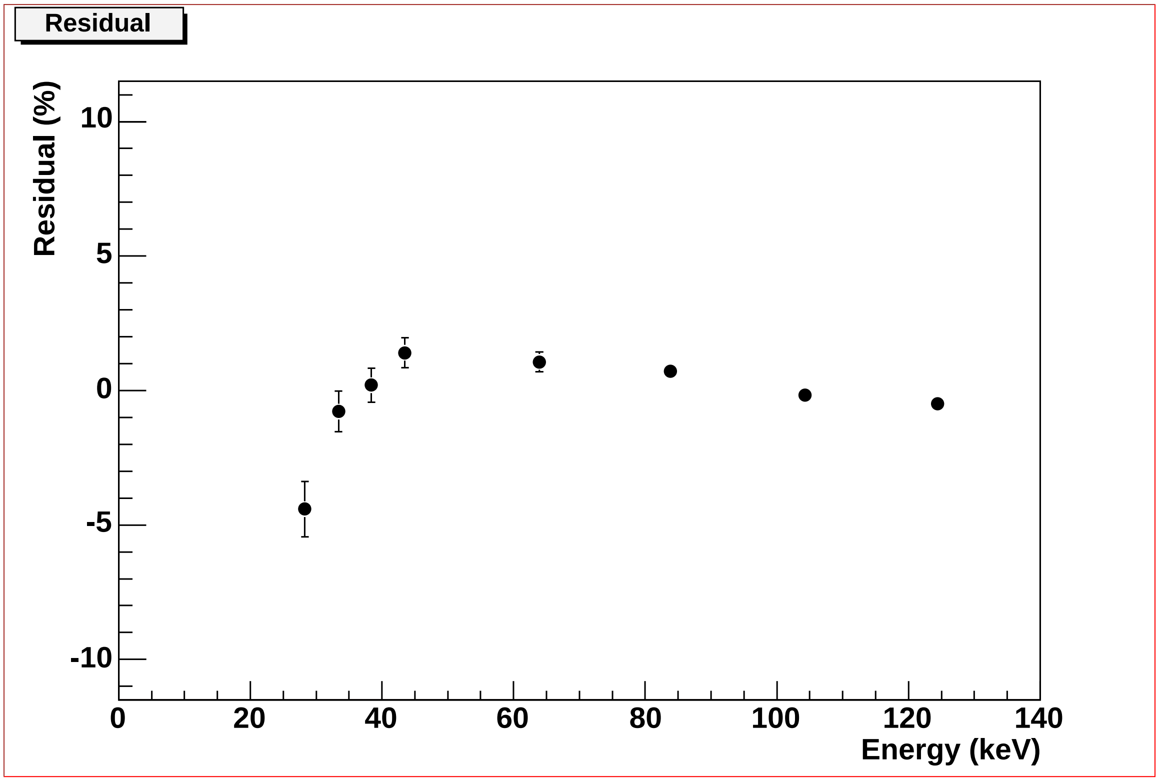

Figure 3.24: Residual of the linear fit for the scintillator disk.

3.2.2 Studies of after-pulsing

The afterpulses of the Suzuno detector are studied with the Kellogg e- gun at a beam energy of 130keV. Most of the afterpulses are attributed to the afterglow of the plastic scintillator, which are single photo-electron pulses. The other small fraction are due to the residual gas ionization in the PMT.

3.2.2.1 Introduction

To measure the detector response at low beam energy, the discriminator threshold is set to about 40% of the amplitude of Single Photo-Electron (SPE) pulse. The detector response at 130keV is shown in Fig. 3.25. Most of the SPE peak(the low energy tail of the spectrum) is due to afterpulses instead of background, since the beam rate is high compared with the background rate. The afterpulses could be a source of confusion to the UCNA experiment, thus the amplitude and time distributions of the afterpulses are studied in detail with the Kellogg electron gun. Studies of the afterpulses are important for the discrimination level, trigger condition, and veto time in the UCNA experiment.

3.2.2.2 Energy spectra of the afterpulses

In the setup for studying after-pulsing, the Suzuno Detector is placed at the end of the e- gun tube. A 25-micron thick mylar film is used to seal the vacuum of the e- gun tube. There is a gap of about 0.5 cm of air between the mylar film and the detector.

The electronics setup to measure the afterpulse energy spectra is shown in Fig. 3.26. The discriminator threshold on each tube is set to about 2.5 times the amplitude of the SPE pulse, to trigger on large pulses. Note that the mean Number of Photo-Electrons(NPE) from each tube at a beam energy of 130keV is about 13. The gate for the charge ADC is delayed relative to the primary pulse, and the amount of delay can be varied to study the afterpulse distribution within different time regions after the primary pulse. For all the cases below, the width of the ADC gate is 100ns.

We carried out measurements of the ADC spectra with 0, 100, 200, 300, 400, 500 and 600 ns delay of the ADC gate. From the measurements, we learned that most of the afterpulses were SPE pulses, except that some large afterpulses occurred during 400-600ns after the primary pulse. They are probably due to electron bombardment of residual gases in the PMT, according to previous studies [54]. From Fig. 5 of a paper by Torre [55], afterpulses due to H_2^+ and He^+ appear in the region of 400-600ns after the primary pulse. The presence of Hydrogen is due to residual water, He can permeate from outside [55].

Detailed descriptions and spectra are shown in Appendix B.

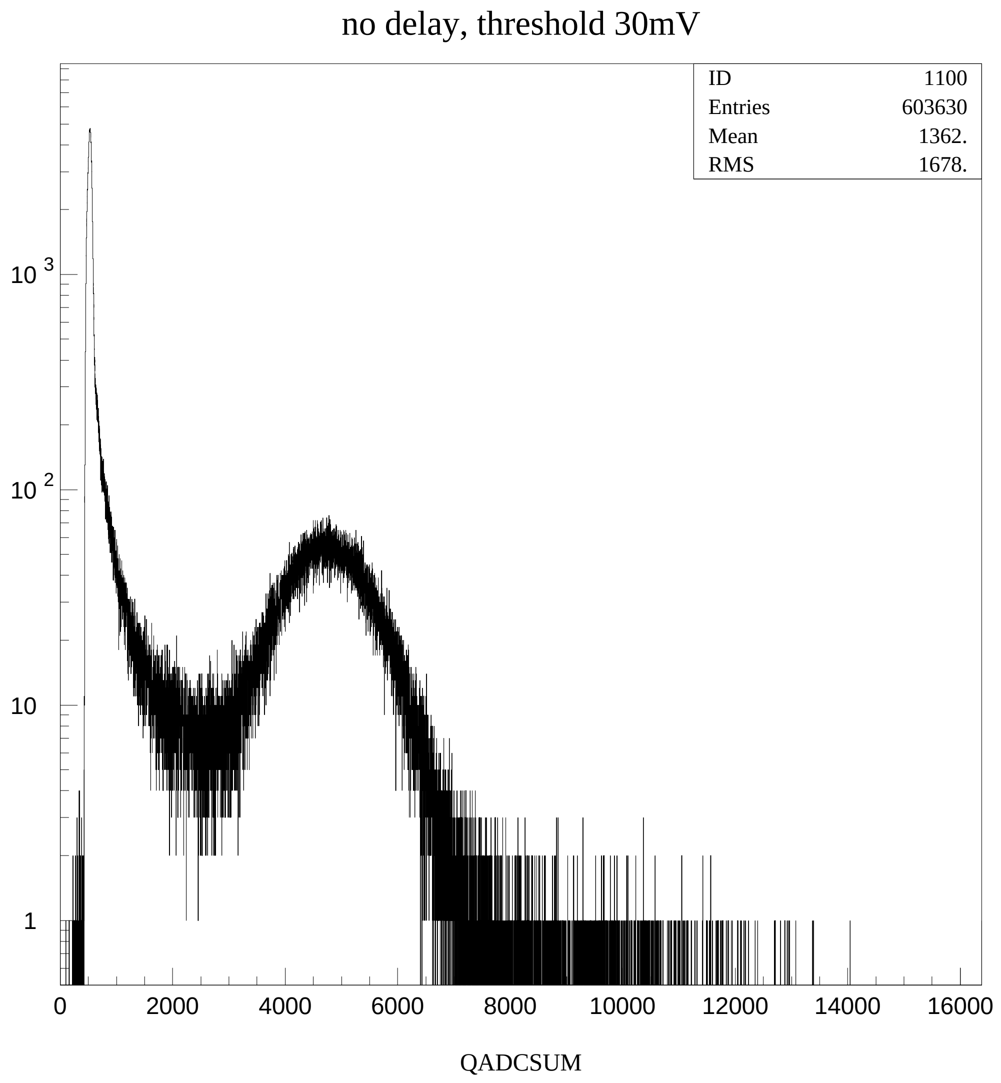

Figure 3.25: Detector response at a beam energy of 130keV, using 1-fold trigger.

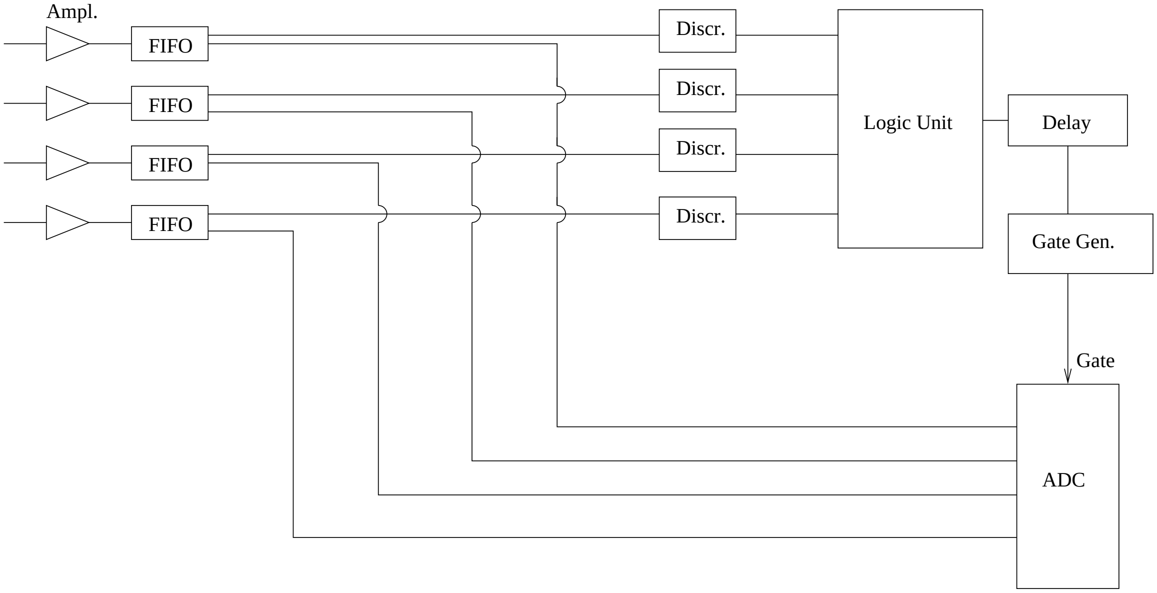

Figure 3.26: Electronics to measure the afterpulse energy spectra

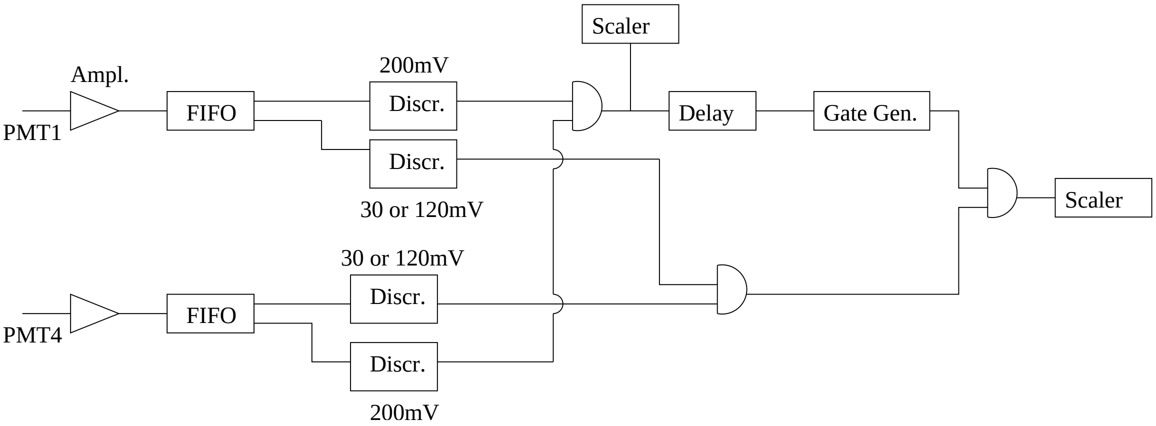

Figure 3.27: Electronics to measure the time distribution of afterpulses

3.2.2.3 Time distribution of the afterpulses

By integrating the above energy spectra starting from the SPE peak under various amounts of delay, we can get the time distribution of the afterpulses. However, to investigate whether we can get rid of afterpulses by a coincidence of 2 tubes, we used scaler counting to look at the time distribution.

The electronics to measure the time distribution of afterpulses are shown in Fig. 3.27. The afterpulsing is studied under two conditions of discrimination levels, 30 and 120 mV. A discriminator threshold of 30 mV corresponds to a 0.4pe threshold(40% of the amplitude of a SPE pulse), while 120 mV corresponds to a 1.5pe threshold. A ratio of counts from the two scalers gives the probability of afterpulses during the time region specified by the gate. The amount of delay for the gate can be varied, and the width of the delayed gate is kept at 100 ns. The time distribution is shown in

Fig. 3.28, under various threshold and coincidence conditions.

Integration of the curve of "PMT1 only, 0.4pe threshold" gives about 70%. Almost all of it is due to the afterglow of plastic scintillator (or in other words, the slow component of the light emission). Note that the NPE in each tube is about 13 at a beam energy of 130keV, thus the percentage of tail emission is about 5%, which agrees with the number given by Birks [53]. In the curve of "PMT1 only, 1.5pe threshold", the large afterpulses due to residual gas ionization can be seen in the region of 400–600 ns. Also as is shown in Fig. 3.28, with 1.5pe threshold, and 2 tubes coincidence, the afterpulses are gone; with 0.4pe threshold, and 2 tube coincidence, the afterpulses disappear 1 μs after the primary pulse.

3.2.2.4 Conclusion

The amplitude and time distributions of the afterpulses are studied at a beam energy of 130keV. Most of the afterpulses(with a frequency of about 70% of the primary pulses) are SPE pulses, due to the slow component of the scintillator light emission. The other afterpulses(with a frequency of about 2% the primary pulses) are larger than SPE, and are attributed to the residual gas ionization in the PMT. The contribution of afterpulses can be eliminated with a 1.5pe threshold and a trigger of 2-tube coincidence. The contribution of the afterpulses can also be eliminated with a 1 μs veto following each pulse, with a 0.4pe or higher threshold and a trigger of 2-tube coincidence. We will see that the DAQ system of the UCNA experiment provides this veto, thus eliminating the afterpulse contamination.

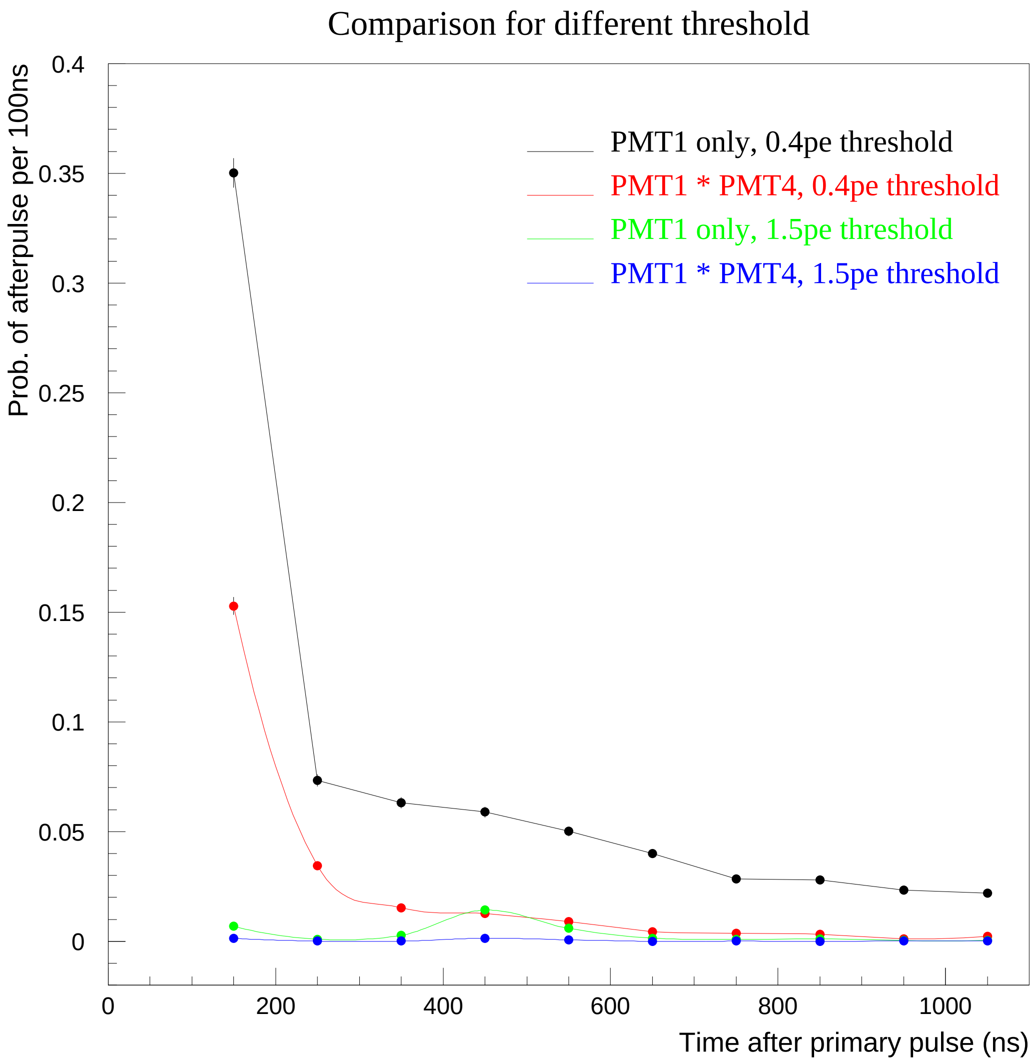

Figure 3.28: Time distribution of the afterpulses, under different threshold and coincidence condition.

3.2.3 Position non-uniformity

Assuming uniform light collection on the edge of the scintillator disk, identical performance of the four light guides, and perfect gain matching of the four phototubes, independence of the detector photo-electron yield on the electron position is expected. In reality, however, none of the three assumptions is perfect, thus the detector response will depend on the electron position.

Measurements of the position non-uniformity were carried out at Kellogg using the electron gun at electron energy of 120 keV. The detector system including the MWPC backed by the Suzuno detector was put at the end of the electron gun. The position of the electron beam was varied by two steering magnets in X and Y direction, and the positions of the electrons were reconstructed from the MWPC cathode information. Typical position distribution reconstructed from the MWPC information was close to a Gaussian with a sigma of about 8 mm. The position spread is mostly due to the electron multiple scattering in the MWPC. The reconstruction process will be presented in the next section Titled “The multiwire proportional chamber”.

Two sets of runs were carried out. In one, the Y steering magnet setting was fixed so that the Y positions of the electrons were about -6 to -10 mm, while varying the X steering magnet setting so that the X positions were changing from -50 mm to 60 mm. Note that the Y positions were not perfectly fixed because the two steering magnets were not perfectly orthogonal. In the other, the X steering magnet setting was fixed so that the X positions were about 0 to -6 mm, while varying the Y steering magnet setting to change the Y positions from -60 to 40 mm. At each setting of the steering magnets, a hundred thousand events were accumulated, and the peak position of the scintillator sum spectrum was extracted with a Gaussian fit. The peak position was compared with the one when an electron was incident on the center of the scintillator disk, such that the position non-uniformity was defined as $(P_i - P_0)/P_0$, where P_0 is the peak position with an electron at the center, and P_i is for an electron hitting at position i.

The position non-uniformity is shown as black dots in Fig. 3.29, as a function of the X position with Y position fixed, and as a function of the Y position with X position fixed. The position non-uniformity is measured to be about 0.2% per mm.

To make a first pass correction of the position non-uniformity, the response of the detector can be modeled as

$$R \propto \sum_{i=1}^{4} \Omega_i(x, y)\epsilon_i \tag{3.11}$$

where ϵ_i is the light collection efficiency for each guide, and is an average of the guide surface quality, imperfections, and grease and glue joint quality. Ω_i is the solid angle subtended by guide i for the light emission at (x,y). In the first pass correction, ϵ_i is assumed to be independent of the light emission position (x,y), and can be obtained from responses of each arm to a centered electron beam. The effect of the first pass correction is shown in Fig. 3.29 as the red points. Obviously,

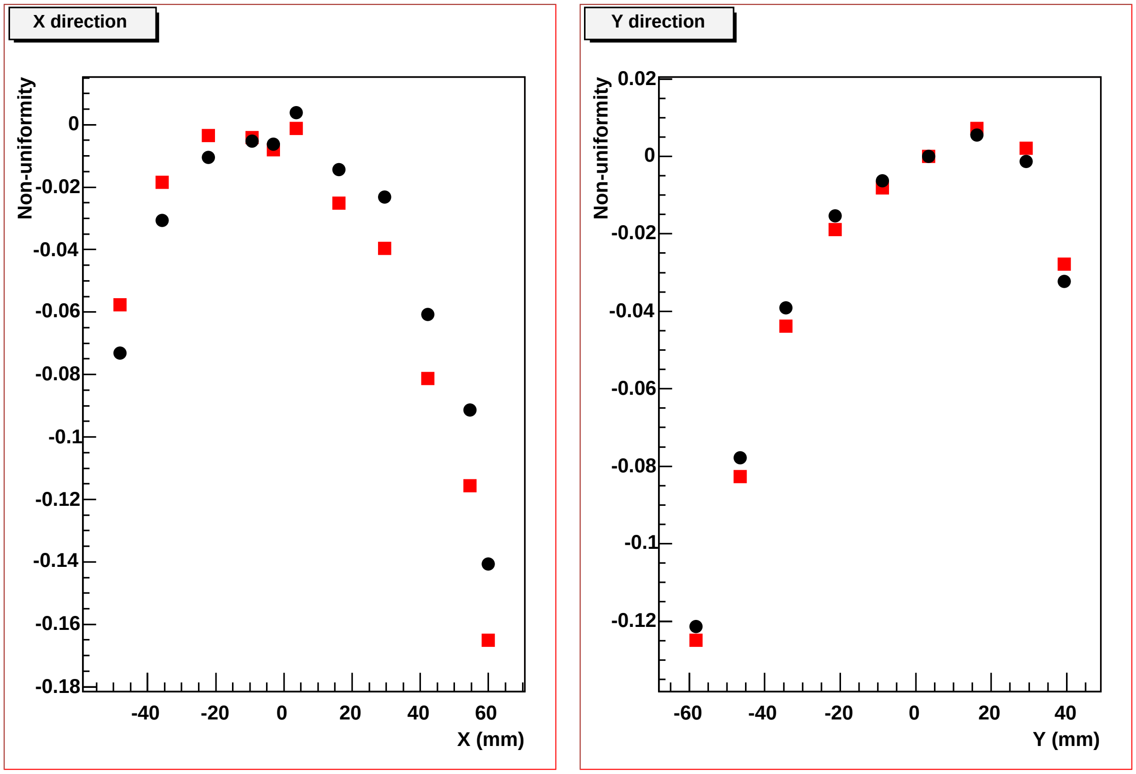

Figure 3.29: Position non-uniformity as a function of the electron positions. Black circles are without any correction, red squares are with the first pass correction applied, as explained in the main text.

this correction does not have much effect, because the gain matching of the phototubes was done very well for a centered electron beam. Therefore, the position non-uniformity in Fig. 3.29 is mostly due to position dependence of ϵ, which is assumed to be independent of position in the first pass correction.

To removed the 0.2% per mm of position non-uniformity, the correction function should be measured in situ by scanning an electron beam into the detector package, as we did with the Kellogg electron gun.

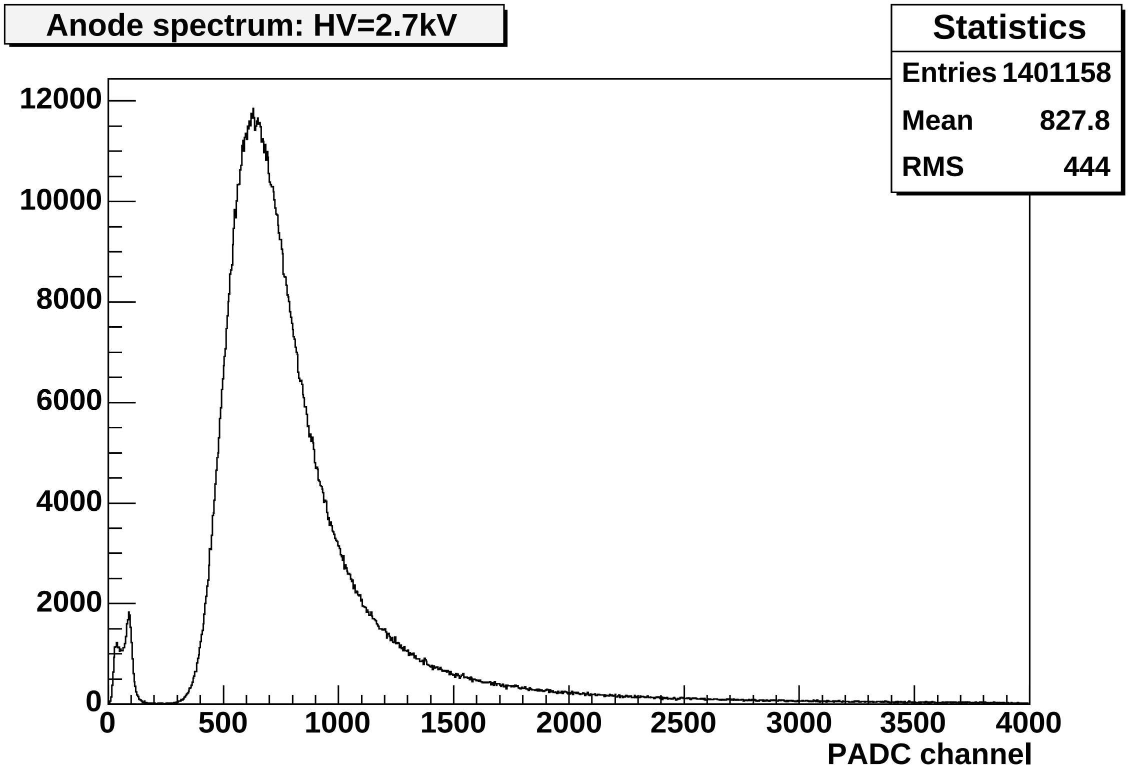

Figure 3.30: The anode spectrum for 120 keV electrons, with 2.7 kV anode bias.

3.3 The multiwire proportional chamber

The response of the MWPC was studied with the Kellogg electron gun, by placing the MWPC backed with the Suzuno scintillator detector at the end of the beam tube. By using the electron gun beam tube as a simulation of the SCS vacuum in the UCNA experiment, the gas handling system for the detector package was also tested successfully. The trigger for data acquisition was provided by a two-fold coincidence of the scintillator PMTs. A 120 keV electron beam was used for the study. The MWPC was filled with 100 Torr neopentane gas.

3.3.1 MWPC efficiency

With the anode bias at 2.7 keV, the anode spectrum is shown in Fig. 3.30. The lower peak is the noise peak, while the higher peak is the energy deposition of 120 keV electrons. The MWPC efficiency is defined as the counts under the higher energy peak divided by the total counts, with the corresponding counts when the electron beam was off (a background run) subtracted. The MWPC efficiency for 120 keV electron was determined to be (100.1±0.1)%.

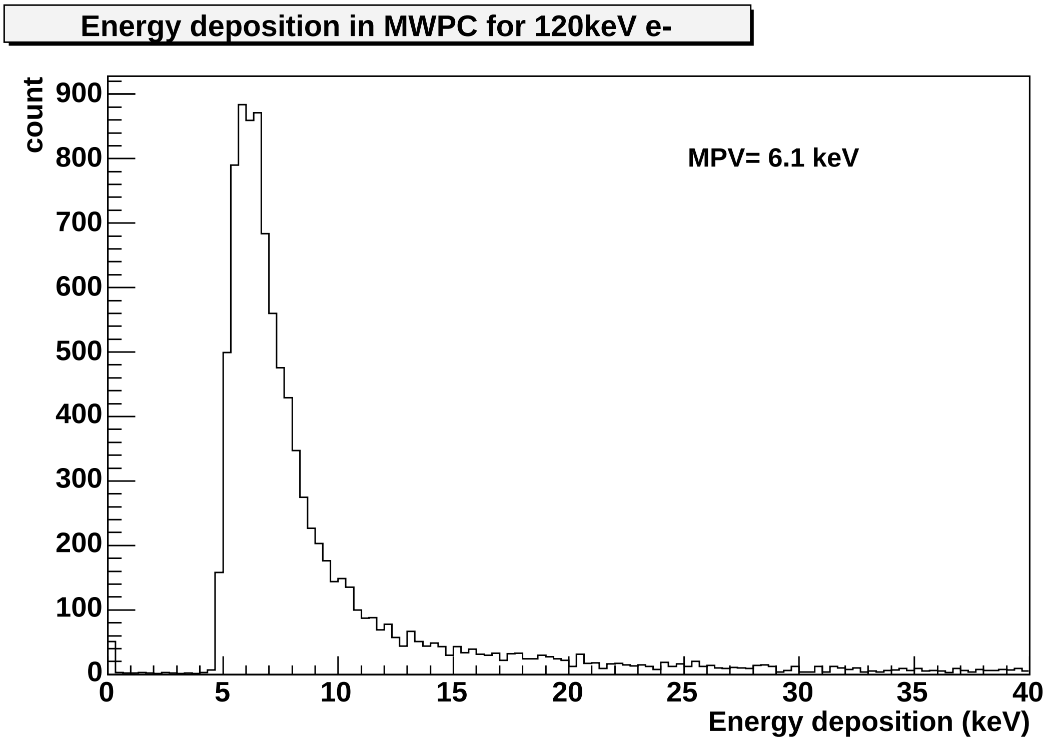

Figure 3.31: Energy deposition in MWPC for 120 keV electrons, simulated with GEANT4.

3.3.2 Background suppression

The energy deposition in the MWPC gas volume was simulated with GEANT4. The distribution is shown in Fig. 3.31 for 120 keV electrons. The Most Probable Energy (MPV) is shown to be 6.1 keV. From the measured anode spectrum (Fig. 3.30), the peak is at channel 630 for MWPC anode biasing at 2.7 kV. This gives a energy calibration point for the anode spectra. Fig. 3.32 shows the background anode spectrum, which can be calibrated with the above calibration point. Thus the fraction of included noise as a function of the cut on energy deposition in MWPC can be extracted, as shown in Fig. 3.33. It is evident that a background suppression of 6% (16.7-fold) can be achieved with an energy threshold of 0.6 keV.

3.3.3 Position response

Position information can be extracted from the cathode signals. As discussed in chapter 2, every 4 cathode wires are grouped to readout in a peak sensing ADC channel, and there are 16 channels in each cathode plane. For each event, fitting the distribution of signals in the 16 channels with a Gaussian function, the centroid gives the position of the event. The cathode plane with wires aligned in the Y direction determines the X position, while the cathode plane with wires aligned in the X direction determines the Y direction. Note that the anode wires are aligned in the X direction.

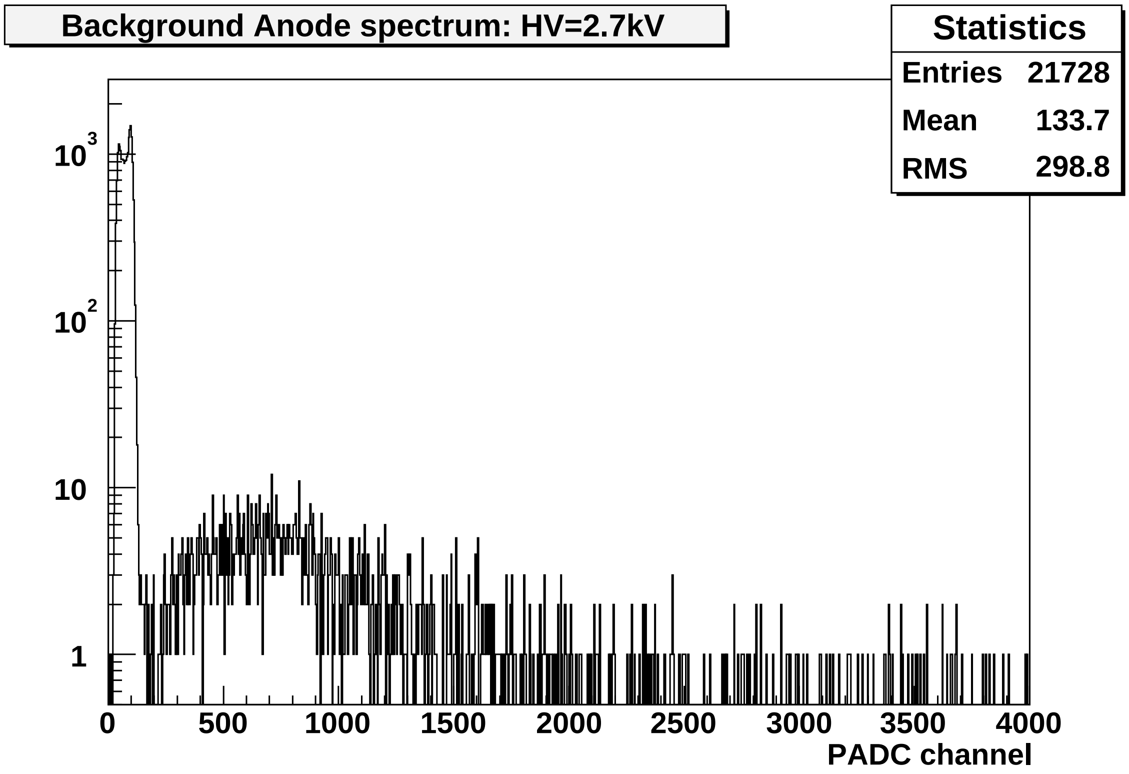

Figure 3.32: MWPC anode background spectrum, with anode bias at 2.7 kV.

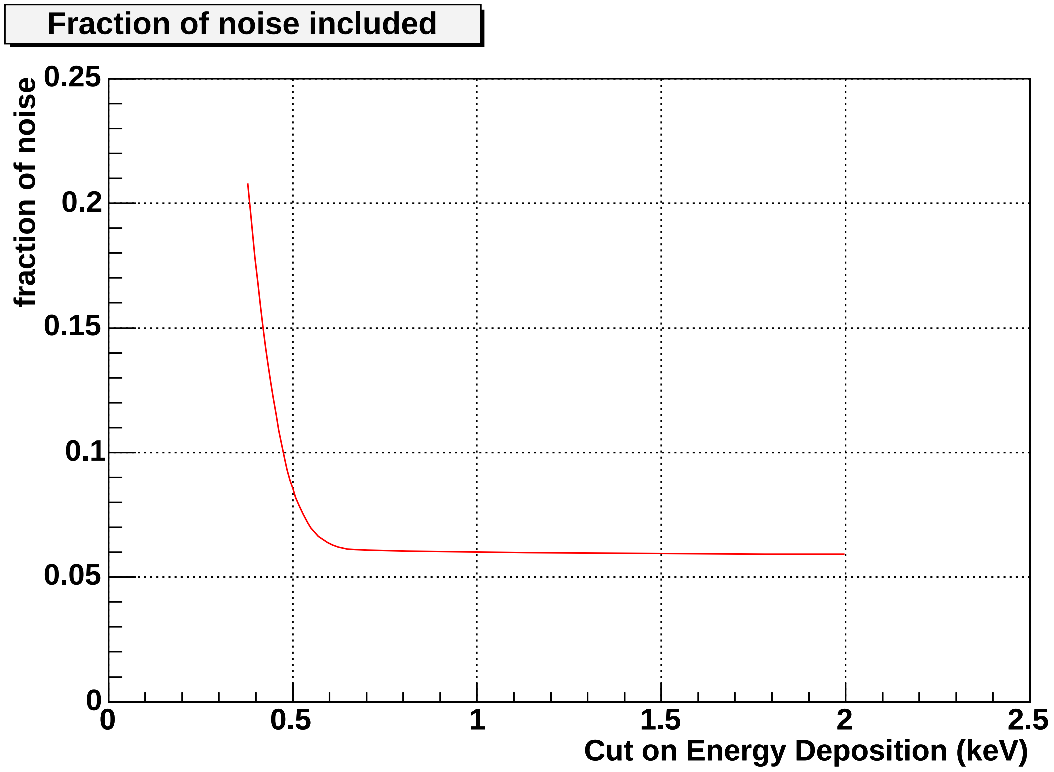

Figure 3.33: The fraction of included noise as a function of the cut on energy deposition in MWPC.

The distributions of X and Y positions are shown in Fig. 3.34, the X and Y positions are reconstructed from the cathode signals for 120 keV electrons, with anode bias of 2.7 kV, and MWPC filled with 100 Torr neopentane gas. The broad distributions in Fig. 3.34 are not due to the position resolution of the MWPC, but due to the electron multiple scattering in the MWPC gas volume instead. The spikes in the Y distribution are attributed to the fact that the cathode wires which determine the Y position are aligned in the same direction as the anode wires, and the space between the spikes is about 2.54 mm, which is the anode wire spacing. The spread of the spikes gives the intrinsic position resolution of the MWPC. For comparison, the results from a GEANT4 simulation is shown in Fig. 3.35. Details of the GEANT4 simulation of the MWPC is given in the next paragraph. The spikes in the Y position distribution is clearly presented, except that they are single lines because no electronic noise was included in the simulation, thus the intrinsic position resolution from the simulation is perfect. Two instead of three spikes are shown in the simulation, because the incidenting electron position was slightly different in the simulation than in the measurements.

Electron multiple scattering clearly smears out the position information. Fortunately in the UCNA experiment, the 0.6 T magnetic field at the β detectors confines the trajectory of the electrons. This is illustrated in Fig. 3.36, where the X and Y positions are reconstructed from the MWPC cathode information for 120 keV incident electron with 0.6 T magnetic field turned on. This figure was obtained with a GEANT4 simulation. In the simulation, the trajectory of an incident electron in the MWPC was divided into 0.1 mm segments. For each segment, the energy deposition in the MWPC was recorded, and the average number of primaries was obtained by dividing the energy deposition by 100 eV (100 eV is approximately the energy deposition required for generation of each primary pair). The number of primaries was then generated from a Poisson distribution with average equal to the average number of primaries. The total collected charge on a segment is the number of primaries scaled by the gain factor, and is assigned to the nearest anode wire. For this segment, the image charge distribution on cathode channels was obtained from a Gaussian distribution, with centroid at the corresponding anode wire for this segment, and sigma of 7mm obtained from measurements with x-ray from a ^{55}Fe source (In the measurements, the x-ray induced a photo-electron in the MWPC gas volume, and deposited all the energy in a focused region. A gaussian fit of the cathode signals then gave the sigma.) The charge on each cathode channel was summed up for all the segments corresponding to an event, and the final charge distribution was fit with a Gaussian function, whose centroid determined the electron position for this event.

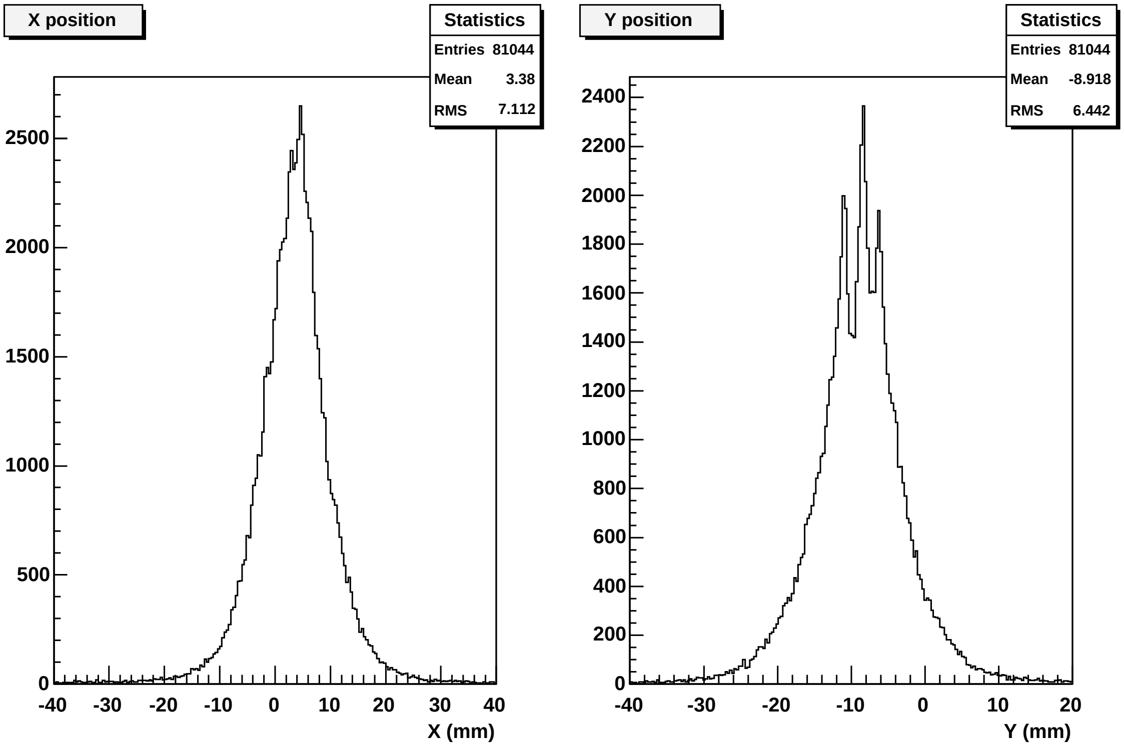

Figure 3.34: Distribution of X and Y position reconstructed from the MWPC cathode signals, for 120 keV electron beam incidenting on (x=3.4mm,y=-8.9mm), from measurement.

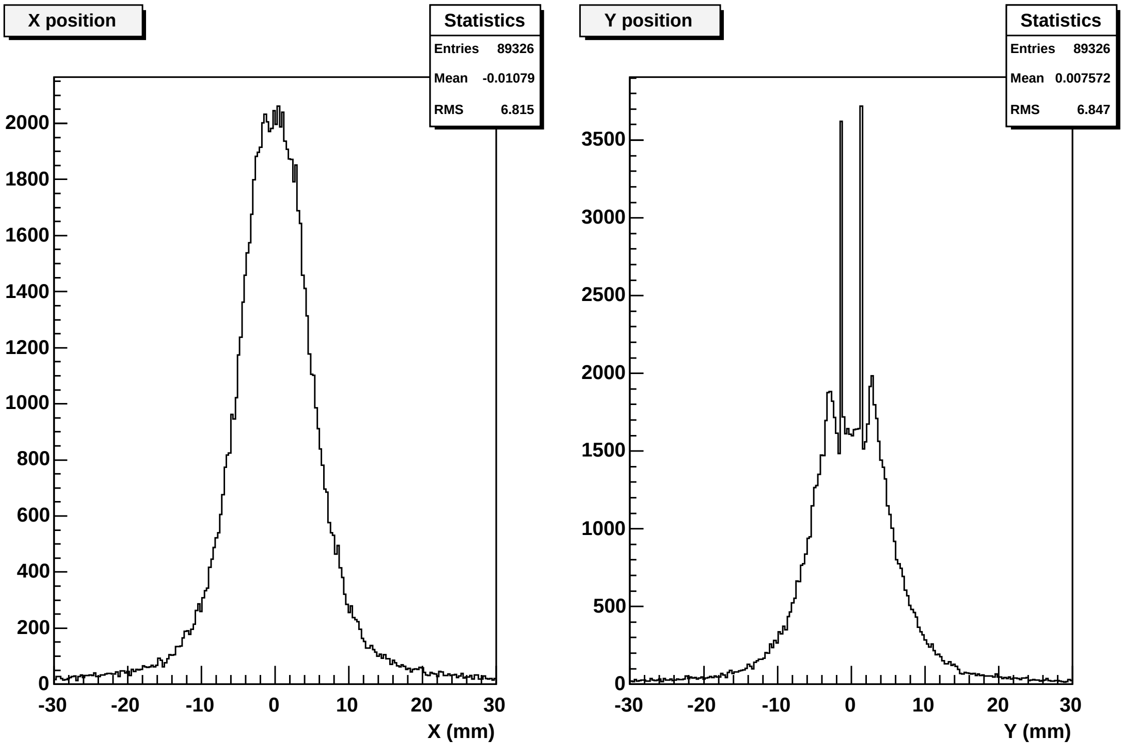

Figure 3.35: Distribution of Y position reconstructed from the MWPC cathode signals, for 120 keV electron beam incidenting on the center of MWPC, simulated with GEANT4.

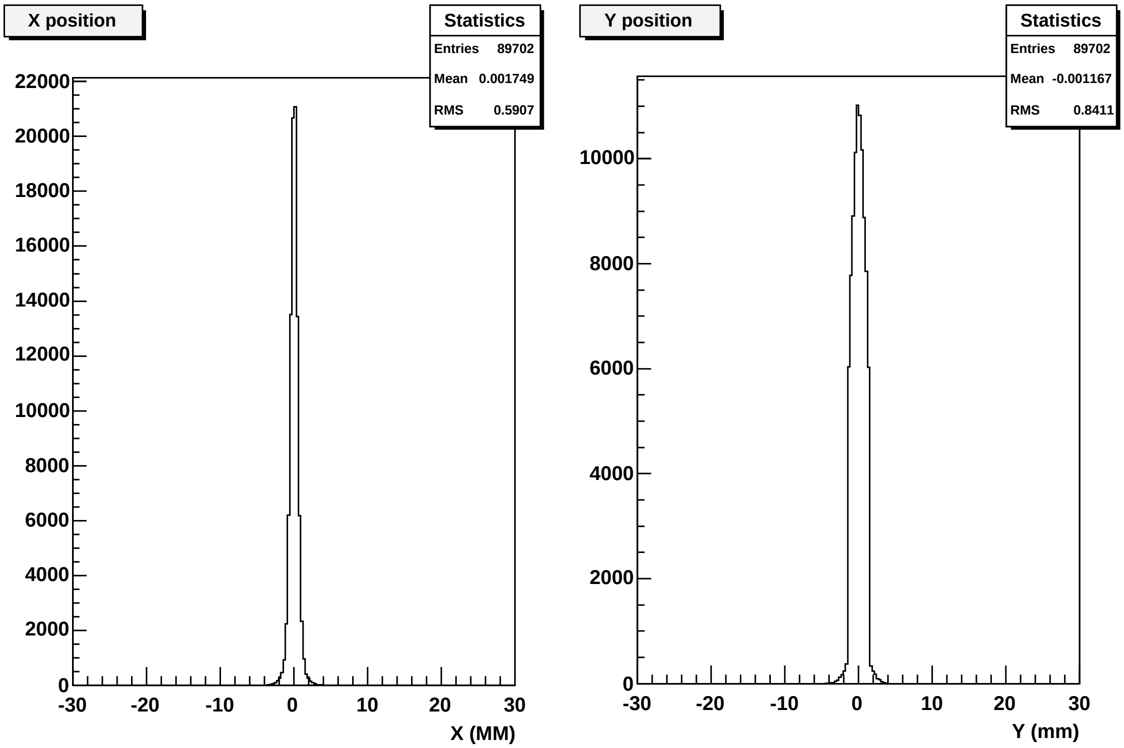

Figure 3.36: Distribution of Y position reconstructed from the MWPC cathode signals, for 120 keV electron beam and with 0.6 T magnetic field, simulated with GEANT4.

Chapter 4

Studies of UCNA Systematics

Several systematic effects in the UCNA experiment were studied with GEANT4 simulations and will be presented in this chapter, focusing on systematics related to beta detection, such as missed backscattering and energy reconstruction of electrons. In a missed backscattering event, the backscattered electron leaves undetectably small energy deposition in the first detector, thus introducing an error in the asymmetry measurement. The beta detector system in the UCNA experiment was constructed with the purpose of minimizing the missed backscattering effect. However, it can not be eliminated, and contributes a large part of the systematics, thus it is very important to characterize it with a Monte-Carlo study.

4.1 Simulation of the UCNA spectrometer with GEANT4

4.1.1 The GEANT4 simulation toolkit

GEANT4 [56] is an Object-Oriented Toolkit written in C++ for the simulation of the passage of particles through matter, widely applied for simulations in areas such as high energy physics, nuclear physics, medical physics, astrophysics, space applications etc.

Some of the features of GEANT4 are: Firstly, there are often multiple physics models for the same physics process. The user can choose the physics model that is the most suitable for his specific experimental requirement, also the user can create his own physics model. Secondly, GEANT4 does not have any default particles or processes, instead, the user must define all necessary particles, and also define all necessary processes and assign them to proper particles. Thirdly, there is no tracking cut in GEANT4, all particles are tracked down to the minimal energy available in each physics model. However, the production cuts exist; each production cut establishes whether a specific kind of particles is to be created as secondaries or not. The production cut is used to solve the infrared divergences for some electromagnetic processes, and is a compromise between calculational accuracy and CPU performance. Fourthly, a set of low energy electromagnetic models are implemented in

Figure 4.1: UCNAg4 generated view of the UCNA spectrometer geometry.

GEANT4 to extend the coverage of electromagnetic interactions of photons and electrons down to 250eV/100eV, and of protons, ions and antiprotons down to < 1 keV.

Validation of GEANT4 physics models have been done comparing with various experimental data and data bases [57]. We have performed comparisons of electron backscattering measurements with GEANT4 simulation, presented in Chapter 6, which showed agreement at the 15% level.

As mentioned above, GEANT4 includes multiple models for the same physics process from which the user can choose. A specific example is the low energy electron/photon processes, which are central to the simulation of the UCNA spectrometer. GEANT4 has its own implementation of the low energy electron/photon processes, and in the recent release, GEANT4 release 7.0 (as of December 2004), it also includes the electron/photon models from PENELOPE except the multiple-scattering model which will be included in the future. Since GEANT4's original low energy models and PENELOPE's models are independent, two simulations of the UCNA spectrometer using each set of models can be performed and can present us an estimate of the model dependent errors associated with the simulation.

The GEANT4-based simulation of the UCNA spectrometer, called UCNAg4 [58], is developed based on GEANT4.5.2. Details about some key components will be shown in the next sections.

4.1.2 Geometry

A UCNAg4 generated view of the UCNA spectrometer geometry is shown in Fig. 4.1, which consists of a 3m decay tube in the center and the UCNA electron detector packages at both ends.

The UCNA electron detector package includes a MWPC backed by a plastic scintillator detector. The scintillation detector is modeled as a 3.5mm thick, 15cm diameter EJ204V plastic scintillator disk. The front surface of the scintillator is positioned 2.2 m from the center of the decay trap. The scintillator is segmented into a dead layer of thickness equivalent to the range of 20 keV electrons in plastic scintillator (see chapter 3), and an active layer with the rest of the scintillator.

In front of the scintillator, the MWPC is modeled as a 5 cm thick, 15 cm diameter gas chamber filled with 100 Torr Neopentane, with 3 wire planes at the center, and with a front window and a back window. In the geometry model, the MWPC has a 2 cm thick active region at the center between the two cathode planes, and 1.5 cm dead region on both sides of the active region. The purpose of the dead regions are to model the two regions between the MWPC windows and cathode

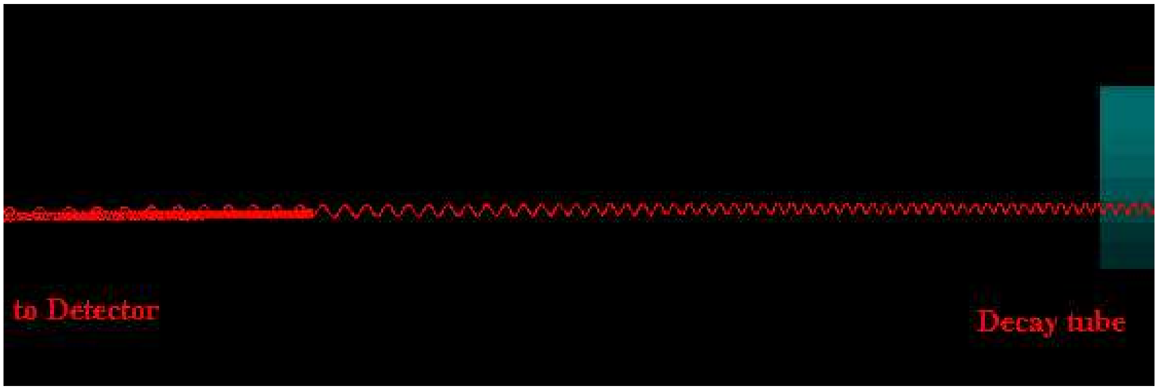

Figure 4.2: UCNAg4 generated view of electron trajectory in the SCS magnetic field.

planes. However, with the introduction of cathode biasing, the dead regions can be reduced or even be eliminated. The MWPC has 2 cathode planes with parallel wires running in each plane, and the wires in the two cathode planes are orthogonal to each other. An anode plane is placed between the two cathode planes, with 1 cm distance to each cathode plane. The cathode planes are made of 50 μm diameter gold-plated aluminum wire with 2.54 mm spacing, and the anode plane is made of 10 μm diameter gold-plated tungsten wire with 2.54 mm spacing. The front and back windows of the MWPC are 6 μm thick aluminized mylar film. The front window has a Kevlar yarn support in the front, which is made of 200 denier Kevlar yarns with 5 mm spacing. These are all included in the UCNAg4 model. An Aluminum tube with 6.5 inch inner diameter and 5 inch length is put in front of the wire chamber to simulate the MWPC amplifier holder.

4.1.3 Magnetic field

The Magnetic field produced by the SCS is modeled as: $Bz = 1T, Br = 0$ for $|z| < 1.5m$, $Bz = 0.6T, Br = 0$ for $|z| > 2.2m$, and the field is sinusoidally connected in the region $1.5m < |z| < 2.2m$, i.e., the field expansion region. Care is taken to model the connection continuously with the requirement of $\bigtriangledown \cdot \vec{B} = 0$, to avoid magnetic field irregularity, such that artificial electron scattering due to field irregularity is eliminated. If necessary, a more realistic field map database can be loaded into the UCNAg4 simulation.

In UCNAg4, a charged particle is propagated in the Magnetic field by integrating the equation of motion using the Runge-Kutta method. Other integrating methods can also be chosen, depending on specific needs of computation speed and precision. Fig. 4.2 shows an example trajectory of an electron in the UCNA magnetic field. In the example trajectory, the electron comes from the decay tube directed towards one of the detectors, is backscattered by the detector, and then mirrored back to the detector by the magnetic field expansion.

4.1.4 Electromagnetic physics

UCNAg4 is based on GEANT4.5.2, while the simulation for comparing electron backscattering measurement in chapter 3 is done with GEANT4.4.0. Comparing with GEANT4.4.0, GEANT4.5.2 improved the way of treating multiple scattering near a material boundary, to better describe backscattering. In the UCNAg4 simulation, 2 parameters have to be set differently from their default values: the parameter "facrange" that limits the step size near a material boundary is set to 0.0099, and the threshold to create secondaries (so-called "cut value" in GEANT4) is set to 1 μm. The "facrange" and the "cut value" were chosen by studies of electron backscattering from bulk targets of Silicon, Beryllium and plastic scintillator with GEANT4.5.2 simulation, where they were chosen by reducing them until the electron backscattered fraction was relatively stable under variation of those parameters, and to be as small as possible for reasonable running time.

The electron backscattering related low energy electromagnetic physics in GEANT4 is partially validated by comparing GEANT4 simulations and electron backscattering measurements done at the Kellogg Lab at Caltech, both with bulk targets(Silicon, plastic scintillator, and Beryllium) and thin Mylar film. As is shown in Chapter 3, these comparisons show that GEANT4 models the electromagnetic physics related to backscattering and energy loss correctly to at least the 15% level.

4.1.5 Event generation

Electrons from polarized neutron decay are generated in the decay tube. The density of the primary decayed electrons are uniformly distributed radially in the region of $r < 1$ cm, and triangularly distributed along the axis of the decay tube. This small radius of $r < 1$ cm is chosen to eliminate decay tube events at this stage.

The initial angle of the electron follows the distribution $1 + \beta A cos\theta$ with $A = -0.1189$. The energy spectrum of the electron follows $PE(E_{\max} - E)^2$. Fig. 4.3 shows the UCNAg4 generated energy spectrum of the primary electrons.

For each event, the following data are recorded for the detector package on each side: time of the hit, angle of the hit at the MWPC front window, and energy depositions in the MWPC front window, back window, dead region, active region, scintillator dead layer and scintillator active layer.

A total of 2×10^7 events are generated. Systematic effects in UCNA due to non-ideal situations in electron detection are analyzed based on these events [59], which are shown in the following sections.

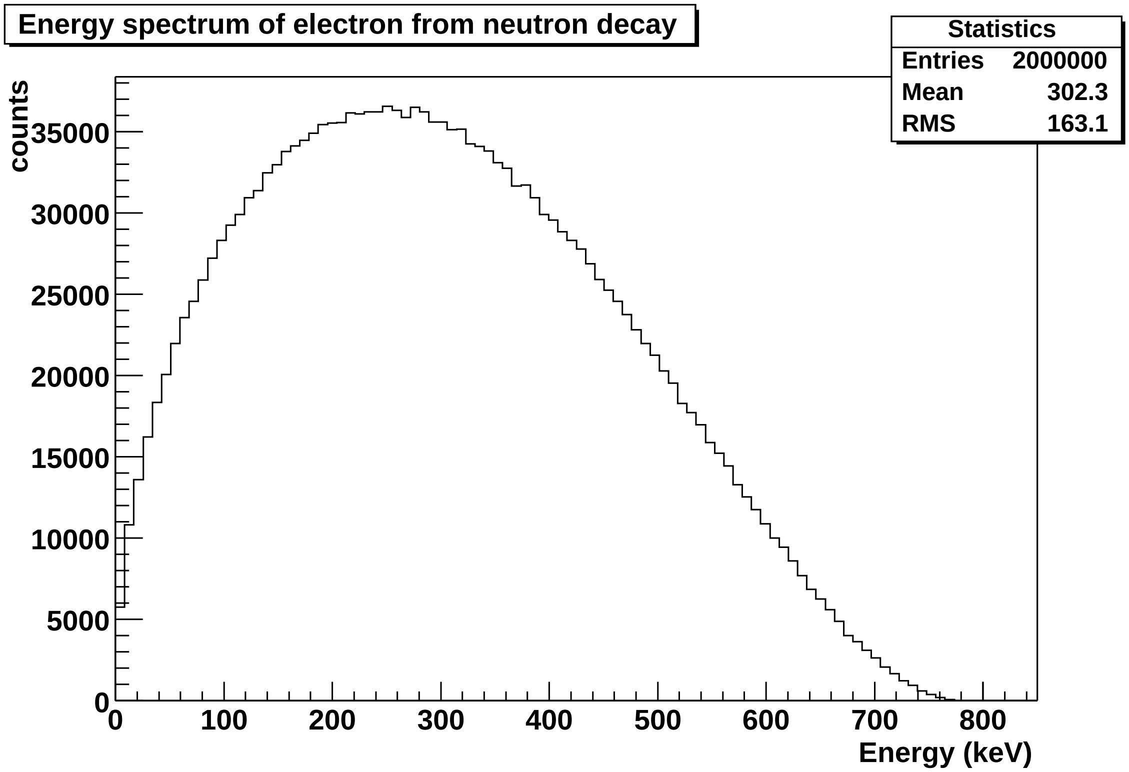

Figure 4.3: UCNAG4 generated energy spectrum of primary electrons.

4.2 Analysis of systematics due to missed backscattering

4.2.1 Theoretical discussion

We define the Missed Backscattering Fraction(MBF) as $MBF = \frac{N_{\mathrm{Lm}}+N_{\mathrm{Rm}}}{N_{\mathrm{Lt}}+N_{\mathrm{Rt}}}$, where N_{Lm} is the number of electrons initially heading towards the left side but backscattered and firing only the right side, N_{Rm} is that initially heading towards the right side but backscattered and firing only the left side, N_{Lt} is the number of electrons initially heading towards the left side, and N_{Rt} is that heading towards the right side.

To consider the effect on "A" due to missed backscattering, the experimental asymmetry can be expressed as (assuming 100% UCN polarization):

$$\begin{aligned} A_{\mathrm{MB}} &= \frac{(N_{\mathrm{Lt}} - N_{\mathrm{Lm}} + N_{\mathrm{Rm}}) - (N_{\mathrm{Rt}} - N_{\mathrm{Rm}} + N_{\mathrm{Lm}})}{N_{\mathrm{Lt}} + N_{\mathrm{Rt}}} \\ &= \frac{N_{\mathrm{Lt}} - N_{\mathrm{Rt}} - 2(N_{\mathrm{Lm}} - N_{\mathrm{Rm}})}{N_{\mathrm{Lt}} + N_{\mathrm{Rt}}} \\ &= A_{\mathrm{exp}}(1 - 2\frac{N_{\mathrm{Lm}} - N_{\mathrm{Rm}}}{N_{\mathrm{Lt}} - N_{\mathrm{Rt}}}) \end{aligned}$$

where $A_{\mathrm{exp}} = \frac{N_{\mathrm{Lt}}-N_{\mathrm{Rt}}}{N_{\mathrm{Lt}}+N_{\mathrm{Rt}}}$ is the experimental asymmetry if there is no missed backscattering. Therefore, the effect on "A" is $(\frac{\Delta A}{A})_{\rm MB} = \frac{A_{\rm MB}-A_{\rm exp}}{A_{\rm exp}} = -2\frac{N_{\rm Lm}-N_{\rm Rm}}{N_{\rm Lt}-N_{\rm Rt}}$.

Since

$$\begin{aligned} N_{\rm Lm} &= \int_{0^o}^{90^o} d\Omega dEW(E)(1+\beta Acos\theta)P_{\rm m}(E,\theta), \\ N_{\rm Rm} &= \int_{0^o}^{90^o} d\Omega dEW(E)(1-\beta Acos\theta)P_{\rm m}(E,\theta), \end{aligned}$$

where $P_{\rm m}$ is the probability of missed backscattering, and $W(E)$ is the primary e- energy spectrum, it is straightforward to show that

$$\begin{aligned} MBF &= \frac{N_{\rm Lm}+N_{\rm Rm}}{N_{\rm Lt}+N_{\rm Rt}} \\ &= \frac{\int_{0^o}^{90^o} d\Omega dEW(E)P_{\rm m}(E,\theta)}{\int_{0^o}^{90^o} d\Omega dEW(E)}, \\ -\frac{1}{2}(\frac{\Delta A}{A})_{\rm MB} &= \frac{N_{\rm Lm}-N_{\rm Rm}}{N_{\rm Lt}-N_{\rm Rt}} \\ &= \frac{\int_{0^o}^{90^o} d\Omega dEW(E)\beta cos\theta P_{\rm m}(E,\theta)}{\int_{0^o}^{90^o} d\Omega dEW(E)\beta cos\theta}. \end{aligned}$$

Therefore, $(\Delta A/A)_{\rm MB}$ can be also obtained from MBF with $\beta cos(\theta)$ weighting, which gives better statistical errors using the same set of simulated events.

Since the MBF gives an estimation of the effect of missed backscattering on "A" except for the $\beta cos(\theta)$ weighting, using the 2×10^7 events set, calculations of the MBF with various energy cuts and with or without MWPC information will be presented in the next section, followed by calculations of $(\Delta A/A)_{\rm MB}$.

4.2.2 Analysis

The total number of events in which the electron is backscattered is 1268948, that is 6.3% of the total events. Let's assume for the following analysis that there is a threshold of 10 keV on the energy deposition in the scintillator active layer, then 588280 events fire both scintillators, thus we know which detector fires first by the timing information from the scintillators, and there events will be correctly identified. In addition, 259438 of the backscattering events have neither of the scintillators fired, which will not be recorded in the UCNA experiment as it is an *OR* of the two scintillators that provides the trigger for data acquisition.

The remaining 421230 backscattering events fire only 1 scintillator, and 157138 of them fire the wrong scintillator. Therefore, assuming no MWPC information, the number of missed backscattering events is 157138, that is 0.88% of the total events that fired at least one scintillator. Fig. 4.4 shows the energy spectrum of the primary electrons for these events, which peaks at about 120keV. Requiring

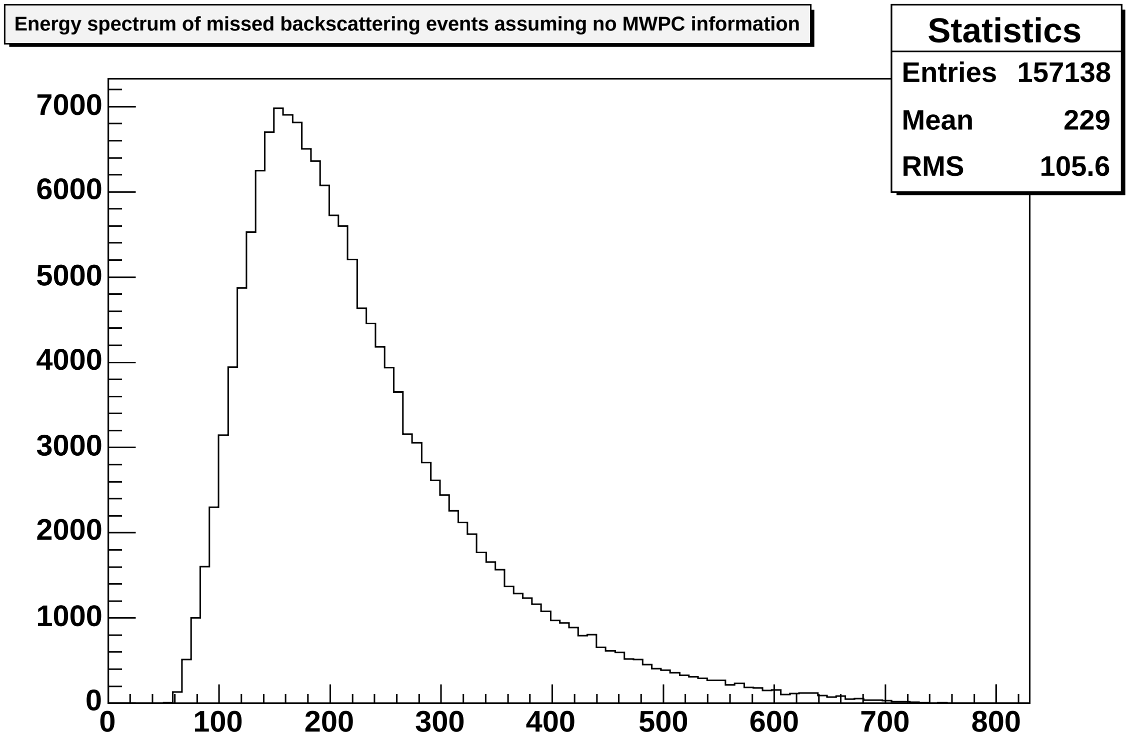

Figure 4.4: Energy spectrum of primary electrons in missed backscattering events assuming no MWPC information

an energy cut of 100keV on the primary electron energy, the number of missed backscattering events is 151462, 0.88% of the total events that fired at least one scintillator. Requiring an energy cut of 200keV, this number will be 80902, 0.58% of the total events that fired at least one scintillator.

To use the information from the MWPC, assume for the following analysis that there is a threshold of 0.5keV on the energy deposition in the sum of the MWPC dead region and active region, because positive bias will be applied on the MWPC cathode planes in UCNA to eliminate the dead region. Among the 157138 missed backscattering events, 22720 events do not fire the MWPC on the opposite side of the fired Scintillator, and thus cannot be identified with MWPC information. This number reduces to 19508 if we require an energy cut of 100keV on the primary electron energy, and 10109 (0.10%) if the energy cut is 200keV.

To see how we can use the information from the MWPCs, Fig. 4.5 shows a scatter plot of the energy deposition in the two MWPCs for the events in which only 1 scintillator fires and the MWPC on the opposite side also fires. The horizontal axis is energy deposition in the MWPC adjacent to the scintillator that does not fire, and the vertical axis is energy deposition in the other MWPC. Assuming that the scintillator that fired is in the initial electron direction, black dots are the correct events, while red dots are the missed backscattering events. From Fig. 4.5, a simple guess would be to use the vertical axis value to distinguish those two events.

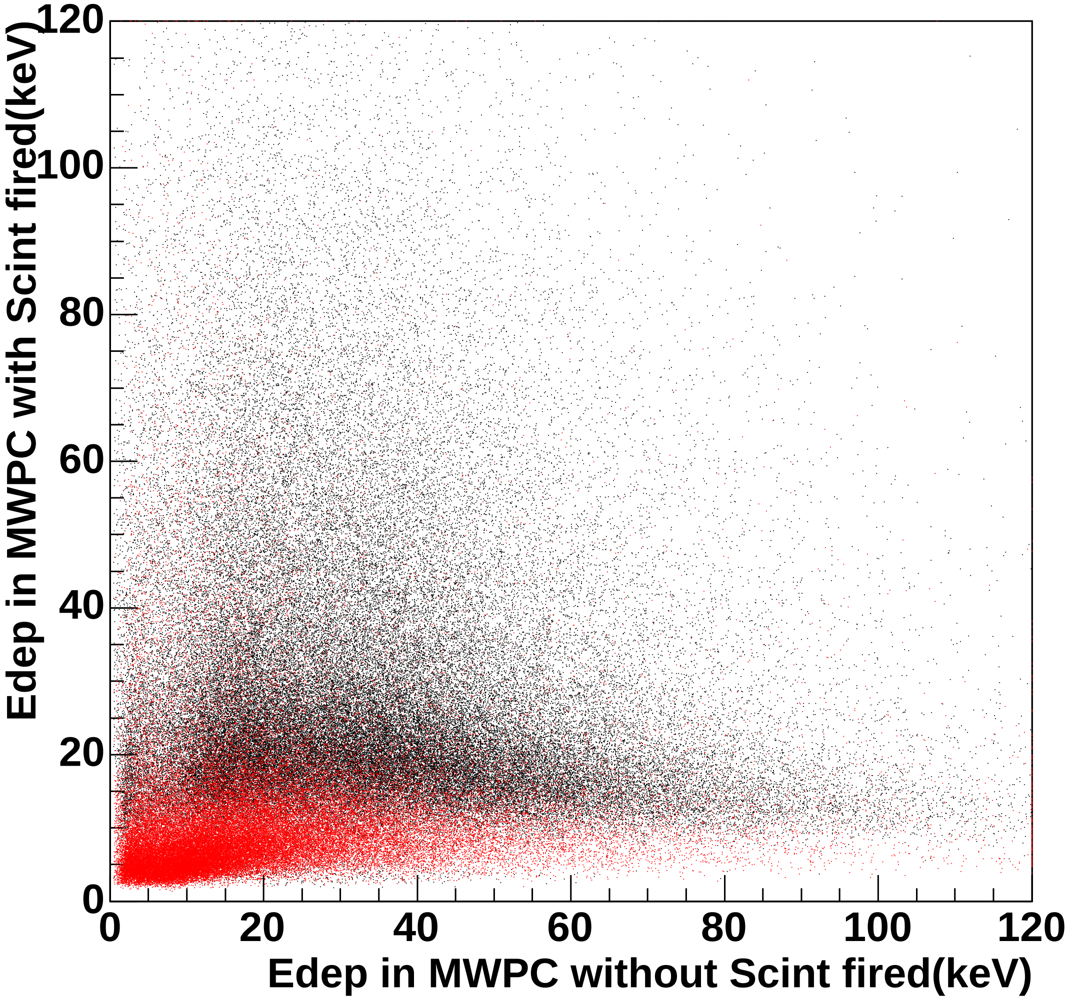

Figure 4.5: Scatter-plot of Edep in both MWPCs. Black dots are the correct events, red dots are the missed backscattering events

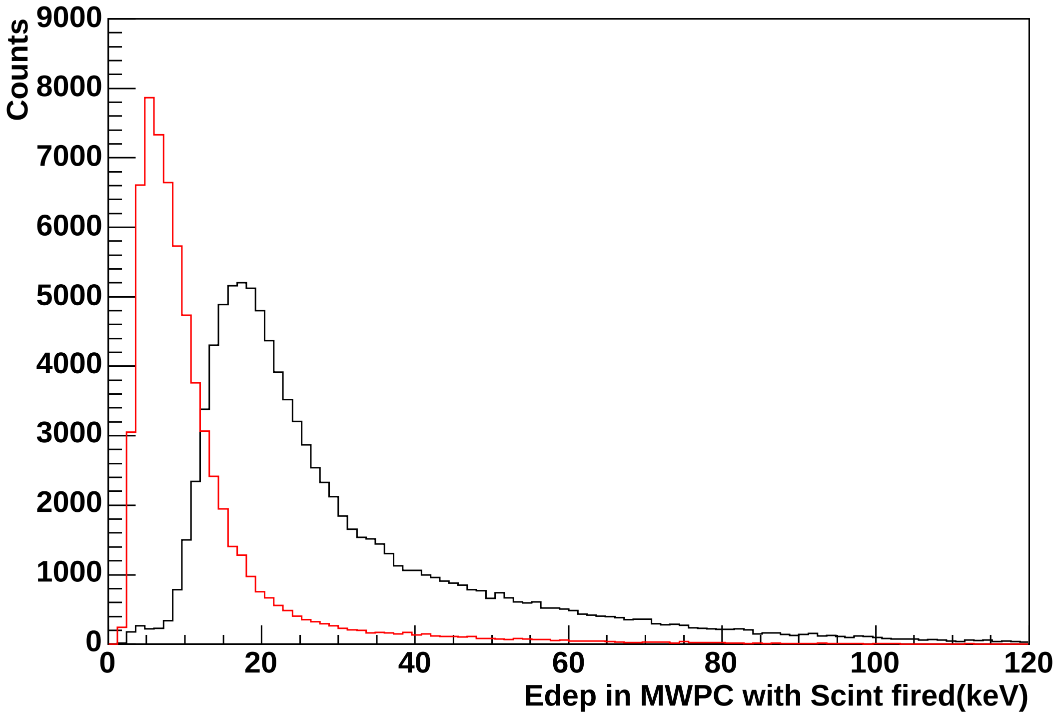

Figure 4.6: Projection of Fig. 4.5 onto its vertical axis. Black histogram is for the correct events, red one is for the missed backscattering events.

Fig. 4.6 shows the projection of Fig. 4.5 onto its vertical axis. From Fig. 4.6, a value of 12keV is the optimum. Therefore, for events in which only 1 scintillator fires and the MWPC on the opposite side fires, if energy deposition in the MWPC adjacent to the fired scintillator is larger than 12keV, we say the initial electron was initially directed toward the fired scintillator, otherwise, it was directed opposite to the fired scintillator. With this assumption, we assign 5871 events of the correct events as missed backscattering events, and assign 20414 events of the missed backscattering events as correct events. Thus the number of the wrongly categorized events due to missed backscattering would be $22720+11232+39401 = 73353$, 0.41% of the total events that fired at least one scintillator. Requiring an energy cut of 100keV on the primary electron energy, this number would be 49094, 0.40% of the total events that fired at least one scintillator with this energy cut. With an energy cut of 200keV, it would be 24500, 0.25% of the total events that fired at least one scintillator with this energy cut.

A summary of the missed backscattering fraction systematics is shown in Table 4.1.

As is shown in Table. 4.1, the missed backscattering fraction does not go up very much when the primary energy cut is decreased below 100 keV. The reason is most of missed backscattering electrons with primary energy below 100 keV have so much energy loss as not to fire the scintillator

Table 4.1: Missed Backscattering Fraction with or without MWPC information

Energy Cut(KeV)	Missed Backscatter Fraction	
	No MWPC information	with MWPC information
30	0.88%	0.41%
100	0.88%	0.40%
200	0.58%	0.25%

on the other side and thus not to be recorded.

To calculate the systematic effect on "A" due to missed backscattering, $(\frac{\Delta A}{A})_{\mathrm{MB}} = -2\frac{N_{\mathrm{Lm}}-N_{\mathrm{Rm}}}{N_{\mathrm{Lt}}-N_{\mathrm{Rt}}}$ is used, and a summary is shown in Fig. 4.7 and Fig. 4.8. Fig. 4.7 shows $(\frac{\Delta A}{A})_{\mathrm{MB}}$ as a function of the primary electron energy. Averaging Fig. 4.7 weighted by the primary e- energy spectrum gives the integrated $(\frac{\Delta A}{A})^{\mathrm{I}}_{\mathrm{MB}}$ due to the missed backscattering effect. Applying various cuts on the primary e- energy, the integrated $(\frac{\Delta A}{A})^{\mathrm{I}}_{\mathrm{MB}}$ as a function of the lower cut on energy can be extracted, as is shown in Fig. 4.8. The higher cut on energy is 745 keV. The errors in Fig. 4.7 and Fig. 4.8 are statistical only.

As discussed before, $(\Delta A/A)_{\mathrm{MB}}$ can be also obtained from MBF with $\beta cos(\theta)$ weighting, which gives better statistical errors using the same set of simulated events, as is shown in Fig. 4.9 and Fig. 4.10.

In the real experiment, the primary energy can only be obtained from the recorded energy deposition in the scintillator detectors and MWPCs, plus an average energy loss for each energy. The average energy loss as a function of the energy deposition is shown in Fig. 4.11. $(\Delta A/A)_{\mathrm{MB}}$ as a function of the energy deposition (corrected for energy loss) is shown in Fig. 4.12. $(\Delta A/A)^{\mathrm{I}}_{\mathrm{MB}}$ as a function of the lower cuts on the energy deposition in shown in Fig. 4.13. The higher cut on the energy deposition is 700 keV.

$(\Delta A/A)_{\mathrm{MB}}$ obtained from MBF with $\beta cos(\theta)$ weighting, is shown in Fig. 4.14 as a function of the energy deposition. $(\Delta A/A)^{\mathrm{I}}_{\mathrm{MB}}$ obtained from MBF with $\beta cos(\theta)$ weighting, is shown in Fig. 4.15 as a function of the lower cuts on the energy deposition.

The effect on "A" due to missed backscattering can be read from Fig. 4.15. For example, with an energy cut of 200 to 700 keV on the energy deposition, the correction due to missed backscattering is $(0.68 \pm 0.01)\%$ without MWPC information, $(0.28 \pm 0.01)\%$ with MWPC information.

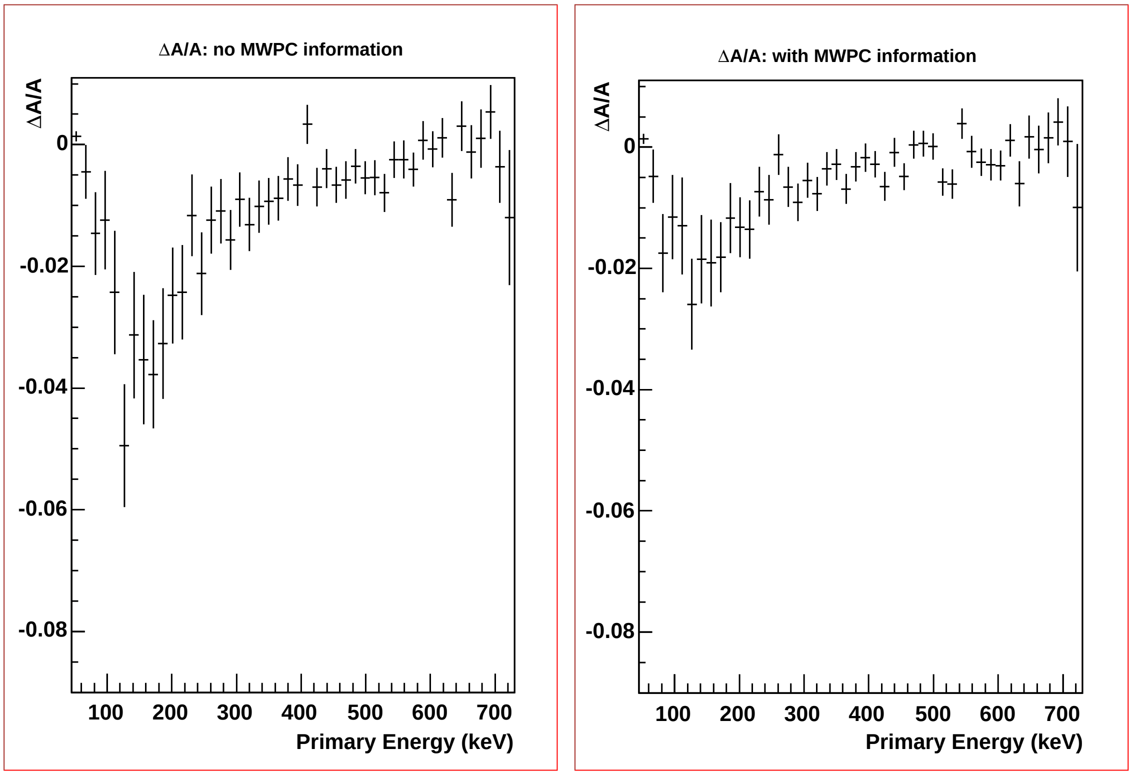

Figure 4.7: $(\Delta A/A)_{\mathrm{MB}}$ as a function of the primary e- energy due to the missed backscattering.

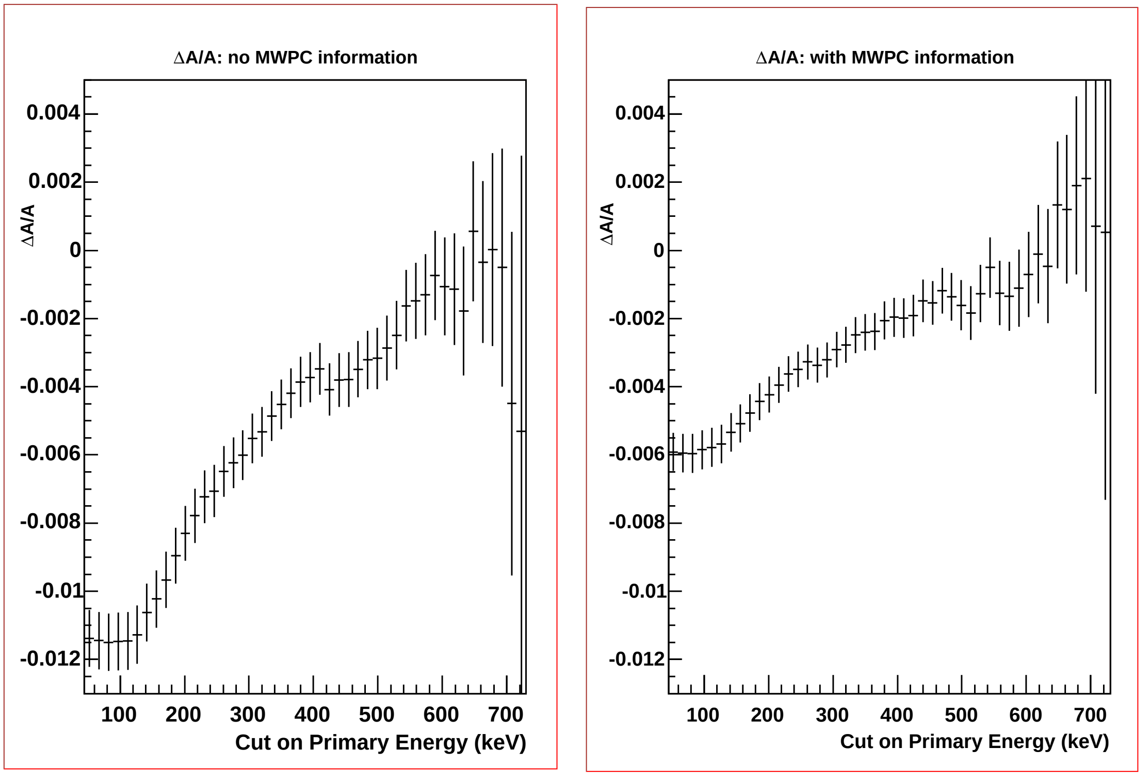

Figure 4.8: $(\Delta A/A)^{\mathrm{I}}_{\mathrm{MB}}$ as a function of lower cuts on the primary e- energy due to the missed backscattering.

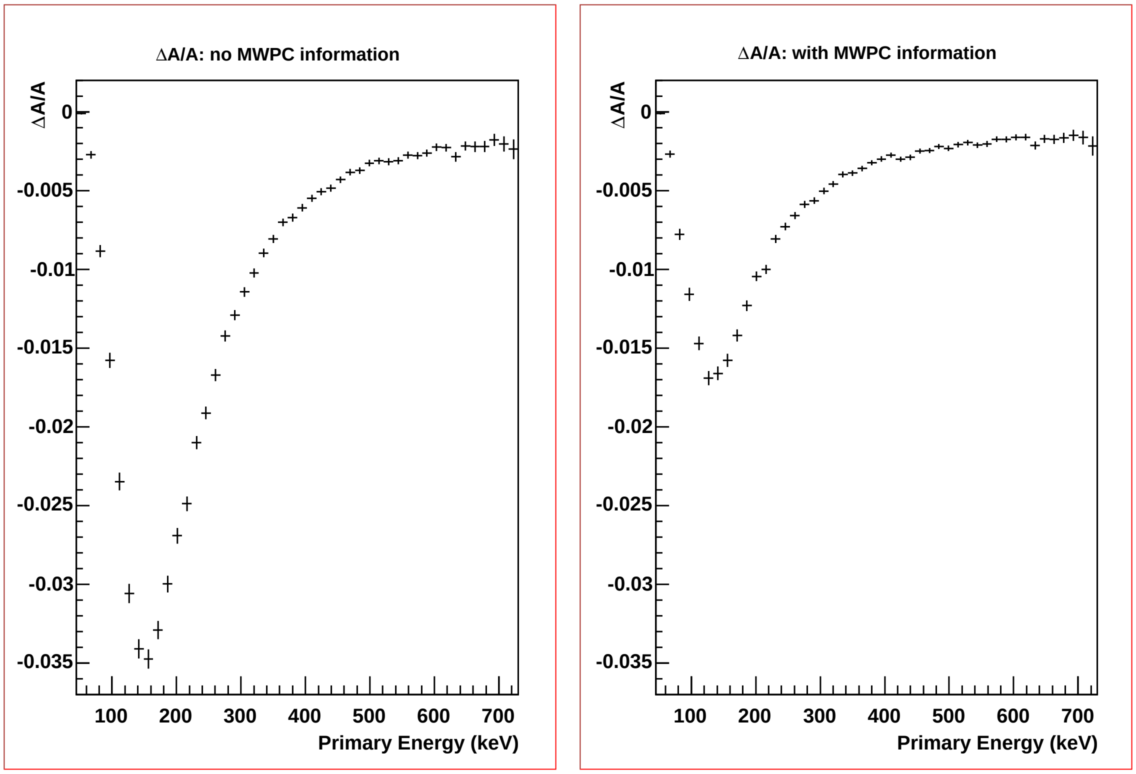

Figure 4.9: $(\Delta A/A)_{\mathrm{MB}}$ as a function of the primary e- energy due to the missed backscattering, obtained from MBF with $\beta cos(\theta)$ weighting.

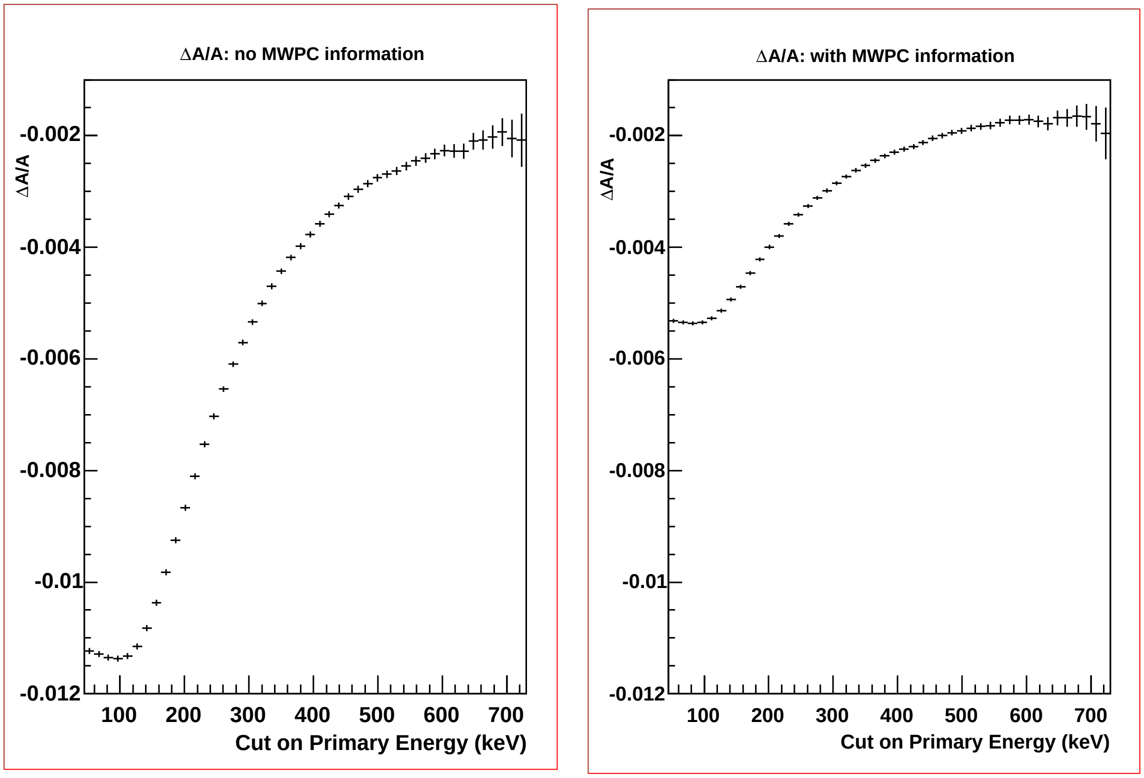

Figure 4.10: $(\Delta A/A)^{\mathrm{I}}_{\mathrm{MB}}$ as a function of the lower cuts on the primary e- energy due to the missed backscattering, obtained from MBF with $\beta cos(\theta)$ weighting.

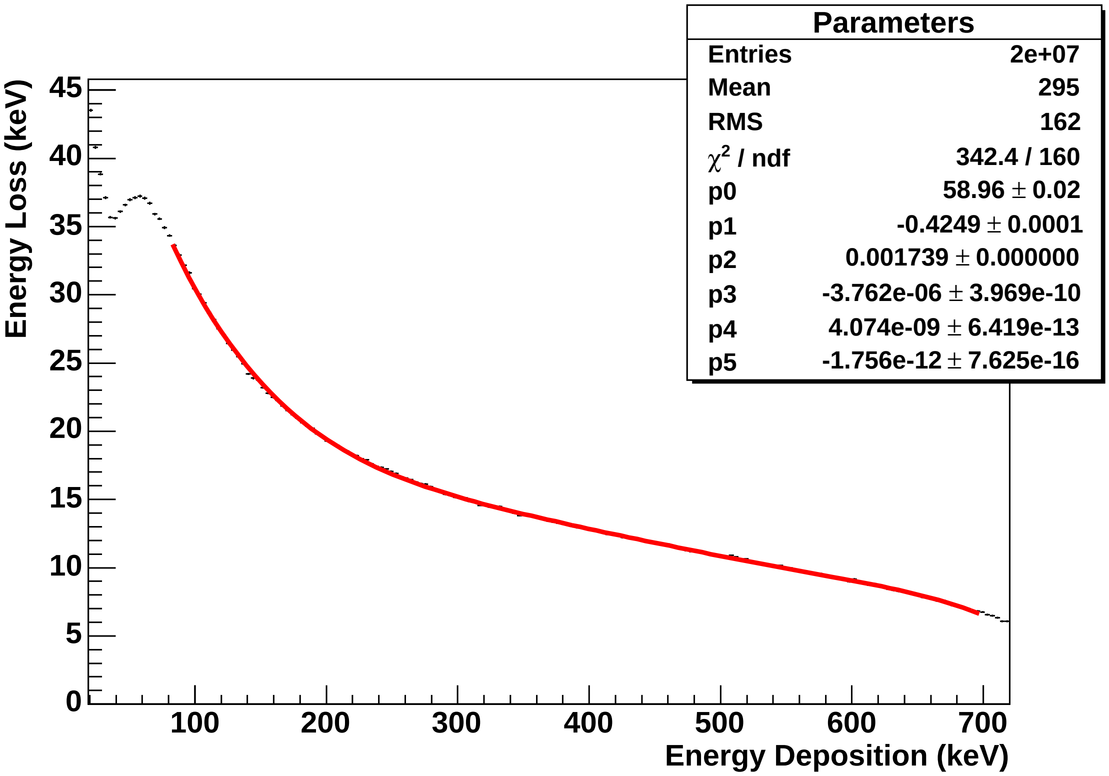

Figure 4.11: Average energy loss in MWPC windows, wire planes and scintillator dead layers, and due to Bremsstrahlung, as a function of the energy deposition in scintillator detectors and MWPCs, based on UCNAg4 simulation.

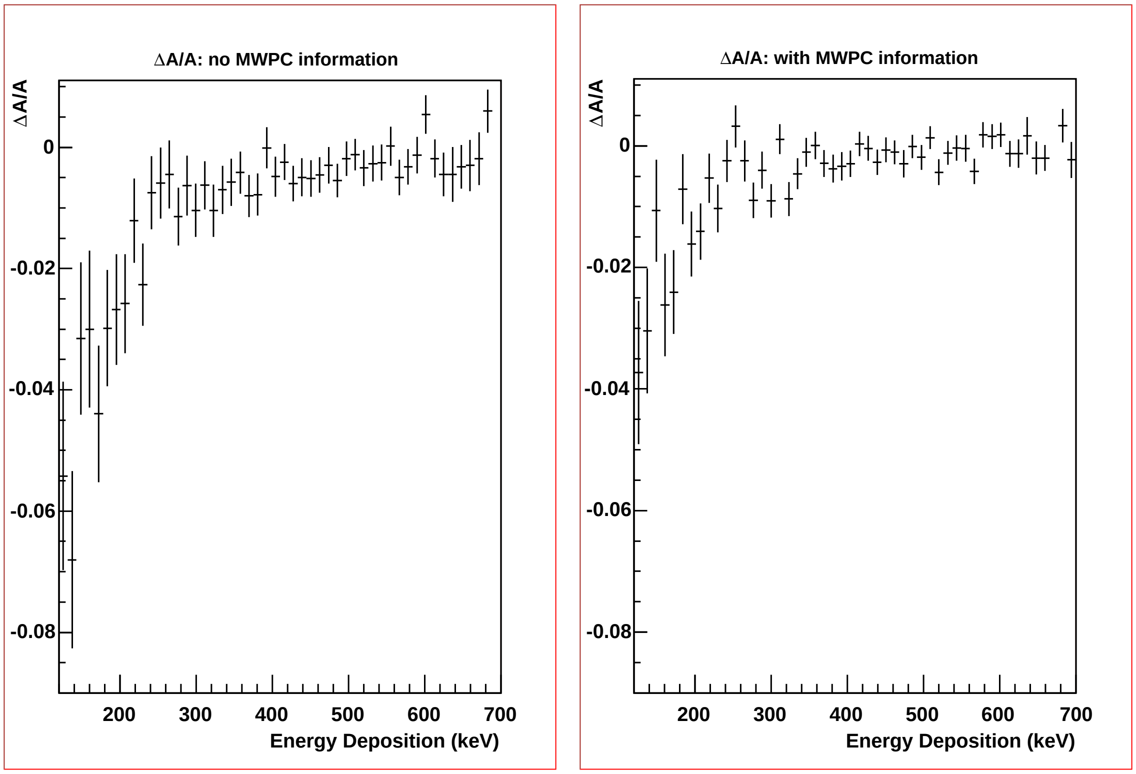

Figure 4.12: $(\Delta A/A)_{\mathrm{MB}}$ as a function of the energy deposition (corrected for average energy loss) due to the missed backscattering.

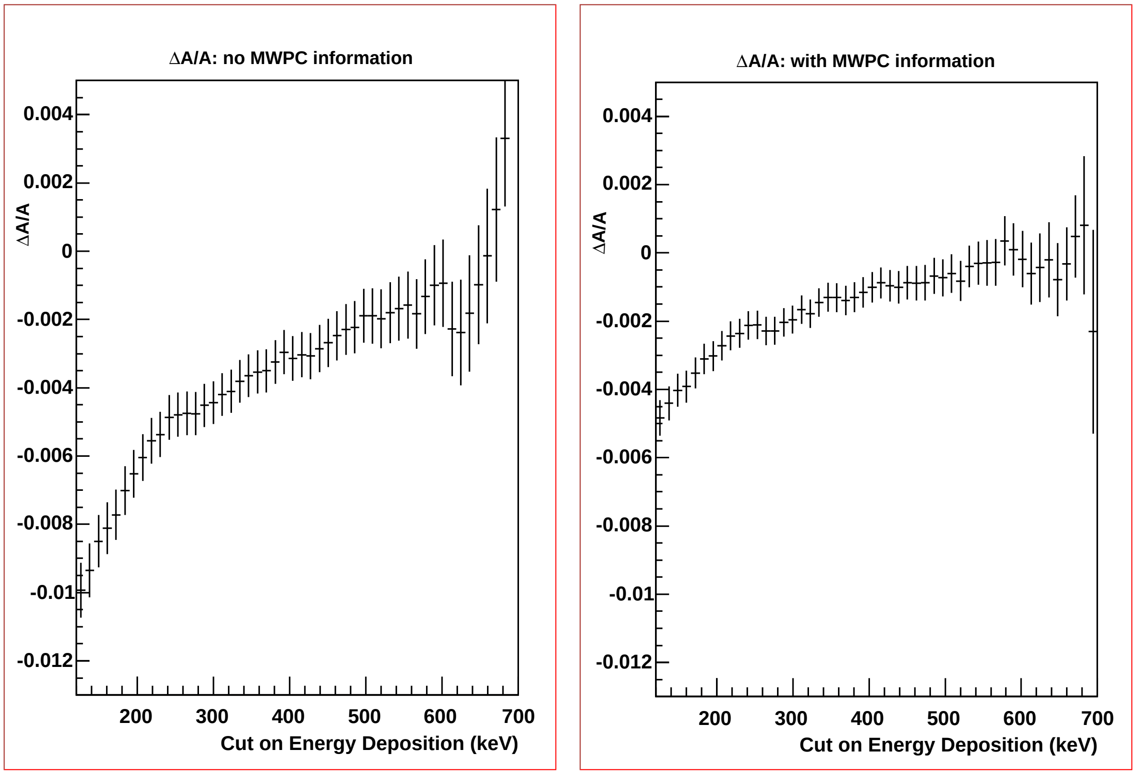

Figure 4.13: $(\Delta A/A)^{\mathrm{I}}_{\mathrm{MB}}$ as a function of lower cuts on the energy deposition (corrected for average energy loss) due to the missed backscattering.

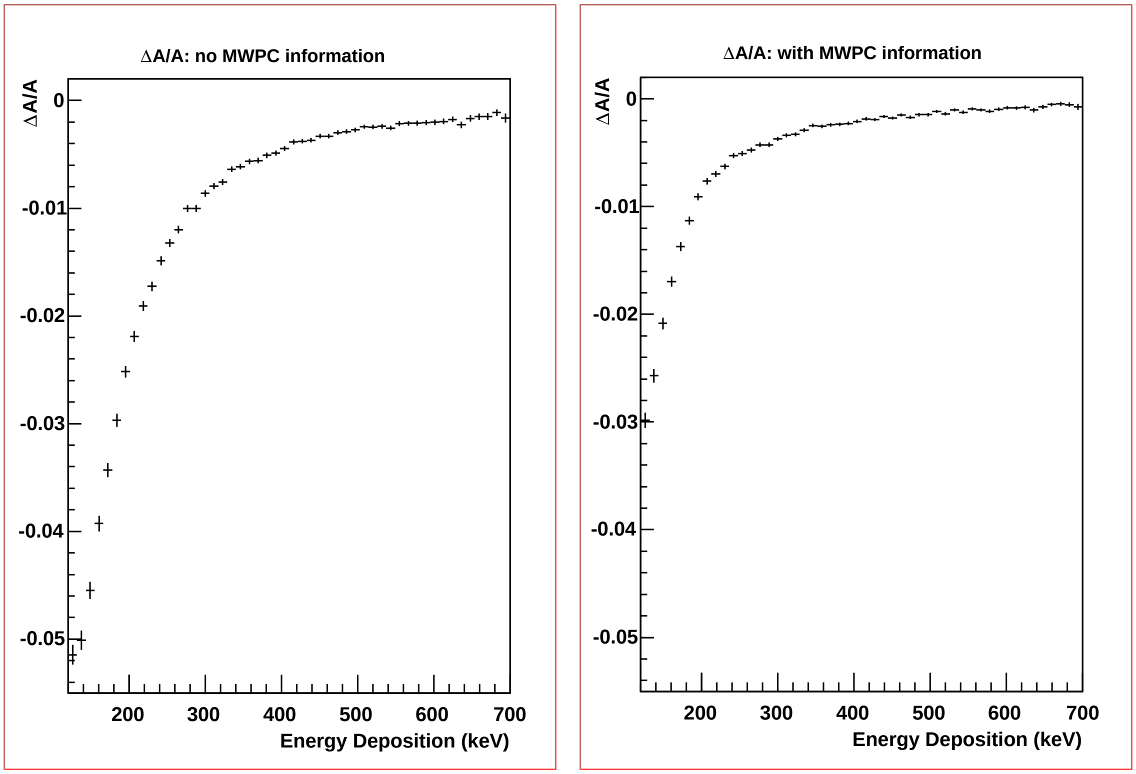

Figure 4.14: $(\Delta A/A)_{\mathrm{MB}}$ as a function of the energy deposition (corrected for average energy loss) due to the missed backscattering, obtained from MBF with $\beta cos(\theta)$ weighting.

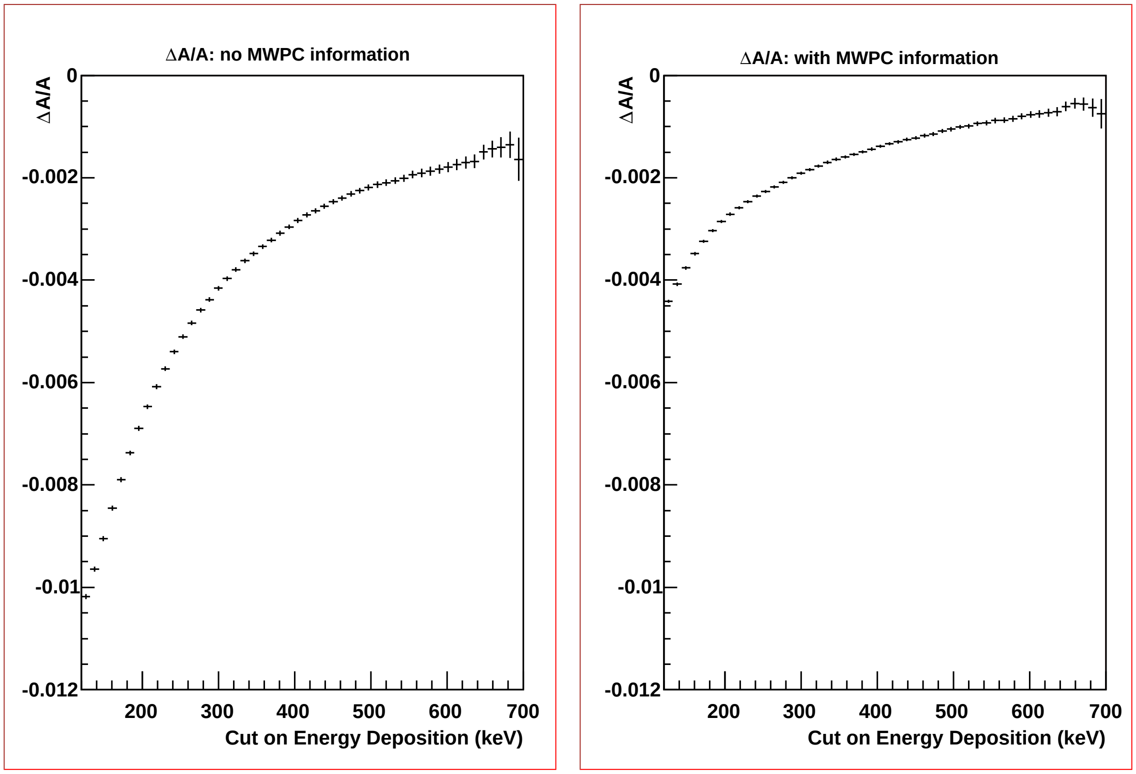

Figure 4.15: $(\Delta A/A)^{\mathrm{I}}_{\mathrm{MB}}$ as a function of lower cuts on the energy deposition (corrected for average energy loss) due to the missed backscattering, obtained from MBF with $\beta cos(\theta)$ weighting.

4.3 Analysis of systematic effects related to energy reconstruction

Since $A_{\text{exp}}(E) = \frac{1}{2}\beta A_0$, where $\beta = P/E_{\text{tot}} = \frac{\sqrt{(2m+E)E}}{m+E}$ is a function of electron energy E, any error δE in the energy reconstruction will induce an effect on “A”:

$$\begin{aligned}(\frac{\Delta A}{A})_{\text{E}} &= \frac{A_{\text{exp}}(E) - A_{\text{exp}}(E-\delta E)}{A_{\text{exp}}(E-\delta E)} \\ &= \frac{\beta(E)}{\beta(E-\delta E)} - 1\end{aligned}$$

Different contributions to this effect are discussed in the following sections.

4.3.1 Linearity

Assuming a 0.05% non-linearity, $\delta E = \pm 0.05\% E$. $(\frac{\Delta A}{A})_{\text{E}}$ as a function of the primary electron energy due to detector non-linearity is shown in Fig. 4.16. $(\frac{\Delta A}{A})_{\text{E}}^{\text{I}}$ as a function of the cuts on primary electron energy due to detector non-linearity is shown in Fig. 4.17.

As is shown in Fig. 4.17, this effect is negligible.

4.3.2 Absolute calibration

Assuming an absolute calibration to $\delta E = \pm 1keV$, $(\frac{\Delta A}{A})_{\text{E}}$ as a function of the primary electron energy due to absolute calibration is shown in Fig. 4.18. $(\frac{\Delta A}{A})_{\text{E}}^{\text{I}}$ as a function of the cuts on primary electron energy due to absolute calibration is shown in Fig. 4.19.

As is shown in Fig. 4.18, $(\frac{\Delta A}{A})_{\text{E}}$ decreases rapidly with e- energy. With a energy cut of 100 keV or more, $(\frac{\Delta A}{A})_{\text{E}}^{\text{I}}$ is less than 0.1%, as is shown in Fig. 4.19.

4.3.3 Average energy loss

Electron energy loss occurs in MWPC windows, MWPC wire planes, scintillator dead layers, and due to Bremsstrahlung. The average energy loss as a function of the primary e- energy is shown in Fig. 4.20, based on the 2×10^7 simulated events.

Using the functional form in Fig. 4.20, $(\frac{\Delta A}{A})_{\text{E}}$ and $(\frac{\Delta A}{A})_{\text{E}}^{\text{I}}$ due to average energy loss can be evaluated, as is shown in Fig. 4.21 and Fig. 4.22. The effect is large, but the average energy loss can be calibrated and added back to the detected energy. Fig. 4.23 shows $(\frac{\Delta A}{A})_{\text{E}}$ as a function of the primary e- energy if the average energy loss is calibrated to an accuracy of ±10% level. Fig. 4.24 shows $(\frac{\Delta A}{A})_{\text{E}}^{\text{I}}$ as a function of the cuts on primary e- energy if the average energy loss is calibrated to an accuracy of ±10%.

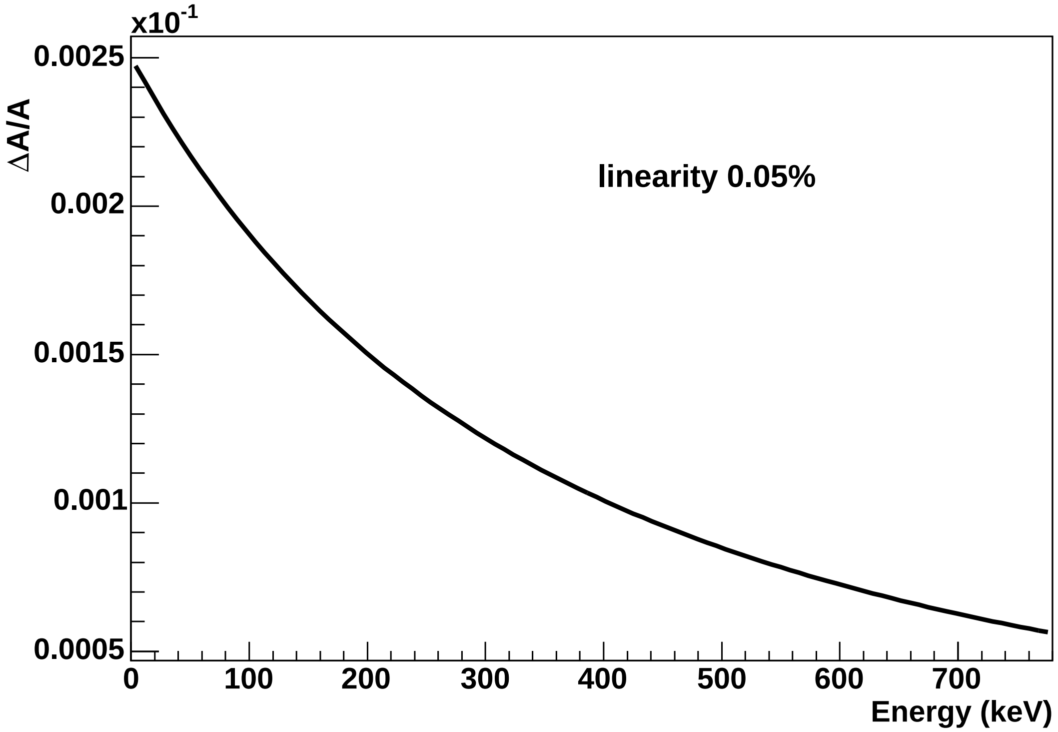

Figure 4.16: $(\frac{\Delta A}{A})_{\mathrm{E}}$ as a function of the primary e- energy due to the detector linearity.

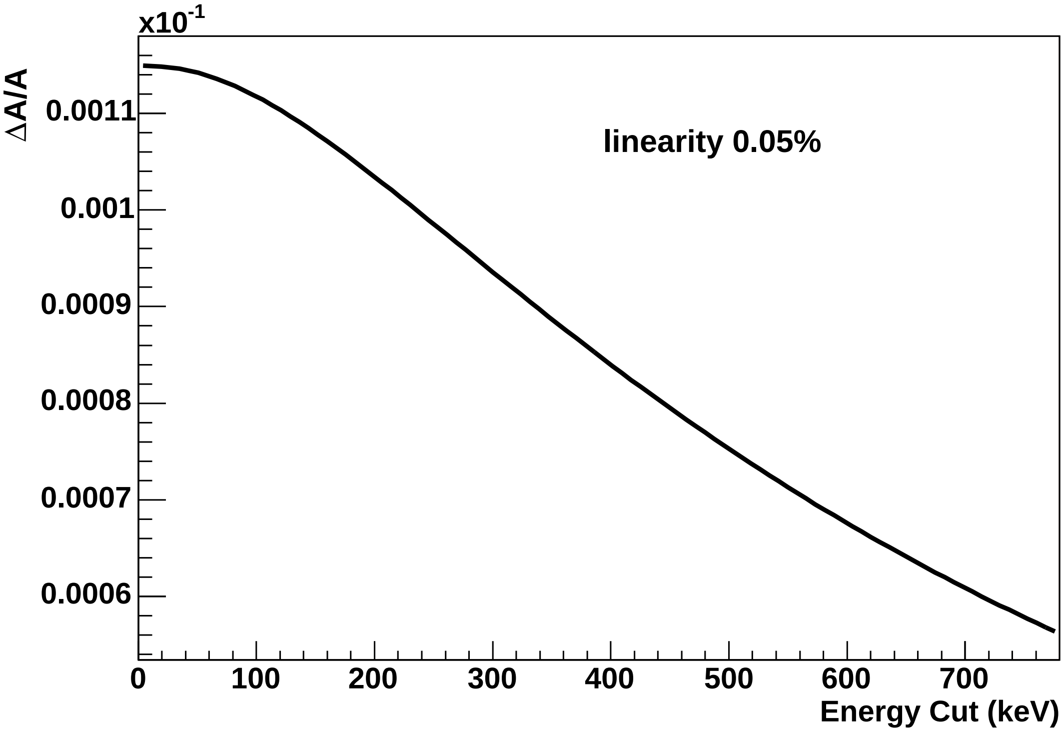

Figure 4.17: $(\frac{\Delta A}{A})^{\mathrm{I}}_{\mathrm{E}}$ as a function of the cuts on primary e- energy due to the detector linearity.

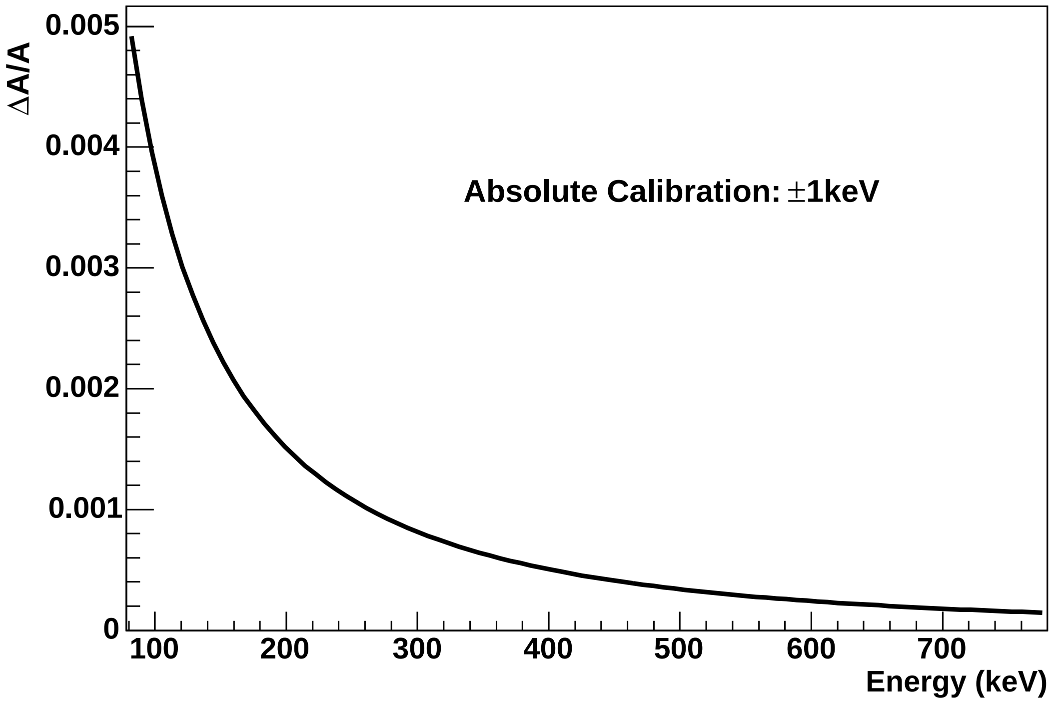

Figure 4.18: $(\frac{\Delta A}{A})_{\rm E}$ as a function of the primary e- energy due to absolute calibration.

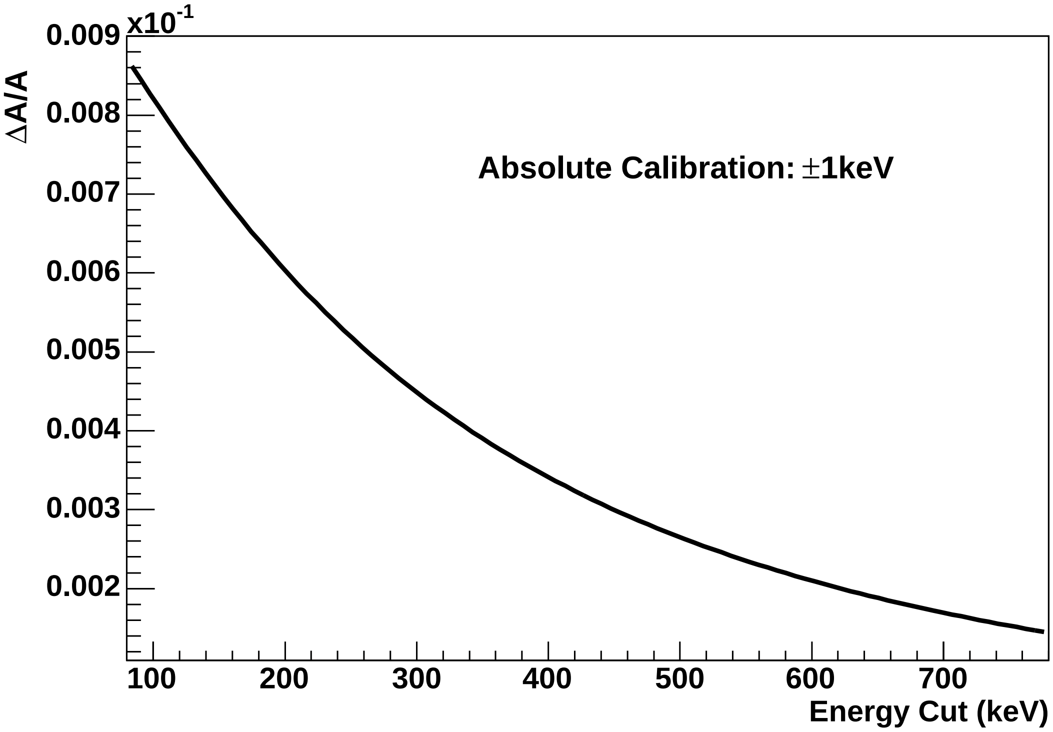

Figure 4.19: $(\frac{\Delta A}{A})^{\rm I}_{\rm E}$ as a function of the cuts on primary e- energy due to absolute calibration.

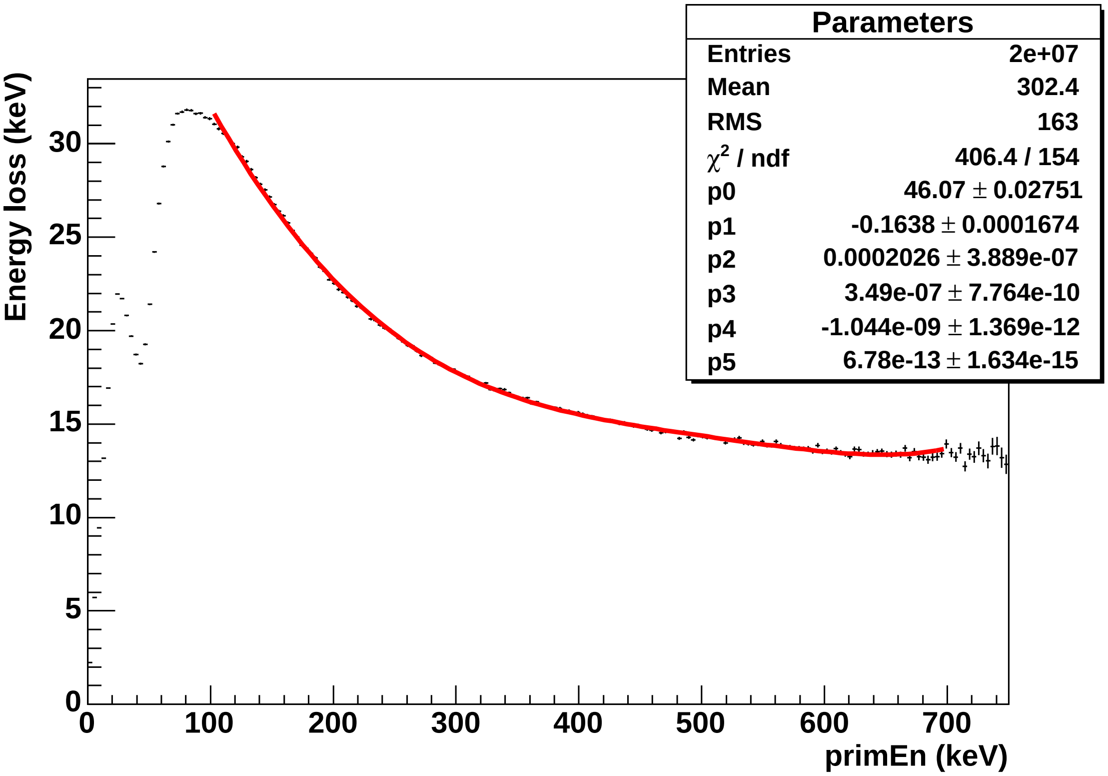

Figure 4.20: Average energy loss in MWPC windows, wire planes and scintillator dead layers, and due to Bremsstrahlung, as a function of the primary e- energy, based on UCNAg4 simulation.

ΔA/A

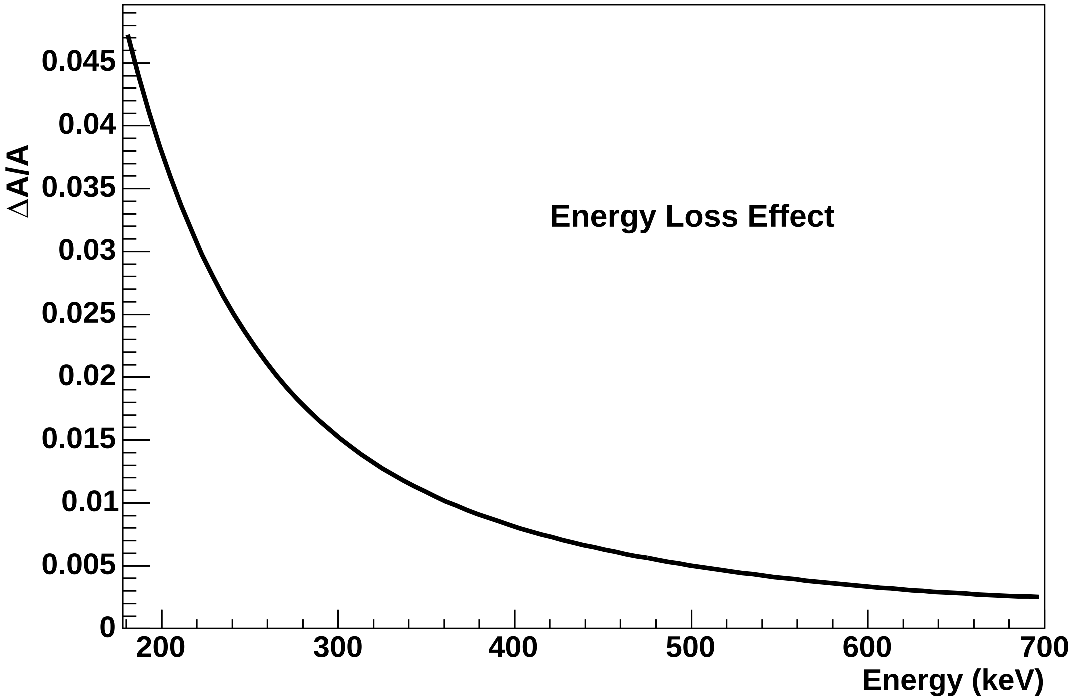

Figure 4.21: $(\frac{\Delta A}{A})_{\mathrm{E}}$ as a function of the primary e- energy due to an average energy loss.

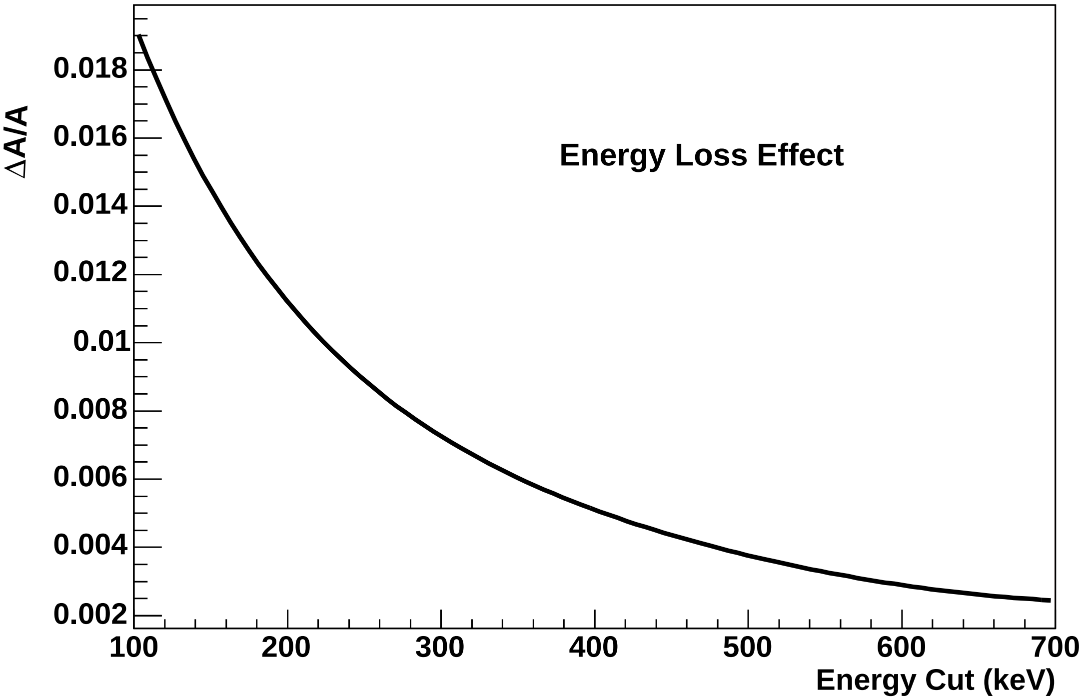

Figure 4.22: $(\frac{\Delta A}{A})^{\mathrm{I}}_{\mathrm{E}}$ as a function of the cuts on primary e- energy due to an average energy loss.

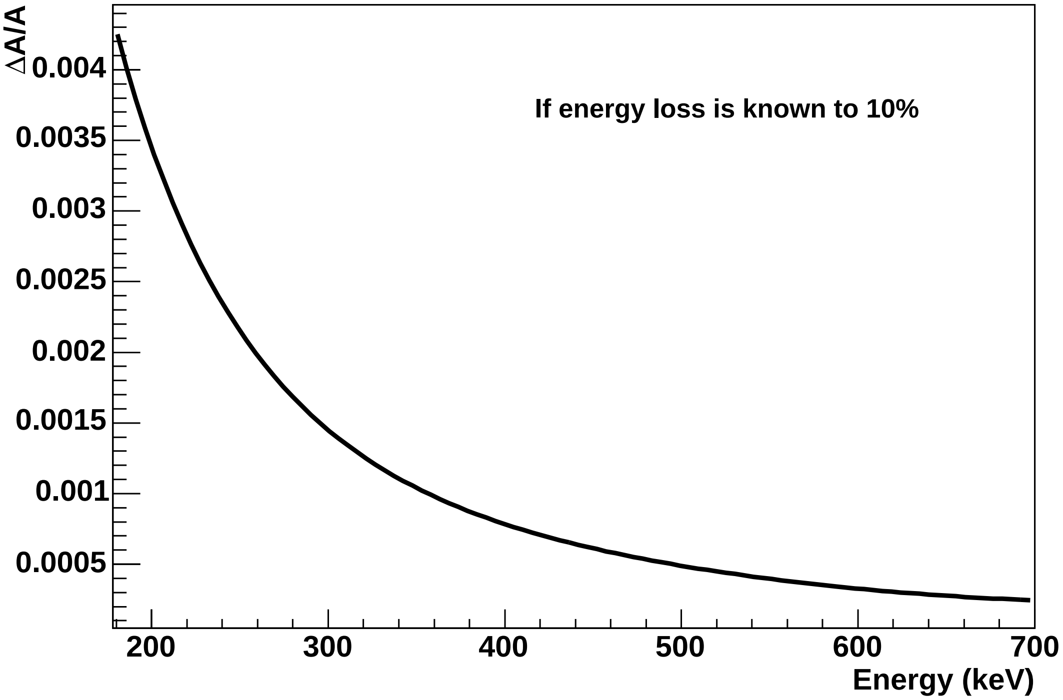

Figure 4.23: $(\frac{\Delta A}{A})_{\mathrm{E}}$ as a function of the primary e- energy if the average energy loss is calibrated to 10%.

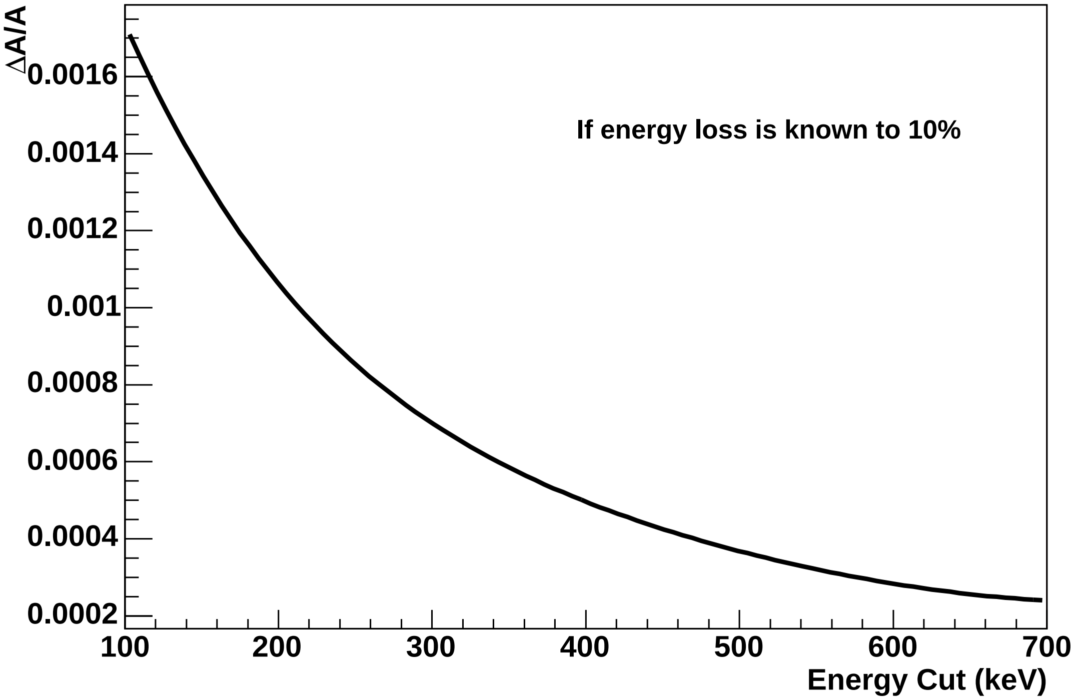

Figure 4.24: $(\frac{\Delta A}{A})^{\mathrm{I}}_{\mathrm{E}}$ as a function of the cuts on primary e- energy if the average energy loss is calibrated to 10%.

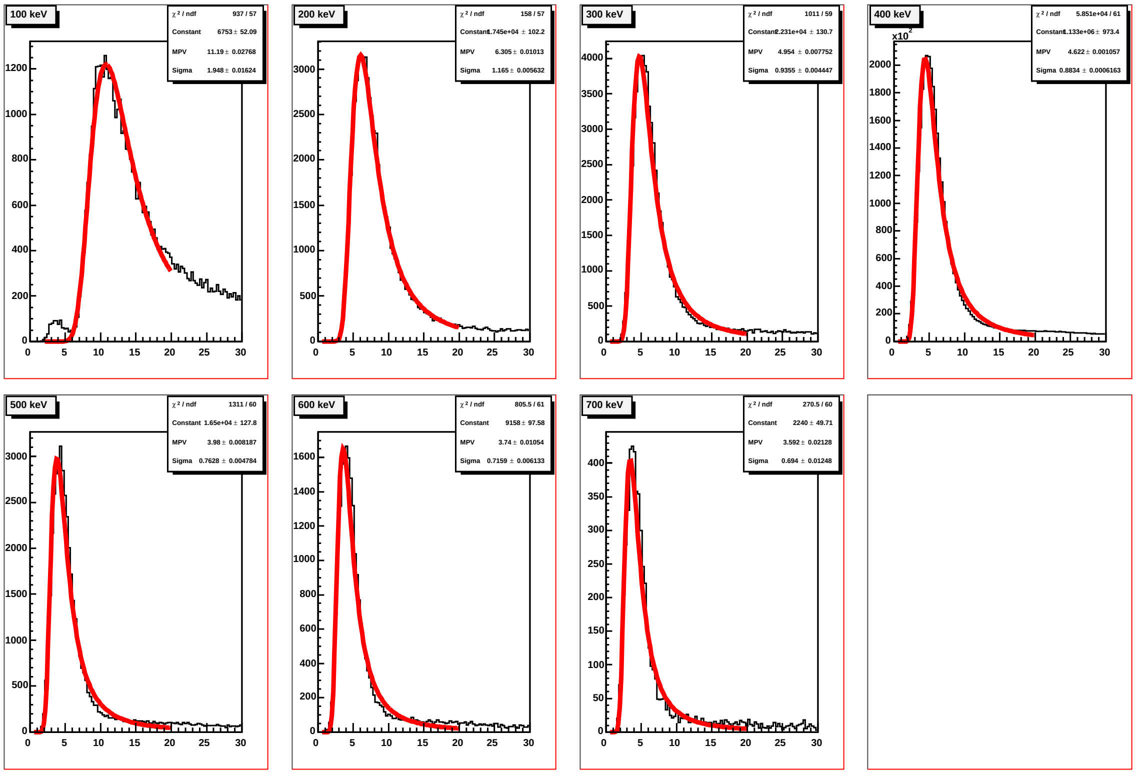

Figure 4.25: Distributions of energy loss when the primary e- energy is 100 ± 1, 200 ± 1, 300 ± 1, 400 ± 1, 500 ± 1, 600 ± 1 and 700 ± 1 keV. Red curves are fits with Landau function.

4.3.4 Straggling in the energy loss

The distribution of energy loss can be approximated as a Landau function if the most probable energy loss is small enough. From the 2×10^7 simulated events, the distributions of energy loss are plotted when the primary e- energy is 100 ± 1, 200 ± 1, 300 ± 1, 400 ± 1, 500 ± 1, 600 ± 1 and 700 ± 1 keV. Each histogram is fit with a Landau function, as is shown in Fig. 4.25, where the energy loss is in MWPC windows, wire planes and scintillator dead layers, and due to bremsstrahlung. The Most Probable Value(MPV) and sigma are extracted from the fits, and plotted as a function of the primary e- energy, as is shown in Fig. 4.26.

A ROOT [60] program was written to generate 1e9 neutron beta decay events. For each event, a random energy loss was generated from the Landau distribution, whose MPV and sigma can be read from Fig. 4.26. The primary e- energy, energy loss, energy deposition and the Left Right direction were recorded, where the summation of energy loss and energy deposition is equivalent to the primary energy. Fig. 4.27 shows the extraction of "A" under various situations of energy reconstruction. The "perfect case" uses the primary e- energy, thus no bias. The "with energy loss" uses the energy deposition, thus biased by energy loss. The "calibrated energy loss" uses a summation of energy deposition and calibrated average energy loss, thus biased by the straggling in

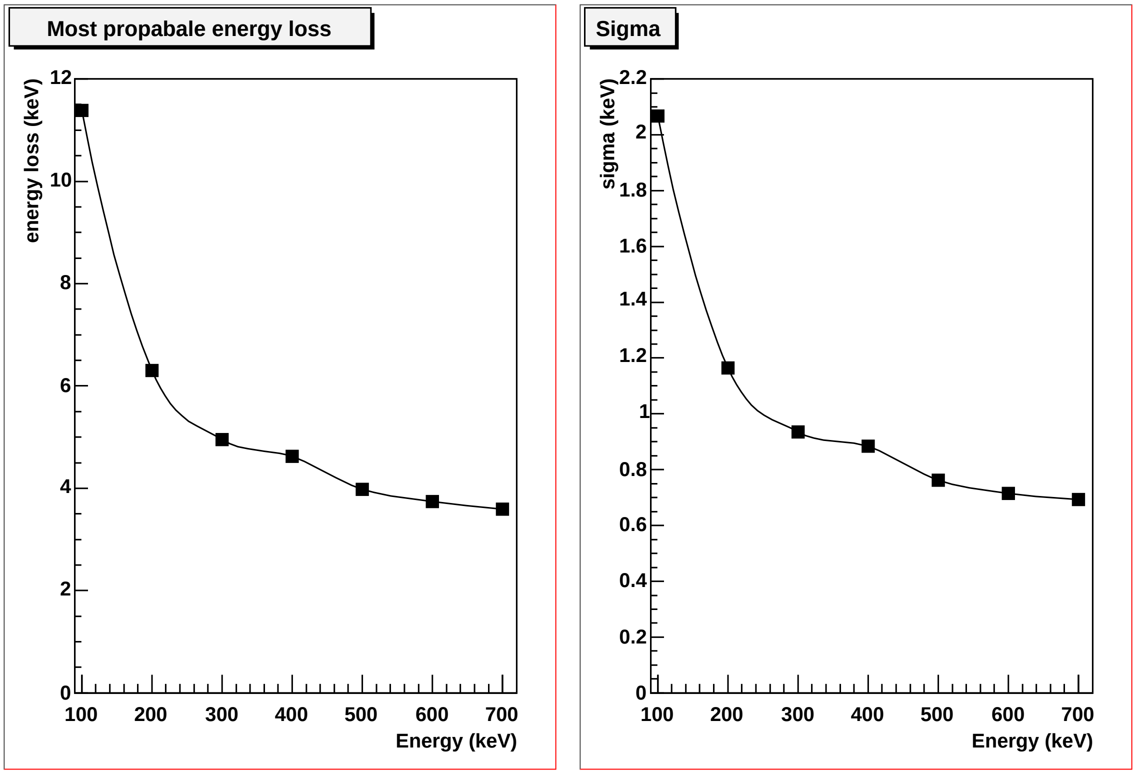

Figure 4.26: MPV and sigma as a function of the primary e- energy.

the energy loss.

From Fig. 4.27, energy loss if not calibrated will lead to a effect of $\Delta A/A = (0.4 \pm 0.1)\%$. If the average energy loss is calibrated and added back to the detected energy, the effect to "A" is negligible: $\Delta A/A = (0.0 \pm 0.1)\%$, that is the effect due to straggling of energy loss.

4.3.5 Energy resolution

As in the section "Straggling of energy loss", the primary e- energy is convoluted with a Gaussian function with sigma equivalent to $\sqrt{2.5E}$ keV (E in keV), and recorded in the 1e9 events. They are used in the extraction of "A", as is shown in Fig. 4.27 under the case of "with energy resolution". From Fig. 4.27, the effect due to energy resolution is $\Delta A/A = -(0.1 \pm 0.1)\%$, which is not statiscally significant.

4.4 Summary

Simulations of the UCNA spectrometer were performed based on GEANT4 release 4.5.2. Systematic effects due to missed backscattering and energy reconstruction are analyzed based on this simulation. A summary of the systematic effects is shown in Table. 4.2. The effects due to detector linearity,

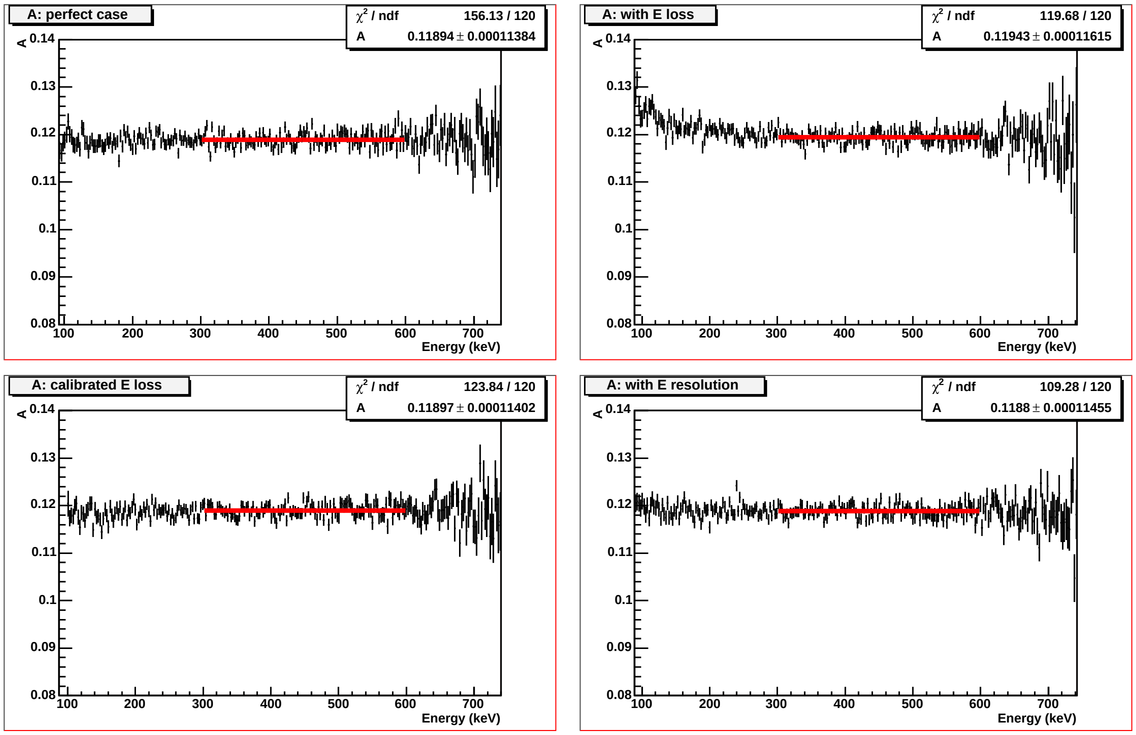

Figure 4.27: Extraction of "A" under various situations of energy reconstruction.

Table 4.2: Systematic effects due to missed backscattering and energy reconstruction

Effect	Assumption	Energy cut	$(\frac{\Delta A}{A})^{I}$
Missed backscattering	with MWPC info.	200-700 keV	(0.28±0.01)%
Detector linearity	0.05% non-linearity	200-700 keV	0.01%
Absolute Energy Calib.	±1keV	200-700 keV	0.06%
Average energy loss	calibrated to 10%	200-700 keV	0.1%
Energy loss straggling		300-600 keV	(0.0±0.1)%
Energy resolution	$\sqrt{2.5E}$ keV	300-600 keV	-(0.1±0.1)%

absolute calibration, straggling in energy loss, and energy resolution are negligible, and the effect due to average energy loss is negligible with a calibration of the average energy loss to the level of 10%. The effect due to missed backscattering is above the 0.1% level, and should be corrected based on this simulation.

Chapter 5

Electronics and Data Acquisition System

5.1 UCNA electronics

The UCNA electronics is a full VME system, with the exception of the “Busy Logic”, which is implemented with a Lecroy 222 gate generator. A full VME electronics system allows more flexibility and control. Table 5.1 lists all modules of the UCNA frontend electronics [61]. The VME modules are made by CAEN [62] and Struck [63].

The trigger logic is shown in Fig. 5.1. Symmetrically there are left and right sides. For each side, an “OR” of PMT sum, 2-fold coincidence of the 4 PMTs, muon veto, and MWPC triggers generates a trigger. An “OR” of the left side, right side, GMS, and pedestal triggers then generates the main trigger. A SIS3600 input register will be used to identify which of the triggers generated the main trigger.

The main trigger is fed to a “busy logic.” There are two reasons why a “busy logic” is necessary. One reason is that some ADC/TDC modules can be re-triggered. The other is that the CAEN PLU V495 modules produce small spikes($\sim 5ns$) on basically any input, which can cause spurious re-triggering. A “busy logic” has to be implemented to prevent re-triggering, such that only one trigger pulse is sent to the ADC/TDC’s, additional trigger pulses are blocked before the ADC/TDC’s finish converting the data. The “busy logic” is implemented with a Lecroy 222 gate generator in latch mode. Fig. 5.2 shows the “busy logic.”

The full layout of the electronics is shown in Fig. 5.3.

Note that the timing between the ADC gates and inputs, the TDC gate and inputs, and the SIS3600 input register strobe and inputs should set appropriately with the help of delays (which are not shown in Fig. 5.3). For the SIS3600 input register, the leading edge of the inputs should appear before that of the strobe, and the trailing edge of the input should appear more than 40ns after the strobe.

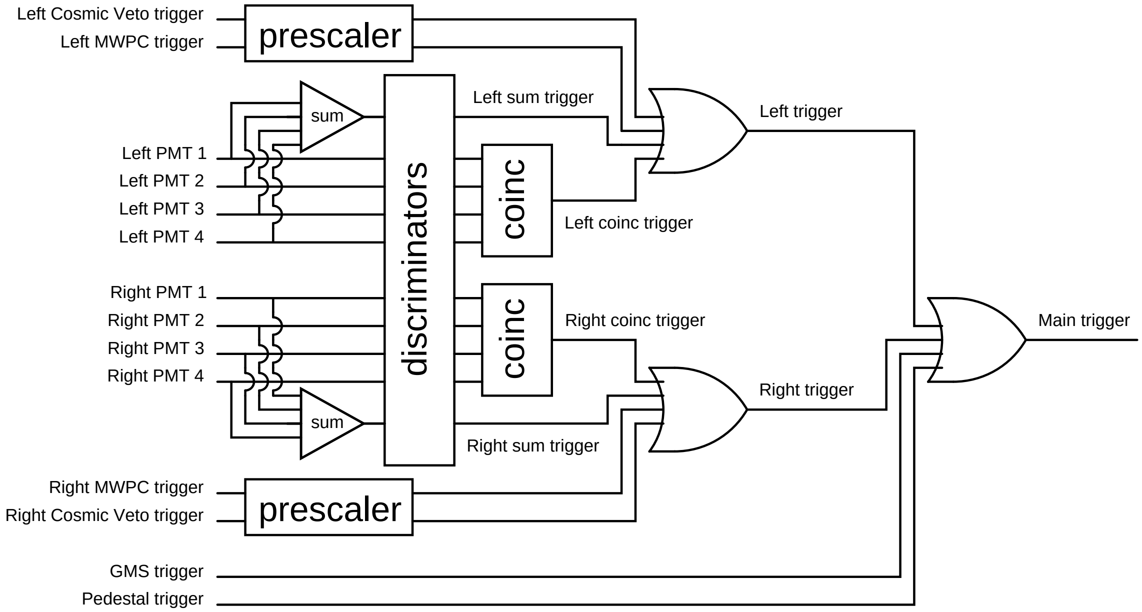

Figure 5.1: Trigger logic for the UCNA experiment.

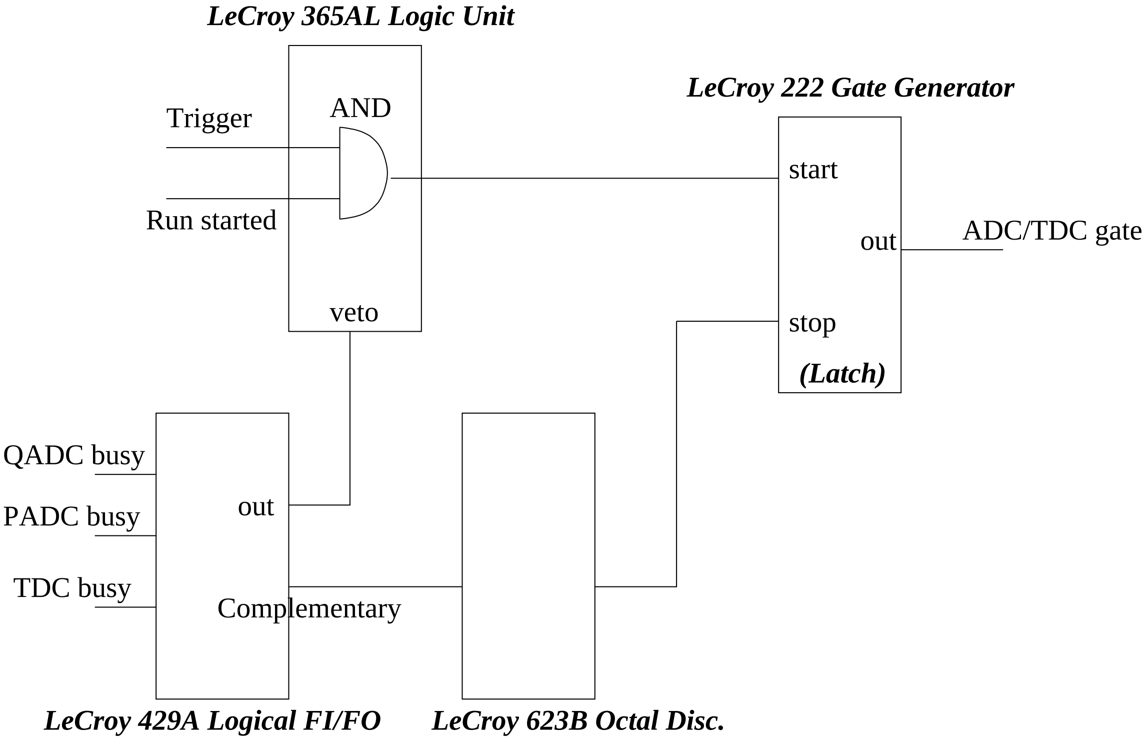

Figure 5.2: Busy logic for the UCNA experiment.

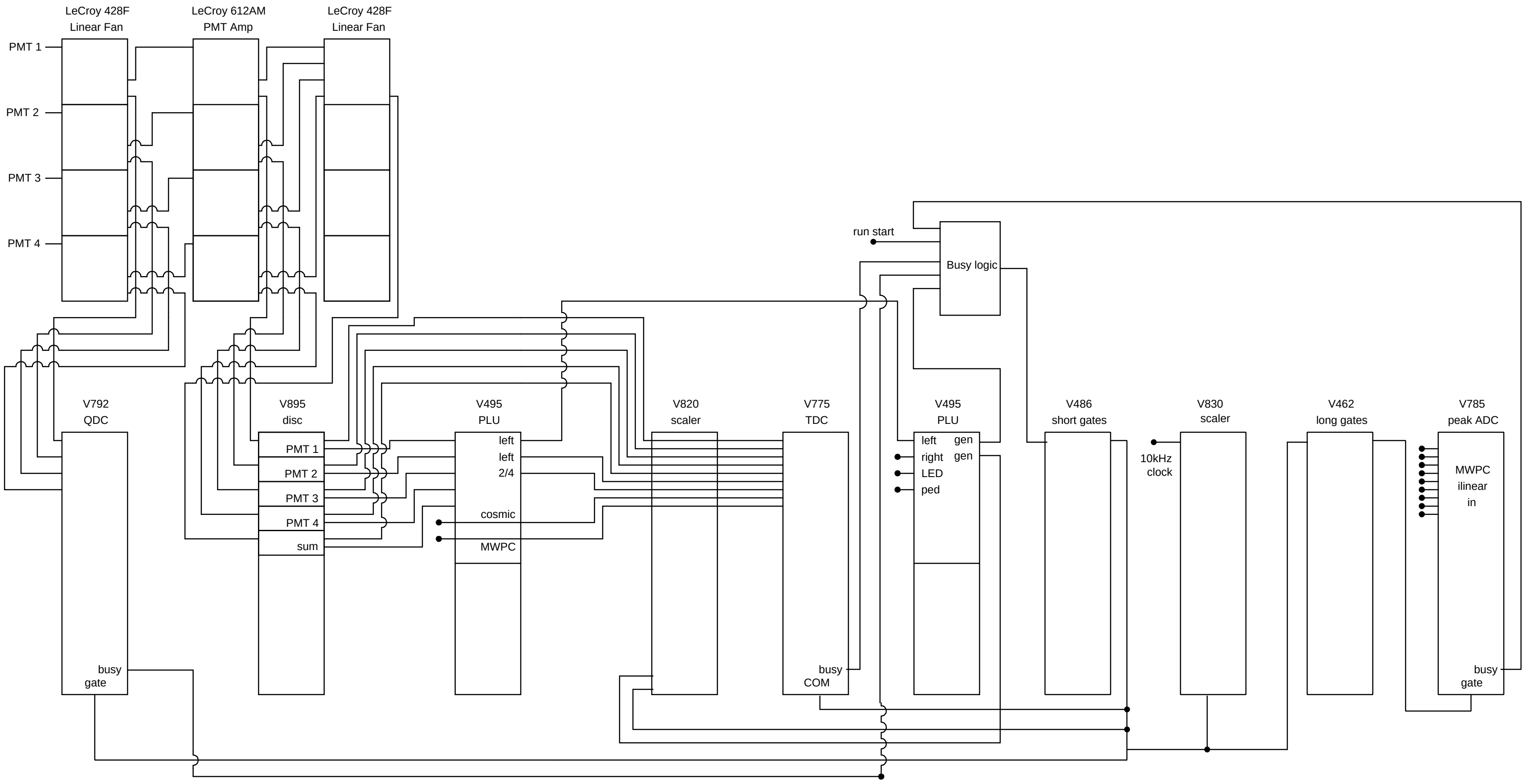

Figure 5.3: Electronics layout of the UCNA experiment.

Table 5.1: Module lists of the UCNA electronics

Item	Features
VME Crate CAEN 6023/631	21 VME 6U cards
SIS1100/3100 PCI/VME	BLT32: 25 MBytes/s
VDIS-2 Dataway Display	VME
SIS3600 Input Register	VME, 32bit, Multi Event(32K events)
QADC CAEN V792AA	VME, 32ch, 5.7μs conversion time 12bit, multievent(32 event)
TDC CAEN V775AA	VME, 32ch, 5.7μs conversion time 12 bit, multievent(32 event), 1200ns range
Peak ADC CAEN V785	VME, 32ch, 5.7μs conversion time 12bit, multievent(32 event), 4V range
Edge Disc. CAEN V895	VME, 16ch, -1 to -255mV Computer programmable threshold and output width
Scaler CAEN V830AA	VME 32bit, 32ch, Multi Event(32K × 32bits)
Scaler CAEN V820AA	VME 32bit, 32ch
Gate Delay Gen. CAEN V486	VME, 8ch, 15-500ns
Gate Gen. CAEN V462	VME, 2ch, 100ns-10s
Trigger PLU CAEN V495	VME, 2 PLU/mod, 8 ECL In and Out/PLU Programmability of any desired logical function
NIM/ECL CAEN V538	VME, 8ch
LeCroy 428F lin. fan	NIM, quad linear fan-in/out
LeCroy 429A log. fan	NIM, quad logical fan-in/out
LeCroy 623B octal discrim.	NIM, -30mV to -1V, output width: 6ns to 150ns
LeCroy 365AL dual quad logic	NIM, 2ch, 4input/ch
LeCroy 222 gate generator	NIM
NIM/ECL level adapter	NIM, 16ch

5.2 Electronics for UCN source study

For studies of the UCN source, a ^{3}He gaseous detector is used to detect UCN, and another ^{3}He gaseous detector is used to detect cold neutrons. Signal from each counter is amplified by a preamp and then a shaping amplifier to generate an analog signal, a “tee” of the analog signal is fed to a Single-Channel Analyzer(SCA) to generate a gate signal. Therefore, 2 signals from each counter are fed to the electronics. In addition, a signal showing the start and the stop of the source flapper is also fed to the electronics, so that we can monitor the flapper moving.

The electronics setup is shown in Fig. 5.4. An “OR” of the UCN detector gate signal, the cold neutron detector gate signal, and the flapper moving signal, generates the main trigger. A SIS3600 input register is used to determine which of these triggers actually generated the main trigger. The analog signals from the gaseous counters are fed to the Peak-sensing ADC (PADC). A 1MHz clock is fed to one channel of the V830 scaler, which is read out for each event to give a timing stamp. The proton beam trigger resets the V830, so that the timing of each event is recorded relative to the proton beam trigger. A ntuple plot of the timing requiring the UCN trigger will then show a Time-Of-Flight spectrum of the UCNs.

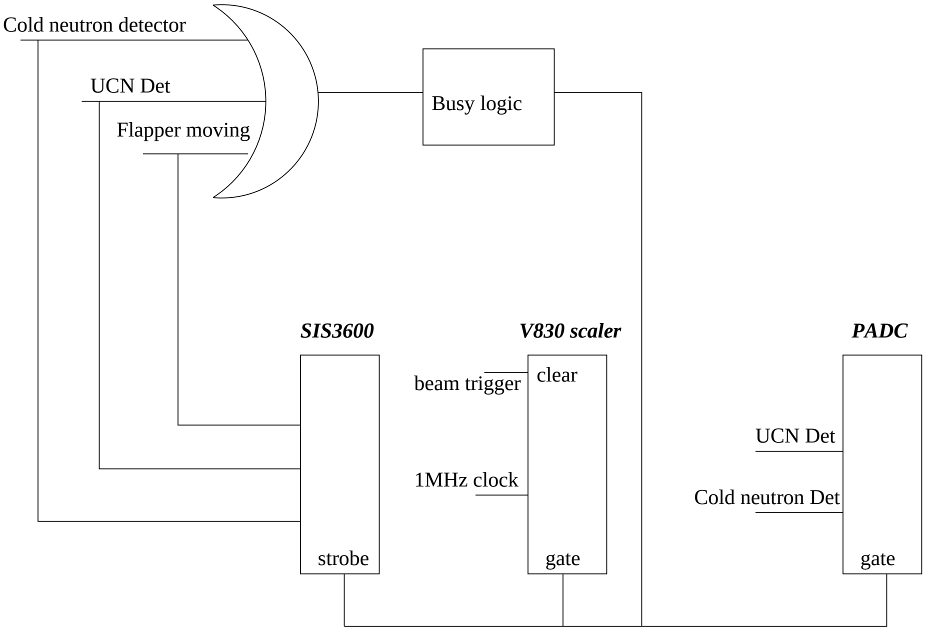

Figure 5.4: Electronics for studies of the UCN source.

5.3 The Data acquisition system

The data acquisition system is based on the MIDAS package [64]. MIDAS is based on a modular networking capability, a central database system, and a modular scheme that allows scalability and flexibility. The MIDAS components are:

- Buffer Manager: Data flow and messages passing mechanism. Buffers can be accessed locally or remotely via the MIDAS server.
- Message System: Specific MIDAS messages flow.
- Online Database: Central information area.
- Frontend: Acquisition code
- MIDAS Server: Remote access server (RPC server).
- Data Logger: Data storage. Data can be written in MIDAS or ROOT format.
- Analyzer: Data analyzer.
- Run Control: data flow control.
- History System: Event history storage and retrieval.
- Alarm System: Overall system and user alarm.
- Electronic Logbook: Online user logbook.

Basic components such as Buffer manager, Online database, Message system, and Ron control are by default operational. The others need to be enabled by the user simply by either starting an application or by activation of the component through the Online database.

MIDAS provides a run control interface through the web using any web browser. “mhttpd” is the MIDAS web server.

The user is supposed to implement the “frontend” and the “analyzer” code. The frontend program refers to a task running on a particular computer which collects data from hardware equipments and sends data to the buffer manager. In UCNA, the frontend is implemented to access the VME system through a PCI/VME fiber optic link. The trigger settings, such as the PLU logical functions, the V486 and V462 output width, and the V895 discriminator threshold, are implemented in the frontend code such that they can be modified in the run control interface(any web browser). To get maximum speed, the frontend is implemented such that it transfers raw data from ADC’s and TDC’s to the data buffer in “block transfer” mode. The frontend keeps polling the “data ready” status of the PADC’s, QADC’s and TDC’s. Whenever any of the ADC/TDC’s has data ready in its memory, The frontend transfers the data to the buffer manager.

The MIDAS event format is a variable length event format. It uses “banks” as subsets of an event. A bank is composed of a bank header followed by the data. Usually a bank contains an array of values that logically belong together. For example, in the frontend code of UCNA experiment, the following banks are used: a PADC bank, a QADC bank, a TDC bank, a SIS3600 bank, a Scaler V830 bank, and a Scaler V820 bank. The length of a bank can vary from one event to another due to zero suppression from the hardware. Beside the variable data length support of the bank structure, another main advantage is the possibility for the analyzer to add more (calculated) banks during the analysis process to the event in process. For example, the frontend generates the raw TDC bank, without decoding the data, to achieve maximum speed. In the first analysis stage, the data can be decoded, and the event can contain a decoded TDC bank in addition to the raw TDC bank.

The analyzer is organized in modules. Modules and banks are registered in “analyzer.c”. Each module is then implemented in a module.c file. The analyzer can be interfaced with either PAW or ROOT. The same analyzer can be used both online and offline. An n-tuple “1” is generated by default with running of the analyzer. The n-tuple contains the banks which are registered in “analyzer.c” and activated through the Online database (The activation can be easily done through the run control interface). In the online analysis, the ntuple only contains the latest 1K events, while it contains the full events in the offline analysis.

In the UCNA experiment, a computer is exclusively used for running of the “frontend” program. The other programs, such as the mserver, mhttpd, mlogger, analyzer, and the run-control interface, are running on the backend computer which is connected to the frontend computer with a normal

Ethernet connection. The SIS1100 PCI card is hosted in the frontend computer, which is connected via a fiber optic link to the SIS3100 VME card hosted in the VME crate.

Tests performed at Caltech shown the DAQ system can run smoothly without inducing any dead time up to an event rate of 12 KHz (Data rate of about 10 MB/s), besides the electronic dead time induced by the ADC/TDC conversion time.

Chapter 6

Results

6.1 Studies of detector backscattering

Electron backscattering is an important systematic effect in the UCNA experiment, since there are plastic scintillators and multiwire proportional chambers with thin mylar windows in the UCNA experiment, and silicon detectors in the updated version of the experiment. Detailed studies of electron backscattering from bulk low Z targets and thin mylar films were carried out using electrons from the Kellogg electron gun(energy up to 130keV). These measurements are compared with electron transport simulations based on the Geant4 and Penelope Monte-Carlo simulation codes, to provide a check on the physics model of the simulation codes, which will be used to simulate the UCNA spectrometer.

6.1.1 Simulation of electron backscattering

Monte Carlo simulation is used as an efficient method to solve the electron transport problems [65]. During the transport, electrons are deflected and lose energy. Angular deflections of the electron are mainly due to elastic scattering with nuclei screened by the surrounding electron cloud. In Monte Carlo simulation, two processes, elastic scattering and energy loss processes, should be considered. Electron backscattering is a special case of the electron transport problems, in that the backscattered electrons result from large total angular deflections (larger than 90 degree). Therefore, simulation of electron backscattering depends heavily on a correct modeling of elastic scattering.

Existing simulation algorithms for electron transport problems can be classified into two different kinds, namely “detailed” simulations and “condensed”simulations. In detailed simulations, all the collisions experienced by an electron are simulated in chronological succession. This simulation can be considered as exact, i.e., it gives the same results as the solution of the transport equation. However, it can be used only if the number of collisions is not too large, a condition fulfilled only for special geometries (such as thin foils), or low enough kinetic energies (up to about 100 keV).

For larger kinetic energies, and thick geometries, the average number of collisions experienced by an electron until it is effectively stopped becomes very large, and the detailed simulation becomes very inefficient. High energy simulation codes use condensed simulation algorithms, in which the global effects of the collisions are simulated at the end of a track segment. A track segment is called a "step," with a length much larger than the mean free path between real collisions, so that a large number of collisions take place along each step. The global effects generally computed in these codes are the net displacement, energy loss, and change of direction of the charged particle. These quantities are computed from the multiple scattering theories used in the codes. The accuracy of the condensed simulations is limited by the approximations of the adopted multiple scattering theories [66].

Most Monte Carlo simulation codes use the multiple scattering theories of Molière [67], Goudsmit and Saunderson [68] and Lewis [69]. Molière's theory is based on certain assumptions about the single scattering differential cross section and incorporates mathematical approximations that make the final distribution fully analytical. In the multiple scattering theories of Goudsmit-Saunderson and Lewis, the exact angular distribution due to multiple elastic scattering after a given path length is calculated by means of an expansion in Legendre polynomials. The theories of Molière and Goudsmit-Saunderson give only the angular distribution after a step, while the Lewis theory computes the moments of the spatial distribution as well. None of the these MSC theories gives the probability distribution of the spatial displacement. Therefore each of the MSC simulation codes incorporates its own algorithm to determine the spatial displacement of the charged particle after a given step. These algorithms are not exact, of course, and are responsible for most of the uncertainties in the MSC codes. Therefore the simulation results can depend on the value of the step length and generally one has to select the value of the step length carefully.

A new class of simulation, the "mixed" simulation algorithms (see, e.g., [66]), appeared in the literature recently. The mixed algorithm simulates the "hard" collisions (those with large scattering angles) one by one and uses a MSC theory to treat the effects of the "soft" collisions (those with small scattering angles) at the end of a given step. Such algorithms can prevent the number of steps from becoming too large and also reduce the dependence on the step length.

In the multiple scattering theories, the properties of the multiple scattering process are completely determined by the transport mean free paths, λ_k, which are functions of the energy in a given material. The k-th transport mean free path is defined as

$$\frac{1}{\lambda_k} = N 2\pi \int_{-1}^{1} [1 - P_k(\cos\chi)] \frac{\mathrm{d}\sigma(\chi)}{\mathrm{d}\Omega} \, \mathrm{dcos}\,\chi$$

where $d\sigma(\chi)/d\Omega$ is the differential cross section of the scattering, $P_k(\cos\chi)$ is the k-th Legendre polynomial, and N is the number of atoms per volume.

The importance of the first transport mean free path has been discussed previously [70], by showing that spatial and angular distributions generated by different elastic scattering processes with equal λ_1 give similar results provided that the scattering processes are at least plural. A screened Rutherford cross section modified by means of a correction factor to obtain correct λ_1 computed by partial-wave analysis, can give a good approximation for plural and multiple scattering [71]. The first transport mean free path (λ_1) values have been calculated by Liljequist et al. [71, 72] for electrons and positrons in the kinetic energy range 100 eV - 20 MeV in 15 materials from $Z = 4$ to $Z = 82$.

The multiple scattering(MSC) model in Geant4 [56, 57] is a “condensed” simulation model, based on the theory of Lewis, and uses λ_1 values from Liljequist et al. [71, 72].

The MSC model in Penelope [73] is a “mixed” simulation model.

6.1.2 Bulk targets: Si, Be, plastic scintillator

6.1.2.1 Introduction

Backscattering of electrons from the surfaces of bulk materials has been studied at low energies largely in relation to materials science applications (e.g., Auger electron spectroscopy and scanning and transmission electron microscopy). For this reason, most detailed studies have been conducted for incident electron energies less than 40 keV [74, 75, 76]. At higher energies ($E >> 1$ MeV) sophisticated Monte Carlo calculations exist [57] that are constrained to reproduce data obtained for nuclear or particle physics applications. However in the intermediate regime (0.04 MeV $< E <$ 1 MeV) there is little data to constrain the simulations. This intermediate energy regime can be important for various beta spectroscopy applications, in particular neutron beta decay ($E_{max} =$ 0.782 MeV). Study of backscattering from plastic scintillator is especially important for the UCNA experiment as scintillator is used as the full energy detector, and no data exists for backscattering from plastic scintillator in this intermediate energy range.

Most of the data that exists in this energy region is based on measurements using electron beams and detecting the backscattering from bulk targets using total electrical currents in Faraday cups (for a recent review, see Ref. [77]). In particular, for carbon and aluminum targets, extensive measurements using this technique exist. We have made measurements for Be, Si and plastic scintillator targets using this technique, and have investigated the effects of secondary electron emission on these types of measurements. In addition, we have conducted measurements using ion-implanted silicon detectors to detect the energy and angle of backscattered electrons, extending the work of Refs. [74, 75, 76] to higher energies. In this way, we can evaluate the reliability of existing models to reproduce the dependence of the backscattering process on energy and emission angle of the backscattered electrons. We have carried out detailed measurements of the energy and angular distributions of backscattered electrons from light materials (Be, Si and plastic scintillator) for incident electron energies between 43.5 and 124 keV [78, 79].

6.1.2.2 Experiment overview

A schematic of the chamber and detector arrangement used to perform the backscattering measurements is shown in Fig. 6.1. The chamber contained a target and a silicon detector on separately rotatable feedthroughs. The chamber, target, and detector were each separately isolated from ground. The electric currents detected by the chamber and the target were integrated using two Ortec model 439 current digitizers.

The Be and Si targets [80] were multiple stopping lengths of Be and Si. Two different Be targets of nominal thicknesses 1.0 mm and 2.0 mm were used. Two different Si targets of thickness 1.0 mm were used. The Be and Si targets were 25 mm by 25 mm square, and were held at one corner

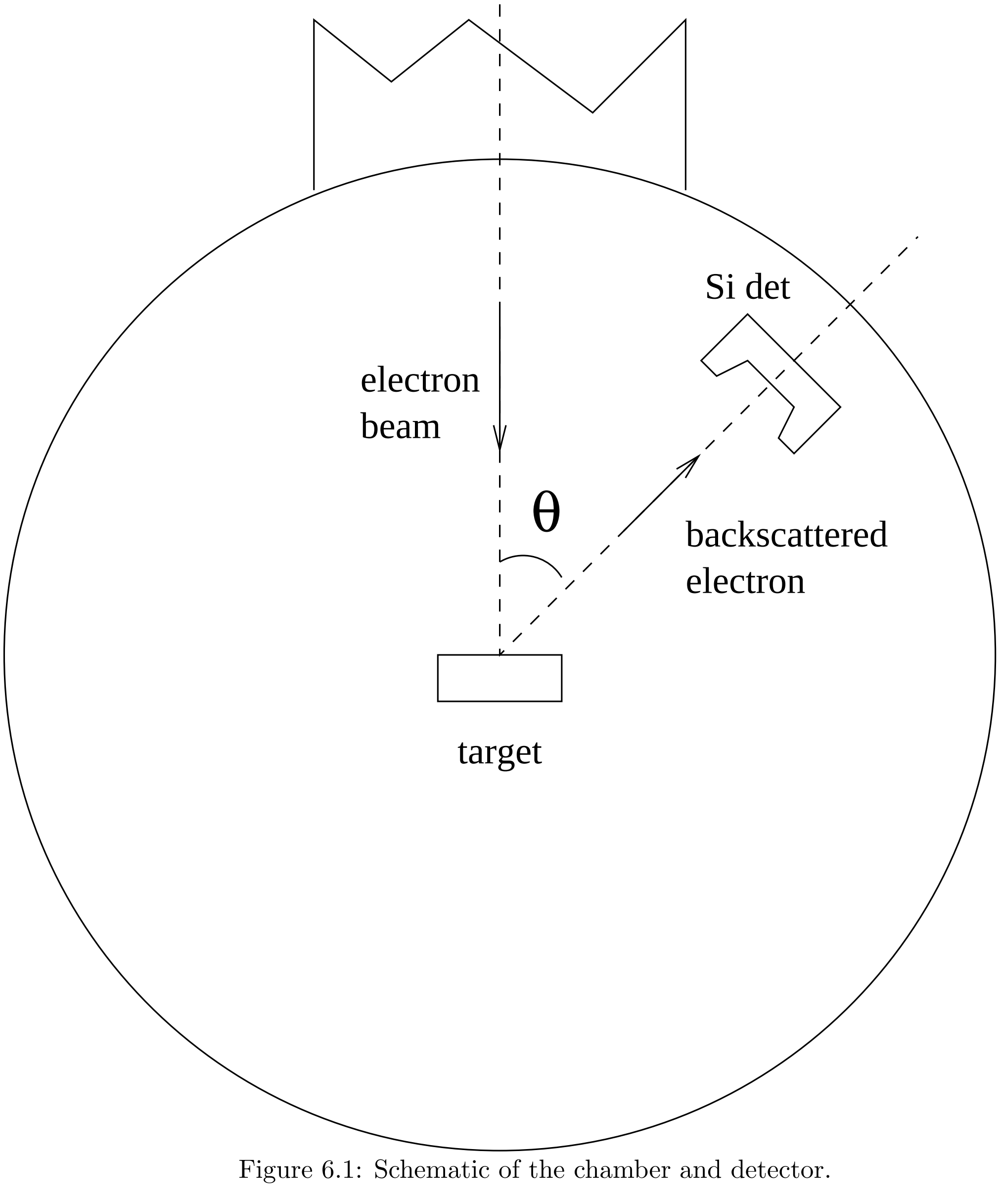

Figure 6.1: Schematic of the chamber and detector.

in a slotted rod by a set screw. The Be targets were nominally 99.0% pure, and had a metallic appearance and the polycrystalline Si target was nominally 99.999% pure.

Measuring backscattering from the plastic scintillator target is challenging, because it is not conductive, resulting in charging and inability to accurately sense the incident beam current. Hence special care was taken to make the scintillator targets. The plastic scintillator targets were obtained from Eljen Technology. [39]. The type of plastic scintillator used was EJ-204, same as the one used in the UCNA experiment. A sample of plastic scintillator was coated with a 50 nm thick layer of aluminum via evaporation. Targets of a suitable size and shape were then cut from this sample, with care taken to preserve the aluminized front face. The resulting targets were 1”×1” square, 3.5 mm thick, with a thinner tab of aluminized plastic projecting from the top for suspension from the slotted rod. The backscattering effect of the aluminum layer is negligible.

The energy and angular distribution of the backscattered electrons was measured using an Ortec ion-implanted silicon detector (Ortec model BU-13-25-300, 25 mm^2 nominal active area and 300 μm nominal depletion depth at 100 V bias). The detector was mounted on a rotatable arm which allowed it to be placed at an arbitrary angle with respect to the target. The target to detector distance was typically 8.5 cm. The detector linearity and resolution was calibrated by placing the detector in the electron beam at very low beam current ($\sim$ 100 Hz). The detector linearity was confirmed to the sub-kilovolt level for these experiments. The energy resolution of the silicon detector was found to be typically $\sigma = 2.5$ to 3.5 keV, and the resolution was independent of energy to less than 0.1 keV.

For fixed filament current, the current detected on the target was maximized in order to tune the beam. The beam tunes for each energy were stored on the computer that controlled the power supplies of the accelerator. In addition, tunes were checked using a scintillator target coated with graphite which produced a visible spot ($\sim$ 3 mm $\times$ 3 mm) indicative of the beam spot size when struck with sufficient current (typically 1 nA).

6.1.2.3 Backscattering measurements

Backscattering measurements were performed for normal beam incidence upon the target. Measurements were performed for incident electron energies of 43.5, 63.9, 83.8, 104, and 124 keV. For each energy, both silicon detector mode and current integration mode measurements were taken.

Silicon detector mode

In the silicon detector mode, silicon detector spectra were acquired for backscattered electron angles of 20 to 80 degrees in steps of 10 degrees. The backscattered angle θ was defined with respect to the normal of the target, as shown in Fig. 6.1.

When the beam was off, the detector rate was typically 100 Hz, due to low energy noise. The detector rate with beam on was typically 5 kHz, and was always kept below 20 kHz, to limit ADC pile-up to below 3% on average across the spectrum. The beam current for each target and detector angle was therefore different, due to the different levels of backscattering. For Si, the current was typically 40 pA, while for Be, it was 300 pA.

Fig. 6.2 shows normalized spectra taken using the silicon detector for a variety of detector angles θ for 124 keV electron beam energy and the Be target. The data are plotted as a function of the digitized pulse height (ADC channel), which is proportional to the energy E deposited in the silicon detector. The data are not corrected for the response of the silicon counter, which had a resolution of about 2.5 keV, and itself suffered from backscattering. Below about 20 keV, contributions from noise in the detector and electronics contributed to the count rate at the few percent level, and so

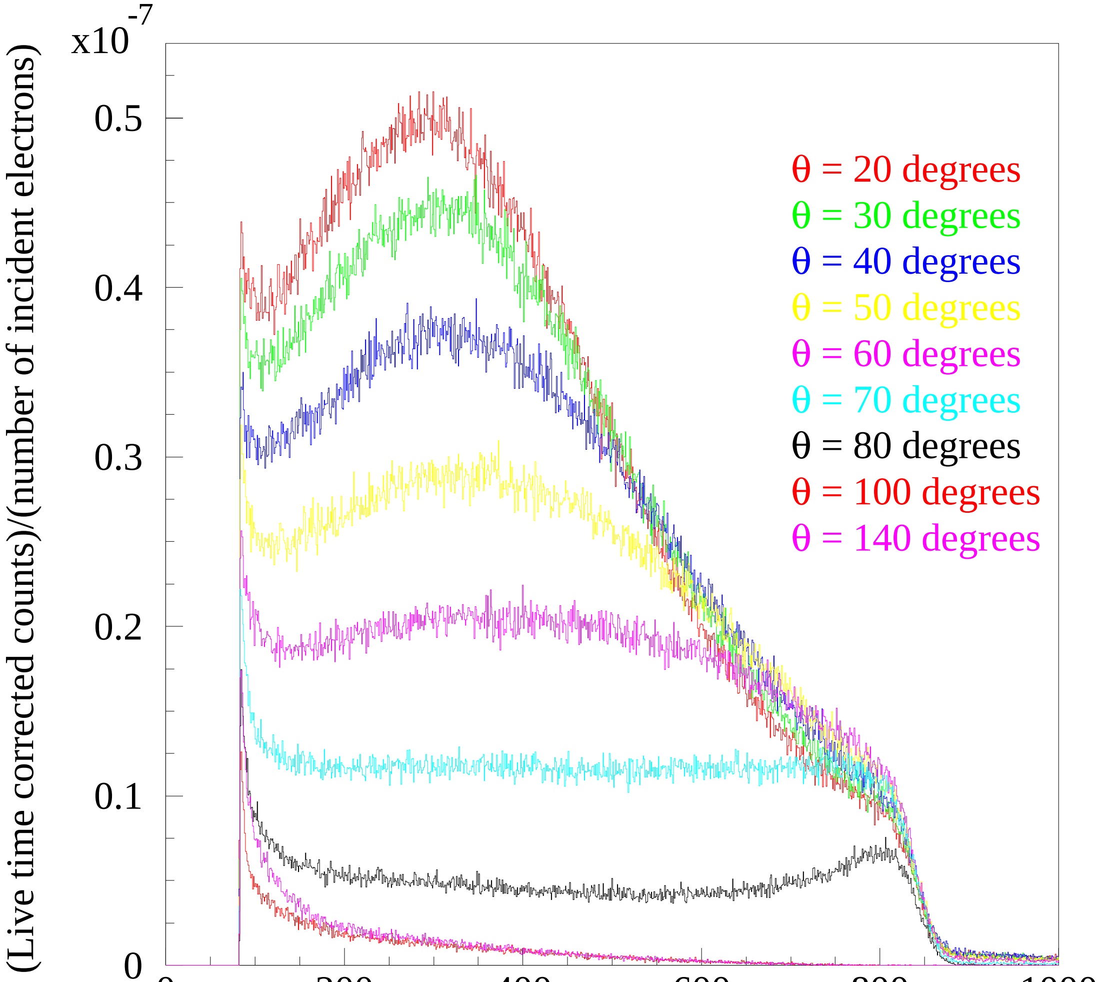

Figure 6.2: Silicon detector raw spectra for normal incidence backscattering from Be target at $E_{\mathrm{beam}} = 124$ keV.

no data is shown beneath that threshold.

A detector rate above electronic noise was also detected for angles $\theta > 90^\circ$, where the detector is shielded from any direct backscattering. It can be seen that the rates at 100° and 140° are significant, especially compared to the 80° measurements. The flux found at $\theta > 90^\circ$ was determined to be due to rescattering from the walls of the chamber, and was confirmed in Monte Carlo studies. In these studies, backscattering from the steel walls and lid of the chamber were included. The chamber floor, dominantly aluminum, had relatively little effect on the chamber background and was not included. The Monte Carlo calculations showed that electrons at $\theta > 90^\circ$ could be produced, and that the result was numerically about 50% larger than the observed chamber background. The disagreement is attributed to the use of a simplified geometry in the Monte Carlo, and uncalibrated treatment of backscattering from these sources.

Motivated by the simulation, experimental studies were carried out lining the chamber walls with stopping thicknesses of aluminized mylar (which has a much lower backscattering fractions). This was found to reduce the chamber background by roughly 50%, a figure in agreement with expectations based on the Monte Carlo.

Based on the Monte Carlo simulations, the 100° data is expected to represent most closely the chamber background for the 80° data, and to represent an upper bound on the chamber background for the other angles. So the 100° data was subtracted from the $\theta = 20^\circ - 80^\circ$ data to arrive at the background-subtracted spectrum. The systematic error in using this subtraction scheme is 3-5% for 124 keV beam energy, peaked at low energy deposition, and is smaller for lower beam energy (as more of the chamber background is moved into the unmeasured region dominated by detector noise).

From Monte Carlo studies and analytical estimations, it was also determined that contributions from X-rays were negligible in both flux (compared to electron backscattering) and in detection efficiency (for the 300 μm thick detector used). Therefore no corrections were made for X-rays.

Systematic uncertainties for silicon detector measurements

Table 6.1 summarizes the systematic uncertainties for the silicon detector measurements. Each effect in the table will now be described in more detail.

Measurements of the backscattered electron yield in the silicon detector were found to be reproducible at the 7% level. The detector active area was measured using an alpha source and various collimators, and found to be consistent with the geometry of the detector to about 4%. The beam spot size and detector size were also measured by scanning the beam across the detector. The detector size was again found to be in agreement with the directly measured value. At the same time, it was observed that no significantly different response for electrons could be seen for the detector as one varied the position of the beam on the detector surface. A simple silicon response function

Table 6.1: Summary of systematic uncertainties associated with silicon detector measurements. The total systematic uncertainty ranges from 11% to 15%, depending on angle, averaging 12%.

Effect	Uncertainty
reproducibility	7%
active area	4%
beam spot size	$5\% \times \sin\theta$
deadtime	3%
alignment	2%
current detection	3%
Total	12% average

including only normal-incidence backscattering was therefore used to convolute Monte Carlo predictions for comparison with the data (see section 6.1.2.5). The beam spot radius was found to be about 1.7 mm, and the beam was always well-centered on the target to this level, limiting a solid angle correction from finite spot size to less than $5\% \times \sin\theta$. Deadtime corrections varied between $< 10\%$ and 50%. However, ADC pile-up was kept below 3% and the deadtime corrections could be performed reliably at that level, using information from fast scalers counting the triggers.

The relative alignment of the beam, target, and detector in the plane of rotation of the detector was measured to the level of 0.5 degrees. This was confirmed by taking measurements of electron backscattering at both positive and negative θ. The residual systematic error due to alignment problems was estimated to be about 2%.

The silicon detector measurements were normalized to the total current detected by the chamber and target. The detection of current was calibrated using a precision picoampere source, and comparison among several well-calibrated picoammeters. The calibration agreed each time at the level 0.3 pA, giving a worst case contribution to the normalization uncertainty of 3%. Integration of low-energy secondary electrons was not a factor for this measurement of current, since the total charge on the chamber and target was collected.

For the plastic scintillator target, the possible effects of charging and incomplete current detection were monitored by observing scintillation light from the electron beam as it struck the scintillator target, on a camera mounted behind the target outside a view-port in the chamber (at $\theta = 180°$). Over the course of taking a complete angular range of data for a particular incident beam energy, the brightness of the scintillation light did not visibly change with time. Previous tests with uncoated scintillator, or scintillator coated poorly with graphite, had shown that the emanation of scintillation light from the target would eventually cease, indicating that the electron beam had been steered away from the central spot on the target. Also discharges would be seen due to arcing from the face of the scintillator to the conducting target rod. No such effects have been seen with the Al-coated scintillator target. To also search for charging, the electron beam could be switched off and on rapidly by inserting a Faraday cup upstream of the chamber. Upon restoration of the beam, the current sensed by the target was found to agree with the value before intercepting the beam with the Faraday cup.

The total normalization systematic uncertainty after background subtraction was therefore 12%, dominated by reproducibility and detector solid angle uncertainties.

Current integration mode

For each energy, current integration mode measurements were also performed. By separately sensing the currents on the target (I_{target}) and the chamber (I_{chamber}), the total normal-incidence backscattered fraction (NIBF) η was determined via:

$$\eta = \frac{I_{\text{target}}}{I_{\text{target}} + I_{\text{chamber}}}. \tag{6.1}$$

However, low energy secondary electrons may be emitted from the surfaces of materials after higher energy electrons strike the surface. In previous experiments, secondary electrons were typically defined to have $E < 50$ eV. If the fraction of secondary electrons produced per high-energy interaction is large, the sensed currents will give an erroneous measure of the high-energy backscattered fraction.

To suppress and quantify the effects of secondary electrons, a cylindrical "cage" of wires (referred to as the grid) was inserted into the setup to provide a potential wall between the chamber and the target. This grid was made of 50 μm tungsten wire, wrapped on a cylindrical copper frame of radius 6 cm and height 8 cm. The grid had 22 vertical wires evenly spaced on the sides. The wires met at the bottom, but had an opening at the top so that the target rod (which holds the target) could be inserted. The grid, target, and chamber could each be biased at different voltages up to a difference of 200 V with leakage currents between elements kept to below 1 pA.

Systematic uncertainties for current integration measurements

Table 6.2 summarizes the systematic uncertainties encountered for the current integration measurements for the Be and Si targets. Each of these uncertainties will now be described in more detail.

Table 6.2: Summary of systematic uncertainties associated with current integration measurements.

Effect	Uncertainty
target rod correction	7%
grid secondaries	1%
reproducibility	5%
current dependence	3%
Total	9%

It was found that biasing the grid at roughly -50 V relative to the chamber and target caused secondaries created on the chamber and target to be recollected by the chamber and target. When the target was biased to +50 V, and the chamber held at ground, the effect of changing the grid voltage from zero to -50 V resulted in changes of 10-30%, depending on the target material and the beam energy. This agreed well with estimates of the effect based on the Penelope Monte Carlo code, and based on measurements of secondary electron emission summarized in Refs. [81, 82, 83].

Due to a small piece of the conducting target rod (held at the same potential as the chamber) penetrating into the top of the grid, there was a residual correction still to be made for secondaries. In the data, this showed up as a residual dependence of η on the relative target/chamber voltage, even when the grid was set to very large voltages. It was found that a correction could be made using the solid angle subtended by that piece of the target rod, and the value of η determined when the grid was not used. This correction amounted to a 7% contribution to the systematic uncertainty in the determination of η.

Secondaries due to high-energy electrons striking the grid could be accounted for at the 1% level. Measurements of η under widely varying beam conditions showed that it was reproducible at the 5% level.

The current dependence of η was also studied from pA to μA in incident beam current, and found to vary at the 3% level. This indicated that electrostatic charging of various non-conducting components in the setup contributed at a small level.

The total fractional systematic uncertainty in η determined from these current-mode measurements was therefore 9% for Be and Si targets.

The plastic scintillator measurements were performed later, with a updated design of the target holding. The target rod correction was reduced to 3% by reducing the solid angle subtended by the relevent portion of the target rod. Other contributions to the systematic uncertainty remain the same as in the Be and Si target measurements. Thus the total systematic uncertainty in current-mode measurements for scintillator target was 7%.

A potential systematic effect with the scintillator target, was from deterioration of the scintillator target by the electron beam. Over the course of an hour, running at beam currents of tens of nA, η was observed to steadily increase with time, plateauing at a value typically 15% larger than its initial value. The transition to larger η was found to occur more rapidly with high beam currents and higher beam energies. The glow of the beam spot on the target was also monitored on the video camera and found to decrease in brightness in a correlated way. The brightness was found to not recover after leaving the scintillator in vacuum over several days, ruling out charging/discharging of the scintillator. Upon removal of an affected target from the vacuum chamber, a small brownish spot within the scintillator could be observed, with no obvious deterioration of the mirror-like aluminized front face. We believe the discoloration, reduction in scintillation light, and increase in η are symptoms of a chemical change in the scintillator, possibly resulting in the liberation of hydrogen, thus increasing the carbon content and hence η. To control this potential systematic, new scintillator target were used and were exposed to electron beams with current less than 1 nA, and for the minimum time possible for currents to be sensed accurately using picoammeters. This resulted in a contribution to the systematic uncertainty of 1%.

6.1.2.4 Results

Silicon Detector Mode

The normalized, background-subtracted spectra accumulated for various detector angles for 124 keV electrons normally incident on Si, Be, and scintillator bulk targets are shown in Fig. 6.3.

The Monte Carlo curves will be described in Section 6.1.2.5. The data are plotted as a function of the dimensionless energy $q = E/E_{\text{beam}}$, where E is the energy detected by the silicon detector and E_{beam} is the energy of the incident electrons, in this case 124 keV. On the vertical axis, $\frac{1}{N_e}\frac{dN}{dqd\Omega}$, the number of counts per incident electron, per unit q, per unit solid angle is plotted. In the absence of the effects of detector response (resolution and backscattering), this would be the normal-incidence backscattered fraction per unit q, per unit solid angle.

In Fig. 6.3(a), for Si, for small backscattered angles ($\theta = 20° - 30°$), a peak is found near $q = 0.65$, and a shoulder found near $q = 0.95$. As the backscattered angle increases, the peak at $q = 0.65$ tends to disappear and shift slightly to higher q, while the shoulder at $q = 0.95$ tends to become more pronounced as events at lower q disappear.

The same trends can be seen in the spectra for a Be target, shown in Fig. 6.3(b). However, in this case, the low-energy peak appears closer to $q = 0.35$. This can be explained by the Be having smaller Rutherford scattering cross section. Electrons therefore penetrate more deeply into the material before scattering.

for a plastic scintillator target, still the same trends is seen in Fig. 6.3(c), with the low-energy peak appear near $q = 0.4$, lying in between the Si and Be cases while being closer to the Be case.

The Si results compare well qualitatively with the results of Refs. [74, 75, 76], which were acquired at lower energies on Si and Al targets. It is difficult to compare directly with these measurements. For Ref. [75, 76], no data is published above 35 keV and more data are displayed for oblique incidence. Ref. [74], while providing data at 40 keV, gives no absolute normalization.

The dependence on beam energy was also investigated. Fig. 6.4 shows the dependence of the backscattered fraction on both the beam energy and the energy of the backscattered electron, integrated over all possible backscattered angles. The integration over angle was performed using a finite sum with 10° bins centered on each measured angle, and the appropriate solid angle weighting. A small correction due to the unmeasured regions at small and large angles was included. The systematic uncertainty in approximating the integral by the sum was typically 4%, from comparison

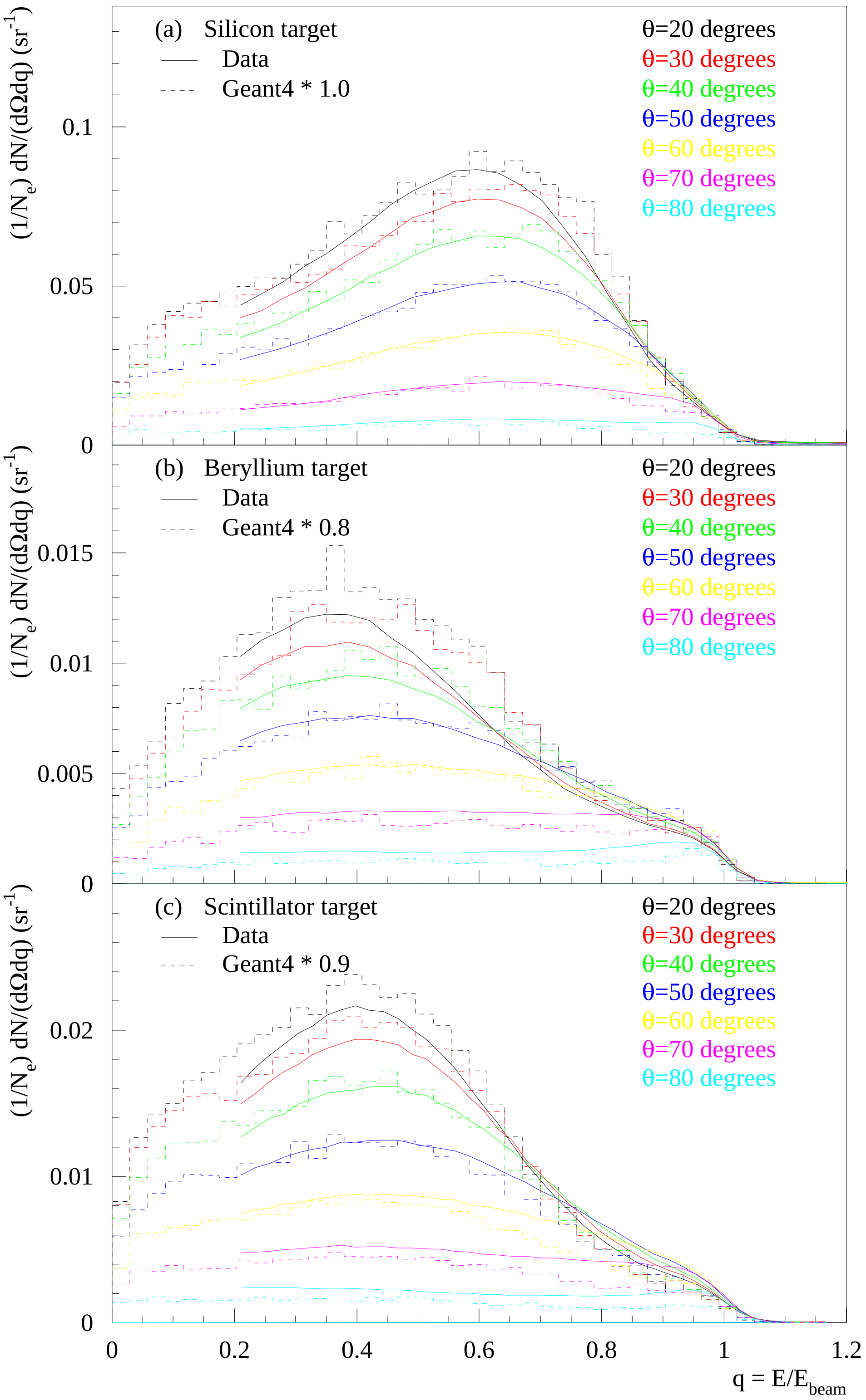

Figure 6.3: Normal incidence backscattering from (a) Si, (b) Be, and (c) scintillator targets at $E_{\text{beam}} = 124$ keV. Curves represent rebinned data taken with silicon detector. Histogram is Monte Carlo simulation based on Geant4. Systematic uncertainty in the normalization of the data is estimated to be 12% on average, ranging from 11% at small angles to 15% at large angles. For Be, a scale factor of 0.8 is applied to the Monte Carlo simulation, and for scintillator, a scale factor of 0.9 is applied, while for Si, no Monte Carlo scale factor is applied.

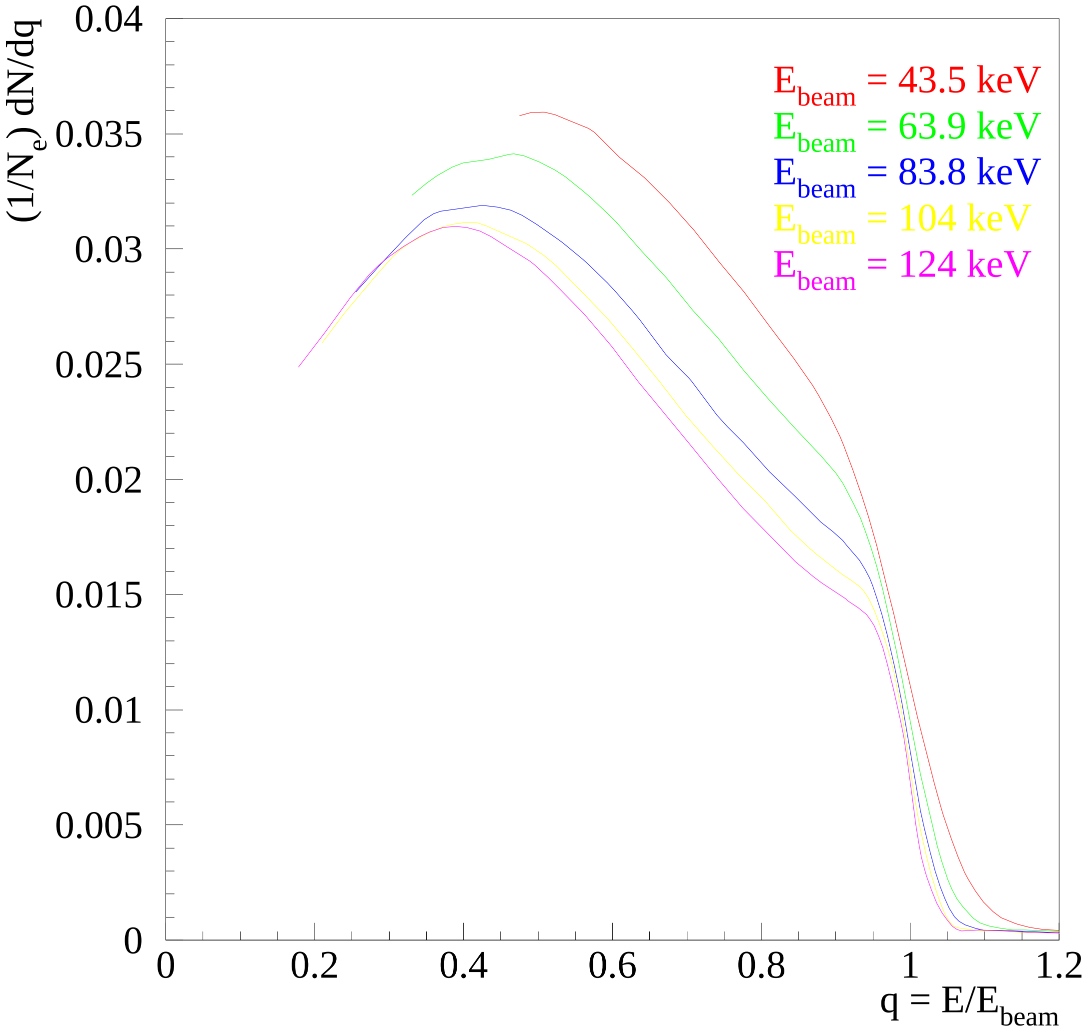

Figure 6.4: Normal incidence backscattering from Be target at each beam energy, integrated over angles. Systematic normalization uncertainty is 13% in each case.

with analytical forms. Angular bin centering corrections were found to be negligible, due to the smoothness of the angular behavior. The overall systematic uncertainty was consequently increased to 13%.

As seen in Fig. 6.4, when plotted in terms of the dimensionless variable q, the curves nearly overlap. The same qualitative behavior can be seen as a function of beam energy for individual backscattered angles. The data are therefore observed to follow a near-scaling behavior. The overall normalization follows the energy dependence of the total normal-incidence backscattered fraction.

The angular dependence of the backscattering fraction can be determined by integrating over energy the data of Fig. 6.3. The result is shown in Fig. 6.5.

A linear fit based on the first 20 keV of data above the analysis cut was used to extrapolate to 50 eV (the defined threshold for secondary electrons), so that these integrals and subsequent integrals could be compared with the current integration measurements. In order to estimate the reliability of the fit, an additional systematic uncertainty was assigned to the extrapolation, based on comparison of this fit to a fit constrained to pass through zero at zero energy. For 124 keV beam energy, this extra systematic uncertainty was of order a few percent.

In order to better estimate the systematic uncertainty in this extrapolation, simulations were performed using Geant4 and Penelope in the unmeasured region 50 eV to 20 keV. In the Geant4 simulation, the backscattered fraction was found to tend toward zero at small backscattered electron energy, in fair agreement with the linear extrapolation method. In the Penelope simulation, the backscattered fraction was found to rise steadily as the threshold of the simulation was reduced. In the range 100 eV to 10 keV, Penelope gave about 10% extra contribution to the integral compared to linear extrapolation, for Be and scintillator, and an extra 4% for Si. To average between the extrapolations implied by Geant4 and Penelope, an additional 5% contribution was added to the Be and scintillator data, and an additional 2% contribution was added to the Si data. The additional uncertainty in each case was taken to be the size of the correction.

The data were integrated over angle, using the same method described in relation to Fig. 6.4, to determine the total normal-incidence backscattered fraction. The results of this integration are shown in Fig. 6.6, and are compared with current integration measurements (described in section 6.1.2.4), Monte Carlo simulations (described in Section 6.1.2.5), and previous current integration measurements due to Drescher *et al.* [84] and Neubert *et al.* [85]. In Fig. 6.6, the total systematic uncertainty, including extrapolation to 50 V and extrapolation over unmeasured angles, is plotted.

Current Integration Mode

The results for η based on our current integration measurements are also shown in Fig. 6.6.

The silicon detector measurements are found to be systematically higher than the current-mode measurements; however, the two methods of are found to agree within the systematic uncertainties.

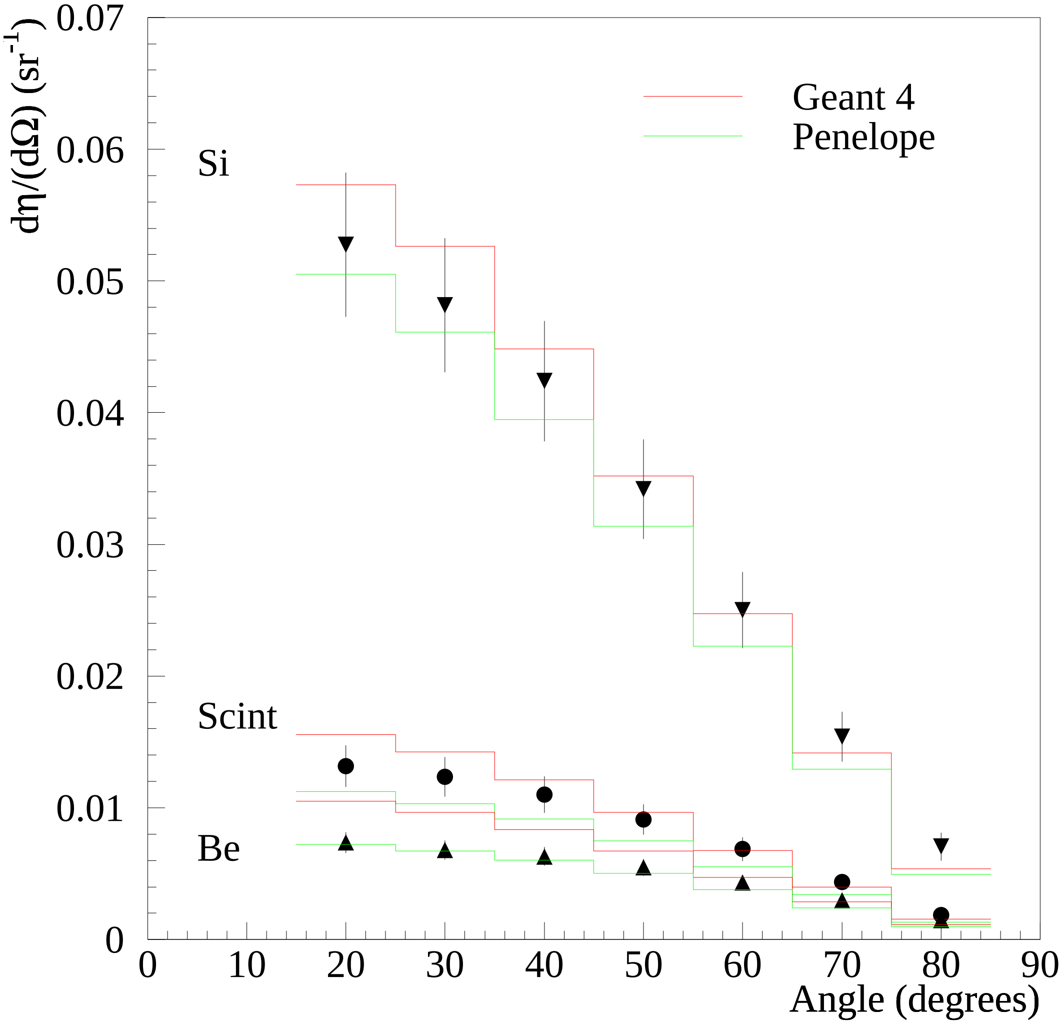

Figure 6.5: Angular distribution $d\eta/d\Omega$ for Be (triangles), scintillator (circles), and Si (inverted triangles) targets at $E_{\mathrm{beam}} = 124$ keV. Black points with error bars indicate data with total normalization systematic uncertainties shown. Red histogram indicates the results of the Geant4-based Monte Carlo simulation. Green histogram indicates the results of the Penelope-based Monte Carlo simulation. No Monte Carlo scale factors are included.

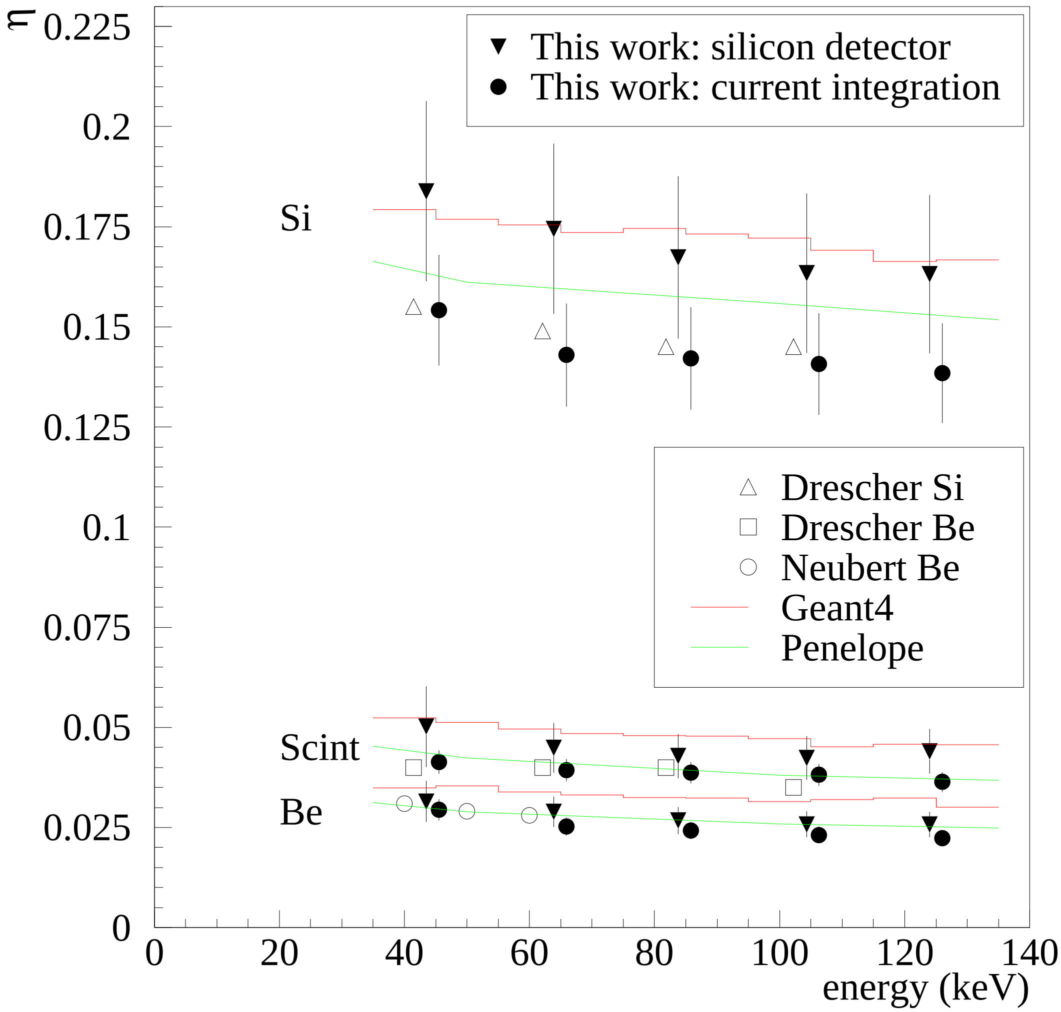

Figure 6.6: Normal incidence backscattering from Be, scintillator and Si targets as a function of incident beam energy. Integrated silicon detector measurements are shown by the inverted filled triangles. Current integration measurements are shown by filled circles. Total systematic uncertainties are shown and the current integration measurements are displaced by 2 keV so that the error bars do not overlap. Previous current integration measurements due to Drescher *et al.* and Neubert *et al.* are displayed. The histograms show the results of the Geant4 and Penelope Monte Carlo simulations with no Monte Carlo scale factor.

In the case of the current integration method, this systematic uncertainty is dominated by residual correction for secondary electron collection due to the penetration through the grid of the target rod. In the case of the silicon detector measurements, it is dominated by reproducibility of the measurements under varying conditions, and by uncertainties in alignment and solid angle effects.

The data are also compared with previous data on Be and Si targets due to Drescher et al. [84] and with data on Be due to Neubert et al. [85]. Both groups used current integration techniques to arrive at their results. Neubert et al. [85] in particular used a second target apparatus to study the effects of secondary electrons, as opposed to the grid used in this work. Only the subsets of their data that overlap the region 43.5 to 124 keV are plotted. The Drescher data on Be are systematically higher than the Neubert data. However, due to the lack of additional data on this element, it is impossible to say which is more accurate. Our data tend to agree with the Neubert data, as do the data of Massoumi et al. [75, 76] taken below 40 keV.

Our data on Si is in good agreement with those of Drescher, and tend to suggest that there could be some systematic effect in either the current integration or silicon detector data for that element. Given the current level of the systematic uncertainties, it is difficult to make a firm statement.

Our data on plastic scintillator to our knowledge are the first in this energy range. As expected, the results lie below the previous measurements on carbon (not shown), and above our data and the Neubert data on Be.

6.1.2.5 Comparison with Monte Carlo

Monte Carlo simulations were conducted using the Geant4 Monte Carlo [57] and the Penelope Monte Carlo [86].

The version of Geant4 used was 4.4.0. In order to achieve a reasonable description of backscattering, it was found that three parameters had to be changed from their default values: the maximum step size, the threshold to create secondaries, and a parameter originally introduced into Geant4 to tune low-energy EM processes. For all our simulations, the maximum step size was set to the range of a 1 keV electron; the threshold to create secondaries was set to 1 μm; and the tuning parameter was set to zero. The step size and threshold parameters were chosen by reducing them until the integral backscattered fraction was relatively stable under variation of those parameters, and to be as small as possible for reasonable running time. The threshold parameter additionally was checked to give good results at low energy for thin targets. The tuning parameter had to be changed to zero, as it had been found to be erroneously set to 1.5 in this version of Geant4. Examples of how to make these modifications were supplied by the Geant4 electromagnetic physics and low-energy electromagnetic physics groups [87].

The version of Penelope used was 2002b. Penelope was studied in detail under the variation of several simulation parameters and was found to be stable. The simulation parameters were therefore chosen to optimize simulation speed consistent with a full detailed simulation. For the comparison with our silicon detector data, the most suitable simulation parameters were found to be: $E_{abs} =$ 10 keV, $W_{cc} = W_{cr} =$ 5 keV, DSMAX = 0.005 cm, and $C_1 = C_2 = 0.05$ [88]. These parameters control energy cut-offs, the maximum step size, and the description of elastic and inelastic scattering in the medium. Particles identified as secondaries by Penelope were included. Secondaries were also studied in separate simulations related to our current-integration measurements, as mentioned earlier.

In both Monte Carlo models, backscattering is defined as any electron which exits the surface of the target. The Monte Carlo simulations included silicon detector response in a simple model including normal-incidence backscattering from the front face. This was validated by the fact that the detector response to mono-energetic electrons did not vary with beam position on the detector face, as discussed in Section 6.1.2.3. Energy smearing based on a 2.5 keV energy-independent energy resolution of the silicon detector was also included. Chamber background effects were studied in separate Penelope-based simulations, as described earlier.

The main difference between Penelope and Geant4 relevant to backscattering is in the treatment of scattering from nuclei. Penelope treats these as Rutherford scattering events exactly using a relativistic screened Rutherford scattering cross section. Multiple electron-atom scattering events, with energy loss (dominated by electron-electron interactions in the target) are found to dominate backscattering at these energies in this model, for thick targets. Geant4, on the other hand, has no exact treatment of Rutherford scattering, relying on sampling from a multiple scattering distribution.

Fig. 6.3 compares the Geant4-based Monte Carlo with our silicon detector measurements at 124 keV. It can be seen that Geant4 somewhat overestimates the Be and scintillator data, while having relatively good agreement with the Si data. The Be data is globally overestimated by roughly 20%, hence a scale factor of 0.8 was applied to the Monte Carlo for this comparison so that the differences between the distributions can be more easily seen. The scintillator data is overestimated by about 10% hence a overall scale factor of 0.9 was applied. In all cases, it is also apparent that the peak near $q = 0.95$ is systematically underestimated. However the positions of the low-energy and elastic peaks are rather well-described by the Monte Carlo. In the case of a Si target, the Geant4 low-energy peak is at a slightly higher q than the data, while for Be and scintillator this peak appears at slightly lower q relative to the data.

Fig. 6.7 compares Penelope-based Monte Carlo with our measurements using the silicon detector. A scale factor of 1.1 is applied to the Penelope simulation in the case of Si. No scaling is applied to the Be simulation. A scale factor of 1.2 is applied to the scintillator simulation. The Penelope simulation in general somewhat underestimates the Be measurements by 5%, underestimates the Si measurements by roughly 10%, and underestimates the scintillator measurements by about 20%. When the Monte Carlo is rescaled, it is apparent that trends in both energy and angle are well

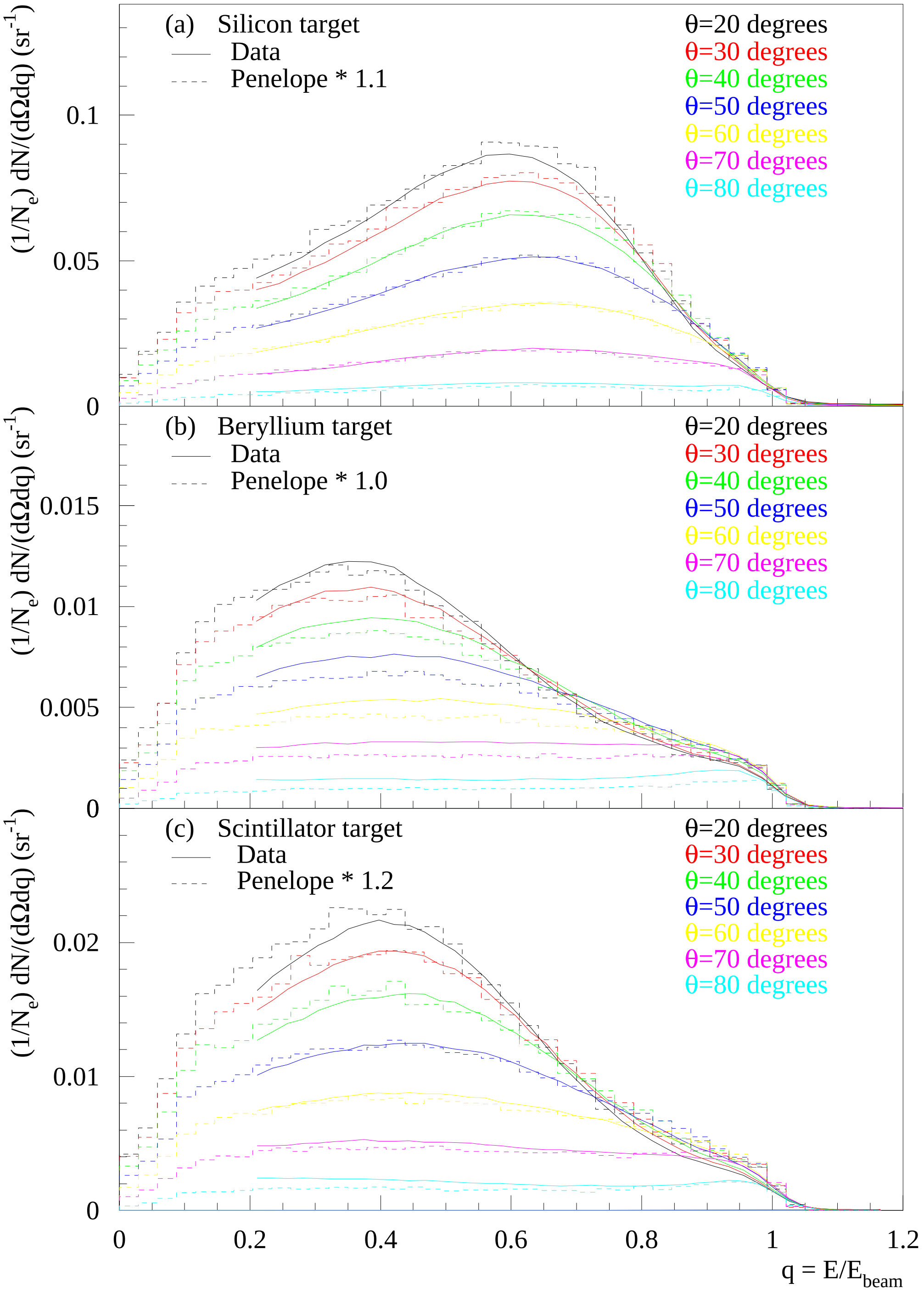

Figure 6.7: Normal incidence backscattering from (a) Si, (b) Be, and (c) scintillator targets at $E_{\text{beam}} = 124$ keV. Curves represent rebinned data taken with silicon detector. Histogram is Monte Carlo simulation based on Penelope. Systematic uncertainty in the normalization of the data is estimated to be 12%. For Si, a scale factor of 1.1 is globally applied to the Penelope simulation, and for scintillator, a scale factor of 1.2 is applied, while for Be no scale factor is applied.

represented by Penelope.

Fig. 6.5 shows the Geant4 and Penelope simulations compared with data for the energy-integrated angular distributions ($d\eta/d\Omega$). No Monte Carlo scale factors are applied for this comparison. The same discrepancies in overall magnitude of backscattering can be seen. As noted previously, the Penelope simulation tends to better describe the angular distribution (aside from the overall scale factor). The Geant4 distributions are somewhat narrower compared to the data and Penelope. Additionally, the Geant4 simulation gives systematically larger backscattering from each material than does the Penelope simulation.

Fig. 6.6 compares the integrated η results for different beam energies with Geant4 and Penelope simulations. The same discrepancies in normalization are again observed. Both Penelope and Geant4 adequately describe the reduction of η as the beam energy increases.

Comparisons of other Monte Carlo models to Geant4, Penelope, and the existing backscattering data were also carried out and were reported elsewhere [88].

6.1.2.6 Conclusion

A detailed data set for normal incidence backscattering from Be, plastic scintillator, and Si bulk targets has been acquired for incident electron energies from 43.5 to 124 keV. Two methods of determining the total normal-incidence backscattered fraction were compared and found to agree within systematic uncertainties. The data agree qualitatively with previous measurements of the double differential distributions of backscatter done at lower energy. They also agree quantitatively with previous measurements using current integration techniques. The data agree well with models implemented in the Geant4 and Penelope Monte Carlo codes. In terms of overall normalization, Geant4 is found to give a good description of the data. Penelope is found to give good agreement in terms of both overall normalization and relative distributions of backscattered electrons in angle and energy. The level of agreement for both simulations is good considering the normalization systematic uncertainties for the present measurements.

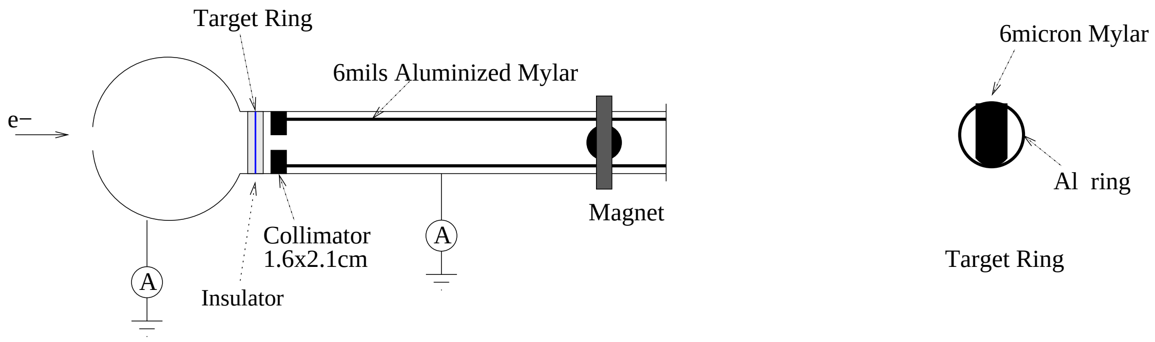

Figure 6.8: Schematic of the setup for the thin mylar NIBF study, with details of the target ring shown on the right.

6.1.3 Thin target: Mylar film

As is discussed in Chapter 2 on MWPC, the MWPC windows are made of 6 μm thick of Mylar film. Backscattering on thin Mylar film in the energy range of neutron decay has never been carried out before, and it is an important systematic effect in the UCNA experiment as it induces missed backscattering in the asymmetry measurement.

We made measurements of 120 keV electron backscattering on 6 μm mylar with current integration method for NIBF and silicon detector method for angular and energy distributions of the backscattered electron. Comparisons with GEANT4 simulation are made based on these measurements [89].

Energy loss in thin Mylar film is also an important systematic effect in the UCNA experiment, besides the fact that energy loss is one of the important processes in electron backscattering. GEANT4 simulations will be utilized to study the systematic effect on the asymmetry measurement, associated with energy loss in detector dead regions such as MWPC windows (Mylar film). Therefore, energy losses in 6 μm Mylar film for incident electron energies from 40 to 120 keV are measured, to constrain the GEANT4 physics modeling of energy loss.

6.1.3.1 NIBF study

The setup to measure the thin mylar NIBF is shown in Fig. 6.8. The chamber is the same chamber for bulk targets measurement. The beam dump is an 8 inch diameter, 4-foot long stainless steel vacuum pipe. The chamber and the beam dump are insulated from each other and from the ground, so that both currents can be measured by current integrators separately. The target ring, which is a piece of 6 μm mylar glued on an aluminum ring, is put in the insulator between the chamber and beam dump. From the measurement of chamber current and beam dump current, we can extract the NIBF. The beam dump is lined inside with 6 mil Aluminized Mylar to reduce the background effect associated with the transmitted electrons scattering from the wall of the beam dump(note that backscattering from mylar is nearly an order of magnitude smaller than from steel). A steering magnet is put near the end of the beam dump, that can deflect the transmitted electrons, to prevent the transmitted electrons from directly hitting the end of the beam dump, otherwise, a fraction of the electrons would backscatter from the end of the beam dump and enter into the chamber, thus inducing a false target backscattering signal. A $1.6 \times 2.1cm$ collimator is placed right after the insulator, to reduce transmitted electrons scattering back into the chamber.

Before we put in the target ring, we studied the effectiveness of the beam dump in terms of background NIBF. Since some of the electrons dumped into the beam dump would scatter back into the chamber, the background NIBF will not be zero in fact. The background NIBF is defined as the chamber current over the sum of chamber and beam dump currents. The results are shown in Table. 6.3. The results were measured at various beam currents. The error due to the chamber leakage current is of the order of 5 % to 10 %.

Table 6.3: Background for NIBF study at 120keV e- energy

magnet current(A)	magnetic field(G)	chamber/(chamber+dump)
off	0	3.3×10^{-4}
1.0	80	3.3×10^{-4}
off(and BPM off)	0	2.5×10^{-4}

Since the magnet did not have much effect on the background, it was turned off in the following NIBF studies, as was the BPM. Then the target ring was put in, and NIBFs were measured with various voltage biases on the target. The suppress the effects of secondary electrons (low energy secondary electrons may be emitted from the surfaces of the Mylar target after higher energy electrons strike the surface), positive voltage was applied on the target. For comparison, NIBFs were also measured under other 2 conditions: target grounded (no bias) and negative bias applied on the target. The results are summed in Table. 6.4. The values measured at +300V are with different beam currents, ranging from 12 to 250 nA. Leakage current corrections are below 10% and decay away with time, thus they are not included in Table. 6.4. Note that the results in Table. 6.4 are without background subtraction. Since the beam is angularly spread after passing through the target(as seen

Table 6.4: NIBF for 6 micron Mylar at 120keV e- energy, without background subtraction

Bias on target	chamber/(chamber+dump)
grounded	1.5×10^{-2}
+300V	0.94×10^{-2}
+300V	1.0×10^{-2}
+300V	1.1×10^{-2}
+300V	1.3×10^{-2}
-300V	4.6×10^{-2}

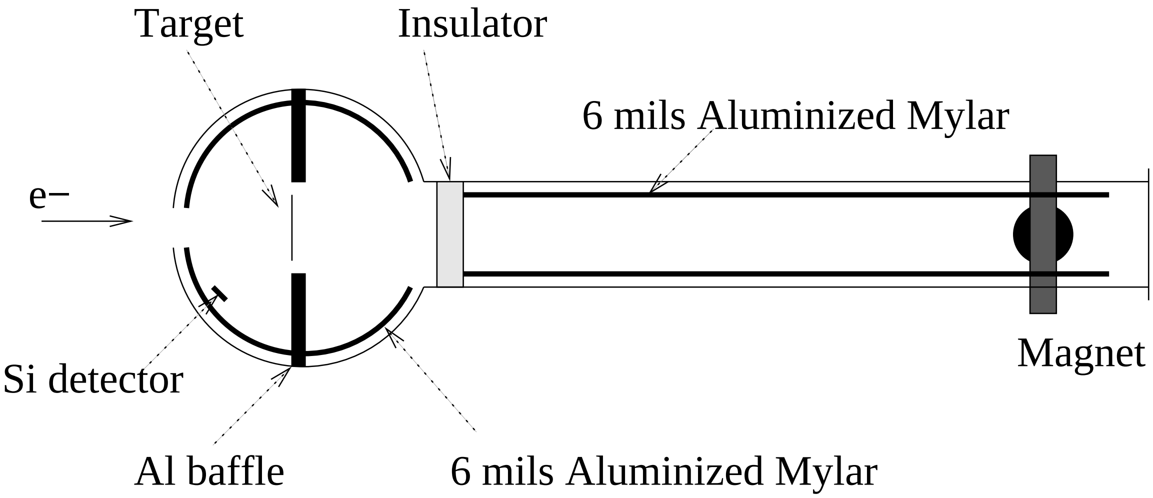

Figure 6.9: Schematic of the setup for measuring energy/angle distributions for thin mylar film.

in fig. 6.14), the background is not the same as in Table. 6.3, which is measured without target, thus there is no beam spread. Without background subtraction, the NIBF is $(1.1 \pm 0.2) \times 10^{-2}$.

6.1.3.2 Energy and angle distributions

The setup to measure energy/angle distributions is shown in Fig. 6.9.

In this mode, the target ring was taken out, and 6 μm mylar target was glued on an aluminum frame, which was attached to the target rod, similar to bulk targets backscattering study. An aluminum baffle was put in the chamber to reduce transmitted electrons scattering to the silicon detector. The silicon detector was put in the chamber to measure electrons at various angles. 6 mil Aluminized Mylar lined the chamber to reduce chamber background.

With target out, the detector is put at 180 degrees to be calibrated with 40, 60, 80, 100, and 120 keV beam. The calibration is shown in fig. 6.10.

As an example of the response of the silicon detector, the detector response for 120 keV electron is shown in Fig. 6.11 with both linear and log scale. A Gaussian fit of the peak gives an energy resolution of 3keV.

With target in, the same measurements were done with detector at 180 degrees. Typical spectra difference between target-in and target-out is shown in fig. 6.12 with beam energy at 40 keV.

From the difference between the centroids, energy loss in 6 μm mylar is extracted, as is shown in Table 6.5. The data is plotted in Fig. 6.13. Note that energy loss from ESTAR is the mean energy loss obtained from the NIST ESTAR data base [90], while energy loss from this measurement is the Most Probable (MP) energy loss. Due to the Landau-like distribution of the energy loss straggling, the most probable energy loss is always smaller than the mean energy loss. GEANT4.4.0 simulations of both mean and most probable energy losses are given in Table. 6.5 and Fig. 6.13. The comparisons

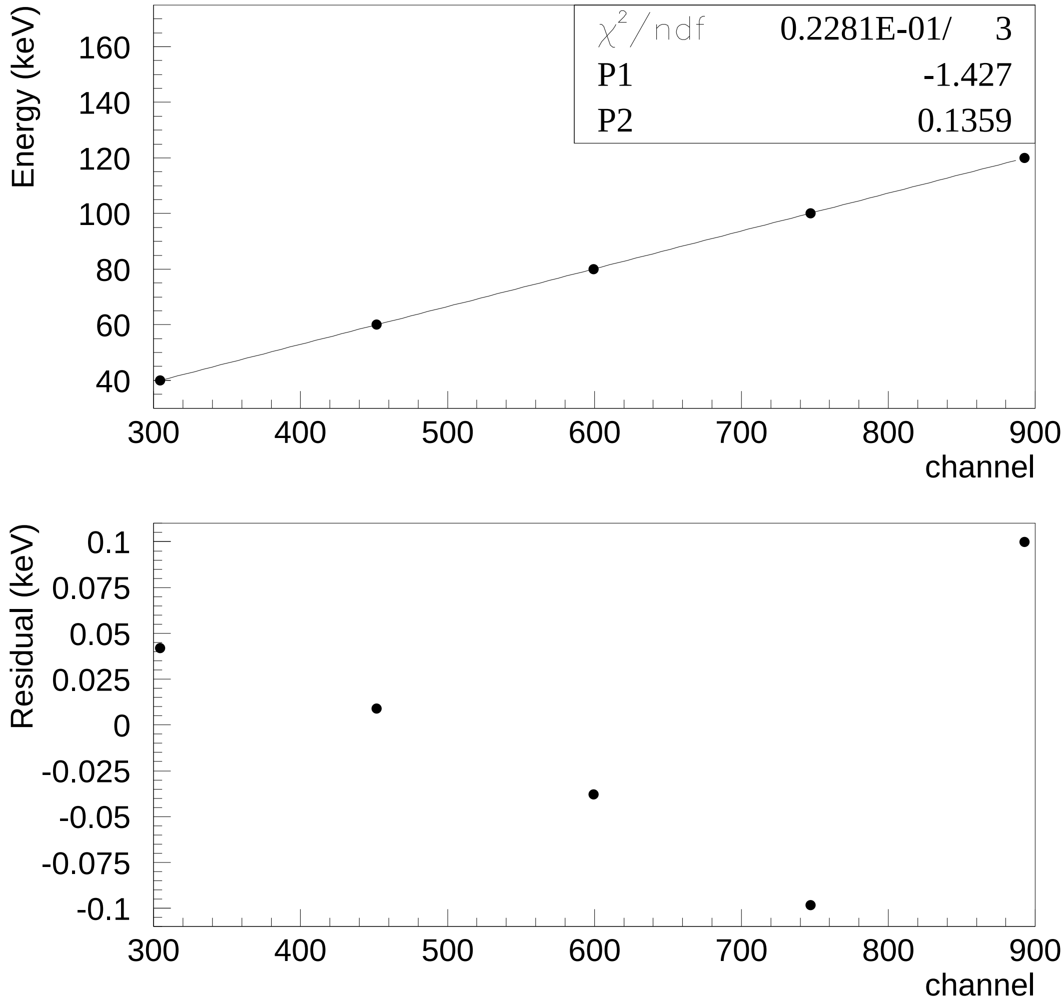

Figure 6.10: Detector calibration (upper plot) and residuals (lower plot).

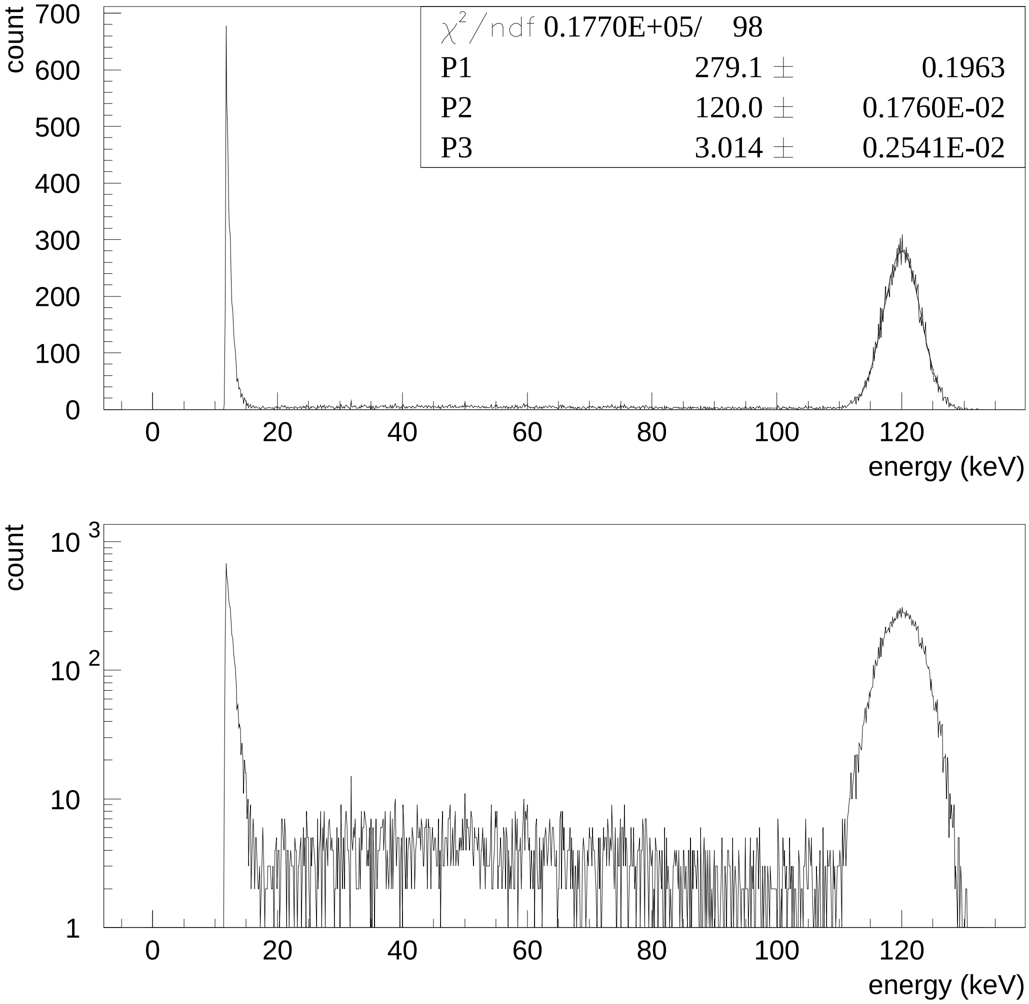

Figure 6.11: Detector response at 120keV. Linear scale (upper), log scale (lower).

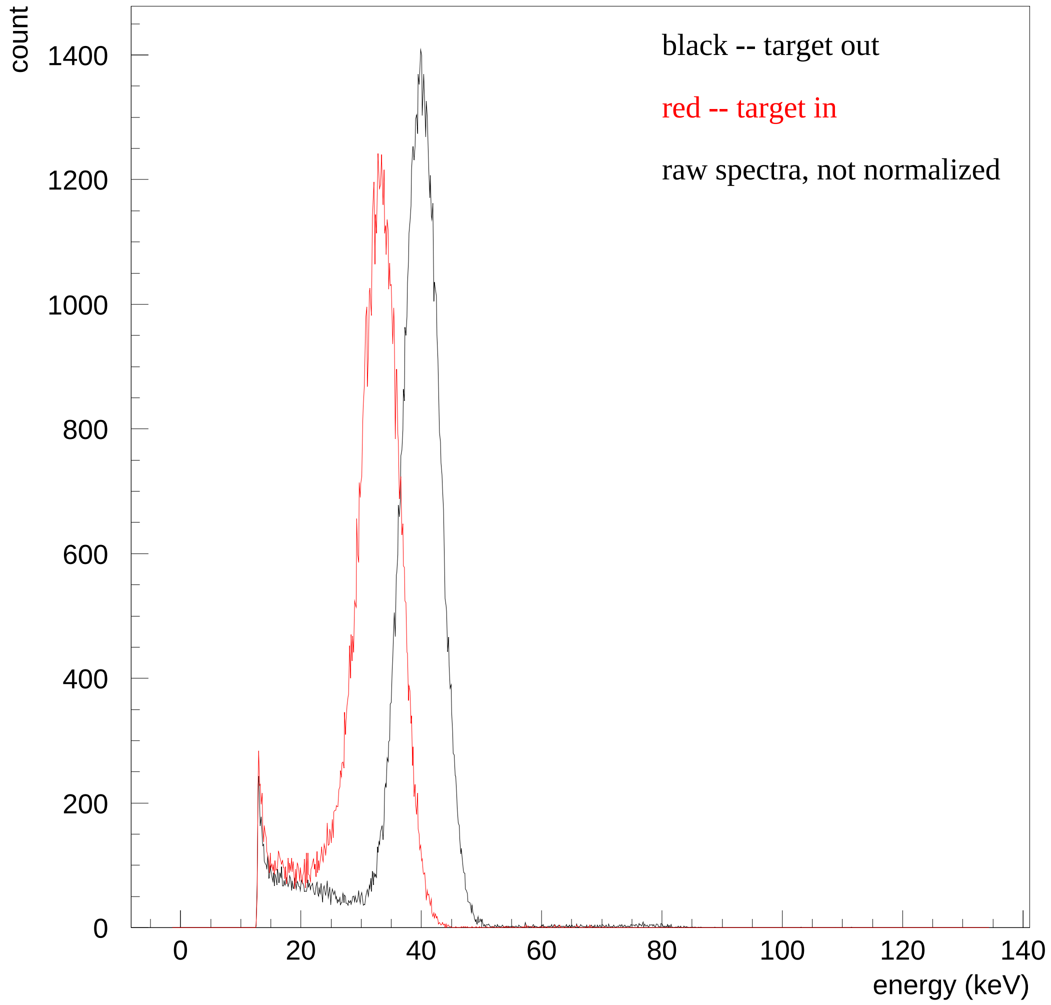

Figure 6.12: Beam into detector at 180 degrees, with target out (black) and target in (red), with beam energy 40 keV.

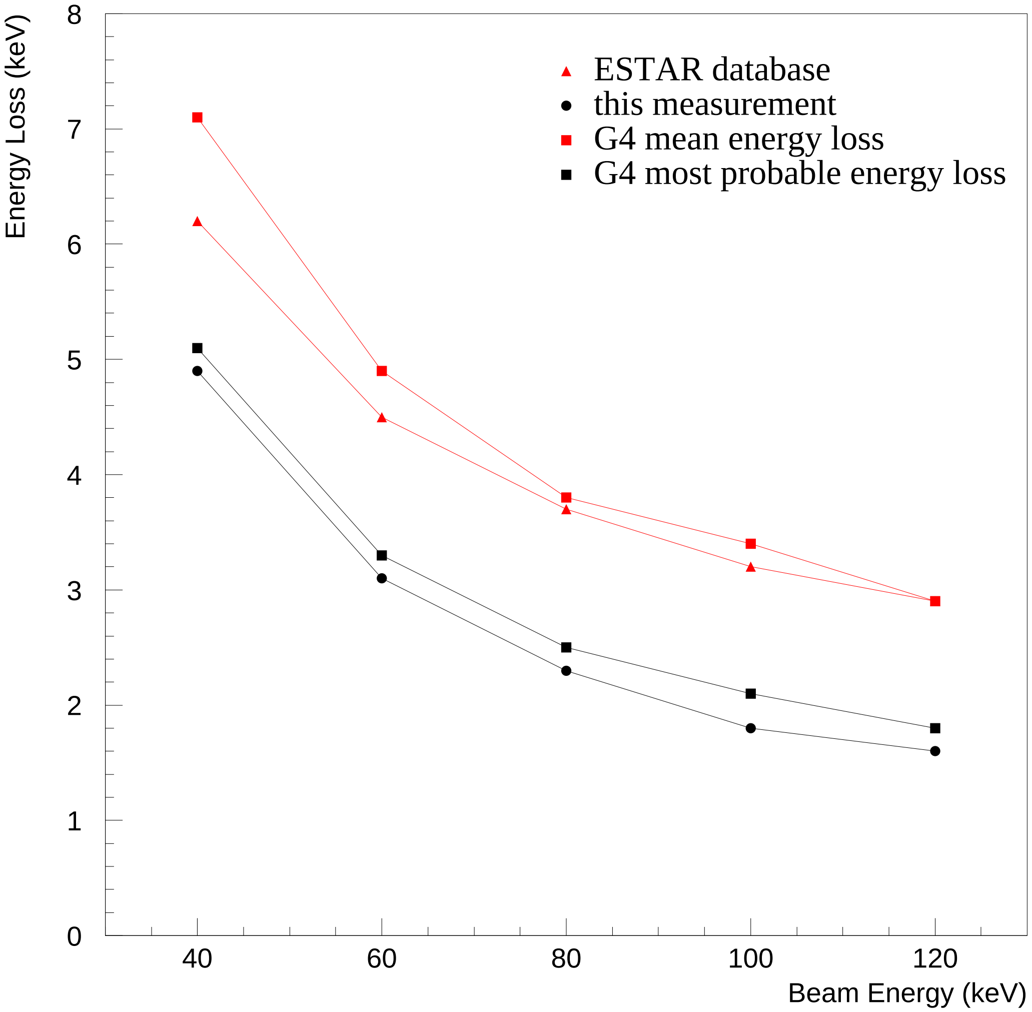

Figure 6.13: Electron energy loss in 6 micron mylar for different beam energies. Red points: mean energy loss; Black points: most probable energy loss.

Table 6.5: Energy loss (keV) in 6 μm mylar.

beam energy (keV)	this measurement	G4 simulation (MP E loss/Mean E loss)	ESTAR
40	4.9	5.1/7.1	6.2
60	3.1	3.3/4.9	4.5
80	2.3	2.5/3.8	3.7
100	1.8	2.1/3.4	3.2
120	1.6	1.8/2.9	2.9

of the measurement with ESTAR data base and GEANT4 simulation show an agreement better than the 15% level.

Without the Aluminum baffle or Mylar lining, the angular distribution for the transmitted electrons at forward angles were measured, with a scalar to count the detector signals in a given time period. The distribution is shown in Fig. 6.14. A Gaussian fit with centroid at 180 degrees gives an angular spread of 8.3 degree.

A GEANT4.4.0 simulation of the forward angular distribution was carried out, as is shown in Fig. 6.15, to be compared with the measurement. A Gaussian fit with centroid at 180 degrees gives an angular spread of 9.0 degree, showing an agreement with the measurement at better than the 15% level. Note that Fig. 6.14 and Fig. 6.15 are with arbitrary normalization, such that the normalization is not to be compared for the two figures.

The energy spectra were measured at forward angles without the Aluminum baffle or Mylar lining, as is shown in fig. 6.16, where the spectra at 90, 100, 110, 120, and 130 degree are absolutely normalized, and the spectra at other angles are relatively normalized to the 130 degree spectrum using the information from fig. 6.14. The low energy tails are mostly detector and electronic noises. The noise level was changing during the runs.

Then an Aluminum baffle was placed between the forward and backward angles to reduce chamber background for backward angles, and the energy spectra was measured at backward angles. Finally, we lined the chamber with 3 layers of 2-mil aluminized mylar to further reduce the chamber background, and measured the energy spectra at backward angles. With these efforts, the chamber background improved a lot. Fig. 6.17 shows the energy spectra at 20, 30, 40, 50, 60, and 70 degrees under these 3 kinds of situations.

As is shown in these plots, the chamber background is worse at smaller angles, and the high energy peak is barely contaminated by the chamber background. The set of spectra under the best background situation (with mylar lining and baffle) are shown in Fig. 6.18 for all backward angles. Simulations with GEANT4.4.0 show the similar two-peak behavior, as seen in Fig. 6.19 for the energy spectrum at 40 degree. Note that the GEANT4 simulation does not include the Si detector response, which introduces additional backscattering on the Si detector and an energy resolution of

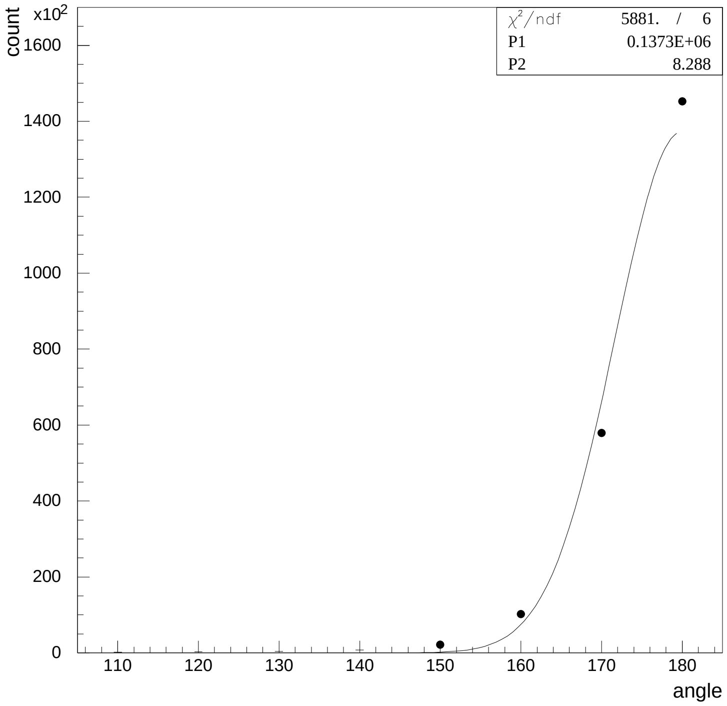

Figure 6.14: Angular distribution for forward angles, with detector noise subtraction, but without chamber background subtraction.

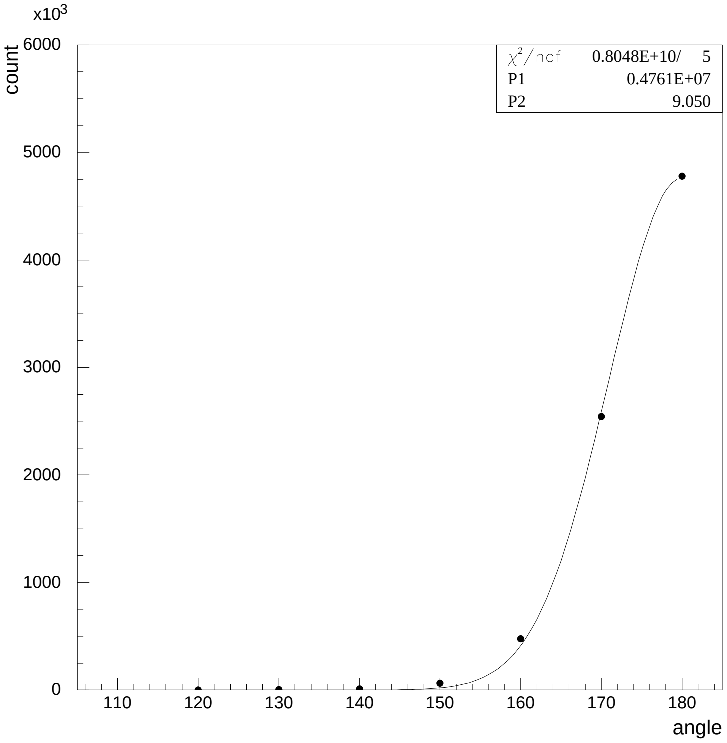

Figure 6.15: Angular distribution for forward angles, simulated with GEANT4.4.0.

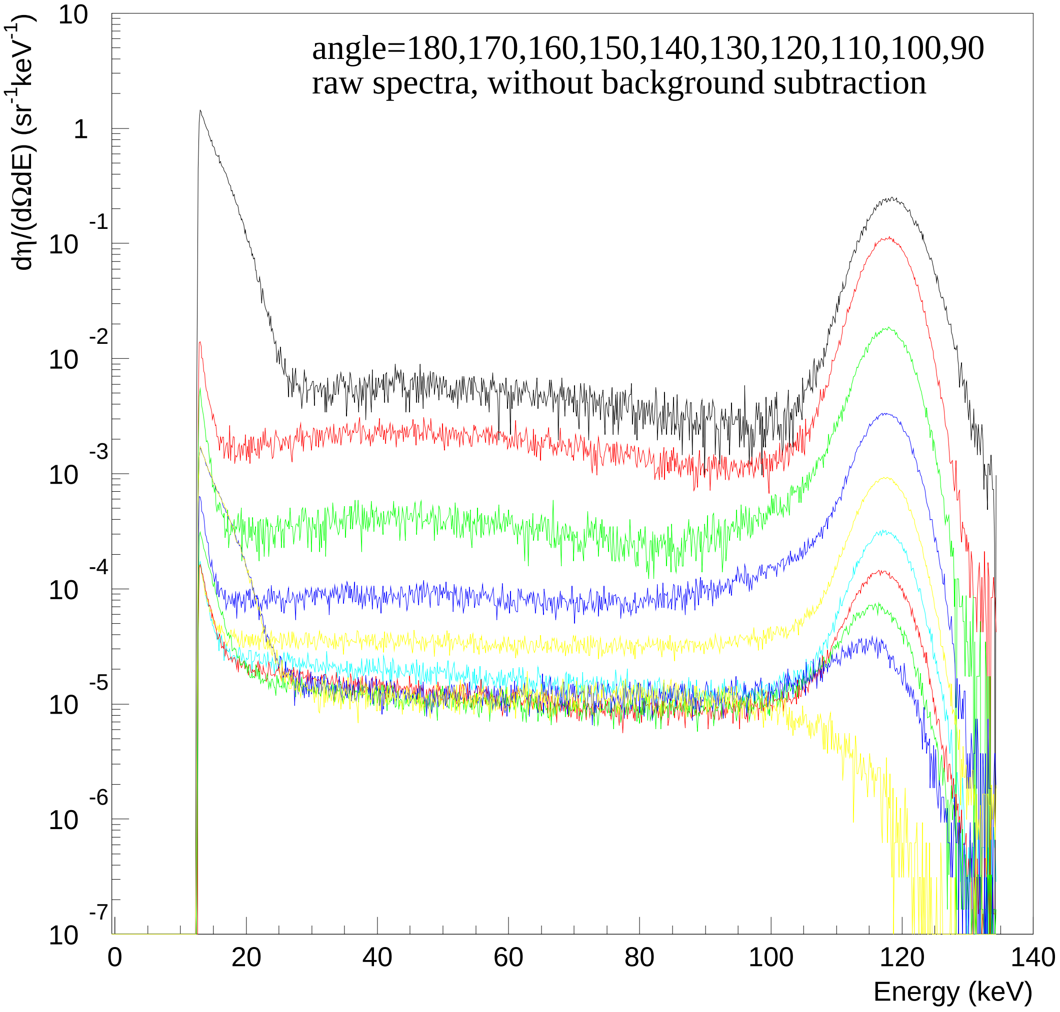

Figure 6.16: Double differential distributions for electrons at forward angles, without background subtraction.

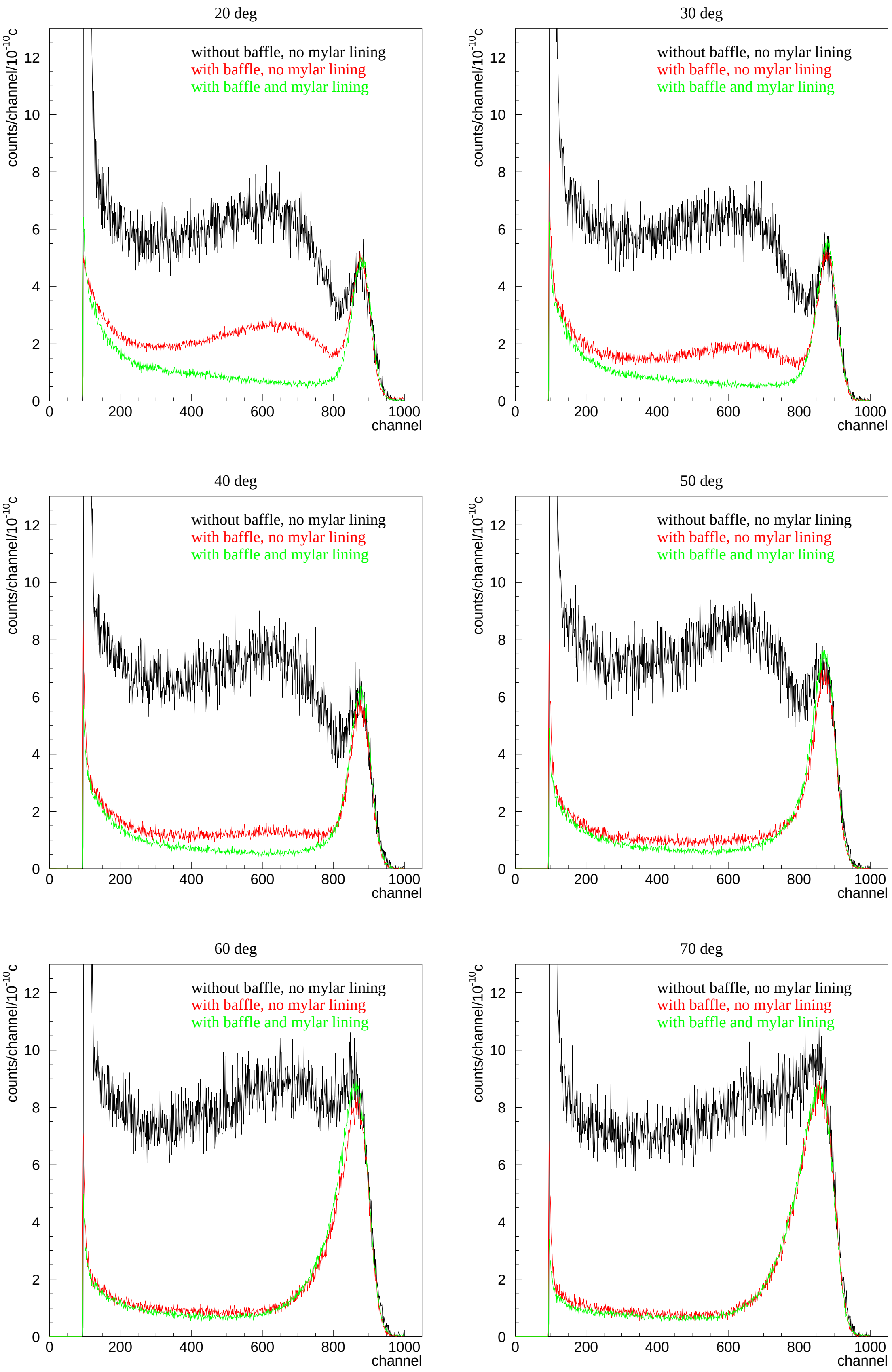

Figure 6.17: Energy spectra at 20, 30, 40, 50, 60, and 70 degrees under 3 different kinds of background situations.

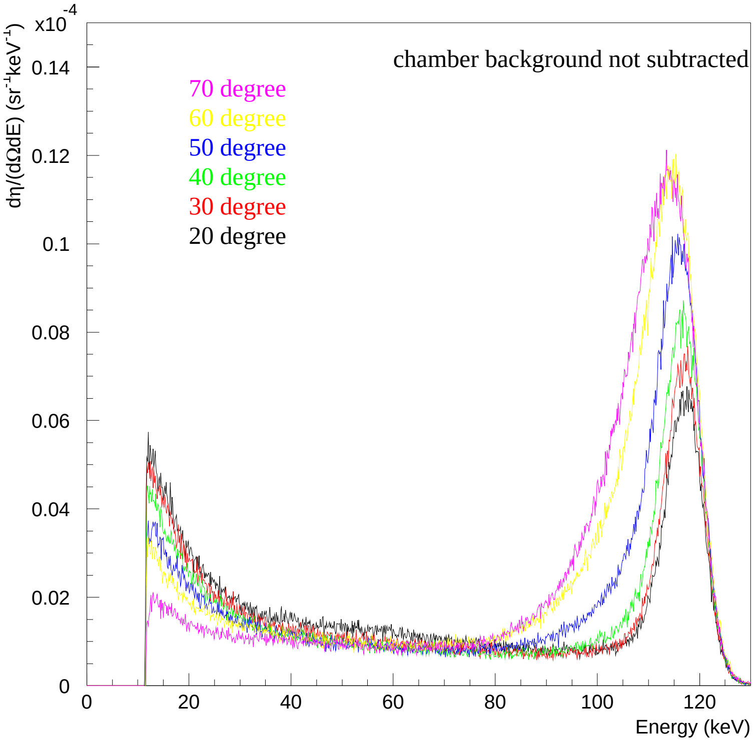

Figure 6.18: Double differential distributions at backward angles, detector noise subtracted, but chamber background not subtracted.

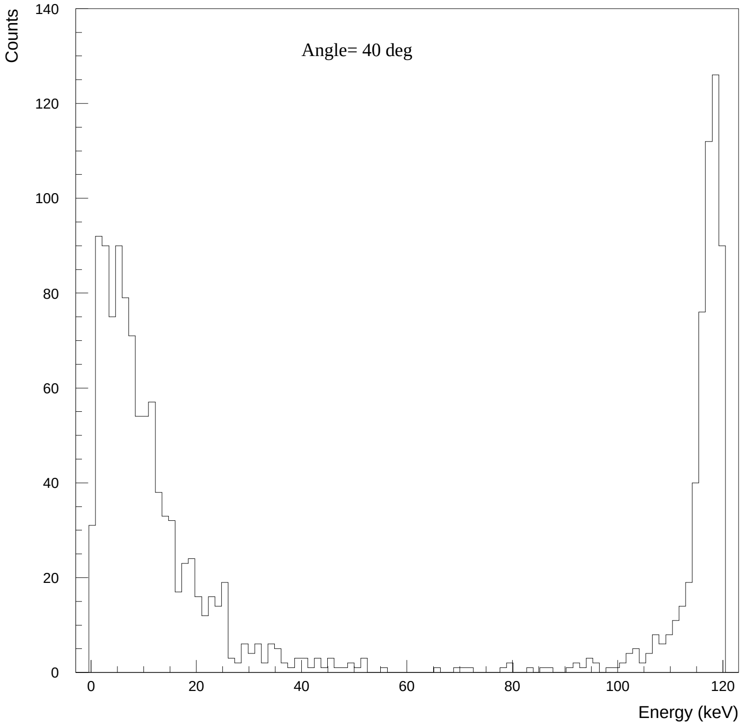

Figure 6.19: Double differential distribution at 40 degree, simulated with GEANT4.

about 3 keV.

To get the angular distribution for backward angles, we can integrate the double differential distributions (Fig. 6.18) over energy. However, since the low energy tail suffers from chamber background which is difficult to measure because it is different for target-in and target-out, and uncertainty in the extrapolation to zero energy, we will integrate only the high energy peak, to be compared with integration of the high energy peak in the GEANT4 simulation of the double differential distributions. Both of the measure and GEANT4 simulation results are shown in Fig. 6.20. While the trends agree, the GEANT4 simulation over-estimates the backscattering by order of 50%.

Integrating the distributions in Fig. 6.20 by angle, leads to the NIBF with only the high energy peak. The integration is done by linearly extrapolating the angular distribution to 0 and 90 degree and integrating from 0 to 90 degree. The results are shown in Fig. 6.20. To get an idea of the error introduced by this integration, Geant4 simulation integrated this way gives 0.18%, while using number of backscattered electrons (with the same energy cut as the integration over energy which leads to the distributions in Fig. 6.20) divided by number of incident electrons gives 0.15% in the simulation.

6.1.3.3 Summary

Scattering and energy loss for electron in 6 μm Mylar film are measured, and compared with GEANT4 simulations. For the angular distribution of the transmitted electrons at forward angles, GEANT4 agrees with the measurements at better than the 15% level. For energy loss in the Mylar film, GEANT4 agrees with the measurements and the NIST ESTAR data base at better than the 15% level. However, GEANT4 simulation over-estimates the backscattering from Mylar film by about 50%.

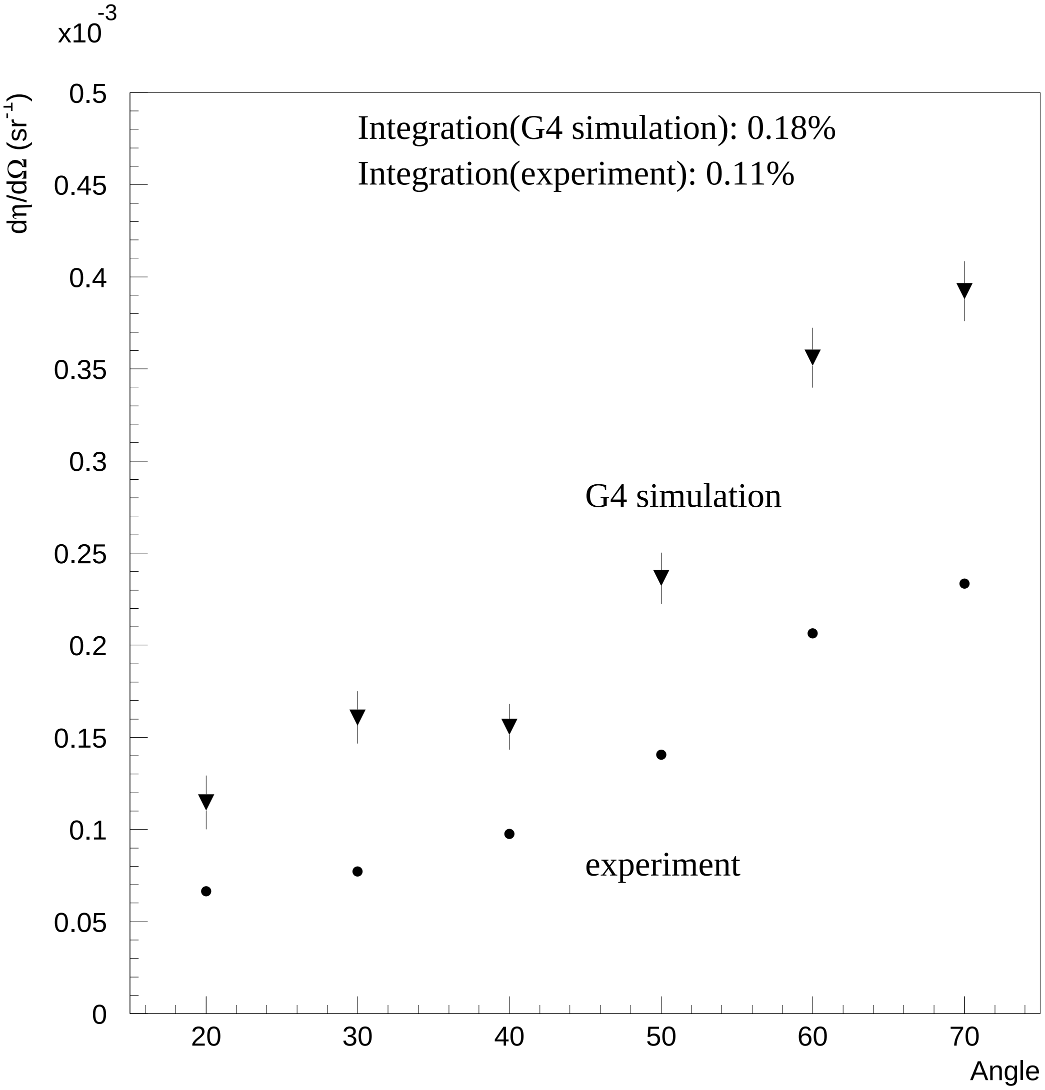

Figure 6.20: Angular distribution for backward angles, high energy peak only.

6.2 Studies of the SD2 UCN source

6.2.1 The prototype SD2 source

A prototype spallation neutron driven SD2 UCN source has been built and tested at LANSCE by the UCNA collaboration [91, 92]. Measurements of τ_{SD} were done with this prototype source. These measurements demonstrate the influences of heating and para-deuterium contamination on the UCN lifetime, and provide a quantitative foundation for the development of SD2 superthermal sources. This prototype source produced bottled UCN densities of $145 \pm 7 UCN/cm^3$, about three times greater than the largest bottled UCN densities previously reported.

A schematic view of the prototype source and apparatus used for the tests is shown in Fig. 6.21 Spallation neutrons were produced by 800MeV protons incident on a tungsten target. The neutrons were reflected by a beryllium box held at near liquid nitrogen temperature, then moderated by a polyethylene layer to produce cold neutrons. The ^{58}Ni coated stainless steel UCN guide containing the solid deuterium converter was contained in the polyethylene cold neutron trap. UCNs produced

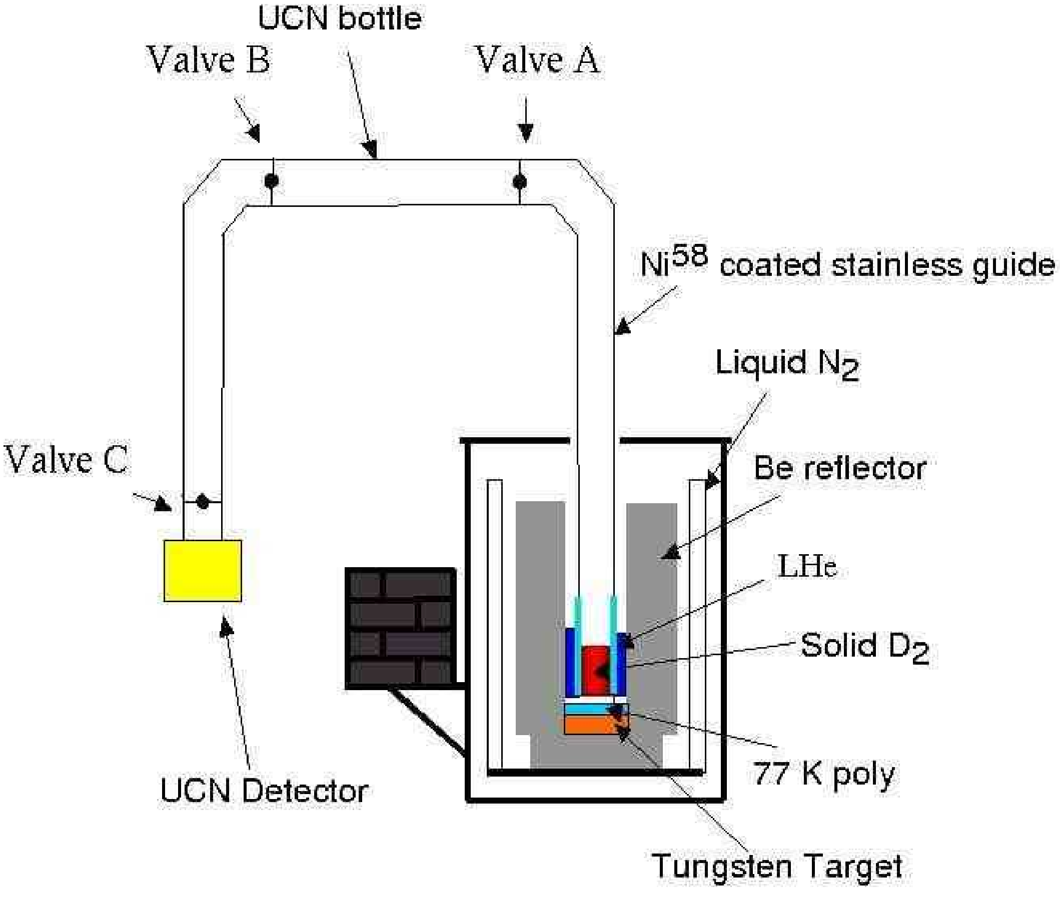

Figure 6.21: Schematic view of the prototype UCN source.

in the SD2, confined by the guide tube with an inner diameter of 7.8 cm, could be directed through a series of valves to the UCN detector. Neutrons were detected in a 5-cm thick multiwire proportional chamber detector filled with a mixture of He-3 at 5 mbar and CF4 at 1 bar. The low He-3 pressure and the large bend angle in the guide resulted in a high degree of selectivity for detecting UCNs in the apparatus. Data were acquired using a multiscalar that scaled the count rate from the detector and was started by the proton beam passing through a toroidal pick up coil.

Up-scatter from phonons in the solid [93], up-scatter from para-deuterium molecules in the solid (spin-relaxation of para- to ortho-deuterium can release 7 meV of energy to UCN) [94], absorption on deuterium, and absorption on hydrogen impurities limit the lifetime of UCNs in SD2. All of these effects have been calculated. The total loss rate is a sum of contributions from these sources:

$$1/\tau_{SD} = 1/\tau_{phonon} + 1/\tau_{para} + 1/\tau_{Dabs} + 1/\tau_{Habs},$$

with the loss rate due to phonon up-scatter having different contributions from the ortho- and para-deuterium in the solid. Establishing the experimental basis to validate these models is essential for the design of a UCN source based on SD2.

Deuterium was prepared in the ortho state using a hydrous iron (III) oxide, $Fe_2O_3 \cdot x(H2O)$, converter cooled to a few degrees below the triple point at 18.7K [95]. In this way the para-fraction was reduced from the room-temperature equilibrium value of 33% to 2-4%. Both the hydrogen contamination and the para-fraction in the SD2 were measured by means of rotational Raman spectroscopy on a gaseous sample taken by warming the deuterium after the UCN measurements.

The deuterium was frozen in the lower part of the cryostat using a liquid helium transfer refrigerator. The temperature of the solid was monitored using a silicon diode thermometer mounted to the outside of the guide tube. The SD2 volume was measured by integrating the flow of gas while growing the solid. The volume was checked when the solid was warmed and the gas was returned to a buffer volume.

If gravity, wall losses, the SD2 potential, and transport effects are neglected, and if the SD2 is thin enough so that its volume is uniformly sampled by the neutrons, the lifetime of neutrons stored in a bottle in contact with SD2 is given by

$$\tau = \tau_{SD} \frac{V}{V_{SD}}$$

We have used this idea to measure the UCN lifetime in SD2. As depicted in Fig. 6.21, valves B and C were open for these measurements.

Results for UCN lifetimes τ_{SD} in SD2 as a function of the SD2 temperature and para/ortho-fractions are shown in Fig. 6.22. The measured lifetimes agree well with theoretical predictions of the up-scatter rate. The main contributions to the UCN lifetime in SD2 have been measured and are quantitatively understood. These data demonstrate the potential of a UCN source based on a spallation neutron driven SD2 converter.

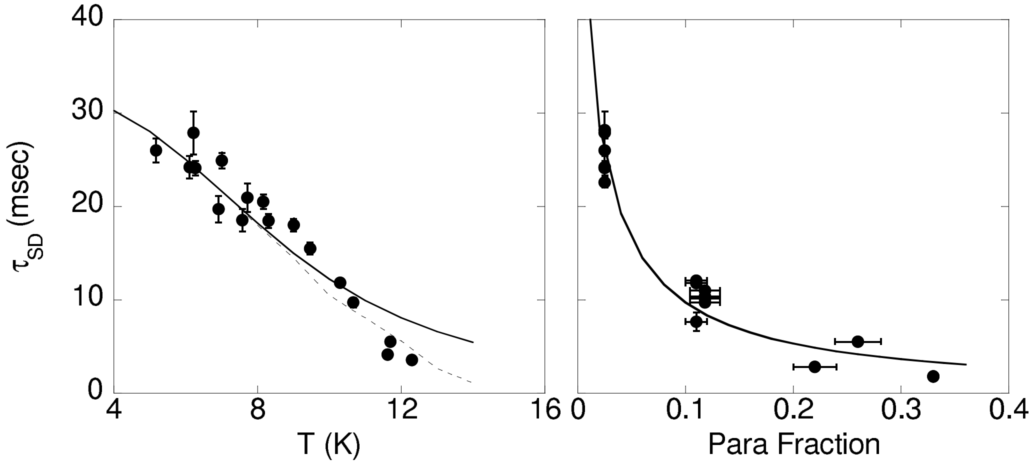

Figure 6.22: (left)Data points are measured SD2 lifetimes as a function of SD2 temperature, with the para-fraction fixed at 2.5%. The solid line shows the predicted temperature dependence. The dashed line is the predict effect of departure from the solid lifetime model due to up-scatter from D2 gas in the guide. (right)SD2 lifetimes as a function of para-fraction for all of the data taken below 6 K. The solid line is the model prediction of the para-fraction dependence at an average temperature of 5.6 K.

Valves A and B define a bottle section. The bottled UCN density as a function of the size of the proton pulse was measured. For these measurements we increased the proton charge delivered to the target using multiple proton pulses delivered within a 1 second interval. These data are plotted, as a function of incident proton charge, in Fig. 6.23.

Tests with large volumes (240 cm^3) and much larger proton pulses were done in order to demonstrate the performance of the prototype source with bottled UCN densities measured. The effect of ballistic heating of the SD2 by radiation from the spallation target was also investigated, and is shown to result in only a small reduction in the rate of UCN production for incident proton pulses of up to 95 μC.

There is a distinct reduction in the ratio of UCN density to incident proton charge at the highest charges. This is likely to be due to the slow rise in the target temperature through the course of the high current runs. Monte Carlo simulation predicts a 10% decrease in the UCN count with the measured 3 K rise in the starting SD2 temperature and correspondingly shorter lifetime of UCN in the SD2.

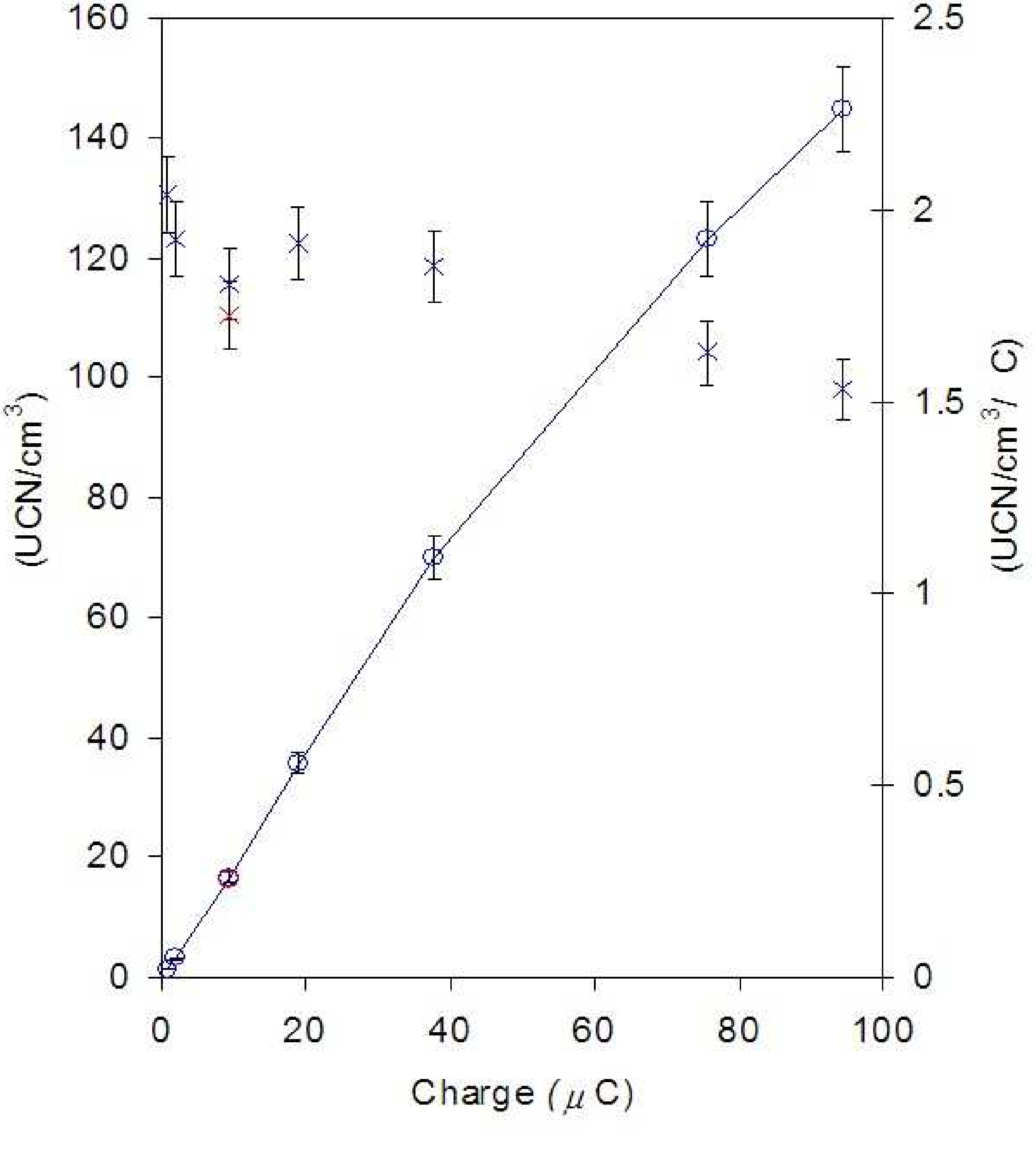

Figure 6.23: Circles display the bottled density as a function of incident proton charge (left axis). Crosses display the ratio of bottled density to the incident proton charge (right axis). The data points are corrected for transport and detection efficiency.

The maximum density achieved in the storage bottle, 145 ± 7 UCN/cm^3, is significantly larger than peak bottled densities reported previously. A single proton pulse of 95 mC would produce an instantaneous density of 44000 UCN/cm^3 in the SD2. Although in principle this is the limiting density that can be extracted from an ideal shuttered source of our geometry using such proton pulses, losses due to absorption on the bottle walls would likely reduce this considerably. Our model predicts that 1300 UCN/cm^3 could be extracted as the limiting density from our source by moving valve A closer to the SD2 in Fig. 6.21, so that the volume containing the SD2 is about twice the SD2 volume. This prediction assumes a 95 μC proton pulse every 10 seconds, with the shutter open for 1 second for each pulse, and with a UCN lifetime of 28 msec in the SD2 (the longest we have measured). This prediction drops to a density of 889 UCN/cm^3 if the wall loss rates are assumed to be 10^{-4}/bounce.

6.2.2 The full-scale SD2 source

Monte Carlo simulations validated by the tests with the prototype source were used to optimize the source geometry, which leads to the design of the full-scale UCN source.

The design of the full-scale UCN source is closely based on the prototype UCN source. The major differences between the prototype source and the full-scale source are: (1) the new source will receive significantly more beam than the prototype; (2) the new source will contain about 2.0 liters of SD2 with a diameter of 20cm (compared to the 200 cc volume and 7.8cm diameter in the prototype); (3) the new source will have a cryogenic shutter installed to close off the SD2 volume between proton beam pulses; and (4) the aspect ratio of the exit guide to the source volume is much lower than in the prototype source. The UCN source and moderator assembly is shown in Fig. 6.24 and a blowup of the UCN source is shown in Fig. 6.25.

The UCN source was tested in two steps. In the first step, a flapper valve was installed in the UCN guide before the PPM (this flapper was called “Mr.F,” to be distinguished from the source flapper). After the flapper valve, a section of UCN guide tube bends 90° and guides the UCN vertically down to a ^{3}He gaseous counter, instead of passing through the PPM. Mr.F was utilized to study the lifetime of UCN in the volume from SD2 to Mr.F under two conditions of the source flapper: open all the time; and flapping with optimum setting of open/close time. In each measurement, the proton pulse was incidenting on the tungsten target every 40 seconds. For each proton pulse, Mr.F was kept close for various amount of time, and then open for 20 seconds to detect the UCN alive. Fig. 6.26 shows the amount of UCN as a function of the time when Mr.F was kept closed, under the condition that the source flapper was flapping. An exponential fit gives the UCN lifetime. Fig. 6.27 shows the result when the source flapper was open all the time. The UCN lifetime was shorter when the source flapper was open, because some of the UCNs would return back to the SD2, and UCN lifetime in SD2 was much shorter than 1 second ($<$ 28 msec as shown in the last section).

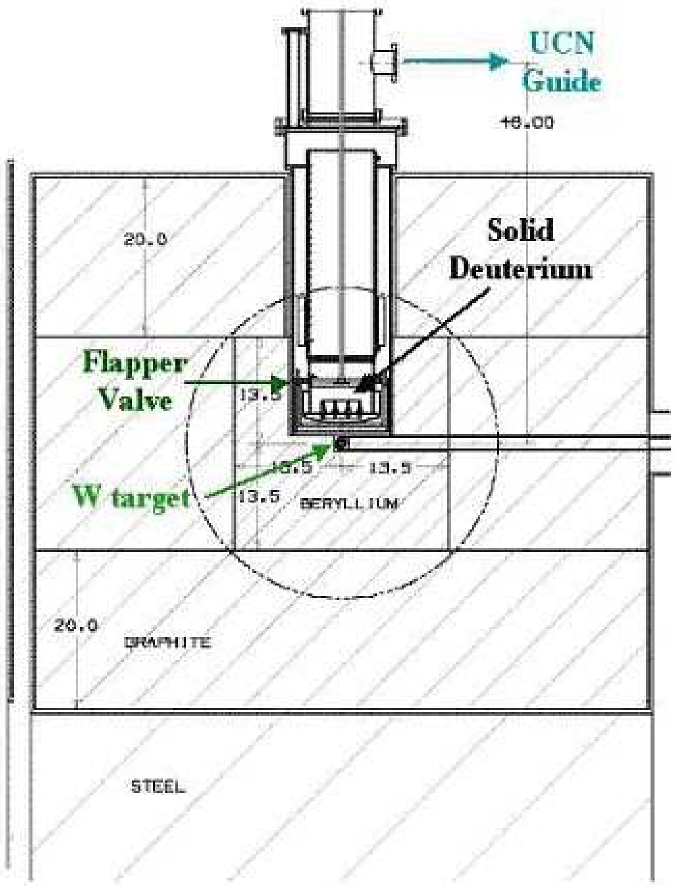

Figure 6.24: The UCN source and moderator assembly.

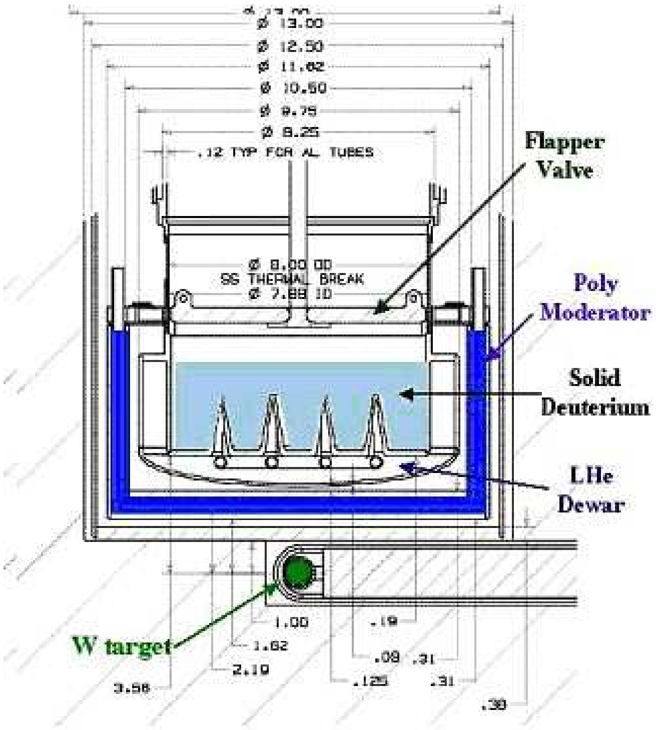

Figure 6.25: Close-up view of the UCN source.

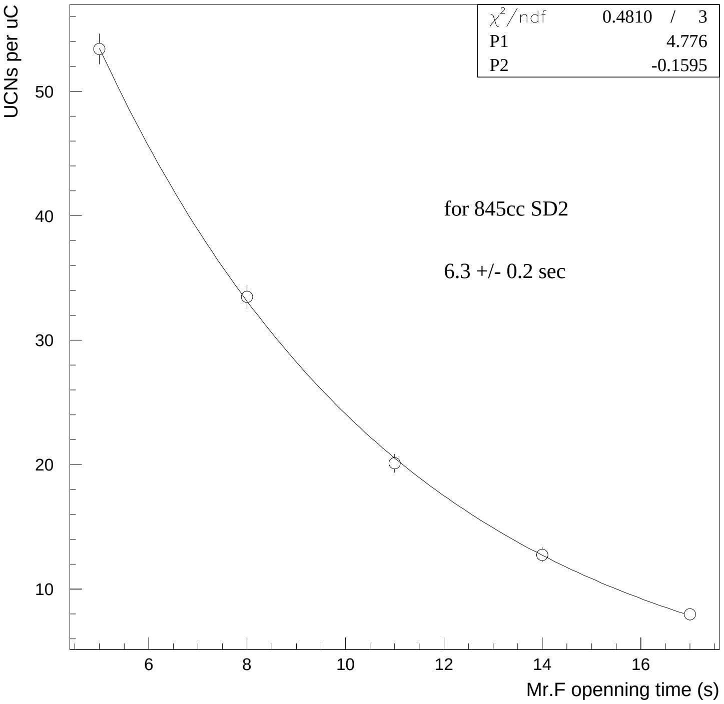

Figure 6.26: Measurement of UCN lifetime with source flapper flapping and 845 cm^3 of SD2.

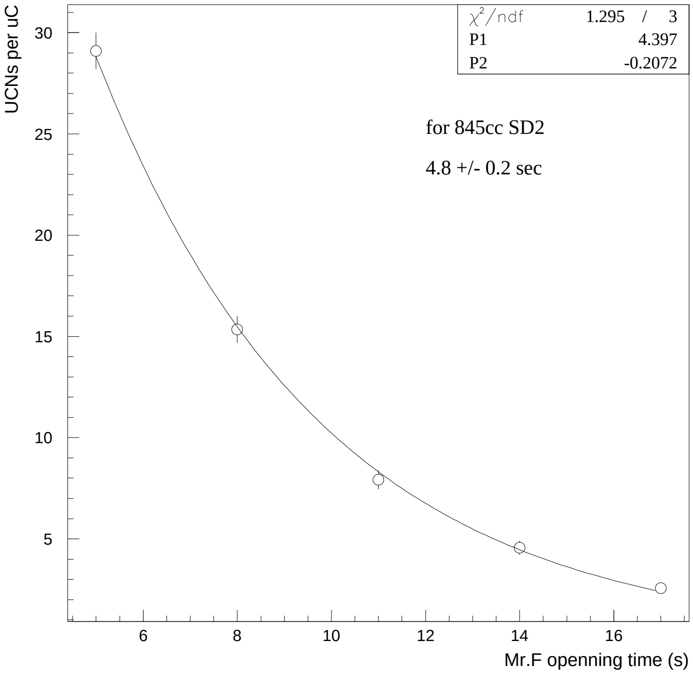

Figure 6.27: Measurement of UCN lifetime with source flapper open and 845 cm^3 of SD2.

In the second step, Mr.F was taken off. The UCN guide was install through the PPM, and the 90° bend UCN guide and the ^{3}He counter were installed after the PPM. Due to safety reasons, a thin ($\sim$ 10 mil) aluminum window located in the bore of the magnet served to isolate the vacuum of the SD2 source from the remainder of the experiment. UCN of the "correct" spin state were then accelerated through the Al window, leading to improved transmission. Fig. 6.28 shows the number of UCN detected in the ^{3}He counter as a function of the magnet field of the PPM. Our measurements done before the PPM indicated $\sim$ 160 UCN/μC entered the magnet, thereby indicating that for field strengths of 6 Tesla the transmission was approaching 50%(maximum expected due to magnetic filtering of the "wrong" spin state).

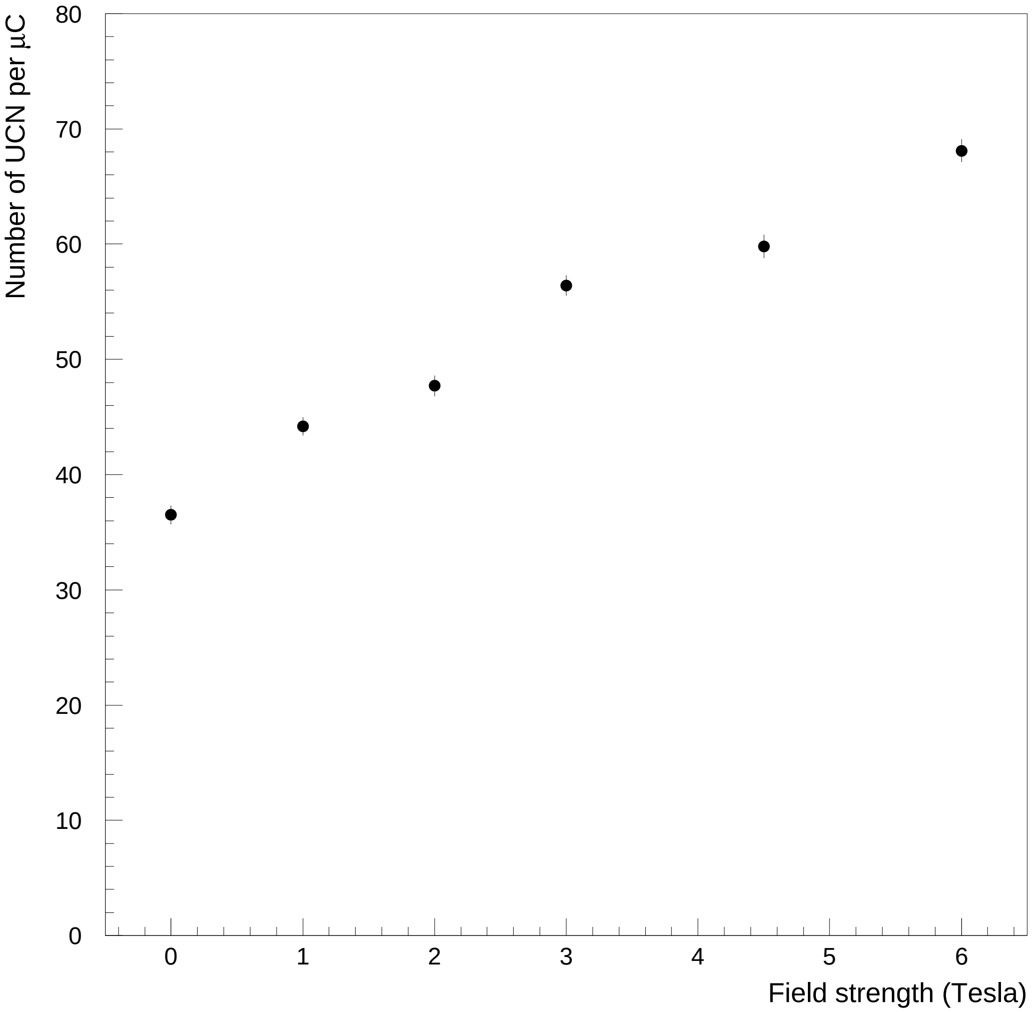

Figure 6.28: Transmission studies through the PPM plotted as a function of the field strength.

6.3 Studies of the SCS spectrometer with beta detector package

The detector package was installed to the SCS magnet, and the SCS magnet was energized. A ^{113}Sn source was placed at 6 inches in front of the MWPC. The size of the ^{113}Sn source is about 2mm in diameter. Electrons from the source were detected with the detector package (MWPC+scintillator detector). The PMT gains were monitored as the SCS magnetic field varied from 0 to 1.0 Tesla. They remain constant within 2.5% under the influence of the SCS magnetic field, with the help of the PMT shielding structure with appropriate current flowing to the shielding solenoids. Electron positions are reconstructed from the MWPC signals. The reconstructed position distributions show focusing due to the SCS magnetic field, as shown in Fig. 6.29, where the electron position distributions under various SCS magnetic fields are presented. A plot of the sigma of the position distributions as a function of the SCS magnetic field is shown in Fig. 6.30.

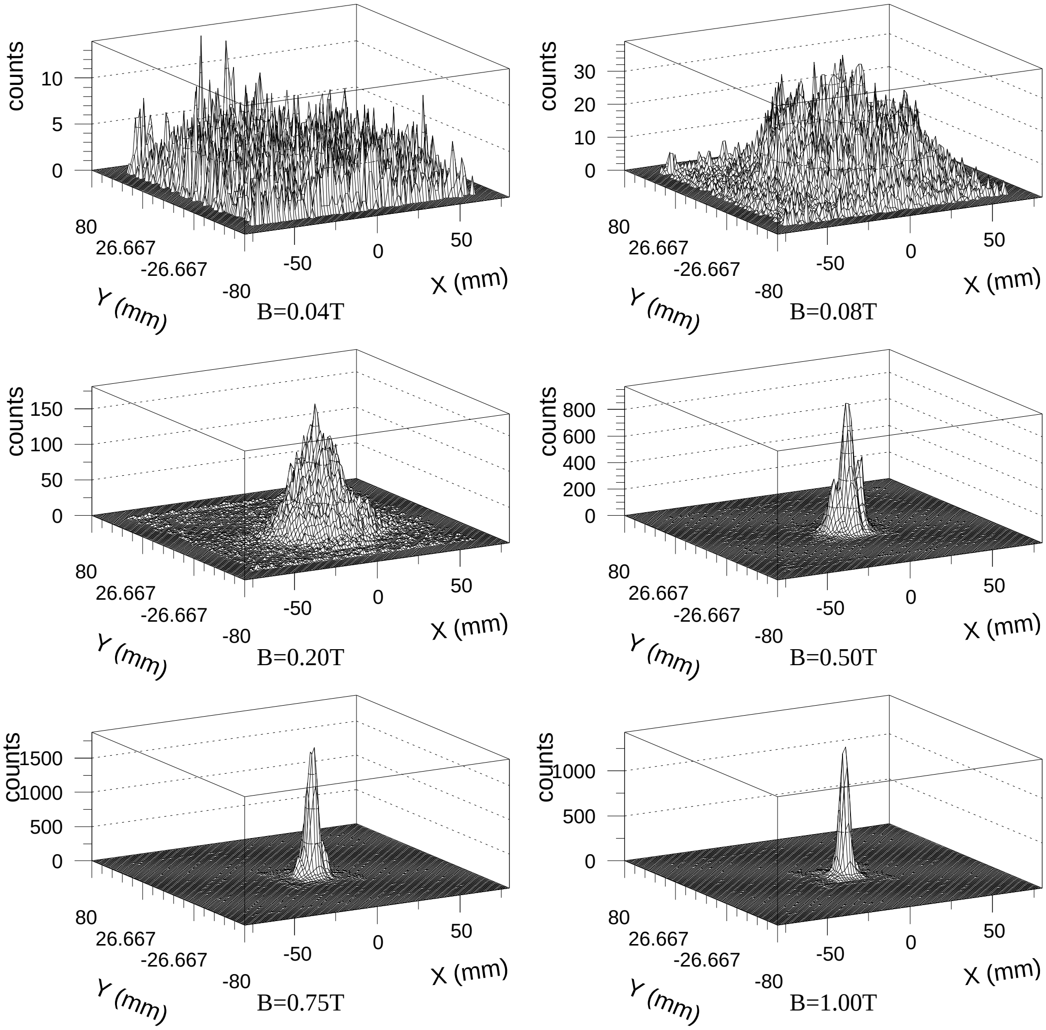

Figure 6.29: Distributions of electron positions reconstructed from the MWPC signals, under various SCS magnetic fields.

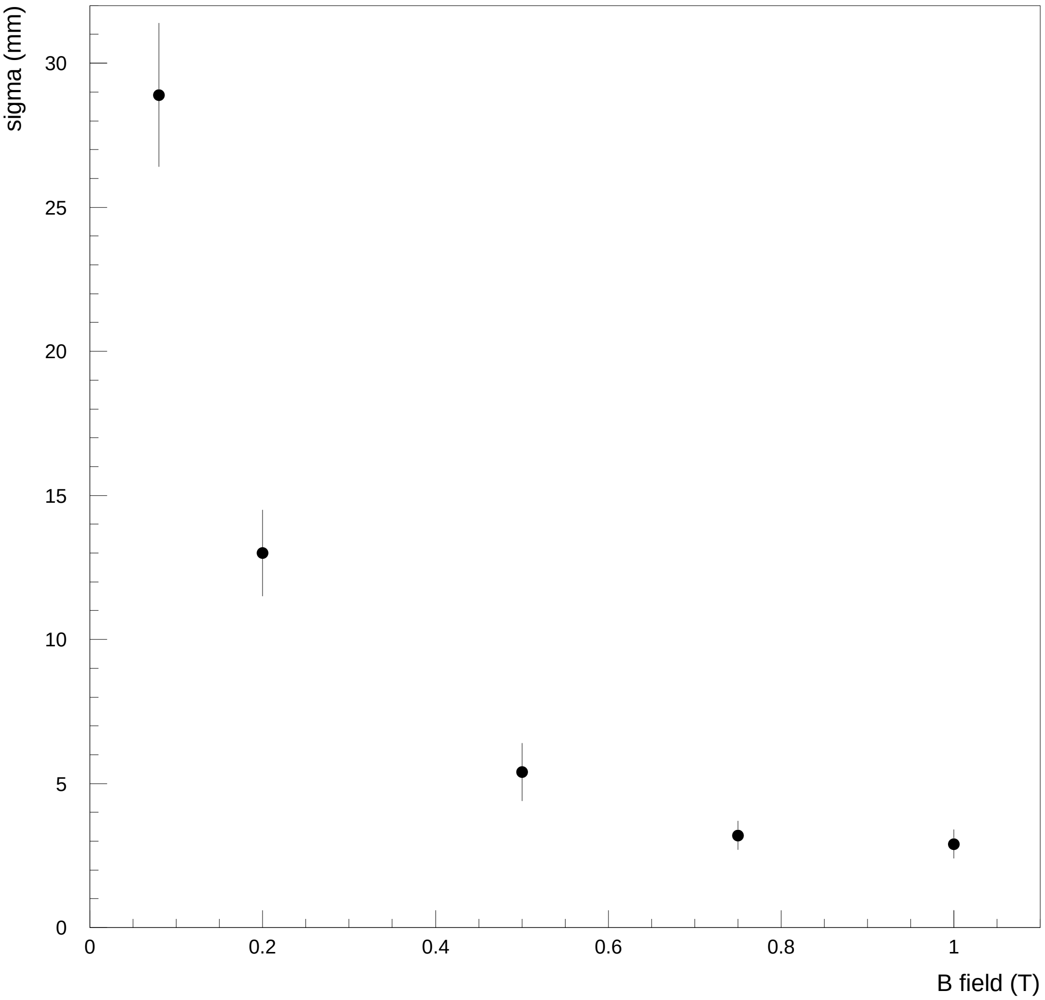

Figure 6.30: The sigma of the position distributions as a function of the SCS magnetic field.

Chapter 7

Conclusion and Future Prospects

The essential elements of the UCNA experiment, including the dedicated spallation-driven solid deuterium UCN source developed by the collaboration, the UCN guides, and the SuperConducting Spectrometer(SCS) including the beta detector system, were commissioned. The UCN source was fully operational with 1.2 liters of solid deuterium at < 6 Kelvin. It produced the highest stored density of UCN ever, exceeding the previous highest density (at a research reactor) by a factor of two. The UCNs were successfully transported out of the source along several meters of diamond-coated quartz guide tubes through the field of a 7-Tesla pre-polarizing magnet. A UCN production of about 70 UCN per μC of proton charge was obtained after the pre-polarizing magnet. The SCS magnet was successfully commissioned, demonstrating 10^{-4} uniformity over 3 meters. The beta detector package was constructed, calibrated and demonstrated to be performing as good as or better than the design goals. The electronics and data acquisition system were set up and fully operational. Studies of systematics for the UCNA experiment based on a full GEANT4 Monte Carlo simulation of the SCS spectrometer were carried out. Detailed measurements of the electron backscattering of low energy electrons were carried out to constrain the GEANT4 electron multiple scattering model.

Commissioning of the full UCNA experiment is in progress and will continue during the next LANSCE proton accelerator run cycle scheduled from September to December 2005. The remaining tasks are installing the UCN guides from the PPM through the AFP to the SCS, which is expected to be finished before early October 2005, and commissioning of the AFP magnet. Events of UCN beta decay in the decay tube inside the SCS will be generated starting in mid-October, and a preliminary physics run is scheduled from mid-October to December 2005. Higher statistics run will continue next year with the goal of a 0.2% measurement of the "A" asymmetry, which will provides a precise determination of the CKM matrix element V_{ud} when combined with results from the neutron lifetime. The value of V_{ud} determined from neutron beta decay can be compared with the value determined from measurements of the superallowed $0^+ \rightarrow 0^+$ nuclear beta decay, and the value determined by requiring that the CKM matrix be unitary. This will provide a sensitive way to search for new physics beyond the Standard Model.

Appendix A

Detailed derivation of 1st-order model formalism

When an electron with momentum p moves in the effective uniform magnetic field B_{av}, the radius of curvature ρ of the trajectory is given by

$$\rho = \frac{p}{eB_{\mathrm{av}}}, \tag{A.1}$$

where B_{av} is the average field in the region $r = 0 \sim r_{\mathrm{eff}}$, given by

$$B_{\mathrm{av}} = \frac{1}{r_{\mathrm{eff}}} \int_0^{r_{\mathrm{eff}}} B(r)\,\mathrm{d}r, \tag{A.2}$$

and is proportional to B_0,

$$B_{\mathrm{av}} = a_1 B_0.$$

Numerically we find $a_1 = 0.911$.

Next we find an expression for θ_1. Using a cylindrical coordinate system, with the z-axis along the axis of the coils and the zero point of z at the mid-plane, the torque $\vec{N}$ that the electron receives and the electron angular momentum $\vec{J}$ are expressed in this coordinate system as follows:

$$\begin{aligned} \vec{J} &= \vec{r} \times \vec{p} = pr \sin\theta \vec{e_{\mathrm{z}}}, \\ \vec{N} &= -erB(r)\frac{\mathrm{d}r}{\mathrm{d}t}\vec{e_{\mathrm{z}}}. \end{aligned}$$

The torque and the angular momentum are related by

$$\vec{N} = \frac{\mathrm{d}\vec{J}}{\mathrm{d}t}.$$

Integrating $N\,\mathrm{d}t$, we get

$$\int N\,\mathrm{d}t = -\int_{r_\mathrm{i}}^{r} erB(r)\,\mathrm{d}r = J - J_\mathrm{i} = pr\sin\theta - pr_\mathrm{i}\sin\theta_\mathrm{i},$$

where we note that the magnitude of momentum p is constant. Therefore,

$$\sin\theta(r) = \frac{r_\mathrm{i}}{r}\sin\theta_\mathrm{i} - \frac{e}{pr}\int_{r}^{r_\mathrm{i}} rB(r)\,\mathrm{d}r. \tag{A.3}$$

Since

$$\sin\theta_\mathrm{i} = \frac{b}{r_\mathrm{i}},$$

we can use equation (A.3) to obtain

$$\sin\theta(r) = \frac{b}{r} - \frac{e}{pr}\int_{r}^{r_\mathrm{i}} rB(r)\,\mathrm{d}r. \tag{A.4}$$

Thus at the effective radius r_eff, the entering angle θ_1 is:

$$\sin\theta_1 = \frac{b}{r_\mathrm{eff}} - \frac{e}{pr_\mathrm{eff}}\int_{r_\mathrm{eff}}^{r_\mathrm{i}} rB(r)\,\mathrm{d}r. \tag{A.5}$$

To express the integral $\int_{r_\mathrm{eff}}^{r_\mathrm{i}} rB(r)\,\mathrm{d}r$ in terms of r_i and B_0, we choose a cutoff radius R_c such that for $r > R_\mathrm{c}$, we can approximate the magnetic field on the mid-plane as dipole field. The answer does not depend on R_c as long as R_c is large enough. For example, we choose $R_\mathrm{c} = 4R$, the dipole approximation is good to 99.6%. The octupole moment is zero [96]:

$$B(r) = -\frac{\mu_0 I R^2}{2r^3} + O((\frac{R}{r})^7). \tag{A.6}$$

Thus

$$\begin{aligned} \int_{R_\mathrm{c}}^{r_\mathrm{i}} rB(r)\,\mathrm{d}r &\simeq -\frac{\mu_0 I R^2}{2}\int_{4R}^{r_\mathrm{i}} \frac{\mathrm{d}r}{r^2} \\ &= -\frac{\mu_0 I R^2}{2}(\frac{1}{4R} - \frac{1}{r_\mathrm{i}}). \end{aligned} \tag{A.7}$$

Using

$$B_0 = \frac{8\mu_0 I}{5\sqrt{5}R}$$

in equation (A.7) we get

$$\int_{R_c}^{r_i} rB(r)\,\mathrm{d}r = -\frac{5\sqrt{5}R^3B_0}{16}(\frac{1}{4R}-\frac{1}{r_\mathrm{i}}). \tag{A.8}$$

For $\int_{r_\mathrm{eff}}^{R_\mathrm{c}} rB(r)\,\mathrm{d}r$, we can express it as

$$\int_{r_\mathrm{eff}}^{R_\mathrm{c}} rB(r)\,\mathrm{d}r = a_2R^2B_0. \tag{A.9}$$

Numerically we find $a_2 = -0.183$.

Substituting equations (A.8) and (A.9) into equation (A.5) gives

$$\sin\theta_1 = \frac{b}{r_\mathrm{eff}} - \frac{e}{pr_\mathrm{eff}}[a_2R^2B_0 - \frac{5\sqrt{5}R^3B_0}{16}(\frac{1}{4R}-\frac{1}{r_\mathrm{i}})].$$

From equation (A.1), we know that

$$\frac{eB_0}{p} = \frac{1}{a_1\rho}. \tag{A.10}$$

Thus

$$\begin{aligned}\sin\theta_1 &= \frac{b}{r_\mathrm{eff}} - \frac{1}{r_\mathrm{eff}}[\frac{a_2R^2}{a_1\rho} - \frac{5\sqrt{5}R^3}{16a_1\rho}(\frac{1}{4R}-\frac{1}{r_\mathrm{i}})] \\ &= \frac{b}{r_\mathrm{eff}} + \frac{R^2}{r_\mathrm{eff}}(\frac{5\sqrt{5}}{64a_1}-\frac{a_2}{a_1})\frac{1}{\rho} - \frac{5\sqrt{5}R^3}{16a_1r_\mathrm{eff}}\frac{1}{\rho r_\mathrm{i}}.\end{aligned} \tag{A.11}$$

From the triangle relation (see Fig. 3.6), we get

$$\frac{\rho}{\cos(\theta_1-\phi_1)} = \frac{r_\mathrm{eff}}{\sin\phi_1}. \tag{A.12}$$

Inserting equation (3.4) into equation (A.12), and solving the quadratic equation for $\sin\theta_1$, we get

$$\sin\theta_1 = \frac{\rho}{r_\mathrm{eff}} - \sqrt{(\frac{\rho}{r_\mathrm{eff}})^2-1}. \tag{A.13}$$

From equation (3.2),

$$\tan\theta_1 = \frac{\rho}{l_1} = \frac{\rho}{r_\mathrm{i}-r_\mathrm{eff}}. \tag{A.14}$$

Combining equations (A.11), (A.13), and (A.14) gives:

$$b + (\frac{5\sqrt{5}}{64a_1}-\frac{a_2}{a_1})\frac{R^2}{\rho} - \frac{5\sqrt{5}R^3}{16a_1}\frac{1}{\rho r_\mathrm{i}} = \rho - \sqrt{\rho^2-r_\mathrm{eff}^2}, \tag{A.15}$$

$$\frac{r_\mathrm{eff}}{\sqrt{1+(\frac{r_\mathrm{i}-r_\mathrm{eff}}{\rho})^2}} = \rho - \sqrt{\rho^2-r_\mathrm{eff}^2}, \tag{A.16}$$

where r_{eff}, a_1 and a_2 are geometric factors: $r_{\mathrm{eff}} = 0.917R$, $a_1 = 0.911$, $a_2 = -0.183$.

For a given R, solving the above two equations numerically for different b's, we obtain a sequence of solutions (b,r_{i},ρ) for point-to-point double focusing.

Next we calculate the deflecting angle ϕ_{d} for a point-to-point double-focusing solution (b,r_{i},ρ). At r_{eff}, the deflecting angle is

$$\begin{aligned}\phi_{\mathrm{d}}(r_{\mathrm{eff}}) &= \frac{e}{p}\int_{r_{\mathrm{i}}}^{r_{\mathrm{eff}}} B\,\mathrm{d}l \\ &\simeq \frac{e}{p}\int_{r_{\mathrm{eff}}}^{r_{\mathrm{i}}} B\,\mathrm{d}r. \qquad \text{(A.17)}\end{aligned}$$

Numerically

$$\int_{r_{\mathrm{eff}}}^{4R} B\,\mathrm{d}r \simeq a_3 R B_0, \qquad \text{(A.18)}$$

where $a_3 = -0.041$.

For $\int_{4R}^{r_{\mathrm{i}}} B\,\mathrm{d}r$, we can approximate the B as dipole field,

$$\begin{aligned}\int_{4R}^{r_{\mathrm{i}}} B\,\mathrm{d}r &\simeq -\frac{\mu_0 I R^2}{2}\int_{4R}^{r_{\mathrm{i}}}\frac{\mathrm{d}r}{r^3} \\ &= -\frac{\mu_0 I R^2}{4}\left[\frac{1}{(4R)^2} - \frac{1}{r_{\mathrm{i}}^2}\right] \\ &= -\frac{5\sqrt{5}R^3 B_0}{32}\left[\frac{1}{(4R)^2} - \frac{1}{r_{\mathrm{i}}^2}\right]. \qquad \text{(A.19)}\end{aligned}$$

Substituting equations (A.18) and (A.19) into equation (A.17), and using equation (A.10), we get

$$\begin{aligned}\phi_{\mathrm{d}}(r_{\mathrm{eff}}) &= \frac{a_3 R}{a_2\rho} - \frac{5\sqrt{5}R^3}{32a_2\rho}\left[\frac{1}{(4R)^2} - \frac{1}{r_{\mathrm{i}}^2}\right] \\ &= -\frac{0.069R}{\rho} + \frac{0.384R^3}{\rho r_{\mathrm{i}}^2}.\end{aligned}$$

According to equations (3.2) and (3.4),

$$\tan\phi_1 = 2\tan\theta_1 = \frac{2\rho}{r_{\mathrm{i}} - 0.917R}.$$

Thus the deflecting angle of the spectrometer is

$$\begin{aligned}\phi_{\mathrm{d}} &= 2[\phi_{\mathrm{d}}(r_{\mathrm{eff}}) + \phi_1] \\ &= 2\left(-\frac{0.069R}{\rho} + \frac{0.384R^3}{\rho r_{\mathrm{i}}^2}\right) + 2\tan^{-1}\left(\frac{2\rho}{r_{\mathrm{i}} - 0.917R}\right).\end{aligned}$$

Appendix B

Energy spectra of the afterpulses

First we measured the spectra with no delay of the ADC gate. In this case, the ADC is measuring the energy spectra of the primary pulses. The ADC spectra for the 4 tubes are shown in Fig. B.1, while the corresponding sum spectrum of the 4 tubes is shown in Fig. B.2. The peak at the high end is the full energy peak corresponding to the 130keV beam energy.

With a 100ns delayed gate, the ADC spectra are totally different from the no delay case, as in this case it is measuring the energy spectra (amplitude distribution) of the afterpulses in the region of 100-200ns after the primary pulses. The ADC spectrum for each tube is shown in Fig. B.3, while the corresponding sum spectrum of the 4 tubes is shown in Fig. B.4. In the spectrum of each tube(Fig. B.3), the first peak is the pedestal. The second peak is a pseudo-pedestal, which is due to the slow tail associated with a large pulse, as is shown in Fig. B.5 captured from the scope. The third peak is the SPE afterpulses. The distance between the second and third peaks corresponds to the amplitude of SPE pulses, showing that the SPE afterpulses in this region are all superposed on the slow tail. In the sum spectrum, the first peak is the pedestal. The second peak is the pseudo-pedestal, whose position is equal to the sum of pseudo-pedestals of the 4 tubes. The third peak(actually a bump) is the SPE afterpules.

With a 200ns delayed gate, the ADC measures the energy spectra of afterpulses in the region of 200-300 ns after the primary pulses. The ADC spectrum for each tube is shown in Fig. B.6, while the sum spectrum of the 4 tubes is shown in Fig. B.7. Similar to the spectra with a 100 ns delayed gate, the pedestal, pseudo-pedestal and SPE peaks are presented here. Note that the pseudo-pedestal peak is closer to the pedestal than the previous case, which is exactly what we expect for the contribution from a tail. As the delay is larger, the pseudo-pedestal should be closer to the pedestal, and merges with pedestal when the delay is large enough so that the tail is gone.

Energy spectra of afterpulses in the region of 300-400 ns are measured with a 300 ns delayed ADC gate. The ADC spectrum for each tube is shown in Fig. B.8, while the sum spectrum of the 4 tubes is shown in Fig. B.9. Note that in this case the pseudo-pedestal is gone. From the spectra with a 100, 200 and 300 ns delayed gate, a trend is shown that the fraction of SPE afterpulses is

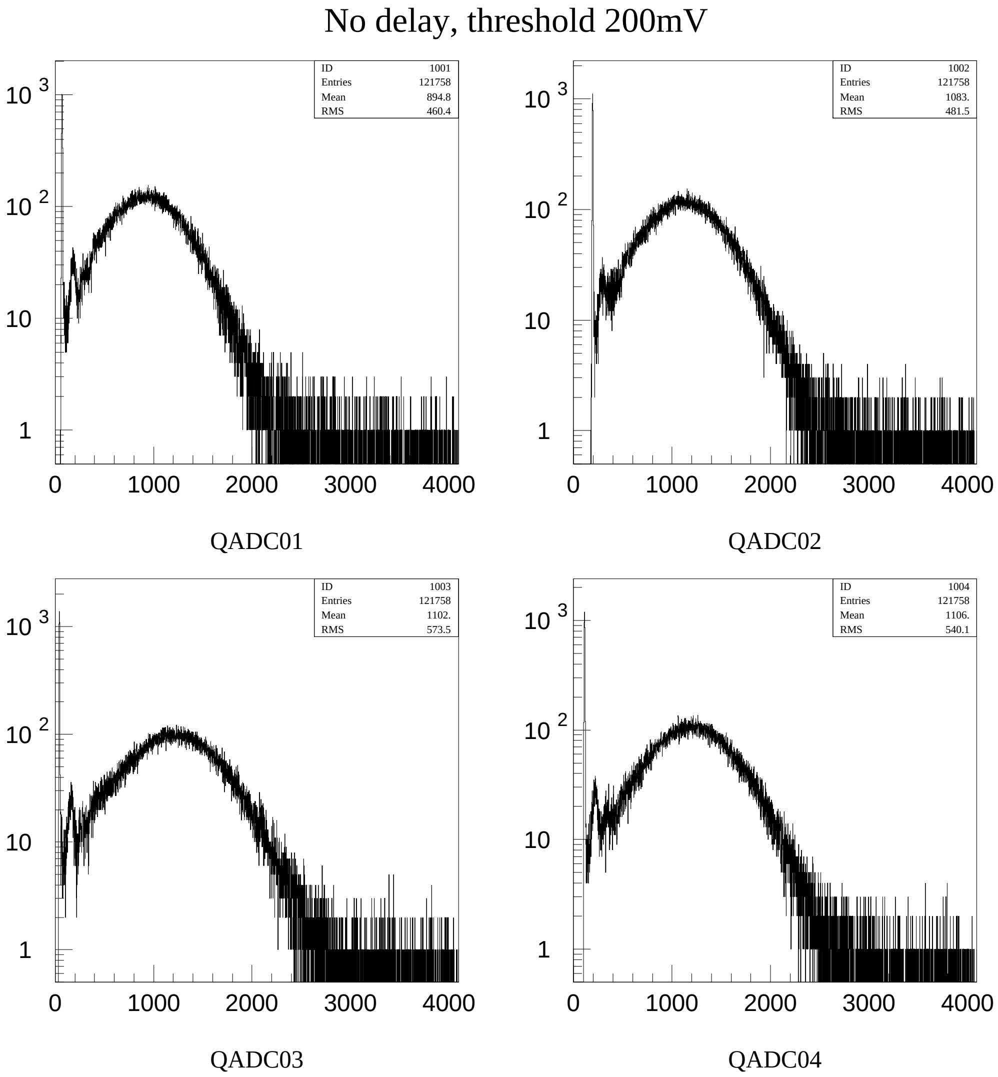

Figure B.1: Normal ADC spectra: PMT 1, 2, 3, 4

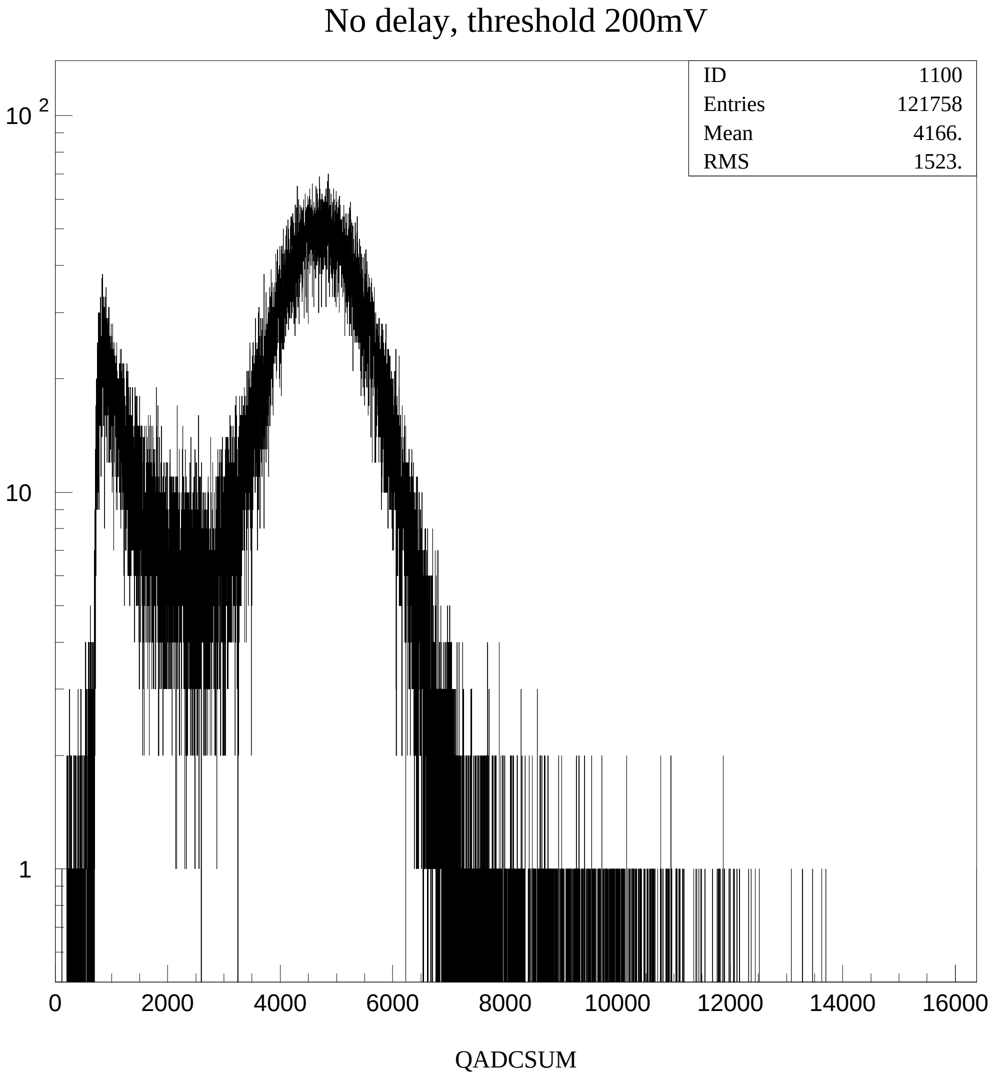

Figure B.2: Normal ADC sum spectrum.

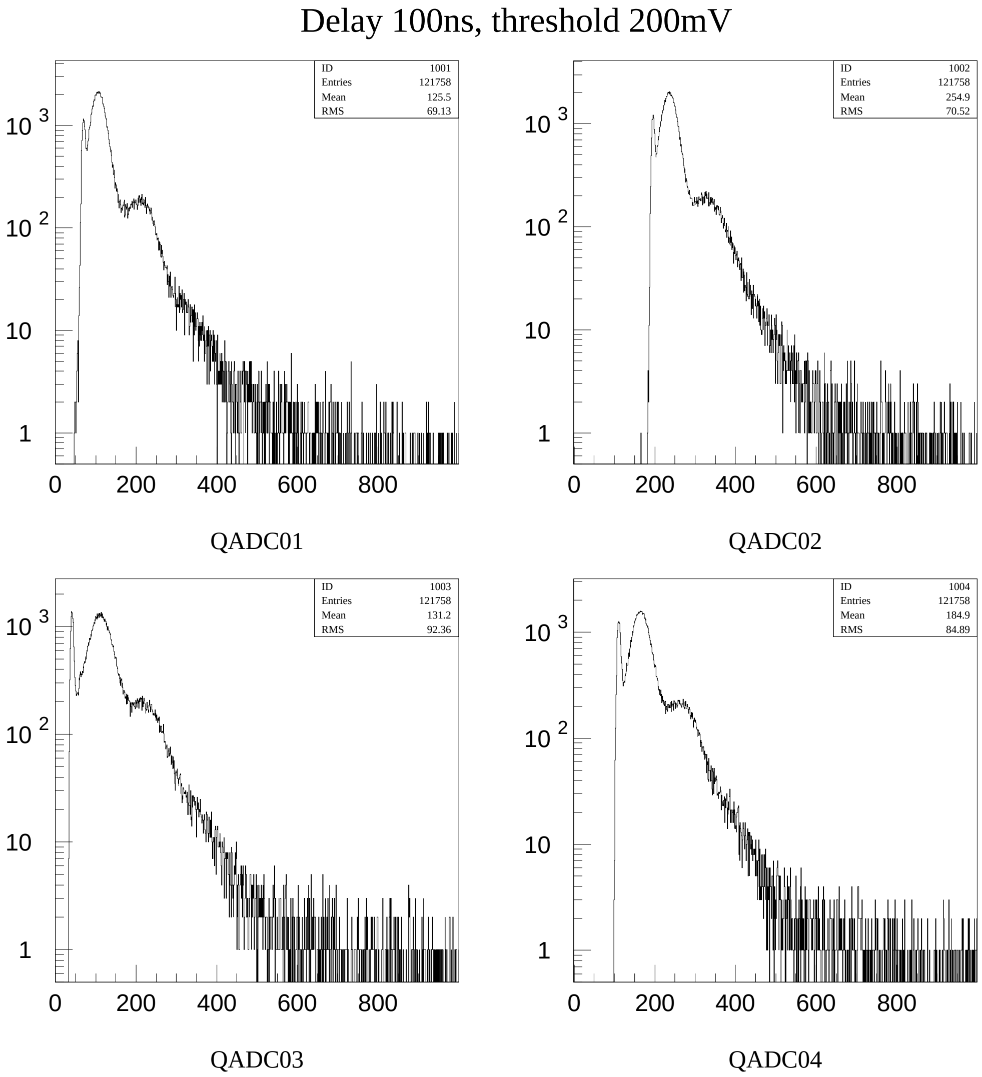

Figure B.3: ADC spectra with 100 ns delayed gate: PMT 1, 2, 3, 4

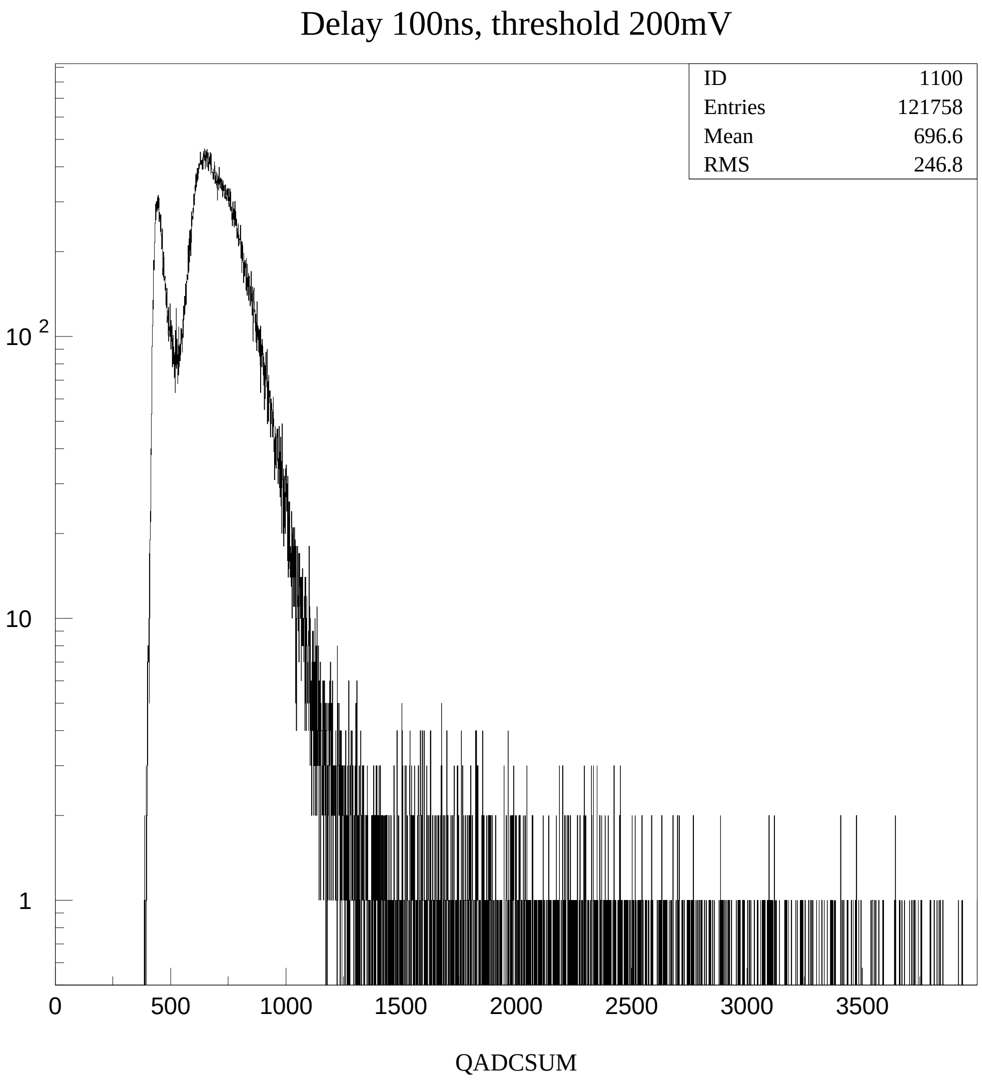

Figure B.4: ADC sum spectrum with 100 ns delayed gate.

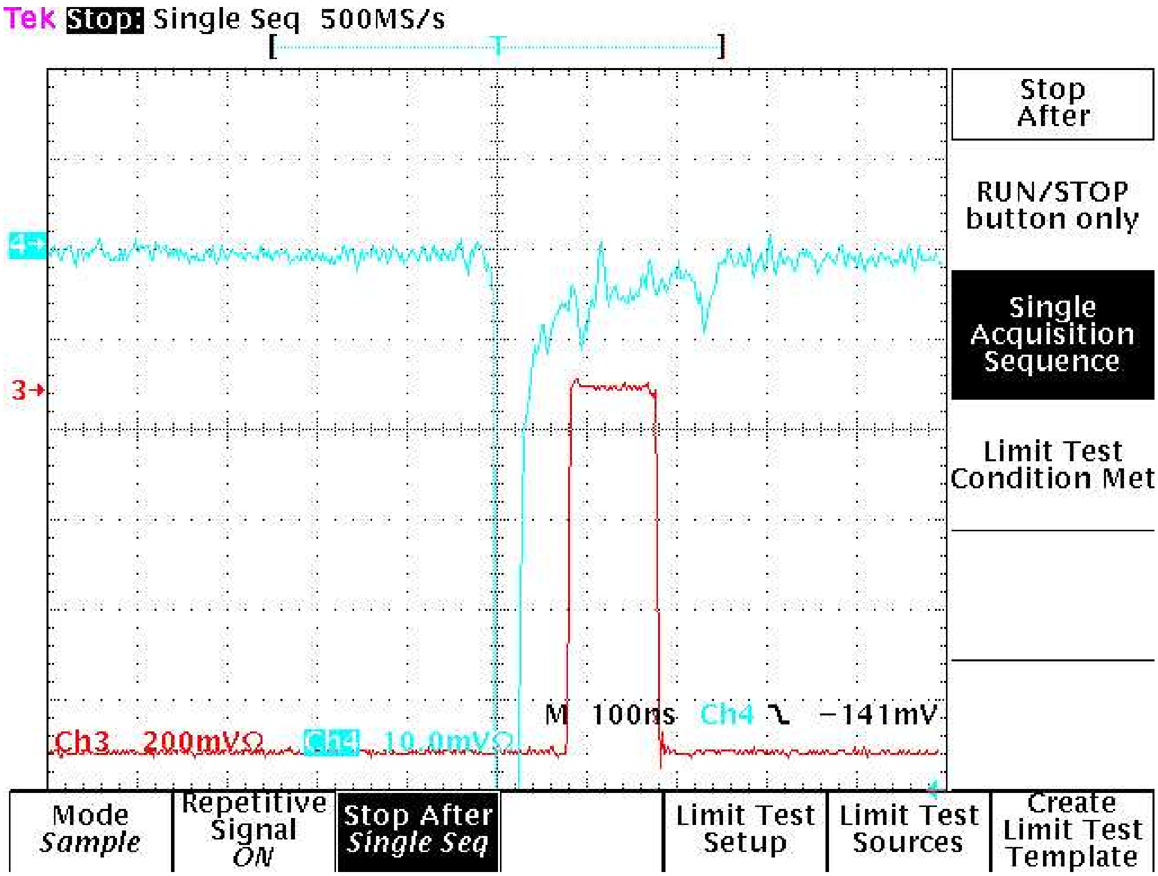

Figure B.5: A sample of pulse from the scope showing the tail associated with it.

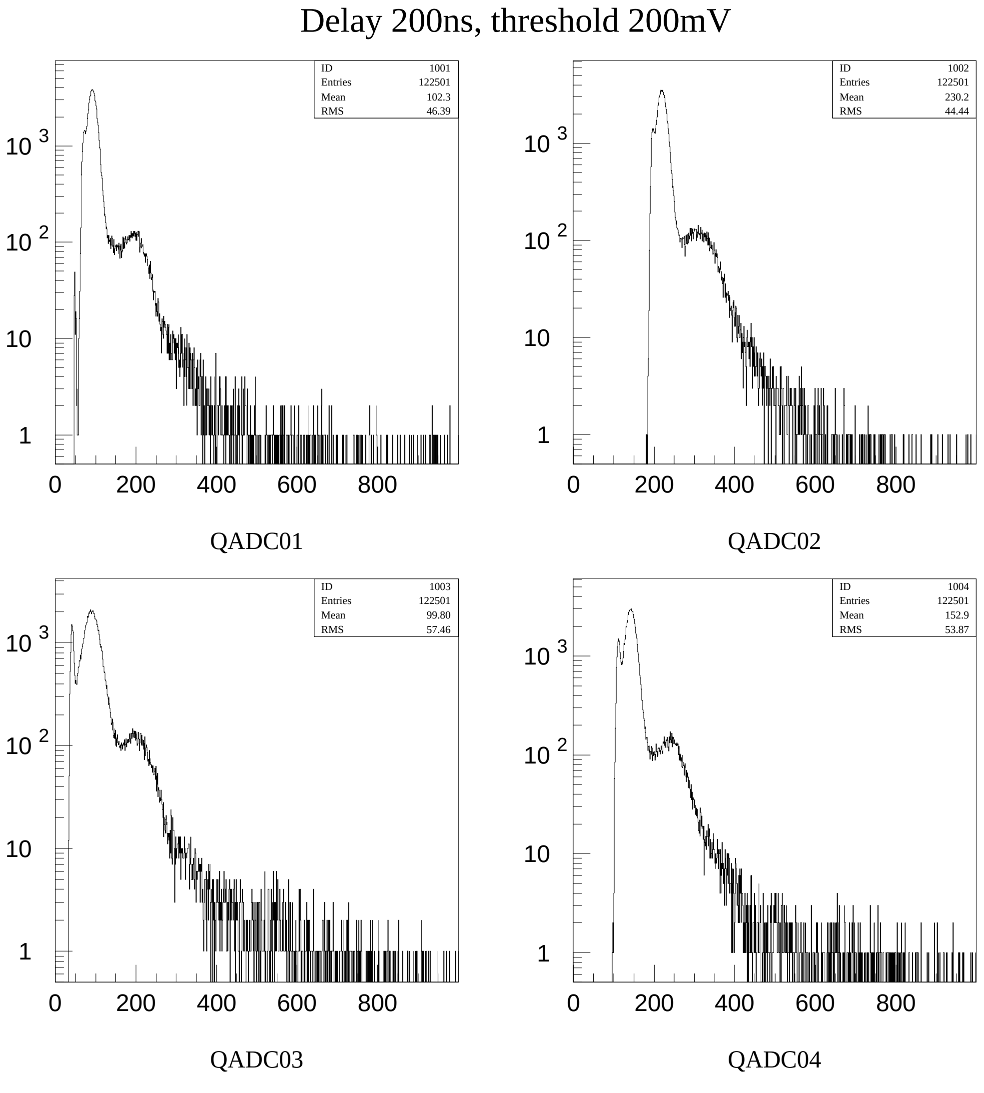

Figure B.6: ADC spectra with 200 ns delayed gate: PMT 1, 2, 3, 4

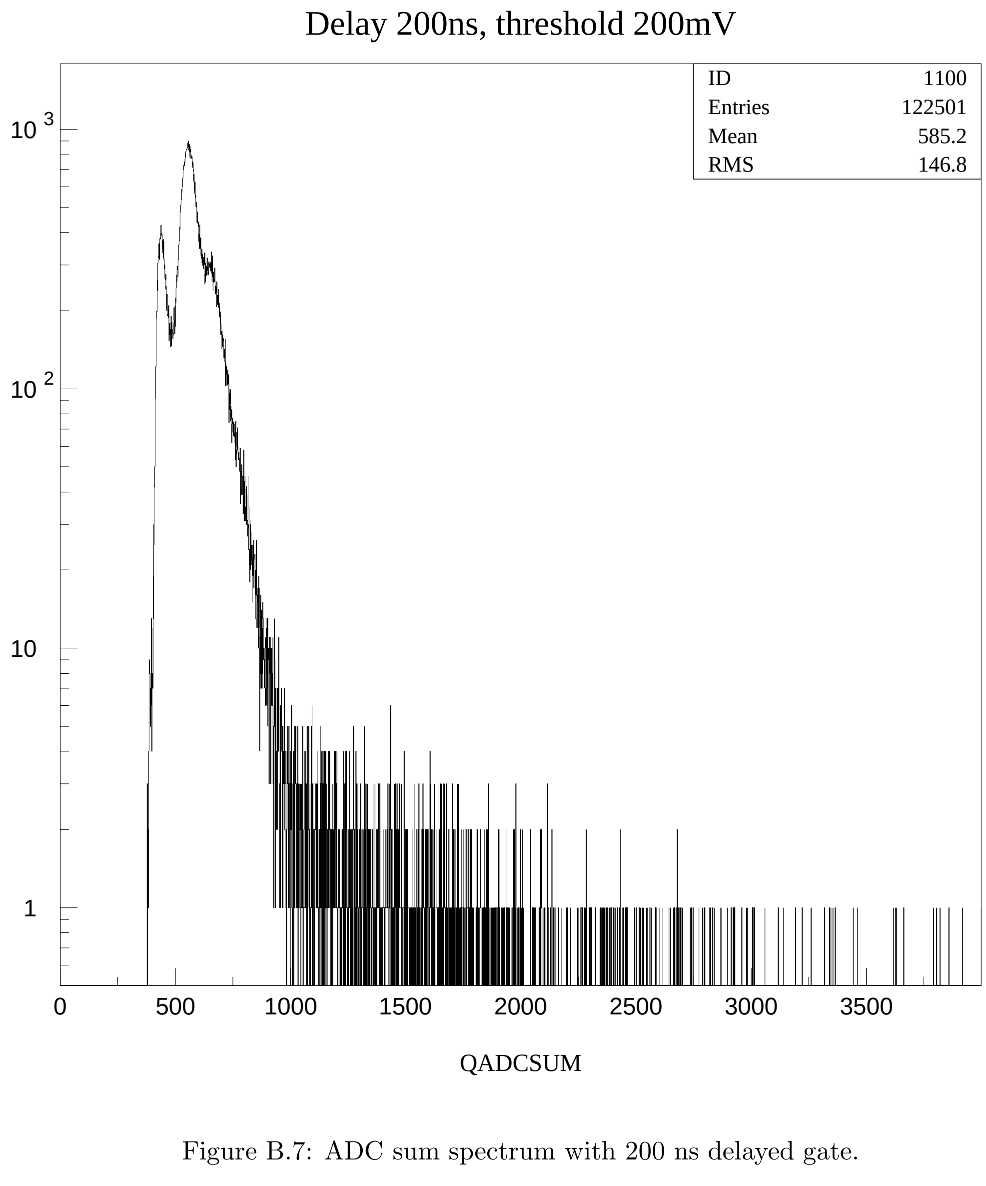

Figure B.7: ADC sum spectrum with 200 ns delayed gate.

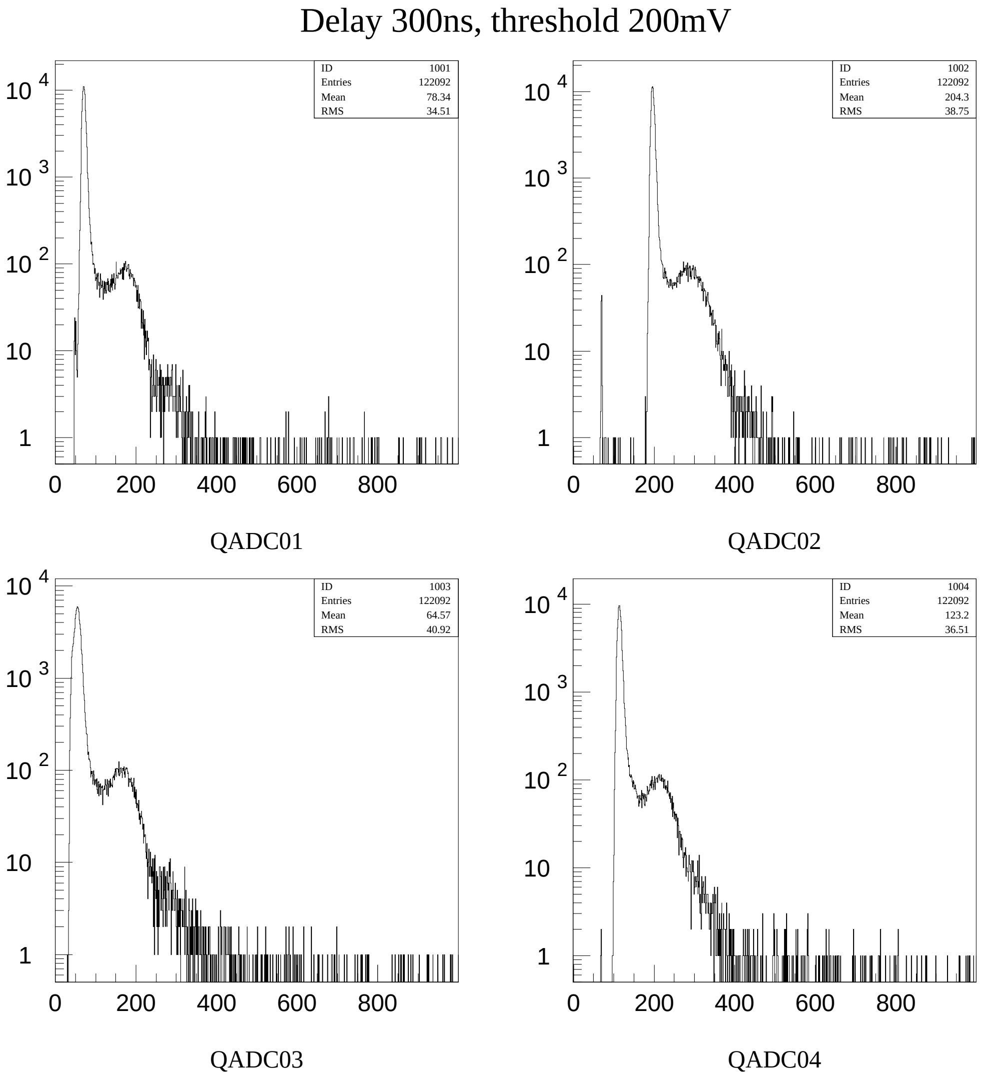

Figure B.8: ADC spectra with 300 ns delayed gate: PMT 1, 2, 3, 4

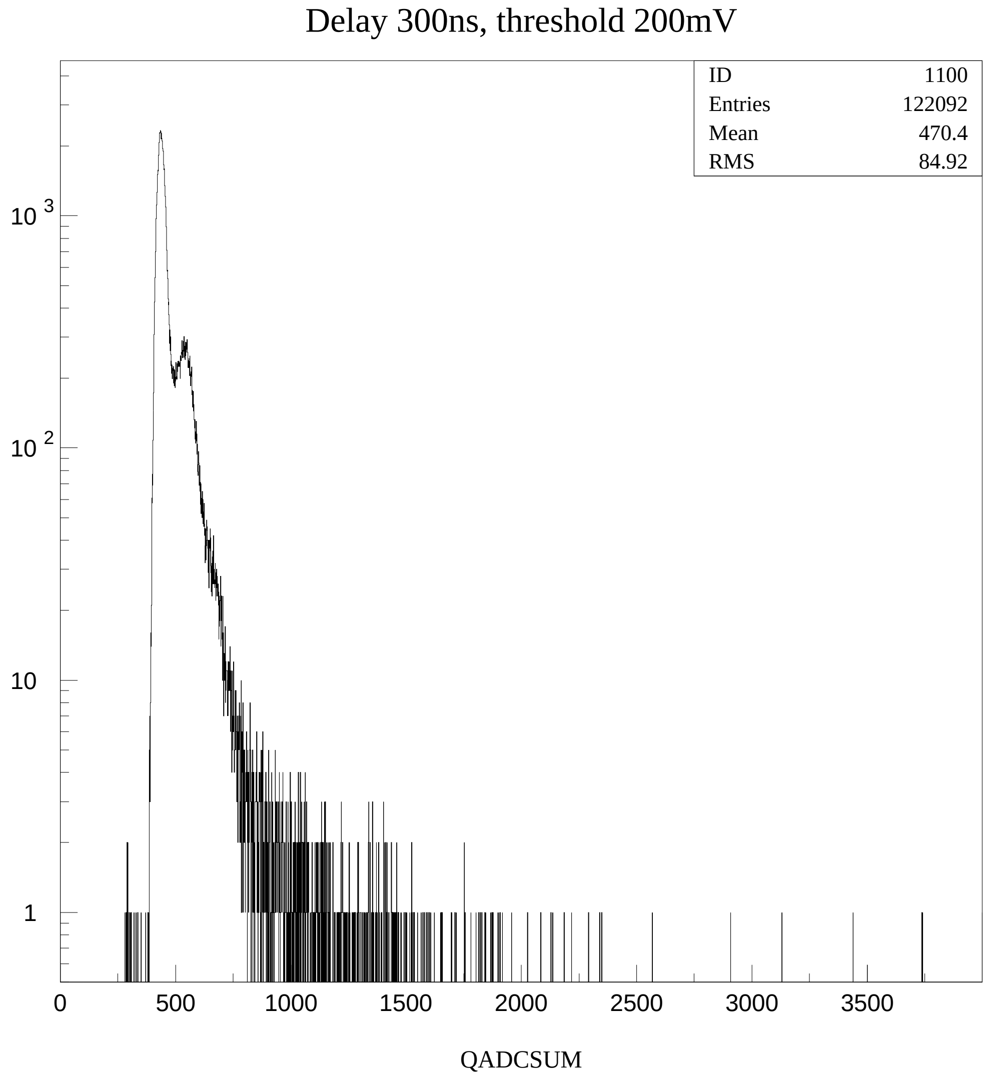

Figure B.9: ADC sum spectrum with 300 ns delayed gate.

getting smaller with larger delay.

With a 400 ns delayed gate, measuring the amplitude distribution of the afterpulses in the region of 400-500 ns after the primary pulses, the ADC spectrum for each tube is shown in Fig. B.10, while the sum spectrum of the 4 tubes is shown in Fig. B.11. These spectra are similar to the ones with 300 ns delayed gate, except that the fraction of SPE afterpulses is smaller, and an excess of pulses higher than SPE pulses is presented. Note that this excess is not presented in the spectrum of tube 2, which is an EMI9954. The other three are Burle8850. We suspect that this excess is specificly for the Burle8850 PMTs.

With a 500 ns delayed gate, the ADC spectrum for each tube is shown in Fig. B.12, while the sum spectrum of the 4 tubes is shown in Fig. B.13. These spectra are similar to the ones with 400 ns delayed gate, an excess of pulses higher than SPE pulses is also presented in 3 of the tubes.

At last we tried with a 600 ns delayed gate, the ADC spectrum for each tube is shown in Fig. B.14, while the sum spectrum of the 4 tubes is shown in Fig. B.15. Now the excess of pulses higher than SPE pulses is gone. Therefore these large afterpulses occur during 400-600 ns after the primary pulse. They are probably attributed to electron bombardment of residual gases in the PMT, according to previous studies [54]. From Fig. 5 of a paper by Torre [55], afterpulses due to H_2^+ and He^+ appear in the region of 400-600 ns after the primary pulse. The presence of Hydrogen is due to residual water, He can permeate from outside [55].

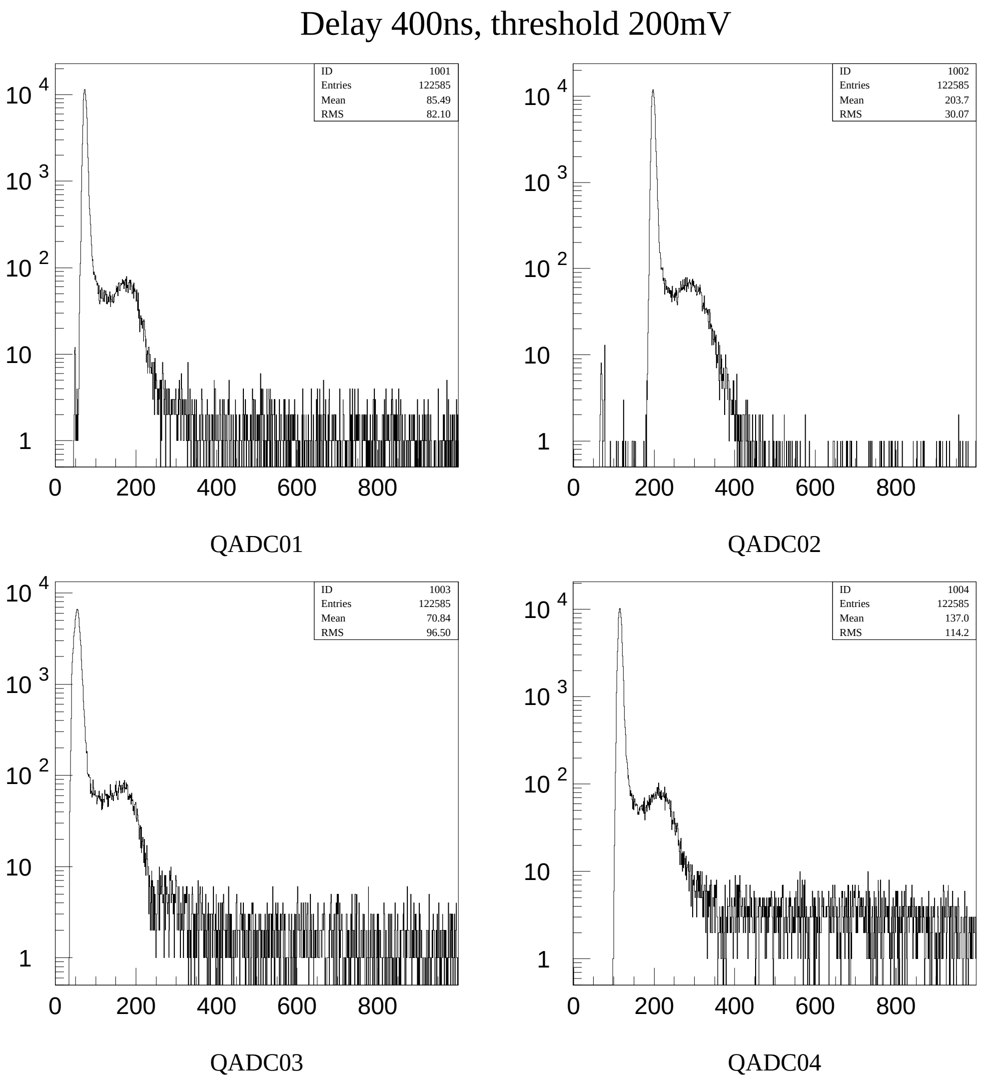

Delay 400ns, threshold 200mV

Figure B.10: ADC spectra with 400 ns delayed gate: PMT 1, 2, 3, 4

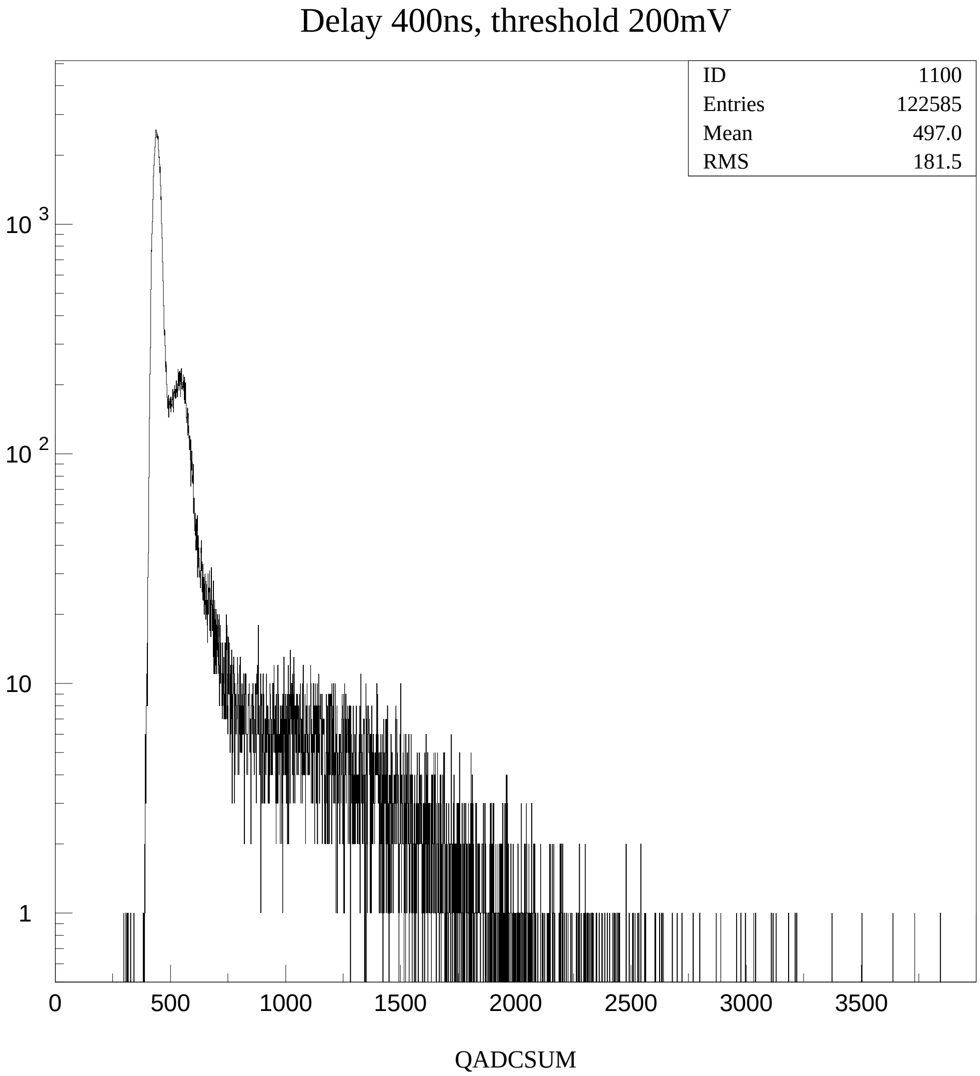

Figure B.11: ADC sum spectrum with 400 ns delayed gate.

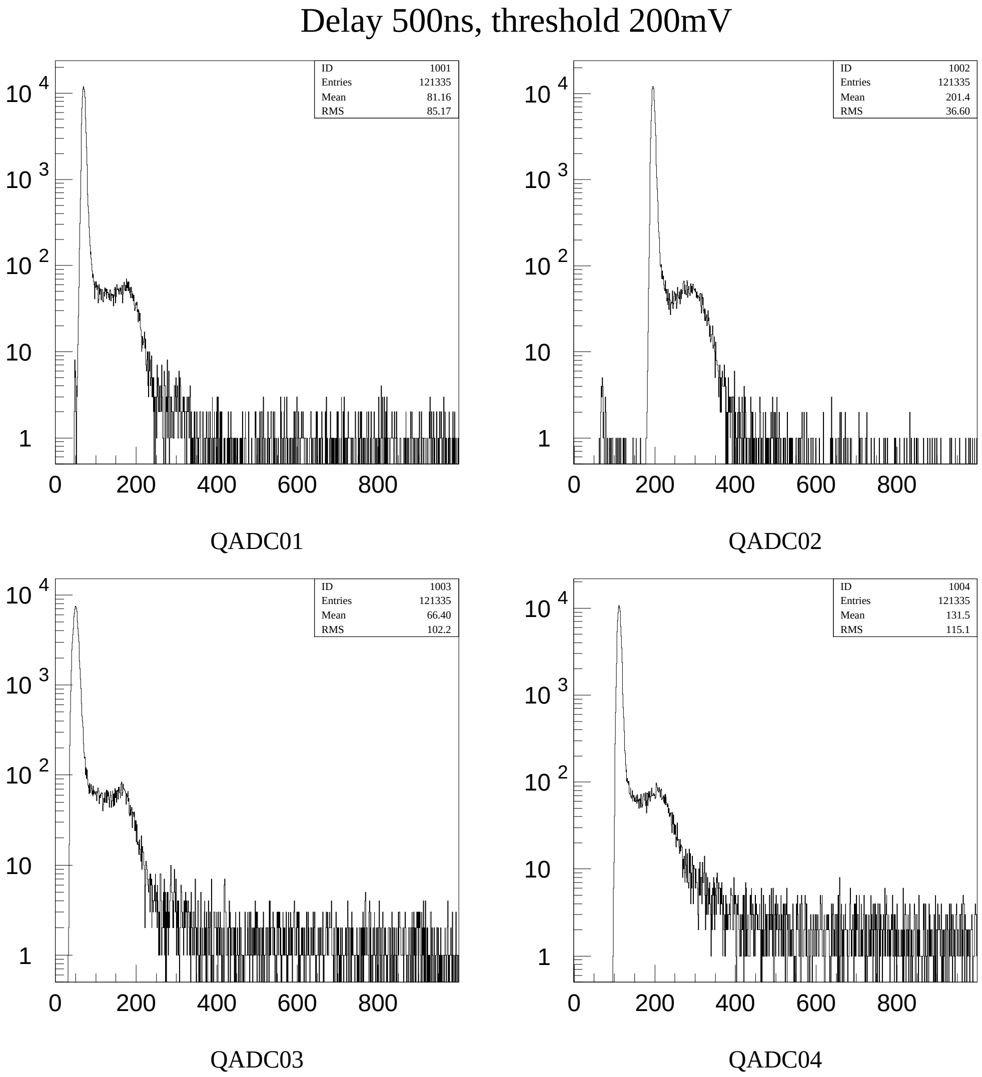

Figure B.12: ADC spectra with 500 ns delayed gate: PMT 1, 2, 3, 4

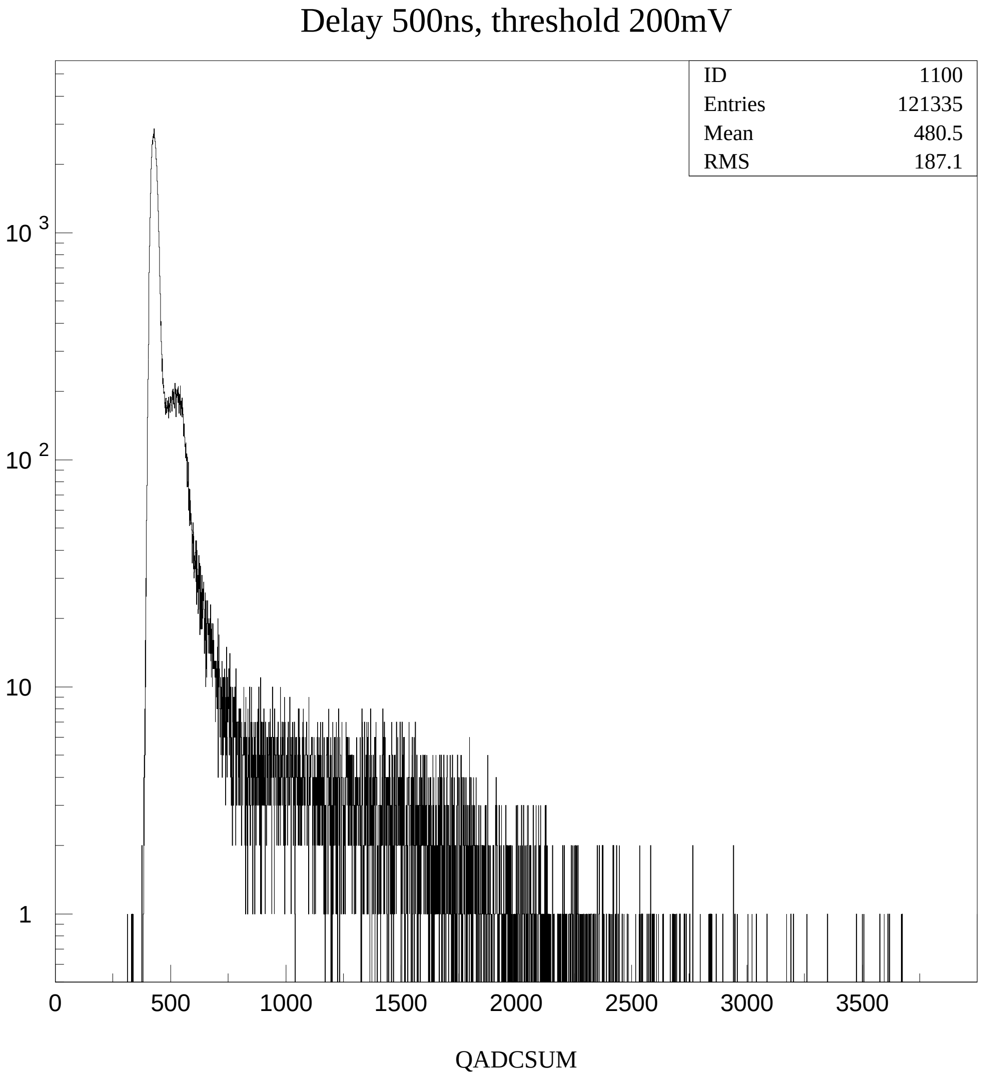

Figure B.13: ADC sum spectrum with 500 ns delayed gate.

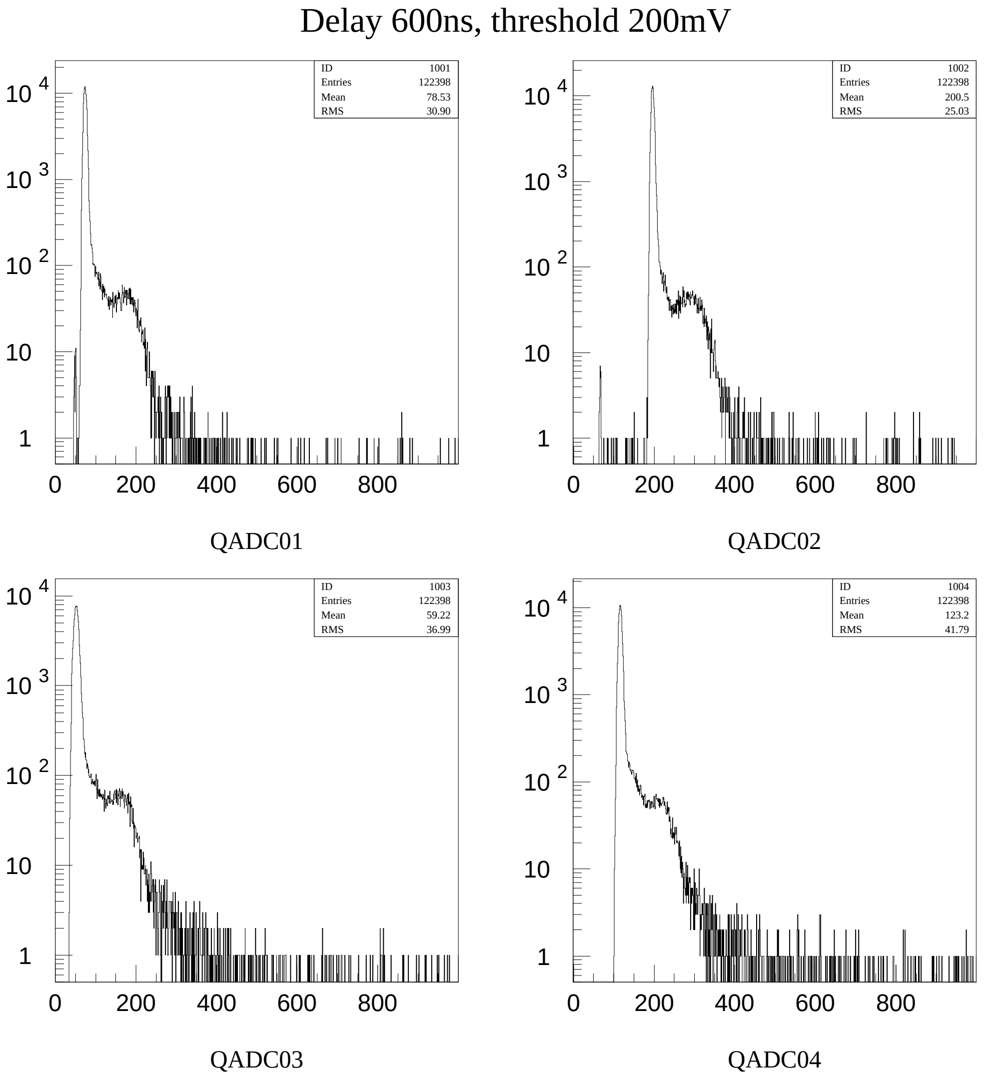

Figure B.14: ADC spectra with 600 ns delayed gate: PMT 1, 2, 3, 4

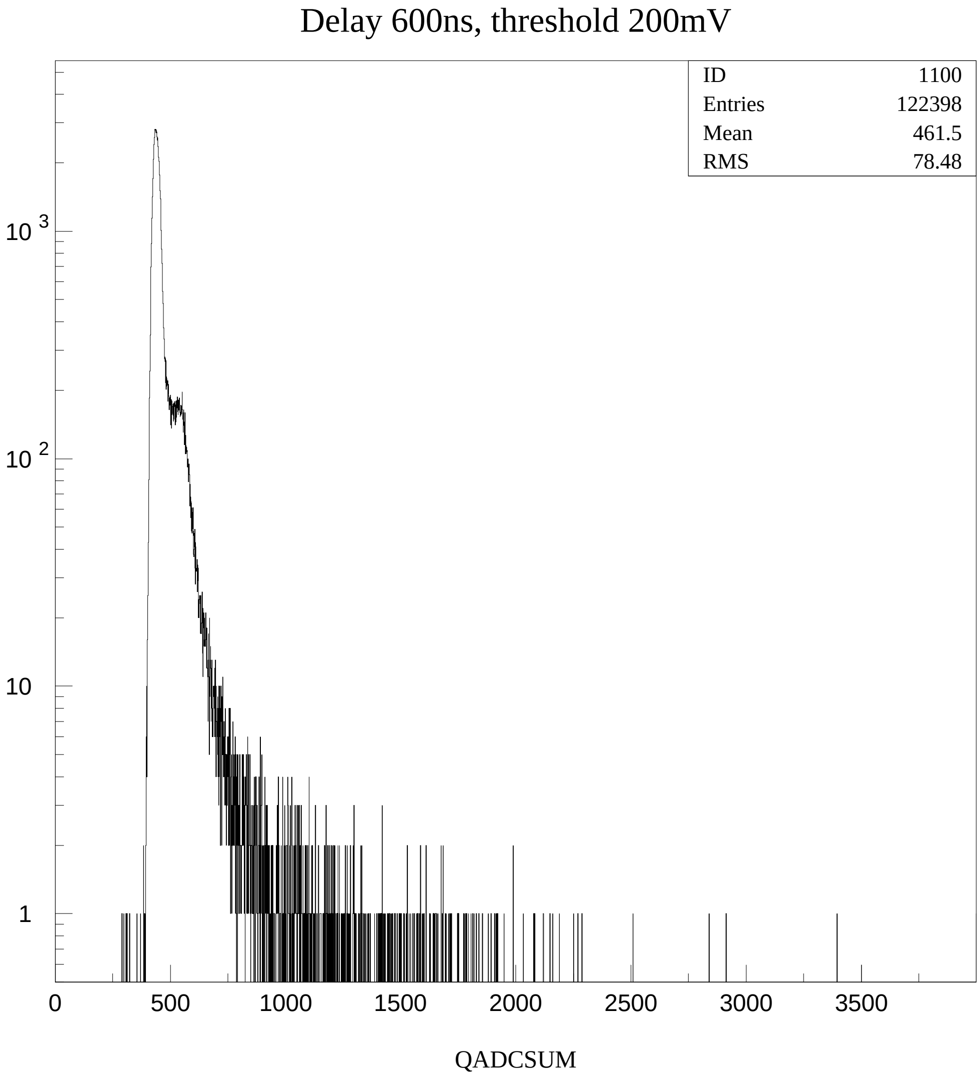

Figure B.15: ADC sum spectrum with 600 ns delayed gate.

Bibliography

[1] B. Holstein, Rev. Mod. Phys. **46**, 789 (1974).

[2] E. Commins and P. Bucksbaum, *Weak Interactions of Leptons and Quarks* (Cambridge University Press, Cambridge, 1983).

[3] J. Jackson *et al.*, Phys. Rev. **106**, 107 (1957).

[4] F. Gluck *et al.*, Eur. Phys. J. **A23**, 135 (2005).

[5] May, 2005, `http://physics.nist.gov/Divisions/Div846/Gp3/FunPhys/littlea.html`.

[6] A. Serebrov, Phys. Lett. **B605**, 72 (2005).

[7] D. Harrington, Phys. Rev. **120**, 1482 (1960).

[8] D. Wilkinson, Nucl. Phys. **A377**, 474 (1982).

[9] S. Gardner and C. Zhang, Phys. Rev. Lett. **86**, 5666 (2001).

[10] A. Sirlin, Phys. Rev. **164**, 1767 (1967).

[11] A. Garcia and M. Maya, Phys. Rev. D **17**, 1376 (1978).

[12] F. Gluck and K. Toth, Phys. Rev. D **46**, 2090 (1992).

[13] R. Shann, Nuovo Cimento **A5**, 591 (1971).

[14] M. Fukugita and T. Kubota, Phys. Lett. **B598**, 67 (2004).

[15] A. Czarnecki *et al.*, Phys. Rev. D **70**, 093006 (2004).

[16] E. Klemt *et al.*, Z. Phys. C **37**, 179 (1988).

[17] P. Bopp *et al.*, Phys. Rev. Lett. **56**, 919 (1986).

[18] J. Dohner *et al.*, Nucl. Instrum. Methods **A284**, 123 (1989).

[19] B. Erozolimskii *et al.*, Phys. Lett. **B263**, 33 (1991).

[20] B. Yerozolimsky *et al.*, Phys. Lett. **B412**, 240 (1997).

[21] K. Schreckenbach *et al.*, Phys. Lett. **B349**, 427 (1995).

[22] H. Abele *et al.*, Phys. Lett. **B407**, 212 (1997).

[23] J. Reich *et al.*, Nucl. Instrum. Methods **A440**, 535 (2000).

[24] H. Abele *et al.*, Phys. Rev. Lett. **88**, 211801 (2002).

[25] I. Towner and J. Hardy, J. Phys. G **29**, 197 (2003).

[26] S. Eidelman *et al.*, Phys. Lett. **B592**, 1 (2004).

[27] Y. Zel'dovich, Sov. Phys. JETP **9**, 1389 (1959).

[28] V. Lushchikov *et al.*, JETP Lett. **9**, 23 (1969).

[29] A. Steyerl, Phys. Lett. **B29**, 33 (1969).

[30] A. Steyerl *et al.*, Phys. Lett. **A116**, 347 (1986).

[31] A. Steyerl and S. Malik, Nucl. Instrum. Methods **A284**, 200 (1989).

[32] R. Golub and J. Pendlebury, Phys. Lett. **A53**, 133 (1975).

[33] R. Golub and K. Boning, Z. Phys. B **51**, 95 (1983).

[34] Z.-C. Yu *et al.*, Z. Phys. B **62**, 137 (1986).

[35] Y. Pokotilovski, Nucl. Instrum. Methods **A356**, 412 (1995).

[36] A. Serebrov *et al.*, JEPT lett. **66**, 802 (1997).

[37] A. Serebrov *et al.*, Nucl. Instrum. Methods **A440**, 658 (2000).

[38] B. Tipton *et al.*, *The beta scintillator detector design report for the UCNA experiment* (UCNA internal report, August 4, 2002).

[39] Eljen Technology, http://www.eljentechnology.com/ej-204.htm.

[40] Burle Photomultiplier Catalog, http://www.burle.com.

[41] Electron Tubes Inc. Photomultiplier Catalog, http://www.electrontubes.com.

[42] T. Ito *et al.*, *UCNA experiment wire chamber baseline design* (UCNA internal report, June 17, 2002).

[43] F. Sauli, CERN Report **77-09** (1977).

[44] J. Yuan *et al.*, Nucl. Instrum. Methods **A465**, 404 (2001).

[45] Group3 Technology Ltd., `http://www.group3technology.com/`.

[46] K. Siegbahn, β-ray-spectrometer theory and design, high resolution spectroscopy, in *Beta- and Gamma-Ray Spectroscopy*, edited by K. Siegbahn, pp. 52–99, North-Holland, Amsterdam, 1955.

[47] D. Roy and D. Tremblay, Rep. Prog. Phys. **53**, 1621 (1990).

[48] K. Siegbahn, Nuclear Physics **1**, 137 (1956).

[49] A. Moussa, Physica **18**, 1120 (1952).

[50] H. Wollnik, *Optics of Charged Particles* (Academic Press, Orlando, 1987).

[51] G. Knoll, *Radiation Detection and Measurement*, 3rd ed. (Wiley, New York, 2000), chap. 8.

[52] J. B. Birks, Proc. Phys. Soc. **A64**, 874 (1951).

[53] J. B. Birks, *The Theory and Practice of Scintillation Counting* (Pergamon Press, London, 1964), chap. 6.

[54] B. H. Candy, Rev. Sci. Instr. **56** (1985).

[55] S. Torre, T. Antonioli, and P. Benetti, Rev. Sci. Instrum. **54** (1983).

[56] The Geant4 Collaboration, `http://cern.ch/geant4`.

[57] The Geant4 Collaboration, S. Agostinelli *et al.*, Nucl. Instrum. Methods **A506**, 250 (2003).

[58] J. Yuan *et al.*, *Simulation of UCNA spectrometer with GEANT4* (UCNA internal report, September 10, 2003).

[59] J. Yuan *et al.*, *Systematic effects due to e- detection in UCNA* (UCNA internal report, December 12, 2003).

[60] The ROOT website, `http://root.cern.ch`.

[61] J. W. Martin *et al.*, *UCNA electronics design, cost, and schedule* (UCNA internal report, February 11, 2003).

[62] The CAEN website, `http://www.caen.it`.

[63] The Struck website, `http://www.struck.de`.

[64] The MIDAS website, `http://midas.triumf.ca`.

[65] M. Berger, in *Methods in Computational Physics, Vol. 1*, edited by B. Alder, S. Fernbach and M. Rotenberg, p. 135, Academic Press, New York, 1963.

[66] J. Fernandez-Varea *et al.*, Nucl. Instrum. Methods **B73**, 447 (1993).

[67] G. Molière, Z. Naturforsch **3a**, 78 (1948).

[68] S. Goudsmit and J. Saunderson, Phys. Rev. **57**, 24 (1940).

[69] H. Lewis, Phys. Rev. **78**, 526 (1950).

[70] D. Liljequist, J. Appl. Phys. **62**, 333 (1987).

[71] D. Liljequist *et al.*, J. Appl. Phys. **65**, 2431 (1989).

[72] D. Liljequist *et al.*, J. Appl. Phys. **68**, 3061 (1990).

[73] F. Salvat *et al.*, Penelope2001, `http://www.nea.fr/abs/html/nea-1525.html`.

[74] P. Gérard *et al.*, Scanning **17**, 377 (1995).

[75] G. R. Massoumi *et al.*, Phys. Rev. Lett. **68**, 3873 (1992).

[76] G. R. Massoumi *et al.*, Phys. Rev. B **47**, 11007 (1993).

[77] T. Tabata, P. Andreo and K. Shinoda, Radiation Physics and Chemistry **54**, 11 (1999).

[78] J. W. Martin *et al.*, Phys. Rev. C **68**, 055503 (2003).

[79] J. W. Martin *et al.*, Phys. Rev. C , (to be published).

[80] The Goodfellow Corporation, 800 Lancaster Avenue, Berwyn, PA 19312-1780.

[81] D. C. Joy, Scanning **17**, 270 (1995).

[82] I. M. Bronshtein and S. S. Denisov, Soviet Physics - Solid State **6**, 2106 (1965).

[83] I. Bronshtein and S. S. Denisov, Soviet Physics - Solid State **7**, 1484 (1965).

[84] H. Drescher, L. Reimer, and H. Seidel, Zeit. Angewandte Physik **29**, 331 (1970).

[85] G. Neubert and S. Rogashewski, Phys. Stat. Sol. (a) **59**, 35 (1980).

[86] J. Sempau *et al.*, Nucl. Instrum. Methods **B132**, 377 (1997).

[87] L. Urban and V. Ivantchenko, private communications (2003).

[88] S. Hoedl, Princeton Ph.D. Thesis (unpublished) (2003).

[89] J. Yuan *et al.*, *Thin mylar backscattering* (UCNA internal report, May 8, 2002).

[90] The NIST ESTAR database, `http://physics.nist.gov/PhysRefData/Star/Text/ESTAR.html`.

[91] C. Morris *et al.*, Phys. Rev. Lett. **89**, 272501 (2002).

[92] A. Saunders *et al.*, Phys. Lett. **B593**, 55 (2004).

[93] Z.-C. Yu *et al.*, Z. Phys. B **62**, 137 (1986).

[94] C.-Y. Liu *et al.*, Phys. Rev. B **62**, R3581 (2000).

[95] C.-Y. Liu *et al.*, Nucl. Instrum. Methods **A508**, 257 (2003).

[96] E. Purcell, Am. J. Phys. **57(1)**, 18 (1989).